The structure and properties of plasma-sprayed 8% yttria-zirconia thermal barrier coatings

Hobbs, Martin K.

Award date:
1989

Awarding institution:
University of Bath

THE STRUCTURE AND PROPERTIES OF PLASMA SPRAYED 8% YTTRIA-ZIRCONIA THERMAL BARRIER COATINGS

submitted by Martin K. Hobbs

for the degree of PhD

of the University of Bath

1989

COPYRIGHT

ProQuest LLC
789 East Eisenhower Parkway
P.O. Box 1346
Ann Arbor, MI 48106-1346

Acknowledgment.

The author is grateful to the following people and organisations for their sponsorship, use of facilities, materials, kind assistance and helpful discussions:

The Science and Engineering Research Council.
Mr. H. Reiter and the staff of the School of Materials Science, University of Bath.
Mr. A. Bennett, Rolls-Royce Ltd., Derby.
T.&N. Technology, Rugby.
Plasma-Technik Ltd., Newport.
Metco Ltd., Chobham.

I am indebted to my family and friends for their support and encouragement.

Finally, I would like to thank my wife, Judith, for her patience, encouragement and typing skills, and without whom, none of this would have been possible.

Summary.

The so-called 'adiabatic' diesel engine attempts to improve thermodynamic efficiency by limiting heat loss from the combustion chamber. Insulation is achieved in practice by incorporating low conductivity ceramic inserts, components or coatings into heat loaded surfaces. Plasma sprayed thermal barrier coatings, consisting of 8% yttria-zirconia, have demonstrated effectiveness and reliability in gas turbines. Thicker coatings intended for diesel engines, however, have not been so successful. Problems associated with transient thermal stress, substrate/coating expansion mismatch, chemical and phase instability and variable properties have been identified.

Performance variations between similar coatings may be attributable to residual stresses developed on cooling after spraying. The effect of processing parameters on residual stress was assessed in two ways. First, a differential etching technique was employed to determine residual stress in the coatings. Process variables such as spray distance, workpiece/sprayhead relative velocity, substrate material and thickness, coating thickness, air cooling and time delay between layers were found to have important effects. Bondcoats were not effective in changing residual stress levels. Second, a theoretical heat transfer model of the spray

process, employing geometrical relationships identical to those used in practical spraying, was developed and used to calculate residual stress levels in model coatings. Good agreement between practical and theoretical results was obtained.

A simplified version of the above model was employed to assess the effects of material properties on insulation effectiveness and coating particle cooling.

The phase stability of sprayed coating samples, using heat treatment temperatures up to 1400C, was investigated using quantitative X-ray diffraction analysis. Differences in the phase stability of chemically similar materials were identified.

Finally, the design of an optimum coating system was discussed in the light of the results obtained in this work.

Contents.

Chapter 1 - Introduction.

1.1 Background.

For more than fifteen years, considerable interest has been shown in improving the efficiency of reciprocating compression-ignition or diesel engines. The impetus for increased engine efficiency has primarily come about because of the rising cost of petroleum fuels. Secondary, but perhaps as important considerations include legislation to reduce the allowable levels of noxious emissions, and the desire to obtain similar performance levels from lower grade or synthetic fuels. Finally, the realisation that fossil fuels are finite resources has prompted moves to reduce consumption.

1.2 Diesel engine efficiency.

The conventional, turbocharged diesel engine typically converts only 36% of the available fuel energy into mechanical work, the remainder being dissipated by the cooling and exhaust systems, [1,2]. Incorporating low conductivity ceramic thermal barriers into the combustion chamber can reduce heat loss to the cooling water to such an extent that the entire cooling system can be discarded, [1,2]. The higher combustion chamber temperature, however, causes heating of the air charge during the intake stroke and the turbocharger

must be re-matched to the engine to maintain volumetric efficiency, [3]. Nevertheless, an improvement in fuel economy can result because of the weight reduction and elimination of water pump parasitic losses, [1,2]. This does not however increase the engine efficiency significantly as the reduced heat loss to the coolant appears as increased exhaust heat energy, [3]. To take advantage of this extra energy, a process known as turbocompounding can be employed. An additional turbine connected to the crankshaft and installed downstream of the original turbocharger recovers mechanical work from the exhaust gases.

The efficiency of this so called 'adiabatic', turbocharged, turbocompounded engine is much improved, with up to 48% of the available fuel energy being converted into useful mechanical work, [1,2]. The overall energy balance for the conventional and the latter type of engine is summarised in figure 1.1.

1.3 Operating conditions.

The operating conditions of a thermal barrier in the combustion chamber are particularly harsh. The material must be able to withstand cyclic temperatures up to 900^{o}C at peak cylinder pressures of 2000psi and be tolerant to thermal up- and down-shocks during the operating cycle, [1]. The combustion environment represents a particular challenge because of the

oxidising, corrosive and explosive nature of the process. Further, thermal gradients both through and across the insulating layer and ceramic-substrate expansion mismatches can lead to high operating stresses, [4,5].

1.4 Insulating material requirements.

Material performance requirements depend to a certain extent on the insulation technique. Currently two routes exist, namely insulation and/or substitution by monolithic ceramics and insulation by ceramic thermal barrier coatings. Generally, either method requires low thermal conductivity materials, resistant to oxidation, corrosion, erosion and thermal shock. Also they should be microstructurally stable at high temperatures. Monolithic ceramics, particularly where they are substituted for existing metallic components , should possess adequate strength and toughness at the operating temperature, similar thermal expansion coefficients to their metallic counterparts, low density and display creep and wear resistance, [2]. The requirements for thermal barrier coatings are somewhat less stringent. Generally the mechanical properties of the underlying metallic substrate are more important in maintaining component integrity. However, a moderate strength and toughness are necessary, together with adequate adhesive strength to operate successfully.

Also, differences in thermal expansion coefficient between substrate and coating must be carefully considered if high operating stresses are to be avoided, [4], and residual stress arising from the spraying process must be controlled to prevent unexpected failures.

1.5 Current materials and applications in diesel engines.

A summary of the properties of some currently available insulating ceramics, and the metallic materials they are intended to replace, is given in table 1.1.

Monolithic ceramic materials can be physically attached to existing metallic components to provide an insulating layer, or complete substitution may be possible. Materials such as partially stabilised zirconia (PSZ), [1,6,7], silicon nitride, [8], silicon carbide, [9,10] and aluminium titanate, [1,10], have been used to make piston inserts, [1,6,8,10], cylinder liners, [1,6,9], valves, valve seats and valve guides, [1,6], exhaust port liners, [1], headface plates, [1,7] and turbocharger rotors, [10]. The exceptional hardness may also be of primary consideration when reduction of wear, particularly under poor lubrication conditions, is necessary, [2,10]. Difficulties exist however in designing components in such brittle materials and

achieving reliability, [3,5]. This has caused a significant change in the mechanical design philosophy for such materials, involving such concepts as that of failure probability, [11].

The alternative route for combustion chamber insulation involves plasma spraying ceramic thermal barrier coatings, generally of stabilised zirconia, onto modified metallic components. Coatings have been successfully applied to piston crowns, [1,4,8,12,13], valve seats and faces, [8,12,13], cylinder heads, [1,12,13], cylinder liners, [2,12,13] and to line exhaust ports, [1]. The obvious advantage of this technique is that existing metallic component designs need only be modified to incorporate the insulating layer. The thickness and properties of the layer can also be tailored to suit the particular application. For example, the wear characteristics of zirconia liner coatings are significantly improved by chromia impregnation, [14]. Another benefit is that the relatively expensive ceramic material can be deposited exactly where needed and of the specified thickness.

However, problems of premature failure have cast doubts on coating durability in the combustion environment. The factors affecting coating lifetime will be discussed fully in chapter 2, but at this stage it suffices to point out that failures have been attributed to a number of causes including

coating-substrate expansion mismatch, [4], stress arising from adverse component geometry, [15], corrosive leaching of coating stabilisers by combustion deposits in engines operating on low grade fuel oils, [16], and variability in coating manufacture, [17]. Significant problems have been encountered in attempts to use thicker coatings. Depending on the material and application, thicknesses of between 3 and 6mm are required to achieve adequate insulation, [2,13,18]. Rapid failures have occurred when coatings in the range 1-2mm are deposited, [4,13,17]. These failures may be attributable to residual or internal stresses that can limit the maximum thickness unless spraying conditions are closely controlled, [19].

1.6 Development of plasma sprayed thermal barrier coatings.

It is obvious that the most successful insulation method will be selected for inclusion into engine designs. Thermal barrier coatings deposited by plasma spraying have demonstrated their potential for efficient insulation, both in gas turbines and diesel engines. However, problems with coating reliability in the latter may prevent their successful commercial application. Until comparitively recently, development relied largely on empirical data and experience and was achieved without a fundamental understanding of the

effects of process variables on the coatings so produced. Further devlopment of thermal barrier coatings, particularly for demanding automotive applications, now requires a greater insight into the spray process and subsequent coating behaviour. This knowledge is essential for the production of reliable, thick, resistant coatings on a repeatable basis.

Chapter 2 - Literature Survey.

2.1 Introduction.

The purpose of this literature survey is to identify those areas of ceramic thermal barrier coating technology where critical aspects of behaviour and performance limit their successful application in insulated diesel engines.

Relevant publications in both gas turbine and diesel engine fields are considered and areas of common experience are identified. A general consideration of the relationships between plasma spray parameters, coating and substrate materials and the properties of the final coating are presented first, followed by a survey of coating performance and failure mechanisms. Finally, having identified those areas where understanding and performance may improve with further work, the relevant literature is considered in detail.

2.2 Zirconia thermal barrier coatings.

A zirconia thermal barrier coating system consists of at least two layers of different materials. A thin metallic bond layer, usually of a nickel base alloy, is deposited onto a roughened substrate to provide oxidation resistance and improve the bonding characteristics of the ceramic-metal interface. Depending on the severity of the operating conditions

and the mismatch in thermal expansion coefficients between substrate and zirconia ceramic, the composition of subsequent layers may be graded from 100% metal to 100% zirconia, or may simply be all ceramic. The thickness of the insulating layer is chosen to provide the required temperature drop under a given set of operating conditions.

2.3 Plasma spray deposition.

As it's name suggests, plasma spraying or plasma 'flame' spraying utilizes the very high temperatures of an arc plasma to soften or melt materials which are subsequently deposited onto a substrate. The process may be carried out in air, inert atmosphere or low pressure and most ceramic and metallic materials can be sprayed.

The device which generates the plasma flame is known as a plasma gun or torch and a simplified schematic diagram is shown in figure 2.1, after [20]. An electrically insulating, enclosed chamber supports a tungsten tipped, water cooled copper cathode and a hollow water cooled copper anode. An arc is struck and maintained between the electrodes using a variable D.C. supply capable of delivering up to 100 kW of electrical power. A gas introduced into the chamber is rapidly dissociated and/or ionized in the high energy arc stream. The relatively cool gas constricts the arc,

raising its temperature, and forces it into the anode nozzle where its temperature is further increased. Almost complete heat exchange occurs between the arc stream and gas, and the pressure/temperature are such that a high velocity (100-200ms^{-1}) neutral or free plasma 'flame' exits from the anode with core temperatures up to 15000K, [20]. A carefully metered supply of powdered material is injected into the 'flame', generally at the nozzle exit. The particles are heated/melted in the plasma and accelerated towards the workpiece, where they impact, deform, cool and solidify rapidly building up a porous, lamellar coating.

The fundamental parameters controlling the quality of plasma sprayed coating have been examined, and fall broadly into three categories related to plasma, powder and substrate, [21,23].

2.4 Plasma torch operating parameters.

The behaviour of particles in the plasma flame and the coatings so produced have been extensively investigated, [22,23,24,25,26,27,28]. For a particular plasma torch configuration, arc current, plasma gas flow and gas composition have been identified as being of particular importance, because they control the temperature and velocity of the flame and therefore the residence time and heating of individual particles.

2.4.1 Plasma arc electrical input power.

At a fixed gas flow rate and composition, higher electrical input power increases the plasma temperature, and therefore enthalpy, because more complete gas ionization occurs. The effect is to increase plasma velocity and decrease particle residence time, [22]. Depending on the particular conditions, increased input power may, [23], or may not, [28], raise particle temperatures, because of the trade-off between heating rate and time available for heating.

The practical effects of increased power levels have been investigated in cyclic burner rig testing of thin (0.32-0.44mm thick) zirconia coatings intended for gas turbine operation, [29,30]. At low power, both bond and zirconia layers contained significant included porosity distributions, leading to low cohesive strength. A minimum arc current, (600A, voltage unspecified), was necessary to obtain a life expectancy of greater than 500 cycles. At higher power levels, improved particle flow was noted, consistent with higher particle temperatures, and the bonding area between particles increased, together with a visible reduction in porosity. The latter was assumed responsible for reducing bond coat oxidation, which may limit the useful life of such coatings, by limiting the extent of gaseous penetration. Microcracking of the ceramic layer

increased with density and was assumed to be beneficial in that it may have contributed some pseudo-ductility to the brittle zirconia layer.

2.4.2 Plasma arc input gas flow.

Variations in plasma gas flow rate similarly affect the plasma flame temperature and velocity. At low flow rates, the mass energy of the flame, [27], and the residence time are increased, [28], leading to improved particle heating but the flame velocity, and hence particle impact velocity, is reduced. Again a balance between the various flame parameters is required to achieve adequate melting. Also, a minimum gas flow is necessary to maintain a stable arc, [27].

2.4.3 Plasma arc gas composition.

Of particular significance is the gas composition. A number of gases are currently used for plasma generation including argon, helium, hydrogen and nitrogen. In the arc stream, the gas molecules are dissociated if diatomic, and then ionized to higher energy states. In the neutral plasma flame, electron-ion and atom-atom recombination processes occur releasing quanta of energy, some of which are transferred to the powder particles as heat. Because a state change is involved, much larger quantities of heat are transferred to the powder than by conduction

or radiation, [20]. Provided that the energy or enthalpy content of the plasma flame is high enough, and the residence time is sufficiently long, the particles are heated and melted. The energy content of the commonly used gases at particular temperatures are given in figure 2.2. It is immediately obvious that both the diatomic gases, hydrogen and nitrogen, possess significantly higher energies in the dissociated and ionized state at lower temperatures. The monatomic gases, argon and helium, only become ionized at very high temperatures. Once more, the choice of plasma gas composition is dictated by the particle melting requirements. For example, at high temperatures, the viscosity of the gases is such that under the same arc current and gas pressure conditions, pure hydrogen gives the highest velocity plasma ($1200ms^{-1}$), and argon the lowest ($400ms^{-1}$), however, the power required to achieve a given current density is the highest for hydrogen (120V) and the lowest for argon (20V). Plasma temperature, within 1000K, was equivalent for argon, nitrogen and hydrogen [23]. Generally, plasma spraying is carried out using argon or nitrogen, with hydrogen added to improve heat transfer. Above the dissociation temperature for hydrogen (~4500K), the mean thermal conductivity is about $5Wm^{-1}K^{-1}$ compared to $0.1Wm^{-1}K^{-1}$ and $0.04Wm^{-1}K^{-1}$ for nitrogen and argon respectively, [23]. Addition of hydrogen in small percentages (5-20%)

raised the voltage necessary to achieve a given current density ie. decreased the conductivity, and the velocity, temperature and enthalpy of the plasma were significantly increased together with the length of the plasma flame, [23,26,29]. It was also shown to improve melting, [26,28], and particles were assumed to reside for a longer distance in the hotter plasma flame, improving the final coating density, [28]. Unfortunately the wear life of electrodes and the risk of consequent copper contamination was increased with hydrogen levels greater than 50%, [28]. Burner rig testing showed that for constant power conditions, the addition of hydrogen to pure argon reduced thermal cycle life, because lower plasma and therefore particle temperatures, and higher velocity, leading to decreased residence time, were experienced. Enhanced oxidation of bond coats, presumably caused by lower density coatings was also noted, [29]. Increasing the power input level for the same argon-hydrogen mixture improved the cyclic lifetime.

2.4.4 Optimisation of plasma torch operating parameters.

The complex interactions outlined above have often led to torch parameter optimization by combination of experiment and experience. An alternative approach, [27], suggests that material deposit efficiency is a

useful measure of flame parameter optimization, and has led to the development of an empirical relationship of the form;

Deposit Efficiency = f(R)

where $$R = \frac{P.H}{A}$$

and P = Electrical input power

H = % hydrogen

A = argon flow.

The deposit efficiency for various materials, including zirconia, alumina and Ni-Al powder, was found to increase smoothly with increasing R ratio up to a maximum. This is illustrated in figure 2.3, after [27]. Above the limiting value, coatings produced were of a similar density allowing optimisation of the constituent parameters of R for economic operation of the plasma torch. Hence a choice of two parameters leads to the third through a limiting R value, although consideration must be given to gun operating stability and electrode life as previously mentioned.

2.5 Thermal barrier coating materials.

Having described the important parameters which affect plasma generation, the next step is to consider

the coating materials themselves.

2.5.1 Bondcoat materials.

Zirconia thermal barrier coatings contain at least one additional metallic bondcoat layer adjacent to the substrate. The function of the bondcoat is to allow some compliance between the ceramic coating and metallic substrate, in order that any thermal expansion mismatch strain may be accommodated and adhesion improved. The ability of the bondcoat to deform freely at high temperatures is thus of particular importance and depends on the extent of internal oxidation, [31]. Therefore the composition is chosen to minimize high temperature oxidation and as a consequence Superalloy type materials have been favoured. An additional benefit is that the layer also provides an oxidation/corrosion barrier to the substrate. Generally, bond coat alloys are based on nickel or cobalt, with additions of chromium, aluminium, yttrium and zirconium, [32,33], and are manufactured by atomisation. The morphology of a typical bondcoat powder material is illustrated in plate 2.1a. The most durable composition was found to contain nickel, 14%-chromium, 14%-aluminium, 0.1%-zirconium, [33]. The reactive nature of this powder is such that best results were obtained when the material was deposited using a low pressure (soft vacuum) plasma spray system.

The metallic 'splats' or layers in the coating were found to have undergone less oxidation in the flame [33]. Good results have also been obtained with air plasma sprayed bond coatings of nickel 17%-chromium, 5.4%-aluminium, 0.35%-yttrium, [32]. In each case the minority addition (Zr or Y) had the greatest effect on oxidation resistance. Simpler, less resistant systems, based on Ni-Cr and Ni-Cr-Al have also been used. Generally bond coat thicknesses in gas turbine applications lie in the range 0.1 - 0.2mm.

2.5.2 The stabilised zirconia system.

Before discussing zirconia powder materials, it is first necessary to consider the technologically important stabilized zirconia system in general.

Pure zirconia, ZrO_2, is a polymorphic material. The cubic phase is stable from the melting point at 2680°C down to 2370°C and has a fluorite type cubic structure. At 2370°C a diffusional transformation to a tetragonal structure begins and this remains stable to approximately 1170°C, [34]. Below 1170°C, and over a significant temperature range, a diffusionless, reversible martensitic transformation occurs, resulting in the formation of monoclinic zirconia, [35]. The pure tetragonal phase cannot be quenched to room temperature, [36]. Accompanying the transformation from tetragonal to monoclinic phase is a large, (~4%)

disruptive volume expansion, which can lead to disintegration of pure zirconia on cooling. The high temperature polymorphs may be 'stabilized' to room temperature by additions of oxides such as calcium oxide (CaO), magnesium oxide (MgO), yttrium oxide (Y_2O_3) and other rare earth oxides including cerium oxide (Ce_2O_3), hafnium oxide (HfO_2) and ytterbium oxide (Yb_2O_3). The phase diagrams of the three most important systems, zirconia-calcia, [37], zirconia-magnesia, [38], and zirconia-yttria, [39], are reproduced in figures 2.4, 2.5 and 2.6 respectively. Addition of the stabilizing oxide permits retention of cubic zirconia to lower temperatures than is possible in the pure state. If sufficient stabilizer is present, and quenching rates are high enough, then the structure may consist almost entirely of the cubic polymorph at room temperature, [40]. Depending on the amount of stabilizer added, the material may be known as partially- (PSZ) or fully stabilized- zirconia (FSZ), the latter containing the greater proportion of added oxide and exhibits almost wholly cubic structures. PSZ on the other hand generally contains a mixture of tetragonal, monoclinic and cubic phases. Ageing of sintered, quenched PSZ in the cubic+tetragonal phase field results in intragranular precipitation of fine coherent tetragonal precipitates. Provided that they remain coherent and below a certain size (0.04mm thick

Mg-PSZ, 0.1mm thick Ca-PSZ) they are metastably retained on cooling to room temperature,[41], and are found to confer considerable strength and toughness to the ceramic.

The origin of these remarkable properties lies in the ability of tetragonal precipitates to spontaneously transform to monoclinic symmetry in the stress field ahead of a growing crack, [41,42]. The phenomena is known as transformation toughening. First, however, sufficient free energy must be supplied to the tetragonal precipitate to initiate the transformation. This energy can be supplied by the strain energy of the stress field ahead of a growing crack, or effectively by removal of the matrix constraints which prevent transformation. In most practical applications the former applies and the volume of the particle increases, (by ~4%), causing a mismatch strain and lowering of the local crack tip stress in a crack-shielding process. Transformation occurs in a wake surrounding the growing crack, whose dimensions are related to the applied stress. A further toughening contribution due to crack blunting or branching may occur with the formation of microcracks around transformed precipitates. A more complete treatment based on thermodynamic and/or fracture mechanics considerations is given in references [35,43,44].

The stabiliy and size of tetragonal precipitates is

also related to the solubility of the stabilizing ion in zirconia. Yttria has the highest solubility of the economically important systems, and also exhibits the largest, most stable tetragonal precipitates, existing in colonies of twinned stacked plates, [34]. The unique stability of yttria-PSZ even allows manufacture of material consisting wholly of tetragonal crystals at low yttria dopant levels (2-4 mol%). The structure is characterised by extremely fine grain sizes, (0.2-1.0μm), allowing the retention of tetragonal symmetry, stability at high temperatures due to its single phase structure and enhanced strength and toughness. The material is commonly termed tetragonal zirconia polycrystals or TZP.

The lower solubility of magnesia in Mg-PSZ and poor diffusion kinetics of Ca-PSZ or Y-PSZ result in the former system being the only one that undergoes eutectoid decomposition in reasonable time scales at elevated temperatures, [34]. Ageing above or below the eutectoid temperature allows the formation of tetragonal or monoclinic zirconia respectively, together with free magnesia. Sub-eutectoid ageing of sintered Mg-PSZ has been investigated particularly because of an enhanced thermal shock resistance imparted to the material by this treatment. At 1200°C-1300°C, cubic zirconia decomposes to equilibrium MgO and monoclinic zirconia cellular structures, [40].

At 1100°C , a stable, ordered δ-phase, $Mg_2Zr_5O_{12}$, grows at the expense of tetragonal precipitates, and transforms to monoclinic zirconia on cooling to ambient temperature. The formation of this latter phase was associated with enhanced thermal up-shock resistance, [45]. Overageing at this temperature results in nucleation and growth at grain boundaries of the previously mentioned cellular monoclinic zirconia and magnesia eutectoid reaction products, [34].

Rapid cooling of yttria-PSZ materials, in the composition range ~2 to ~7 mol% yttria, suppresses the normal diffusion controlled cubic-tetragonal reaction in favour of a displacive, composition-invariant transformation to a tetragonal phase, denoted t', containing an excess of yttria. [39]. Ageing in the cubic+tetragonal phase field for sufficient time allows a diffusion controlled reaction to occur such that colonies of low-yttria tetragonal precipitates form in a high-yttria cubic matrix, the compositions of each phase being determined by their respective solvus'.[34]. High-yttria tetragonal phase, t', has been observed in arc melted samples, [39], zirconia-8 wt% yttria quenched single crystals, [46], and plasma-sprayed zirconia-8.6 wt% yttria thermal barrier coatings, [47]. Examination of the single crystals in a T.E.M. revealed a blocky, twinned t' matrix containing antiphase domain boundaries and colonies of low-yttria,

twinned tetragonal precipitates, which grew at the expense of t' during ageing at 1600°C. Similar twinned crystals are observed in arc melted samples, [39]. The high yttria tetragonal phase, t', found in thermal barrier coatings was denoted 'non-transformable' in recognition of the fact that it does not undergo the martensitic tetragonal-monolinic transformation. The phase is stable during crack propagation and on grinding, i.e. removal of matrix constraint. Small percentages of monoclinic and cubic phases were also present at room temperature. Ageing at 1200°C-1600°C for up to 100 hours increased the proportions of cubic and monoclinic phases and decreased that of tetragonal (t'+t), although the equilibrium ratios suggested by the phase diagram for this system were not attained, [47]. The phase diagram for the zirconia-yttria system, fig 2.6, contains extra phase boundaries near the bottom axis which illustrate the majority phases obtained when rapid quench cooling rates are experienced.

2.5.3 Zirconia thermal barrier coating materials.

It is apparent from the preceeding section that, depending on the nature and quantity of stabilizing oxide, plasma sprayed zirconia coatings may contain a number of separate phases, each with a particular set of properties. Zirconia may exist as either cubic,

tetragonal (transformable and non-transformable) and monoclinic polymorphs, together with free stabilizing oxides and ordered oxide phases. The actual phase structure and composition of the final coating depends initially on the powder manufacturing process and the type and quantity of stabilizing oxide.

Stabilized zirconia powders intended for plasma spraying are manufactured by several alternate routes and each confers on the particles a unique set of characteristics which ultimately affect their performance. Commonly used stabilizing materials include yttria (6-20 wt%), magnesia (20-25 wt%), calcia (5-8 wt%) and more recently ceria.

Commercially available powders have been extensively investigated to determine their suitability for coating manufacture, [28,48,49,50]. Broadly, powders are divided into two types: those which are mixtures of the constituent oxides and those where some attempt at 'alloying' has been carried out. The former are generally produced by spray drying mechanical mixtures into spherical shapes and characterized by chemical inhomogeneity. This tends to be carried over to the coating because realistically, insufficient time is available during the melting/solidification process for complete reaction and stabilization to occur. The problem is further aggravated when larger particle sizes are utilised. The result is that coatings

contain, in general cubic and/or tetragonal phases, interspersed with monoclinic zirconia and free oxide particles, and the presence of monoclinic zirconia may prove adverse during thermal cycling. Stabilization prior to spraying can be achieved chemically by co-precipitation or by fusing/sintering at high temperatures.

Fine co-precipitated powders are simply agglomerated by spray drying whereas mechanical mixtures are sintered (to improve chemical homogeneity) and spray dried. An alternative method relies on casting or fusing bulk materials followed by crushing/grinding.

The morphology of these latter materials is characterised by blocky, angular, irregular particles with high surface area to volume ratios. However the control of particle size requires classification, whereas spray dried materials are produced in controlled size distributions. The morphology of various types of zirconia powder is illustrated in plates 2.1b to 2.1f.

Fully stabilized materials generally contain high proportions of cubic material, whereas partially stabilized powders may contain tetragonal+cubic mixtures. Usually, small volume fractions of monoclinic material are present, but these are reduced by optimum plasma spraying conditions. Incomplete stabilization of spray dried then sintered materials may occur depending

on the economics of prior heat treatment.

2.6 Interaction with and melting of powder particles in the plasma flame.

The interaction of both bondcoat and ceramic powder particles with the plasma depends not only on the previously discussed flame parameters eg. temperature, velocity, residence time, but on injection conditions, particle shape, size range and density [22,23,24,25,26,27,28,48,51,52].

Injection of powder particles into the flame is a complicated process and demands optimum conditions to achieve complete melting. The plasma itself has a significantly higher viscosity and a very high velocity (100-250ms^{-1}) compared to the surrounding atmosphere. Consequently injection of a particle of given density and size into the hottest part of the flame requires a particular trajectory and velocity. If the particles are moving with insufficient momentum, they simply do not enter the hot core of the flame. Similarly if the powder has too high an injection velocity or the particles are too large, they pass through the flame and exit on the opposite side unmelted, figure 2.7. Obviously, then an optimum injection velocity is required to place a particle of a given size and shape into the plasma core. Further, the plasma has only a limited enthalpy and so an upper limit must be placed

on the powder injection rate into the flame for successful melting, [27].

The site and parameters of powder injection are also important. Generally, the powder is introduced radially into the plasma flame immiediately downstream of the nozzle exit. Misalignment may result in incomplete melting and/or low deposit efficiency. Alternatively, the powder may be introduced into the nozzle throat through a radial injection hole [52]. Particle morphology and density, nozzle dimension and position, carrier gas flow and powder feed rate reproducibility all control the velocity and optimum injection of powder material into the plasma flame, [52].

For a given powder, then, containing a range of particle sizes, only a certain proportion will undergo optimum melting, and clearly this phenomena would be aggravated if a wide size range is utilized. Once into the flame, particles are accelerated rapidly, according to their mass and shape until their speed equals that of the surrounding gas flow. Subsequently a braking effect occurs and particles begin to slow down. Again, this maximum in particle velocity will not occur at exactly the same point in the flame for different size particles, this effect is illustrated in figure 2.8. Further, zirconia has an extremely low thermal conductivity, and so melting, to a certain extent, must be controlled by the conduction of heat through the

particle. Larger particles may, therefore, not be completely molten by the time impact occurs and particles with higher surface/volume ratios ie. not spheroidal, will undergo more complete melting. Smaller particles may alternatively vaporize if the melting conditions are such that superheating occurs, or change their composition by evaporation at a rate dependant on the stabilser. A consideration of the competing effects of powder morphology has been carried out in ref. [52], and is summarised below:

(i) The peak mean velocity of particles increases with decreasing size, but at a large distance from the nozzle, the deceleration of the smaller particles is higher than that expected for larger sizes.

(ii) For the same particle dimensions, those of a low density material will achieve higher peak velocities but their deceleration rate will be higher.

(iii) Alteration of plasma torch parameters to increase plasma velocity increases mean particle velocities but decreases in-flame residence time available for melting.

(iv) Increasing the powder injection velocity (up to a limit) causes the particles to penetrate further into the high velocity jet core and results in higher mean particle velocities.

Injection of a powder material with a given size range, shape and density therefore produces a stream of

particles which may be in different states of heating, melting or solidification and with a distribution of velocities and trajectories upon substrate impingement. A complete understanding of the behaviour of a particular powder in a plasma flame would then require a detailed knowledge of the temperature profile of the gas stream, the particle dwell time in the plasma flame and the mechanism of heat transfer from the gas stream to the particles. Generally, however this information is not available, and so optimum melting conditions are determined by experiment. It is apparent also that narrow and small size range powders have found favour because of the ease of obtaining optimum conditions for the majority of the particles.

An interesting illustration of conditions necessary for complete melting suggests that for a particular material, particles which undergo optimum melting reside inside a 'box' in a three dimensional space defined by particle surface temperature, particle diameter and particle velocity, [53]. The melting conditions are therefore chosen such that the majority of powder material lies within the 'box'. This concept is illustrated in figure 2.9.

2.7 Interaction of plasma flame and heated particles with the substrate.

Plasma flame and particle-flame interaction parameters considerably affect the velocity and temperature distribution of particles projected towards the substrate. The interaction of such heated and fast moving particles with the substrate is of prime importance in determining the final properties, adhesion and structure of the coating, [27,28,48,49,51,52,54,55,56,57,58,59].

To achieve a high quality, dense deposit a large fraction of the particles must be molten on impact. Insufficient melting allows the thin part-melted outer layer to spread over the deposit, whereas the unmelted core deforms into a hemispherical shape. Alternatively, a molten droplet impacting the substrate spreads out radially to form a thin disc or splat, [52]. Poor bonding, however, may lead to curling away from the substrate at the edges of particles. A high velocity and particle temperature are therefore necessary to achieve good contact between particles, and low porosity, [27,28,48,51,52,54]. Increasing torch/substrate spray distance beyond the point where particles slow and begin to cool increases the liklihood of poor interparticle bonding and material flow, [27,28,52,55,57]. Alternatively, too short a spray distance can cause substrate overheating, coating

cracking and insufficient residence time for particle melting to occur, [27,55].

2.8 Interparticle and substrate-coating adhesion.

The mechanisms of particle/substrate and inter particle bonding are not well understood, however a number of alternatives have been suggested, [52,58,59]. It is generally accepted that substrate surface roughening by grit blasting improves adhesion but no definitive explanation of the beneficial effects has been advanced, [19]. However, mechanical anchoring may result from impacting material flowing around roughness peaks and into undercut regions of the substrate surface. In addition, materials in close contact are expected to undergo some physical attraction resulting from Van der Waal's forces. Alternatively, interdiffusion leading to a metallurgical bond, or a chemical reaction where intermetallic or other compounds are formed, remain possibilities. In practice, two or more mechanisms are expected to operate simultaneously.

Application of a thin metallic bondcoat layer generally improves ceramic coating adhesion, and its contribution is assumed to be that of a thermal expansion mismatch strain isolation layer between metallic substrate and ceramic coating. Generally, those bondcoats which perform best are ductile at

operating temperatures, and the ability to remain plastic ultimately depends on the oxidation resistance of the particular alloy, [31]. Techniques exist for measuring coating adhesion, [58], and failures are characterised either by adhesive or cohesive fracture.

2.9 Microstructural features of thermal barrier coatings.

Ceramographic examinations of as sprayed coatings show that a background level of porosity is present in the majority. It occurs because of the liquid to solid volume shrinkage on cooling (~10%) in zirconia, [27,28,48], and the presence of large unmelted particles or where low particle temperature/impact velocity reduce particle flow. Other microstructural features include inter- and trans-lamellar shrinkage cracks, planar cracks between successive coating layers or spray passes and vertical crack networks leading to coating segmentation, [27,28,48,52,55,57]. Shrinkage cracking in ceramic particles arises because of their inability to plastically deform in tension on cooling from the solidification temperature. Such cracks are not expected to be found in the more ductile metallic bondcoat layers. In addition, rapid solidification of particles, substrate heating during spraying, thermal gradients and expansion coefficient mismatches between coating and substrate lead to the buildup of residual

stresses in coated layers [19,27,48,52,55,57,60]. These may cause spallation, interlaminar cracking and coating segmentation after spraying if conditions are not closely controlled. This can be achieved, for example, by air cooling during spraying, substrate preheating and adjustment of gun/workpiece separation or coating thickness per spray pass.

Ultimately, the cooling rate of particles impacting onto the substrate and other particles is controlled by the interface heat transfer coefficient. Poor contact would be expected to reduce the cooling rate, [52]. Another effect may be that particles which initially impact onto a 'cold', high conductivity metallic substrate experience significantly different freezing conditions to those experienced by subsequent particles impacting onto a hot, low conductivity ceramic layer.

In depositing a thermal barrier coating, the plasma torch and workpiece are moved relative to each other at a particular speed, allowing the buildup of given thicknesses of coating material in successive passes. Depending on component size and for a given relative velocity, the deposition conditions for a similar coating specification will be expected to vary. Similarly, the necessity for automated deposition to maintain reproducible plasma spray parameters is evident, [48,52,55], since hand operated systems can lead to variable gun/workpiece spray distances and

traverse rates resulting in uneven coating thickness.

A typical microstructure of an as sprayed zirconia thermal barrier coating containing 8wt% yttria is illustrated in plate 2.2. The porous ceramic layer was deposited over a nickel-chrome-aluminium bond layer by repeated passes of a plasma torch. The substrate material is aluminium alloy, which had been roughened by grit blasting with coarse alumina sand.

2.10 Mechanical and thermal properties of plasma sprayed zirconia coatings.

The effectiveness of zirconia thermal barrier coatings for insulation ultimately depends on their mechanical and thermal properties. The former are important because the material must be capable of withstanding operating stresses and displaying sufficient adhesion to operate in the diesel engine combustion chamber environment. The latter properties are of equal importance because they determine the coatings' thermal resistance and response to thermal shock. A review of existing literature data shows there to be considerable variation in measured properties, which in turn may be attributable to variations in coating microstructure eg. porosity, crack density, degree of melting, which result from varying spray conditions. Nevertheless, a summary of available mechanical data is given in table 2.1 and thermal

property data in table 2.2 together with their literature references which describe the appropriate measurement techniques.

2.11 The response of thermal barrier coatings to residual and environmental stress.

Considerable effort has been expended in studying the performance of zirconia thermal barrier coatings in engine and test-rig operating environments in an effort to isolate and improve the life-limiting factors affecting their performance. Of fundamental importance are considerations of the stress states to which coating systems are subjected. These may be broadly divided into two components. First, residual stresses which develop on cooling after coating deposition and second, thermal stresses which occur when the coatings interact whith the high temperature operating environment.

2.11.1 The origin and effects of coating residual stress.

Residual stresses within ceramic thermal barrier coatings originate in the temperature difference between the heated coating particle and the relatively cool substrate, [48,73,74]. The rapid cooling of a molten ceramic droplet results in a liquid to solid volume contraction of approximately 10%. Once

solidification is complete, the constraint of the underlying substrate or previously solidified material restrains further thermal contraction in the particle and a tensile microstress distribution is established because the temperature of the substrate remains relatively constant. Stress relief by microcracking through the 'splat' thickness must occur because the ceramic material is unable to support large tensile strains. The degree to which microcrack networks are formed ultimately depends on the temperature and elastic properties of both particle and substrate, the expansion coefficient of the ceramic, the yield strength of the substrate and effectiveness of particle-substrate and particle-particle bonds. Build-up of the coating continues and a compliant structure of micro-cracked lamellar 'splats' able to deform by partially reversible sliding over one another is developed, [75]. A small level of residual tensile stress, related to the 'plasticity' afforded by the microcrack networks is then expected to be supported by the coating layer.

In addition, macroscopic sources of residual stress operate which are related to the temperature gradients and expansion coefficient differences between coating and substrate during plasma spraying, [48,73,74]. At the start of deposition, the coating and substrate materials are at widely different temperatures. Due to

the heat input from the plasma torch and hot coating material, substrate temperatures will rise progressively during spraying to some mean temperature. Similarly, each layer of ceramic material will cool to a particular temperature, which is unlikely to be unique through the coating thickness because of its low thermal conductivity and heating effects of the plasma torch, [76]. On completion of the coating procedure, and cooling to room temperature, a strain difference results, due to the expansion coefficient mismatch between ceramic and substrate. A simplified analysis of this process has been carried out in which the temperatures of the coating and substrate layers are assumed to be uniform but different, [76]. The strain difference is then given by:

$$\Delta\varepsilon = \alpha_{sub}(T-\overline{T}_{sd}) - \alpha_{ceramic}(T-\overline{T}_{cd}) \qquad 2.1$$

where α_{sub} = substrate thermal expansion coefficient

and $\alpha_{ceramic}$ = ceramic thermal expansion coefficient

$\overline{T}_{sd}$ = mean substrate temperature after deposition

$\overline{T}_{cd}$ = mean ceramic temperature after deposition

T = room temperature.

If the metal substrate is assumed to be rigid and

massive, then the tangential residual stress in the coated surface of a cylindrical bar is given by:

$$\sigma_t^{res} = \frac{E_c}{(1-\gamma_c)}\left[\alpha_{sub}(T-\overline{T}_{sd}) - \alpha_{ceramic}(T-\overline{T}_{cd})\right] \qquad 2.2$$

where E_c = ceramic elastic modulus

and γ_c = Poisson's ratio for the ceramic.

The expansion coefficients of Superalloy, cast iron and aluminium alloy substrates are all larger than that of partially stabilized zirconia. Assuming that T_{sd} and T_{cd} are equal, (which they would be at the interface between coating and substrate), on cooling to room temperature a shear stress will be developed which is maximised at the substrate-ceramic interface and the coating is subject to a compressive stress. Two possible mechanisms for failure then exist. First, if the shear strength of the ceramic layer or of the metal-ceramic interface is exceeded, then spalling may occur by shear fracture, particularly at free surfaces. Alternatively, the compressive stress developed in the ceramic layer above the interface may result in a tensile buckling or lifting stress near the centre of the specimen, figure 2.10. This in turn may cause a spallation failure if it exceeds the tensile strength of the ceramic layer or that of the interfacial bond. Regardless of the failure mode, the higher the value of

mean temperature or so called 'stress free' temperature from which the coated substrate cools after spraying or the greater the expansion mismatch, the higher will be the stress developed, leading to a greater chance of failure.

The situation in reality is somewhat more complicated because the coating at the 'stress free' temperature is in fact subjected to a stress equivalent to the effective 'yield strength' of the pseudo-plastic ceramic coating. Also, the practical thermal barrier coating system contains a bondcoat whose expansion coefficient and temperature will lie between those of the ceramic layer and substrate, and containing its own prior residual stress distribution. Perhaps as important, the ceramic coating layer is unlikely to have a unique temperature equal to that of the substrate. The resulting temperature profile would lead to a stress gradient through the coating on cooling. If the coating is of sufficient thickness, then the surface region may be in tension at room temperature leading to cracking in the upper section of the coating, figure 2.11, [77]. The stress gradient also produces shear which may lead to interlaminar cracking particular at sites of existing shear stress such as the boundaries between subsequent spray passes. These latter effects have been observed in practice when thicker ceramic coating produced with poor temperature

control have been observed to crack both parallel and perpendicular to the coating plane, [19,24,55,74,78,79,80].

An additional source of residual stress can occur when significant proportions of transformable tetragonal phase (t') are present during cooling, [48]. Over the martensitic transformation temperature range, the (~4%) volume expansion associated with the formation of monoclinic zirconia will further contribute to the compressive stress field unless matrix constraints are relaxed by microcracking. Obviously, the extent of this component is related to the uniformity and degree of stabilization of zirconia after plasma spraying.

2.11.2 The origin and effects of coating thermal stress.

In addition to residual stress, the coating system is subjected to operating stress due to transient and isothermal temperature conditions. The sum of these two components may be sufficient to cause coating failure when resolved stress exceeds the adhesive or cohesive strength of one or more layers in the coating.

Analysis of the stresses generated during high temperature coating operation have been carried out, [76,77]. Slow heating/cooling of a thermal barrier coating system is expected to produce a tensile stress

in the coating plane, despite the higher temperature and temperature gradient through the ceramic layer. This is because the expansion coefficients of candidate substrate materials, particularly aluminium, are so much higher than the zirconia layer. At the ceramic metal interface, the expansion of the substrate is constrained by the lower expansion coating, leading to compressive stress in the substrate and a corresponding tensile stress in the zirconia layer. Near the hotter, exposed surface of the ceramic, however, this tensile stress will be reduced because the material will have expanded to a greater extent, more closely matching substrate expansion. The temperature gradient through the coating therefore ensures that the maximum shear stresses are concentrated at the ceramic-bondcoat-substrate interface, and that shear stresses will be developed throughout the ceramic layer because of the stress gradient, figure 2.12. On heating to a given coating temperature from ambient, the thermal stress developed in the coating on a rod specimen, after [77], is given by:

$$\sigma_T = \frac{E_c}{(1-\nu_c)}\left[(\bar{\alpha}_m - \bar{\alpha}_c)(T_o - T_a)\right] \qquad 2.3$$

where E_c = elastic modulus of ceramic

and ν_c = Poisson's ratio of ceramic

$\bar{\alpha}_c$ = mean coating expansion coefficient

$\bar{\alpha}_m$ = mean substrate expansion coefficient.

Example calculations carried out in reference [77] suggest that the available plasticity of ceramic coatings is exceeded by approximatele 100%, implying that tensile cracking through the thickness would occur to relieve the stress generated and improve the strain tolerance of the coating. Any tensile stress produced would also tend to reduce residual compressive stresses or relieve them if cracking occurs, reducing the tendency for coating spallation. Tensile cracking, however, may only occur if the tensile strength of the ceramic layer is exceeded before the critical shear stress of the ceramic layer or ceramic/bondcoat interface is reached, [81]. In thicker coatings, necessary for effective insulation in advanced diesel engines, the tensile force is spread over a larger cross-sectional area. With increasing thickness, a point is eventually reached at which the critical shear stress is less than the tensile rupture force. At the edge of flat coated surfaces, the shear stresses are largest and edge delamination or lifting may then occur when the critical shear stress is exceeded.

Potentially more serious are the effects of rapid heating transients or thermal shocks which generate compressive stresses in the coating plane. These may interact with existing compressive residual stress to give a normal tensile stress that exceeds the fracture strength of the coating, resulting in spallation,

[76,77]. Rapid heating, despite favourable expansion differences between coating and substrate, generates compressive stress in the coating plane because a high thermal gradient is established through the low conductivity coating thickness, the substrate temperature remaining relatively constant. Constrained expansion of the surface layers of the zirconia coating by the cooler material below causes high in-plane compressive stresses at the exposed surface, figure 2.13. The tangential, transient stress on the surface of a rapidly heated coated rod, after reference [76], is given by:

$$\sigma_t^{trans} = \frac{-\alpha_c . E_c . Q . h}{(1-\nu_c) . A . K_c} \qquad 2.4$$

where α_c = thermal expansion coefficient of ceramic

and E_c = elastic modulus of ceramic

ν_c = Poisson's ratio of ceramic

K_c = thermal conductivity of ceramic

h = thickness of coating layer

Q/A = heat flux/unit area.

On a round, coated bar, the normal tensile stress, σ_n , is given by:

$$\sigma_n = \frac{h\sigma_t}{R} \qquad 2.5$$

where σ_t = tangential stress in ceramic coating surface

and R = radius of bar.

Summing the tangential residual stress, equation 2.2, and tangential transient stress, equation 2.4, allows the calculation of the total normal tensile stress, σ_n^{total}. After reference [76] this is given by:

$$\sigma_n^{total} = \frac{h.E_c}{R(1-\nu_c)}\left[\frac{\alpha_c h Q}{K_c A} + \alpha_c(T-\overline{T}_{cd}) - \alpha_s(T-\overline{T}_{sd})\right] \qquad 2.6$$

2.12 The effect of bondcoat layers on coating performance.

The use of metallic bondcoats has long been known to improve the performance of ceramic coatings on metallic substrates. The bond layer has been associated with strain isolation or relief of expansion mismatch stress. In addition, their chemically resistant properties provide both an oxidation and corrosion barrier to the underlying substrate.

2.12.1 The influence of bondcoats on residual and operating stress.

The effect of bondcoats on residual stress in ceramic coatings is complex and not well understood. In addition, plasma spraying the bondcoat material would be expected to confer a residual stress on this layer

on cooling, and the magnitude and extent to which this stress is modified by a subsequent ceramic coating is unknown.

Generally, bondcoat alloys exhibit thermal expansion coefficients intermediate between zirconia and substrate layers, and intuitively this may be expected to reduce local expansion mismatch shear stresses at the ceramic-metal interface region. Further, M-Cr-Al-Y bondcoat materials have been shown to deform at strain rates of 0.1% per second above 850°C, [31], and significant plasticity can occur at very low stress levels and at much lower temperatures, [61]. Stresses arising from expansion mismatches across the ceramic-bondcoat-substrate interface may then be expected to be relieved by fairly rapid plastic deformation of the bondcoat at operating temperatures, [31]. Depending on the plasticity of the particular bondcoat, and the magnitude of the mismatch strains to be accomodated, the bondcoat then functions as a strain isolating layer reducing the tensile stresses in the ceramic coating at operating temperatures. If bondcoat deformation did not occur, slow heating would simply develop tensile stresses in the ceramic layer and probably result in through-thickness cracking, [31], while on cooling, the tensile stress would be relieved. Bondcoat deformation, on the other hand, would result in compressive in-plane stresses in the ceramic layer,

whose size must depend critically on the cooling rate, and the ability to deform at lower temperatures, figure 2.14.

2.12.2 Influence of bondcoat oxidation on coating lifetime.

Progressive oxidation, by reducing the bondcoats' ability to deform rapidly on cooling, may cause a gradual increase in compressive stress in the ceramic layer, and, an increased expansion mismatch thermal cyclic stress across the bondcoat-ceramic interface. This eventually leads to crack propagation of existing flaws in the brittle ceramic layer above the bondcoat where compressive stresses are highest. When the normal tensile stress developed across the interface exceeds the remnant strength of the microcracked ceramic layer, spallation results, [31]. A model for thermal barrier coating life, based on oxidation of the bondcoat layer, has been developed for gas turbine thermal barrier coatings, [82], and oxidation has been identified as a necessary condition for coating spallation to occur in burner rig tests, [83].

Obviously, oxidation depends not only on bondcoat composition, [32], and operating temperature, but the ease with which oxidising species can penetrate the zirconia layer. Increased porosity and microcracking, together with the oxygen ion transport properties of a

particular zirconia composition then become rate controlling factors, (fully stabilized zirconia is used as an oxygen sensor at high temperatures because of its enhanced oxygen ion transport properties). Further, the use of low-pressure plasma sprayed M-Cr-Al-Y bondcoats, where initial oxidation due to the deposition process is virtually eliminated, exhibit enhanced coating durability, [52]. An important factor in considering the plastic deformation of the bondcoat is that it must occur at constant volume, [84]. Porosity, then, is a pre-requisite in the bondcoat layer if this is to be achieved, but remains at odds with the need to limit oxidation.

2.13 Other factors affecting static and cyclic stress levels in zirconia coatings.

At high operating temperatures, several other effects have been observed which alter the balance of stress in coating systems and can lead to failure.

2.13.1 Creep deformation.

Investigation into the high temperature deformation behaviour of coating materials have not been confined to the bondcoat layer. Several workers have observed that creep deformation can occur at elevated temperatures in zirconia coating layers under stress, [68,69,70]. Exposure to tensile stress for extended periods caused plastic deformation. On cooling to

ambient, the now extended coating returned to its original dimensions, under the influence of the more massive substrate, and was subjected to compressive in-plane stress. Again, the effect depends on exposure time, temperature and operating stress and may contribute to coating spallation.

2.13.2 Chemical instability.

The chemical stability of zirconia coatings at high temperatures may not be sufficiently high to prevent destabilization occurring after extended periods of exposure. Any monoclinic material formed as a consequence may lead to volume expansion related stresses and/or microcracking when the material is subjected to thermal cycling. The resistance to loss of stabilizer due to thermal exposure increases in the order $MgO < CaO < Y_2O_3$, with CaO loss occurring in bulk zirconia at 950°C, [60], and precipitation of MgO from cubic solid solution in plasma sprayed coatings soak tested at 1000°C, [88].

2.13.3 Corrosive leaching of stabilizer materials.

Destabilization may also occur in coatings incorporated in engines operating on low grade or residual fuel oils. Contaminants such as sodium, potassium, vanadium, iron, lead, phosphorous and sulphur react to form either gaseous or liquid

combustion products that penetrate through porous or microcracked coatings. Leaching out of stabilizing oxides then occurs, ultimately causing coating failure. The problem may occur in both gas turbine and diesel engines and in the latter, the corrosive species have been identified as sodium sulphate, sodium vanadates and vanadium pentoxide, [12,16,48,78,80]. Reactions were found to occur between molten deposits and coatings which removed MgO, CaO and Y_2O_3 from solid solution, leading to destabilization. The porous nature of the coating probably increased the surface area for attack. Additional problems due to salt solidification during thermal cycling were noted. Expansion mismatches between the solidified salt and coating caused spallation, and 'hot spots' related to increased thermal conductivity occurred because of local densification. The most durable system incorporated a chromium corrosion barrier layer between bondcoat and ceramic to protect the bondcoat and substrate materials from attack, [80], and utilized an Y_2O_3 stabilized zirconia layer.

2.14 Coating of diesel engine components.

Early attempts to coat diesel engine pistons with thick (several mm) zirconia thermal barrier coatings met with limited success, [2,4,8]. Finite element stress analysis suggested that spallation failures in

the centre of piston crowns were caused by thermal expansion and thermal gradient related stresses. The calculated stresses in coated aluminium pistons were approximately four times those in similarly treated cast iron pistons, and both exceeded the adhesive/cohesive strength of the coating system. A limiting coating thickness of 0.8mm was specified above which spallation was found to occur and aluminium substrate materials were precluded from further investigation because of high expansion mismatch stresses at the coating-substrate interface. No consideration, however, was given to the effects of residual stress on coating performance.

Further attempts to coat exhaust valves, cylinder heads and piston crowns in marine diesel engines operating on low grade fuels again demonstrated a maximum thickness, (0.4mm). Residual coating stresses were identified as the limiting parameter in the build up of thick coatings, [78].

2.15 Improved thermal barrier coating systems.

Subsequent investigations have identified the important factors necessary to produce thicker coatings with adequate thermal shock resistance.

2.15.1 Choice of coating materials.

Of the various combinations of ceramic and bondcoat

composition, the most durable are those based on 8 wt% Y_2O_3 with M-Cr-Al-Y or M-Cr-Al-Zr bondcoats. The latter have been identified as providing the best oxidation resistance, particularly when applied by low-pressure or vacuum plasma spraying onto sputter cleaned substrates, [82,89].

Partially stabilized zirconia, containing about 8 wt% Y_2O_3 usually contains a majority of non-transformable tetragonal phase, t', after plasma spraying. Very high temperature exposure results in a gradual conversion to low-yttria tetragonal (t) and high-yttria cubic (f) phases, without the formation of monoclinic phase, [90]. Numerous sources have identified this composition as having the best performance, even in corrosive operating environments and particularly in higher operating temperature gas turbine applications, [31,88,89,90,91,93]. The superiority of this material depends on the final coating having a uniform distribution of stabilizing oxide. This is generally achieved in materials which are pre-reacted or 'alloyed' before spraying.

Fully stabilized cubic yttria-zirconia has been shown to develop microcrack networks above the ceramic-bondcoat interface after plasma spraying, whereas partially stabilized yttria-zirconia generally does not contain such localised cracking.

Thermal cycling stresses associated with expansion

mismatch and decreased bondcoat plasticity due to oxidation ultimately cause microcracks to propagate in the brittle, flawed, highly stressed ceramic above the bondcoat and result in spallation. The high starting defect density in fully stabilized zirconia coatings reduces the amount of thermal cycle damage that can be sustained before failure, [31]. Also, partially stabilized yttria-zirconia is tougher and more resistant to structural changes at high temperature, so that crack propagation would be expected to be reduced, [88]. Any further improvement in adhesive or cohesive strength and toughness should further improve coating durability, [77].

2.15.2 Reduction of coating stress by careful design.

Improved coating performance may also be achieved by careful manufacture and design, allowing close control of residual, transient and steady operating stress.

Residual stress control generally attempts to reduce the biaxial, in-plane compressive stress developed in the ceramic layer and shear stresses developed across the metal-ceramic interface on cooling after spraying.

Examination of the residual stress related terms of equation 2.6, given below, shows how this may be achieved.

$$\sigma_n^{total} = \frac{h.E_c}{R(1-\nu_c)}\left[\frac{\alpha_c h Q}{K_c A} + \overbrace{\alpha_c(T-\overline{T}_{cd}) - \alpha_s(T-\overline{T}_{sd})}^{\text{residual stress related terms}}\right] \quad 2.6$$

Perhaps the most obvious effect occurs if the expansion mismatch between coating and substrate is minimized. This generally favours heavier cast iron pistons and cylinder heads with similar expansion coefficients to zirconia. High expansion, weight-saving aluminium alloys, despite their obvious advantages, simply aggravate expansion mismatch related stress.

Alternatively, forced cooling of both coating and substrate during deposition reduces both substrate, $\overline{T}_{sd}$, and coating, $\overline{T}_{cd}$, temperatures and therfore reduces the differential contraction. Reduction of coating temperature while spraying might be expected to aggravate in-plane compressive stress but experience shows that reduction of the through thickness temperature gradient is more important. This effect is considered to be of particular relevance in thicker ceramic coatings where appreciable gradients may develop during uncooled deposition. Tensile stress at the exposed surface and shear stress through the

thickness may combine to cause both horizontal and vertical cracking, with resulting poor performance, when insufficient cooling is used, [24,27,48,55,73,74,76,77,78,79]. Air cooling, however is relatively inefficient, [27], and liquid cooling of substrates has been employed. Maintained substrate temperatures of between 20°C and 315°C were found to increase thermal cycle durability during burner rig tests, [94].

Whereas it is relatively easy to maintain constant cooling conditions on simple testpiece geometries such as plates or bars, the problems of transferring and achieving similar spray conditions and cooling on complicated component geometries should not be underestimated, [95]. Further, the variable heat sink capacity of changing section thicknesses needs to be taken into account, if uniform substrate temperatures are to be maintained.

Reduction of temperature can be achieved in alternative ways, for example, by reducing torch input power, increasing the thermal mass of the substrate and depositing material in more rapid, thinner passes thereby decreasing the time span during which heat is input, [83]. Another technique employs an air blast perpendicular to the plasma flame thus shielding the substrate and removing slow moving, unmelted particles, [24].

Control of heating transient stress may be necessary to prevent early failure of coating systems. Examination of equation 2.6 again shows how this may be achieved.

$$\sigma_n^{total} = \frac{h.E_c}{R(1-\nu_c)}\left[\overbrace{\frac{\alpha_c h Q}{K_c A}}^{\text{factors controlling transient stress}} + \alpha_c(T-\bar{T}_{cd}) - \alpha_s(T-\bar{T}_{sd})\right] \quad 2.6$$

Reduction of residual stress requires a minimization of the expansion mismatch between ceramic and substrate. This is achieved either by increasing α_c or reducing α_s . Unfortunately, a conflict occurs when trying to minimize transient stress since high values of α_c are obviously not desirable. Careful optimization is therefore necessary to achieve the best performance.

Again conflicts occur when considering both conductivity and thickness terms. For effective insulation, a large thickness and low conductivity are necessary but these both tend to increase thermal transient stress, [76].

The enhanced heat flux in higher performance engines may also give rise to increased transient stress.

Steady state thermal stresses are adequately described by equation 2.3

$$\sigma_{thermal} = \frac{E_c}{(1-\nu_c)}\left[(\bar{\alpha}_m - \bar{\alpha}_c)(T_o - T_a)\right] \qquad 2.3$$

While thermal stress at operating temperatures is expected to be relieved by tensile through thickness cracking, the extent to which it occurs may have some bearing on the ability of oxidising and corrosive species to penetrate the ceramic layer. Optimisation therefore, requires a reduction in expansion mismatch between coating and substrate but again with due regard for the requirements of transient stress resistance.

At first sight one possible solution to this conflict can be achieved by incorporating layers of intermediate expansion coefficient material between ceramic and substrate. An obvious example is the use of a bondcoat with intermediate properties. An alternative is to utilize layers of combined ceramic+metal or 'cermet', (usually consisting of mixtures of zirconia and bondcoat material). The composition can be continuosly varied from 100% metal to 100% ceramic or several distinct layers of constant composition may be used, figure 2.15, [57]. Difficulties have, however, been encountered with this latter technique because the enhanced oxygen transport properties and porous nature of the ceramic layer cause oxidation and growth of the

metallic component leading to spallation, [31,95]. Further, grading is only useful for reduction of stresses in the steady state. Diesel engines operate under transient conditions and under extreme conditions the substrate may actually be hotter than the coating layer, [15].

Both equations 2.3 and 2.6, which describe the response of ceramic thermal barrier materials to thermal excursions, contain terms that are related to the elastic properties. An obvious technique for reducing stress levels is to reduce the elasic modulus by microstructural modification. In a brittle ceramic material, such as plasma sprayed zirconia, this may be achieved in a number of ways. Perhaps the simplest technique is to introduce controlled distributions of porosity and/or randomly oriented microcracks, [55,94]. These would be expected to enhance the particle sliding deformation mechanism already described, [75], reducing elastic modulus and improving strain tolerance in tension and compression. Increased porosity however would allow oxidising/corrosive species to enter the coating and perhaps accelerate alternate failure mechanisms. Another disadvantage of this method is that it would uniformly reduce elastic modulus, whereas to resist impact and pressure transients during engine operation requires a high modulus perpendicular to the coating plane, typical of compact, low porosity

coatings.

An alternative technique, designed to introduce anisotropic modulus properties into the coating depends on the formation of through thickness segmentation cracks. In the coating plane, the elastic modulus is effectively reduced to zero and lateral relative movement of 'islands' of material confers strain tolerance on the coating. Perpendicular to the coating plane, the elastic modulus remains high due to the dense structure of the coating, [55,92]. A schematic diagram of a segmented coating structure is illustrated in figure 2.16 , after ref. [92]. Segmentation can be achieved in a number of ways. In thicker coatings it may already exist on cooling after deposition, particularly where residual stresses have been allowed to build up because of inadequate cooling, [55]. The presence of horizontal, planar crack networks however is to be avoided because this seriously impairs coating properties. Fine powders, because they result in dense coatings, are also prone to segmentation, [94]. Alternatively, segmentation may be achieved by post-spraying heat treatment, either by laser glazing, [94], or by vacuum heat treatment, although the latter is difficult to achieve because residual stresses at the coating-bondcoat interface cause skewing or horizontal deflection of vertical cracks, [95].

The concepts of strain tolerance and residual stress

control may be combined to produce a coating with adequate thermal shock and spallation resistance when the operating thermal cycle is known. Substrate temperature control plays an important role in optimizing the balance between tensile operating stress, leading to segmentation, and residual in-plane compressive stress, [94]. This concept is illustrated in figure 2.17.

Finally, design of an insulating layer must pay full regard to component geometry and coating thickness if adequate thermal shock resistance is to be achieved. The remaining terms in equation 2.6 describe component geometry:

factors related to component geometry

$$\sigma_n^{total} = \underbrace{\frac{h \cdot E_c}{R\,(1-\nu_c)}}\left[\frac{h\,\alpha_c\,Q}{k_c\,A} + \alpha_c\left(T-\overline{T}_{cd}\right) - \alpha_s\left(T-\overline{T}_{sd}\right)\right] \quad 2.6$$

Clearly when substrate radius of curvature is minimized, then normal stresses are reduced. A number of geometrical requirements have been identified, which must be satisfied when thicker coatings are applied to actual components, [15]. These are summarised below:

(i) Sharp edged sprayed coatings can only be produced by subsequent grinding.

(ii) Acute angled layer boundaries should be avoided.

(iii) Where encapsulation is necessary, corner radii

should be twice the layer thickness.

The effect of coating thickness on normal tensile stress is somewhat complicated. Residual stresses are proportional to coating thickness while transient stresses are related to the square of thickness. Either component may be reduced by decreased thickness but this is at odds with the insulation requirements of efficient engines. Obviously a balance between desired thermal shock resistance and adequate insulation must be determined.

When spray parameters and substrate geometry are considered and optimized along the lines of the above for thicker coatings, then useful insulation with good performance may be achieved, [13].

2.16 'State of the art' coating of diesel engine components.

Zirconia coatings, between 2 and 3mm thick have achieved up to 50 hours of engine operation without spalling, but only after extensive development and thermal shock testing had been carried out. For a given coating thickness, the mean surface bond strength varied little even after 10000 engine simulation thermal cycles. However, thicker coatings were found to be weaker, presumably because of crack networks, but were undamaged after 100000 thermal cycles, [13].

An important factor in developing such reliable

coatings was careful control of spray parameters including the use of robot spraying equipment. This was considered vital to the manufacture of homogeneous and reproducible quality coatings. The importance of using automated spray equipment has been emphasised by several workers. Variable coating thickness and density, microcrack networks, poor spallation resistance and lack of reproducibilty have all been attributed to the use of manual spray systems, [13,48,52,96].

2.17 Choice of subjects for detailed investigation.

It is apparent from preceeding sections of this review that several important areas exist where further work may improve understanding and application of thermal barrier coatings in diesel engines.

Three subjects were chosen for detailed investigation and these are summarised below.

(i) Determination of residual stresses in zirconia thermal barrier coatings, particularly in relation to spray parameter variables.

(ii) Modelling of the plasma spray process to assess the effects of spray parameters on temperature distributions within coatings during deposition and the development of residual stress on subsequent cooling to room temperature.

(iii) Investigation of the phase stability of candidate zirconia thermal barrier coatings at elevated temperatures for extended ageing periods.

Parts (i) and (ii) were selected particularly because of their importance in predicting the response of a thermal barrier coating to transient heating or thermal shock conditions. A detailed knowledge of the residual stress distribution and how particularly it is affected by spraying parameters should lead to the manufacture of more durable thermal barrier coatings.

The latter section attempted to provide useful data for determining a safe time/temperature operating envelope for zirconia coating materials. This information was considered essential if structural changes that may lead to early failure are to be avoided during engine operation.

2.18 Determination of residual stress in zirconia thermal barrier coatings.

Thermal spraying was originally developed to allow the surfaces of metallic components to be modified or repaired by deposition of a metallic overlay coating. The importance of residual stress in determining the adhesion and performance of such metallic coatings was soon realised and techniques were developed to measure residual strain. Residual stresses were then calculated from a knowledge of the elastic properties of the

substrate and coating materials. Of the more common methods developed for metallic coatings, several have been applied, with some success, to the determination of residual stress in refractory coatings.

One of the earliest methods is known as the Sachs' boring-out technique, [97]. Simply, a round bar is coated with material and strain-gauges or other measurement devices are attached to the curved surface. Metal is removed from the centre of the bar by boring or drilling, and the diameter of the drill is progressively increased. Measurement of deflections during this process allows calculation of the residual stress pattern in the coating, [98]. Several variations exist depending on the particular geometry of the coated part. Thin walled tubes or rings may be coated on the outer or inner curved surfaces and strain gauges attached to the uncoated surface either before or after deposition. Coating material is removed layer by layer, either by turning or grinding and the stresses calculated from measured deflections, [99,100]. Alternatively, electrochemical polishing may be used to remove the metallic substrate, [101]. A recent development monitors residual strain during deposition via strain gauges attached to the rear face of the substrate, [102].These techniques are summarised in figure 2.18.

An alternative route, often used to determine stress

in sheets or plates, is the hole-drilling method, [103]. Three strain gauges are mounted in a circle or 'rosette' onto the surface of a coated part, such that they surround a small area of material, figure 2.19. A high speed drill progressively removes material from this central area and relaxation around the hole is monitored by the strain gauges as a function of hole depth. The arrangement of gauges allows the determination of residual principal stresses throughout the coating and substrate thickness, [104,105].

A final destructive technique relies on the inertness of zirconia coatings to allow chemical dissolution of the metallic substrate and bondcoat layers. The free ceramic layer undergoes relaxation and bending on substrate removal and careful measurement of the radius of curvature allows determination of residual stress in the attached coating, figure 2.20, [69].

Non-destructive determination of residual stress in coated components can be effected in a number of ways. One of the simplest relies on measurements of the deflection of coated test strips after spraying. Sufficiently thin substrates allow stress relaxation by bending and the magnitude of residual stresses can be determined from a knowledge of the elastic properties of each layer and measurement of the radius of curvature, figure 2.21, [106,107].

X-ray diffraction can also be used to measure

residual stress in coatings. The concept relies on determination of lattice strain from diffraction peak shifts and broadening compared to unstressed material. Measurements at different angles to the coating surface allow calculation of principal residual stresses, [108,109,110,111].

To assess the suitability of each technique for determination of residual stress in thermal barrier coatings, a number of criteria related to the effectiveness and accuracy of the technique were applied to each method. The results are summarised in table 2.3. For production situations, where routine non-destructive examination is necessary for quality control, the obvious technique for real component geometries is X-ray diffraction. This was discounted as an experimental method, however, because the depth of penetration of X-rays is usually quite small (20-50μm), the irradiated area is necessarily limited to a few mm^2 and the measured lattice spacing represents an average over the irradiated volume. Further, the technique is unlikely to be able to provide information on the variation of residual strain with coating thickness. Similarly, strip deflection techniques, although non-destructive, rely on the presence of a sufficiently thin substrate to allow bending and relaxation to occur, and the stresses measured are again macroscopic average values over the coating thickness. Even

allowing for the latter point, actual components may have relatively thick cross-sections that will prevent substrate deflection.

A semi-destructive technique, based on measurements of stress buildup during deposition, was discounted because of the difficulties of instrumenting actual or testpiece geometries during plasma spraying on rotating carousels. Of the remaining destructive methods, a lack of knowledge about the relationships between residual stresses measured on continuously sprayed, small diameter rods or rings, compared to those in intermittently sprayed flat topped pistons, cylinder heads or flat test pieces precluded the use of these methods. Further, progressive removal of layers of brittle ceramic coating material by grinding or machining is almost certain to induce damage and alter the stress state. Also, when strain gauges are attached to the porous coatings, it is inevitable that some adhesive will penetrate into the material. Subsequent curing expansions/contractions together with local densification and bonding would then alter the residual stress distribution significantly.

Similarly, the hole drilling technique relies on attachment of strain gauges to the surface of porous coatings and again is highly localized in application. This latter consideration may give cause for concern, particularly where the coating properties vary over the

surface eg. when segmentation cracking is present.

The remaining method of determination, based on substrate dissolution, is also subject to certain assumptions and limitations. Simply, removal of the substrate and bondcoat by chemical etching allows the 'free' ceramic coating to relax and attain equilibrium. Subsequent calculations, based on bending theory and assuming the elastic properties of the coating are uniform through the thickness, allow the determination of residual stress in the coating plane. An important assumption at this point is that remaining residual stresses in the relaxed 'free' ceramic coating are negligible but this need not be so, they may simply balance out. If the properties of the coating are non-uniform then this would further invalidate this assumption. Another problem with this technique is that the attachment of strain gauges to the coating prior to dissolution is precluded because of adhesive impregnation, the stiffening effect of the strain gauge plus adhesive on very thin coatings and the need to protect the gauge from corrosive attack during etching. Measurement of dimensional change is therefore limited to mechanical or optical methods, with consequent reduction in accuracy and repeatability. Finally, in order to remove the stiffening effect of transverse curvature and allow the free coating to achieve complete relaxation in one direction, it is necessary to

cut long, thin testpieces from the original coated testbar, figure 2.22. It is assumed that cutting thin strips of coated material from larger plates does not significantly alter the stress distribution within the coating since the constraints are supplied by the relatively massive substrate. Also both coating and substrate materials are assumed to have sufficiently high elastic modulii that shear stress effects are minimised at the cut edges, figure 2.23. Further, any sectioning damage is minimised by polishing of the cut edges. These assumptions may not be altogether unjustified because the microcracked nature of ceramic thermal barrier coatings must give rise to stress discontinuities within the coating, figure 2.24. Finally, the original technique, as described in reference [69], does not include any measurements of linear dimensional changes in the coating plane on substrate removal. Rather, it was assumed that residual stress was entirely described by equivalent bending moments, derived from the curved profiles of free coatings. As an important improvement to this method, linear dimensional changes and their associated residual stress components are considered in this work in an attempt to more accurately describe the stress state, figure 2.25.

Despite these limitations, it was felt that the technique provided a useful method of quantifying

residual stress in thermal barrier coatings because of its macroscopic nature, simplicity both in terms of testing requirements and calculation, avoidance of adhesive ingress problems associated with the use of strain gauges and provision of data at both coating-substrate and free surfaces.

2.19 Modelling of temperature distributions in thermal barrier coatings during and after deposition and prediction of residual stress.

The temperature distribution and dimensions of both coating and substrate do not remain constant during plasma spraying for a number of reasons:

(i) The deposition temperatures of consecutive layers of coating material change because of conductivity differences and preheating effects in the underlying material.

(ii) Repeated passes of the plasma torch serve to preheat the underlying material and substrate.

(iii) Heating of both substrate and coating results in thermal expansion.

On completion of the spray process, cooling throughout the coating and substrate gives rise to further differential contractions between the various materials. It is these varying contractions which cause residual stresses. Any thermal gradients may then give rise to stress gradients within the coating and

substrate. It is important then in any model which attempts to calculate residual stresses from temperature distributions to acccurately predict not only the final temperature distribution at the end of spraying but to consider the origins of thermal gradients during deposition.

Once coating is complete, the assumption is made that brittle ceramic coating layers subject to tensile contraction stresses are essentially free of residual stress. Cooling from the 'stress free' temperature may then result in compressive stress in the ceramic coating layers. The degree to which the calculated values of final residual stress simulate those generated in practice depends on the choice of stress free temperature, the accuracy with which the initial 'stress free' temperature distribution can be predicted and the values of elastic and thermal properties for each component material.

A number of mathematical models of varying complexity exist. These attempt to calculate, through finite difference and finite element heat transfer analysis, the temperature distributions in plasma sprayed coatings, [112,113,114,115,116,117,118]. The task of calculating residual stress has been limited to fewer investigations, [115,116,118]. Much of the important theory necessary to develop such treatments has been adequately reviewed elsewhere and will not be

reproduced here, [119].

While the important effects of such process variables as deposition rate, substrate temperature and coating thickness have been identified, and the compressive nature of residual stresses in thin thermal barrier coatings has been reproduced, [118], these models generally do not consider the important geometrical aspects of plasma spraying. For example, deposition of coating material is usually assumed to be continuous ie. the surface of the coating is treated as a steadily advancing boundary. This is obviously different from reality where discrete particles arrive at intermittent intervals. Further, the plasma torch is generally assumed to be fixed in relation to the substrate and to supply a constant heat flux. In practice, this situation rarely occurs because coatings are built up by successive passes of the plasma torch, and therfore heat input will be cyclic in nature, with the duration and intensity of heat flux controlled by the relative velocity of workpiece and sprayhead and the torch-substrate separation respectively. Development of a realistic model of ceramic thermal barrier coating deposition in this instance then included heat transfer conditions established by previous workers, but modified to include the cyclic variations in heat flux and material deposition rates associated with a particular spraying geometry. The model was then

expected to produce more realistic temperature distributions in model ceramic thermal barrier coating systems and hence residual stresses more closely related to those developed in practice. The inclusion of realistic material data into the model was considered of great importance in achieving worthwhile results, and where necessary, measurements on actual coating materials were carried out to determine the relevant properties.

2.20 Investigation of phase stability in zirconia thermal barrier coatings at elevated temperatures.

2.20.1 Comparison of available techniques.

A number of techniques are available for phase analysis of zirconia materials. The most popular are those based on electron microscopy and X-ray diffraction analyses. The former, in addition to providing high resolution images of the constituent phases, has been successful in determining the local chemical composition and crystal structure of precipitates in both bulk, [46,120,121] and plasma sprayed yttria-zirconia, [90,122]. Despite this, the method does not lend itself to routine quantitative coating analysis because of the destructive and time consuming process of thin foil manufacture, necessarily centred on a highly localised area of interest. X-ray

diffraction, on the other hand, can be used to non-destructively examine actual coatings in-situ and provide the absolute accuracy necessary for determination of lattice parameters. The latter method was therefore selected for quantitative phase analysis of zirconia thermal barrier coatings.

2.20.2 Quantitative phase analysis using X-ray diffraction.

In an X-ray powder diffractometer, the diffracted intensity, I, from the surface of a thick slab of crystal powder is described by the following equation, after reference [123]:

$$I = I_o K \left(\frac{1}{V^2}\right)\left[|F|^2 \cdot p \cdot \left(\frac{1+\cos^2 2\theta}{\sin^2\theta \cos\theta}\right)\right]\left(\frac{e^{-2m}}{2\mu}\right) \qquad 2.7$$

where I_o = intensity of the incident X-ray beam

and K = constant relating to radiation and beam size

V = volume of unit cell

F = structure factor

p = multiplicity factor

e^{-2m} = temperature factor

μ = linear absorption coefficient

$\frac{1+\cos^2 2\theta}{\sin^2\theta \cos\theta}$ = Lorentz polarisation factor.

The principle of quantitative analysis of a

crystalline substance in a mixture by X-ray diffraction relies on measuring the relative intensity of one or more diffraction lines of this substance with respect to a given line of another standard substance, [124]. Generally, this method requires that relative intensities are measured from known mixtures with the standard substance, allowing the construction of a calibration curve. In the 'polymorph' method, high temperature zirconia phases are assumed to be polymorphic with monoclinic zirconia and the internal standard is omitted, [123], leading to the following relationship:

$$I_{m(111)} + I_{m(11\bar{1})} = I_{H(111)} \qquad 2.8$$

I_m and I_H refer to the integrated intensity of monoclinic {111} reflections and high temperature tetragonal or cubic polymorphic {111} reflections respectively. If the high temperature cubic phase is assumed to be equivalent to stabilized cubic zirconia, [125], then equation 2.8 can be re-written as:

$$X_M = \frac{I_{m(111)} + I_{m(11\bar{1})}}{I_{m(111)} + I_{m(11\bar{1})} + I_{c(111)}} \qquad 2.9$$

where X_M = weight fraction of monoclinic phase

and $I_{c(111)}$ = integrated intensity of (111) stabilized cubic zirconia.

Intensity calculations based on equation 2.8 show that it is accurate when Zr^{4+} ions alone are assumed to contribute to the diffracted intensity. Inclusion of oxygen ion and effective cation scattering factors for stabilised cubic material into equation 2.8 result in large discrepancies between theory and experimental results, [125]. If, however, the presence of stabilizing ions is ignored, errors are reduced to approximately 5% in equation 2.9. Correction of integrated intensity for Lorentz polarization factors further improves accuracy, with linear calibration curves for ZrO_2-MgO and ZrO_2-CaO giving standard errors of between 2 and 3%, [125]. There is no theoretical justification for the use of equation 2.9 although cation-vacancy complexes may induce cancelling errors, [125].

Attempts to further improve the accuracy of equation 2.9 introduced corrections for both structure and multiplicity factors, [40]. This can be achieved by re-writing equation 2.7:

$$I_i = \frac{K R_i V_i}{2\mu_m} \qquad 2.10$$

where I_i = intensity of phase, i, in mixture, m

and V_i = volume fraction of i

$$R_i = \frac{1}{V_i^2}\left[|F|^2 p. \left(\frac{1+\cos^2 2\theta_i}{\sin^2\theta_i \cos\theta_i}\right)\right](e^{-2m_i})$$

μ_m = linear absorption coefficient of mix, m.

Re-arranging, the ratio of volume fractions of monoclinic and cubic phases is given by:

$$\frac{V_C}{V_M} = \frac{\left[R_{M(11\bar{1})} + R_{M(111)}\right] I_{C(111)}}{\left[I_{M(11\bar{1})} + I_{M(111)}\right] R_{C(111)}} \qquad 2.11$$

Only Zr^{4+} and O^{2-} ions are allowed to contribute to intensity and the effect of stabilizing ions is ignored. Assuming that the intensity of reflections is proportional to their R values, and Vc + Vm = 1, then equation 2.11 can be simplified, [40], to:

$$V_M = \frac{1.603\, I_{M(11\bar{1})}}{1.603\, I_{M(11\bar{1})} + I_{C(111)}} \qquad 2.12$$

The problems of $(111)_m$ and $(111)_c$ peak overlap are thus removed. The above relationship has been alternately expressed in terms of mole fractions, and extended to the analysis of three phase mixtures, consisting of tetragonal, cubic and monoclinic material, [47]. This latter aspect has been made possible by the use of high angle diffraction data where tetragonal and cubic peak separation is improved. The following relationships are widely used, [47,91,126,127,128,129], to determine the phase compositions of zirconia coatings:

$$\frac{M_M}{M_{F,T'}} = \frac{0.82\left(I_{M(11\bar{1})} + I_{M(111)}\right)}{I_{F,T'(111)}} \qquad 2.13a$$

$$\frac{M_F}{M_{T'}} = \frac{0.88\, I_{F(400)}}{\left(I_{T'(400)} + I_{T'(004)}\right)} \qquad 2.13b$$

$$M_{T'} + M_F + M_M = 1 \qquad 2.13c$$

Unfortunately, the structure factors originally used to calculate the R parameters in equation 2.12 have subsequently been shown to be incorrect, [130], and the corrected equation is given below:

$$V_M = \frac{2.374\, I_{M(11T)}}{2.374\, I_{M(11T)} + I_{C(111)}} \qquad 2.14$$

Also if the R parameters are assumed proportional to their respective intensities then a 30% error occurs in equation 2.8, [130]. Experimental calibrations carried out on pure tetragonal+monoclinic mixtures are described quantitatively by the following equation:

$$F_t = \frac{I_{t(111)}}{I_{t(111)} + I_{M(111)}} \qquad 2.15$$

However it cannot be justified theoretically, [130]. It is also successful in describing monoclinic+cubic mixtures when the tetragonal reflection is replaced with the relevant cubic data. A comparison between the calculated results from alternative formulae are given in table 2.4 for 60% cubic/40% monoclinic integrated intensities, after [130], and shows that equation 2.15

is the most accurate.

Calculation of R parameters for equation 2.15 gives the ratio $R_{m(111)}/R_{t(111)} = 0.32$ whereas theory predicts that it should be unity. Apparently, the reliability of R value based equations is questionable because small variations in atom position, and hence structure factor, have pronounced effects, and sufficiently accurate data is not available, [130].

An alternative approach, designed to allow calculation of volume fractions from intensity ratios, utilizes two forms of X-ray diffraction analysis in order to develop a non-linear calibration curve for pure tetragonal+monoclinic zirconia mixtures, [131].

The monoclinic integrated intensity ratio, Xm, is given by:

$$X_m = \frac{I_{m(11\bar{1})} + I_{m(111)}}{I_{m(11\bar{1})} + I_{m(111)} + I_{t(101)}} \qquad 2.16$$

where $I_{t(101)}[f.c.t.] \equiv I_{t(111)}[b.c.t.]$

Assuming that:

$$I_m = V_m H_m \qquad 2.17$$

where V_m = volume fraction of m

and H_m = theoretical intensity of 100% m.

Equation 2.16 becomes:

$$V_m = \frac{P X_m}{1 + (P-1) X_m} \qquad 2.18$$

where $P = \frac{H_{t(101)}}{H_{m(11\bar{1})} + H_{m(111)}}$

Theoretically, the value of P = 1.340, based on available data. Using the whole powder-pattern fitting technique to calculate the actual volume fraction of monoclinic zirconia, Vm, in various mixes, and the integrated intensities of the relevant peaks to calculate the intensity ratio allows a calibration curve to be constructed. Assuming the same functional form as equation 2.18, a fit of the calibration curve produced a value of P = 1.311 $\pm$ 0.004, [131]. The latter was considered more accurate than the theoretical value because of the amount of data used in its calculation. If the error in Xm is less than 1%, then Vm can be calculated to within $\pm$ 1.2% over the whole composition range. Later, theoretical calculations of P based on a similar analysis for CaO, MgO and Y_2O_3 stabilised cubic+monoclinic systems of different compositions allow the determination of volume fractions of these phases when the chemical constituents and intensity ratio are known, [132]. Using equation 2.18 and a P value from the latter analysis, similar results to those presented in table

2.4 are obtained, Vc = 65.1%, Vm =34.9%, but derived from a theoretical basis. From the preceeding considerations it is apparent that a significant proportion of published results of phase analysis of zirconia coatings by X-ray diffraction is carried out using equations which do not have sound theoretical origins. Despite the limitations described above, the technique described by equations 2.13a to c was used in this study. Results obtained in this manner were expected to be reasonably accurate and to be directly comparable with the majority of published literature data.

Generally, where analysis of coating behaviour has been carried out, the temperatures were similar to those experienced in gas turbine operation ie. greater than 1150°C, [47,126,127,129]. In one instance, calcia stabilized coatings intended for lower temperature diesel engine use were annealed at 550°C and 900°C for 100 hours and de-stabilisation was found to occur at the latter temperature due to stabilizer evaporation, [51]. Experience with gas turbine engine thermal barrier coatings suggests that the most durable coating materials are those based on nominally 8 wt% yttria P.S.Z, [91]. This material therefore was selected as an important candidate for insulation of diesel engine components by plasma spraying and formed the basis of this investigation. A systematic study, then, over a

temperature range reflecting present and future operating temperatures, was expected to provide important data for assessing the suitability of this material as an insulating thermal barrier coating.

Chapter 3 - Experimental Procedure.

3.1 Introduction.

This chapter describes in detail the materials, facilities and experimental methods used in this investigation. Areas covered include:

(i) Plasma spray facility.

(ii) Coating materials.

(iii) Evaluation of optimum powder feed and melting conditions.

(iv) Determination of coating residual stress.

(v) Manufacture of coated testpieces.

(vi) Microstructural examination.

(vii) X-Ray diffraction analysis of powders and heat treated coating materials.

(viii) Measurement of coating elastic modulus.

(ix) Measurement of coating thermal expansion coefficient.

(x) Measurement of specific heat capacity of coating materials.

3.2 Plasma spray facility.

3.2.1 Existing laboratory plasma spray equipment and methods.

A schematic diagram of the plasma spray facility existing at the start of this study is given in figure

3.1. A Metco 3MB plasma torch was mounted in a cradle inside the spraying booth, such that the plasma flame pointed vertically downwards. Testpieces to be coated were attached to the upper surface of a small trolley located under the plasma torch. Alternating transverse movement of the trolley along a straight track was achieved by a reversing air ram system, and the gun/cradle assembly was capable of movement in an orthogonal direction by virtue of a hand operated linear screw arrangement. Simultaneous operation of ram and linear screw allowed the plasma flame to be scanned across the surface of the testpieces.

Powder, injected radially into the flame below the torch anode nozzle exit, was melted and accelerated towards the moving testpiece below where a coating of the desired thickness was built up in successive passes.

Air cooling of the samples was achieved by forcing compressed air into a perforated tube, closed at one end and mounted underneath the testpieces, such that cooling air jets were directed onto the back face during spraying.

3.2.2 Limitations.

A detailed study of the effects of plasma spray parameter variations on coating residual stress requires that uncontrolled variation in coating

properties and quality ie. lack of repeatability, should be avoided. The existing facilities were reviewed during trial operation with these factors in mind and a number of important limitations were identified.

(i) The trolley/ram system was capable of operation at one nominal speed only, ~($0.13ms^{-1}$), and despite the provision of air accumulators and pressure regulation valves, the traverse speed was found to vary with inlet air pressure.

(ii) The alternating trolley motion resulted in sample thermal histories that were mounting position dependant. For example, testpieces attached to the ends of the trolley received two rapid thermal transients followed by a long period of cooling, while those in the centre experienced more regular thermal cycles.

(iii) The hand operated gun/cradle traverse system was inaccurate and subject to operator error. As a result, surface finish and coating thickness were variable.

(iv) Air cooling was limited to the back face of testpieces, and subject to inlet pressure variations. No facilities were available for adjustment of inlet pressure and flow rate to controlled values.

(v) The workpiece-nozzle separation distance or spray distance was in general fixed, although spacer blocks

were available for limited adjustment.

(vi) The powder feed rate was found to be variable and difficult to control. Also when preparing thermal barrier coatings the change in materials from bondcoat to zirconia layer required cleaning and adjustment of the single feeder unit.

Many of the limitations outlined above have been previously identified in the literature review as contributing to coating variability and poor quality. Also the lack of controlled continuously variable adjustment of important spray parameters such as workpiece/sprayhead relative velocity and spray distance prevented a detailed investigation from being attempted. The plasma spray facilities were consequently upgraded to provide the necessary control and range of adjustment for a detailed investigation.

3.2.3 Description of upgraded spraying facilities.

A schematic diagram of the improved plasma spray facility is given in figure 3.2. The gun orientation and mounting cradle were retained, but the linear screw arrangement was removed and the gun/cradle assembly permanently fixed to the roof of the plasma spray booth. The trolley/track arrangement was discarded in favour of a flat turntable. Testpieces were then attached to the upper surface using bolts. The whole unit was capable of movement along one axis, front to

back, by provision of linear bearing slides and a lead screw.

To allow the necessary control of gun/workpiece relative velocity and traverse rate, high power stepper motors and 90°, 15:1 reduction gearboxes were employed to provide motive power. The turntable centre shaft was driven directly, by a stepper motor/gearbox assembly mounted underneath, through shock absorbent couplings, figure 3.3. Provision of a locking bush in the centre of the turntable allowed for rigid attachment to the rotating shaft. Height adjustment was achieved by sliding the turntable unit up or down the central shaft and fixing at the required position, figure 3.4.

Traversing of the turntable assembly was achieved by a similar stepper motor/gearbox/coupling arrangement attached to a lead screw. The rider for the lead screw was fixed to the underside of the turntable carrier. Motor rotation then caused the turntable to track underneath the plasma flame at a known rate, figure 3.5.

Accurate, reproducible control of motor speeds was achieved by using a microcomputer. This was necessary because the effective path of the plasma flame on the rotating/traversing turntable was spiral. To achieve a constant coating thickness over the whole of the turntable surface area required a constant relative linear velocity between a point on the table surface

directly below the plasma flame and the plasm torch itself. As the radius of the spiral was decreased, the angular velocity was increased to maintain a constant linear velocity, according to equation 3.1:

$$v = r\omega \qquad 3.1$$

where v = linear velocity (ms^{-1})

and r = radius (mm)

ω = angular velocity (radians s^{-1}).

The computer was programmed to generate motor drive pulses, via an interface, such that a constant linear relative velocity was maintained, during the spraying process. This was achieved by creating a table of numbers in the computer memory, related to the required motor speeds. As the rig operated, successive numbers were converted to drive pulses at particular frequencies, allowing continuous adjustment of the motor speeds. Libraries of such speed tables were created and stored on floppy disc prior to use, such that controlled operation simply required loading of the relevant data into memory for use by the control program.

The powder feed system was improved by obtaining a high quality twin powder feed unit, capable of simultaneous, separately variable, independant feed of both bondcoat and ceramic material. An additional

powder injection nozzle was fixed to the plasma torch, allowing separated injection of both powders and avoiding problems of contamination.

The air cooling system was also uprated by provision of separate front and back face cooling jets, and pressure and flow meters to aid reproducibility. Height adjustment of the cooling arrangement was provided to maintain constant jet/workpiece distance at different spray distances. The turntable surface was manufactered from perforated steel sheet to allow effective back face cooling of samples attached to it. The modified cooling arrangements are illustrated in figure 3.6.

The specifications of the improved facility are summarised below:

(i) Accurately controlled linear relative velocity between workpiece and sprayhead in the range 0.01 to 0.99ms^{-1}, and at traverse rates of 1,2 and 4mm rev.$^{-1}$.

(ii) Infinitely variable spray distance in the range 40 to 200mm.

(iii) Testpieces all have similar thermal history by virtue of rotating deposition geometry.

(iv) Reproducible, constant thickness coatings over whole of spray area.

(v) Testpieces up to 100mm diameter can be accommodated on turntables.

(vi) Variable, controlled, reproducible air cooling

in the range 0 to 2 bar and 0 to 100 $lmin.^{-1}$, distributed over whole of turntable surface.

(vii) Variable, accurate, independant and simultaneous feed of bondcoat and zirconia powder materials, with independant adjustment of carrier gas pressure and flow rates for each material.

Photographs of the complete spray apparatus, powder feed unit and computer/interface are shown in plates 3.1, 3.2 and 3.3 respectively.

An additional facility for monitoring testpiece backface temperatures during spraying was incorporated into the spray rig, and is illustrated schematically in figure 3.7. Platinum resistance thermometers were chosen as the sensing elements because they did not require the use of compensating cables. This was of particular importance because the rotating spray geometry necessitated construction of rotating electrical contacts. Backface temperatures were recorded continuously during coating of some testpieces using a calibrated bridge and chart recorder. Good thermal contact between the sensor and testpiece was achieved by the use of silicone heat sink compound.

3.3 Coating materials.

Two partially stabilised zirconia powder materials, manufactured by alternate routes and containing nominally 8 wt% yttria, were selected for this study on the basis of their superior performance in gas turbine applications. Powder A was manufactured by fusing, crushing and grinding while powder B was sintered and spray dried. The bond coat material consisted of a nickel-chromium atomized alloy powder to which had been added aluminium powder and an organic binder. The chemical composition and particle size analysis of the as supplied materials are given in tables 3.1 to 3.3. Samples of each powder were examined in a scanning electron microscope to assess their morphology and the zirconia materials were subjected to X-ray diffraction analysis to determine their phase structure and degree of stabilisation.

3.4 Evaluation of optimum powder feed and melting conditions.

3.4.1 Calibration of powder feed unit.

The powder feed unit selected for this work provided a metered flow of material in a dry carrier gas (argon). Control of feed rate was achieved in the unit by depositing powder material from an agitated hopper into an accurately machined channel on a small

turntable. Particles were lifted from the channel and entrained into the carrier gas by a pick up duct and positive gas pressure. Powder feed rate was regulated by the rotation speed of the turntable, indicated as 0-100% RPM.

As the density and size range of each powder was dissimilar it was necessary to establish the feed rate versus % RPM relationship for each. Care was taken to ensure that initial conditions of carrier gas pressure and flow rate were sufficient to entrain all material into the gas stream when operating at maximum speed. Provided that subsequent adjustment prevented powder build up within the unit, material feed rate was simply related to indicated rotational speed.

Calibration was carried out for both metallic and ceramic powders by capturing the material, over a timed period, in weighed containers. Zirconia powders were predried at 110°C for 1 hour to prevent 'caking' in the feed hopper.

3.4.2 Optimisation of powder melting conditions.

Plasma torch operating parameters used throughout this investigation were maintained at constant values recommended by the manufacturer and are summarised in table 3.4.

Powder injection and deposition conditions for the bondcoat material were similarly well established and

also remained constant, table 3.5.

Optimum injection parameters to maximise deposit and melting efficiency for zirconia powders A and B were unknown for the particular combination of apparatus used in this investigation and were subsequently evaluated.

Deposit efficiency was measured by passing grit blasted and weighed aluminium alloy plates, 100mm square by 3mm thick, beneath the plasma flame at a known constant speed, spray distance and turntable radius with the traverse system inoperative. Subsequent weighing of the coated plates gave the amount of material deposited per radian per second and comparison with the known powder feed rate allowed efficiency to be calculated. Deposit efficiency, over a range of injection conditions and at a fixed material delivery rate, was subsequently evaluated by varying feeder gas pressure or flow rate at intermediate, fixed values of gas flow rate or pressure respectively. Calibration curves of weight deposited per unit length of spray pass, for both variable flow and pressure conditions, then allowed the determination of powder injection conditions for maximum deposit efficiency.

Particle melting efficiency was investigated using a scanning electron microscope. Sections cut from deposit efficiency test plates were sputter gold-coated to avoid charging effects and evaluated for completeness

of melting and entrainment of unmelted material.

3.4.3 Determination of deposit efficiency of zirconia materials as a function of spray distance.

Using optimum injection and melting parameters determined at a fixed spray distance and feed rate in the previous section, similar tests were carried using efficiency plates but the spray distance was systematically varied. Subsequently, a calibration curve of deposit efficiency versus spray distance was determined for each of the zirconia powders. No allowance for the variation in melting/deposit efficiency with spray distance and therefore residence time, was included in this investigation.

3.5 Determination of in-plane coating residual stress.

Test bars, approximately 70mm long by 5mm wide, were cut from coated test plates using a thin abrasive cutting wheel. Regardless of testplate size, bars were always sectioned in a direction parallel to the tangential spray path. Larger 100mm$^{\square}$ plates allowed additional bars to be cut from an orthogonal direction. Subsequent polishing of cut edges was necessary to provide accurate measurement datums and to remove cutting damage. The length of each bar was recorded at a number of fixed locations across the width.

Each test bar was immersed in a solution chosen to

etch away substrate material and bondcoat leaving the inert coating undamaged. The relevant media are given in table 3.6. Each coating was then washed in distilled water and dried.

In-plane residual stresses were determined by effectively calculating the strain necessary to return the relaxed free coating to its original profile and dimensions when attached to the substrate. The technique is illustrated in figure 3.8. First the thickness and radius of curvature of each free coating were determined. Bending strains, induced in the ceramic on restoring the curved free coating to its original profile, were calculated at the top or exposed surface and the ceramic-metal interface using equations 3.2a and 3.2b respectively:

$$\text{Exposed Surface Strain, } \varepsilon_{c_s} = \frac{t}{2r - t} \qquad 3.2a$$

$$\text{Interfacial Surface strain, } \varepsilon_{c_i} = \frac{t}{2r + t} \qquad 3.2b$$

where t = coating thickness (m)

and r = radius of curvature (m).

Subsequently, each curved free coating was flattened between parallel metal plates to mimic the application of the above bending strain. Any change in dimension along the long axis of the coating layer was determined by careful measurement. The overall linear strain to

return the flattened free coating to its original long axis dimension was then calculated using equation 3.3:

$$\text{Linear Strain, } \varepsilon_l = \frac{(l_o - l)}{l_o} \qquad 3.3$$

where l_o = original length (m)

and l = free length (m).

At each surface, the total strain was then given by the algebraic sum of the two strain components, equation 3.4:

$$\text{Total Strain, } \varepsilon_{tot} = \varepsilon_c + \varepsilon_l \qquad 3.4$$

Determination of the total strain at each surface in two orthogonal directions then allowed the calculation of biaxial in-plane residual stresses using equations 3.5 and 3.6 which incorporated suitable elastic constants for the coating materials:

$$\text{Total Surface Strain in } x \text{ direction, } \varepsilon_{t_x} = \frac{1}{E_c}(\sigma_x - \nu_c \sigma_y) \qquad 3.5$$

$$\text{Total Surface Strain in } y \text{ direction, } \varepsilon_{t_y} = \frac{1}{E_c}(\sigma_y - \nu_c \sigma_x) \qquad 3.6$$

where σ_x = stress in X direction (Pa)

and σ_y = stress in Y direction (Pa)

E_c = Youngs modulus (Pa)

ν_c = Poissons ratio.

As no differential contraction between coating and substrate existed normal to the coating plane, the component of stress due to this effect was assumed to be zero. However, the Poisson effect of the biaxial residual stress within the coating was such that a perpendicular stress, σ_z, must be developed. This was calculated using equation 3.7:

$$\sigma_z = -\nu_c (\sigma_x + \sigma_y) \qquad 3.7$$

3.6 Manufacture of coated testpieces.

Flat testpieces, either 100mm long by 25mm wide strips or 100mm square plates, were cut from rolled sheet material and drilled to accept mounting bolts, figure 3.9. Each sample was marked for identification, and grit blasted using coarse alumina under the conditions in table 3.7. Subsequent ultrasonic cleaning in alchohol served to remove oil and grit residues.

Samples for residual stress determination were not annealed prior to use for two important reasons.

(i) Current industrial practice does not generally include stress relief annealing, after grit blasting, in the coating process. As the results of this work were intended to highlight the importance of typical spray parameters, departures from typical coating situations were avoided as far as possible.

(ii) Plasma spraying was expected to raise substrate temperatures to such an extent that stress relief would occur naturally during the process.

Testpieces to be coated were bolted to the upper surface of the turntable assembly and rotated at a constant linear workpiece/sprayhead relative velocity, while traversing at a fixed rate per table revolution under the sprayhead. Coating was achieved during a number of complete cycles of the rig. One cycle consisted of twenty revolutions of the turntable while traversing into the booth and a further twenty revolutions traversing back to the the rest position. A traverse rate of 4mm rev^{-1} was maintained throughout this investigation allowing coating over a maximum turntable radial length of 80mm.

The plasma torch and powder feed units were operated continuously throughout the coating cycle, invariably using the torch parameters in table 3.4 and powder dependant injection conditions determined earlier. Only the zirconia powder feed rate was altered to allow deposition of a given thickness per coating cycle, depending on the linear relative velocity, spray distance and material type.

Deposition of bondcoat material was fixed using one set of parameters, table 3.5, designed to provide a layer 0,1mm thick. No variation of bondcoating parameters was included in this investigation, other

than where the bondcoat was omitted to determine its effect on residual stress.

Where necessary, cooling was provided by air jets fixed above and below the turntable, at predetermined pressures and flow rates.

Several programmes of coating deposition were carried out. Each was designed to investigate the effects of controlled spray parameter variation. The technique described in section 3.5 was used to determine residual stress within coatings. In addition, representative samples from each batch of testpieces were sectioned and prepared for microstructural examination. Deposition conditions were chosen to investigate the effects of the following parameters:

(i) Substrate plate size, measurement orientation and ceramic powder type.

For reasons of economy in terms of ceramic powder usage, it was considered desirable to manufacture testpieces using the 100mm by 25mm plate size described earlier. However, the use of these samples precluded accurate measurement of transverse coating strain, by virtue of the small length dimension of testbars (<25mm). Precise measurements were however possible on testbars sectioned parallel to the long axis of such samples, but minimisation of the sprayed area required that the long axis of each plate be aligned

tangentially to the circumference of the coating table.

Unfortunately, to calculate biaxial coating stress required that measurements be taken in both transverse and longitudinal dimensions on each plate, normally requiring the larger 100mm by 100mm size. A programme of coating deposition was therefore undertaken, to determine whether the measured values of transverse and longitudinal strain determined on 100mm by 100mm plates were related to those obtained simply from the longitudinal measurements gained from 100mm by 25mm testpieces. Both sizes of test plate were coated during the same operation under varying spray conditions described in set 1 of table 3.8. Similar sets of testpieces were prepared using both powders A and B, deposited over 0.1mm of bondcoat on aluminium substrates in an attempt to quantify any differences arising from material type.

(ii) Time delay between coating cycles.

Standard industrial practice is to build up ceramic thermal barrier coatings by semicontinuous deposition, however, an alternative is to allow each layer to return to room temperature between subsequent coating cycles. To determine the effect of such methods on coating residual stress, 0.2mm thick ceramic coatings, over 0.1 mm of bondcoat on aluminium substrates, were prepared for measurement with parameter set 2 of table

3.8, using powder A. Samples produced by intermittent deposition were subjected to single coating cycles and allowed to cool to room temperature before further build up.

(iii) Ceramic coating thickness.

The importance of achieving viable, thicker ceramic coatings has already been emphasised. A program of coating was therefore conducted using parameter set 3 in table 3.8, to assess the development of residual stress in thermal barrier coatings with increasing ceramic thickness. Test plates were coated continuously, but in stages, with ceramic material A, over 0.1mm of bondcoat on aluminium substrates, up to a thickness of 1.2mm. A minimum delay between stages of coating, typically 30 seconds, was necessary to remove samples of intermediate thickness.

(iv) Workpiece/sprayhead relative velocity.

Workpiece/sprayhead relative velocity may have an important effect on residual stress in thermal barrier coatings. This is because residence times under the plasma flame, and therefore heating effects, are closely related to velocity. A comprehensive spray program was carried out to quantify this effect over a range of relative velocities at two extremes of spray distance. Test plates were prepared using

workpiece/sprayhead separation distances of 65mm and 110mm, over a range of relative velocities of 0.1ms^{-1} to 0.5ms^{-1}. At each distance, coatings of a constant thickness were produced, regardless of velocity, by adjusting the number of coating passes. The deposition conditions are summarised in parameter set 4 of table 3.8. Coatings were prepared using material A, deposited over 0.1mm of bondcoat on aluminium substrates.

(v) Air cooling during spraying.

The majority of samples produced throughout this study were deposited using air cooling because this is generally accepted to improve coating quality. The effect, however, of air cooling conditions on coating residual stress is not well known and so a program of deposition was carried out to investigate the optimum siting of cooling jets over a range of workpiece/sprayhead relative velocities. Ceramic coatings, 0.4mm thick, were produced using parameter set 5 in table 3.8, on aluminium substrates with 0.1mm of bondcoat using material B. Testplates were manufactured with either no air cooling, back face, front face or combined back and front face cooling. Where cooling was employed, each air delivery tube was mounted 40mm from the relevant face and air pressure was adjusted to achieve a flow rate of 100 litres per minute per tube. Platinum resistance thermometers were

mounted in good thermal contact with the back face of some samples and temperatures were recorded throughout the spray process.

(vi) Presence of a bondcoat.

From previous considerations, it is obvious that intermediate layers of bond coat alloy improve the adhesion and performance of ceramic thermal barrier coatings. The effect of bond coats on coating residual stress is unknown and for this reason a program of coating was carried out with bond layers omitted, using testpieces described in the previous section for comparison. A limited set of exactly similar conditions were employed, involving either no air cooling or combined back and front face cooling of the aluminium substrates.

(vii) Substrate material properties and thickness.

Aluminium substrates have been utilised throughout this study because they are representative of piston materials employed in current diesel engines and represent the greatest challenge in terms of thermal expansion mismatch tetween substrate and coating. The choice of plate thickness, about 3.5mm, was a balance between a nominal piston crown thickness and the time taken to cut out and etch away the substrate on test bars. Ceramic coatings are, however, envisaged to

provide insulation for a variey of metallic substrates of varying dimensions throughout insulated engines.

The effect of material properties and substrate thickness on ceramic coating residual stress was therefore of considerable interest and a coating program was designed to investigate their behavious under varying conditions.

Substrates of aluminium, copper and mild steel were chosen for their range of material properties. Typical values are given in table 3.9. Samples were prepared using parameter set 6 in table 3.8. Ceramic coatings, 0.3mm thick, of powder A were deposited over 0.1mm of bondcoat onto 100mm by 25mm testplates in three thickness ranges, summarised in table 3.10.

(viii) Thickness of industrial coatings.

As part of a collaborative effort to evaluate residual stress effects in industrial standard coatings on candidate substrate materials, coatings were prepared using parameter set 7 in table 3.8. Ceramic coating thicknesses of 1mm, 2mm and 3mm were built up by continuous deposition over 0.1mm bondcoats on aluminium and mild steel substrates. Specially prepared zirconia ceramic powders, based on material A, were used to manufacture the coatings. To improve deposit efficiency, the coarse starting powder was ground and then spray dried by the supplier. Spherical particles

in three narrow size ranges were produced, centred around mean diameters of 13μm, 21μm and 28μm. The powders were denoted C1, C2 and C3 respectively, and sets of samples were produced from each type for analysis.

3.7 Microstructural examination.

Samples for ceramographic examination were cut from test strips and plates using an abrasive cutting wheel and water based lubricant. The direction of rotation was always such that the wheel cut down through the coating first, to prevent lifting and spallation of ceramic material. Samples were mounted in cold-cure epoxy resin and subsequently prepared using a Struers automatic polishing machine. A summary of the method is given in table 3.11. The polishing technique was optimized for the ceramic material in order to reduce 'pull-outs' or disintegration of the brittle coating.

Subsequent examination was carried out using a reflected light microscope and photographs were taken using both grey and green filtered light for optimum results.

Polished sections, testpiece segments and powder materials for scanning electron microscope examination were first sputter coated with a thin layer of gold to prevent electrostatic charging effects. Analysis was carried out using a JEOL 35C microscope.

3.8 X-Ray diffraction analysis of powders and heat treated coating materials.

Zirconia powder samples for analysis were prepared by packing the material into a 20mm square hole cut into a small, 2mm thick, aluminium plate, backed with a microscope slide. The exposed surface was smoothed by passing a microscope slide over it, and another slide was used to contain the powder.

Coating samples for analysis were manufactured using parameter set 5 in table 3.8, on 100mm square aluminium alloy plates, without bondcoats. The plates were cut into 10mm square sections using an abrasive cutting wheel and substrate material removed using sodium hydroxide solution. Both powder materials A and B were used to manufacture free coating segments, nominally 0.35mm thick.

Subsequently, coating samples of each material were subjected to heat treatment in air in the temperature range 800°C to 1400°C for extended periods up to 100 hours. The samples were inserted into a furnace, at the heat treatment temperature, in alumina boats. On completion of the exposure period, the boats were removed from the furnace and the coatings cooled rapidly in still air to retain their high temperature structure. The heat treatment program for these materials is summarised in table 3.12.

Powder, as sprayed and heat treated coating materials

were analysed using a diffractometer and nickel filtered copper k_{α} radiation. Each sample was extensively analysed over two angular ranges, 27° to 34° and 72° to 77° of 2θ, at a scan speed of 0.125° of 2θ per second. Full scale deflections were adjusted to 2000 and 200 counts respectively.

Output data from the diffractometer, in the form of a continuous paper trace, was analysed visually to determine any gross structural changes.

Sections of each trace, between 72° and 77° of 2θ, were digitised and stored on magnetic disc for analysis by the suite of computer programs, designated 'X-RAY'. The software was developed to aid manipulation of X-Ray data into a standard form and to subsequently deconvolute overlapping peaks into their original components. Deconvolution was achieved using a non-linear, least squares iterative technique, capable of resolving up to 5 separate reflections, described in the Appendix. This allowed the determination of both integrated intensity for subsequent phase analysis, using equations 2.13a to c, and angular position for lattice parameter measurements.

3.9 Measurement of zirconia coating elastic modulus.

Thick test bars of free zirconia coating, in the range 1 to 3mm thick, originally prepared for residual stress analysis using parameter set 7 of table 3.8,

were subsequently tested to determine their elastic modulus.

A non-destructive sonic resonance technique, originally developed to measure the modulus of brittle graphite materials, was employed, (133). The test bars were mounted on p.t.f.e. supports at their nodal points and excited into resonance at their fundamental frequency. Measurement of this frequency together with the mass and dimensions of the test bar allowed the dynamic modulus to be calculated using equation 3.8:

$$\text{Dynamic Elastic Modulus, } E = \frac{A_r m f^2}{w} \qquad 3.8$$

where $Ar = 1.0959\left(\frac{t}{l}\right)^{-2.9571}$

and t = thickness (mm)

l = length (mm)

w = width (mm)

m = mass (Kg)

f = fundamental frequency of vibration (Hz).

3.10 Measurement of zirconia coating thermal expansion coefficient.

The apparatus used to measure zirconia coating thermal expansion coefficient consisted of a vertical quartz rod dilatometer, illustrated schematically in figure 3.10. A 1.25mm thick section of free coating, 30mm long by 5.5mm wide, prepared using parameter set 3

in table 3.8, was used for the determination. The coating segment was loosely supported by two semi-circular section 'cheeks' along its length, and rested on the bottom end of a quartz tube. A slotted quartz rod was placed over the other end and was attached to a displacement transducer.

The whole apparatus was thermally cycled up to 750°C at 10°C per minute and the thermal dilation of the coating recorded versus temperature. The linear thermal expansion coefficient was calculated using equation 3.9:

$$\text{Thermal Expansion Coefficient, } \alpha = \frac{\Delta l}{l_o \Delta T} \qquad 3.9$$

where Δl = expansion over temperature change ΔT

and ΔT = temperature change

l_o = original length.

The process was repeated over several thermal cycles to determine if any permanent dilations occured.

3.11 Measurement of specific heat capacity of coating materials.

The specific heat capacity at constant pressure, Cp, of zirconia materials A and B was measured using a du Pont differential scanning calorimeter.

Before use it was necessary to run a baseline scan

using two empty sample pans and lids so that their contribution to measured heat capacity could be eliminated. Subsequently, weighed samples of starting powder, as sprayed free coating or heat treated free coating (1400°C for 2H) were encapsulated in sample pans and cycled to 650°C at a heating rate of 30°C per minute in a nitrogen atmosphere.

A plot was made of the heat flow versus sample temperature and the base line scan was superimposed on the same axes. The specific heat capacity of each sample was calculated at 25°C intervals in the range 25°C to 650°C by measuring the difference in heat flow between baseline and full sample pans, and using equation 3.10:

$$\text{Specific Heat Capacity, } C_p = \left[\frac{60 \cdot E \cdot \Delta_{qs}}{H_r}\right] \cdot \frac{\Delta Y}{m} \qquad 3.10$$

where E = cell calibration constant (= 1.058)

and Δ_{qs} = heat flow axis range scaling in mW cm^{-1}.

H_r = heating rate in °C min^{-1}

ΔY = difference in heat flow between baseline and sample at temperature of interest in J

m = sample mass in mg.

Chapter 4 - Theoretical Model.

4.1 Introduction.

The importance of a thorough understanding of the properties and behaviour of thermal barrier coatings has already been emphasised in the preceding chapters. The response of zirconia coatings to thermal and mechanical transients has been documented, e.g. [4], but determination of absolute stress levels relies heavily on assumptions about the initial state of the coatings themselves. In particular, residual stresses have been related to average coating and substrate temperatures during spraying, implying that uniform stress distributions exist throughout the thickness of the coating on cooling after deposition, e.g. equation 2.6. Several workers, however, have shown this assumption to be incorrect in both metallic and ceramic coatings, with important consequences for two layer thermal barrier systems, [69,100,101,104,105]. Attention has therefore turned to predicting temperature distributions in model coating systems during the plasma spray process, [112, 113, 114, 115, 116, 117, 118, 119], with the ultimate aim of predicting residual stress levels, [115,116,118].

The complexity of the problem, involving both transient heat and fluid flow calculations, has led to a number of simplifying assumptions which may affect

the applicability of the solutions obtained. Generally, the plasma spray process is envisaged as consisting of a fixed heat source, (the plasma torch), from which heat is transferred by conduction and radiation to the coating particles and substrate, and from where heat is lost to the surroundings at a known rate. The coating is generally considered to build up at a known constant rate i.e. as a steadily advancing boundary, and the temperature distribution on completion of spraying facilitates calculation of residual stresses from a knowledge of the elastic and thermal properties of coating and substrate materials. A particular disadvantage of the preceeding method is that it does not consider the geometrical aspects of deposition. For example, most practical plasma spraying involves relative movement between the plasma torch and workpiece to allow for the build up of a uniform coating layer over the component surface. A consequence of the latter is that macroscopically, the coating is formed intermittently from material deposited at a non-uniform rate, by a heat source whose intensity varies with time. At a microscopic level, a coating is formed from discrete particles, rather than a continuous flow of molten material, whose arrival rate at the surface again varies with time. These latter considerations were considered to be of particular importance in developing a more realistic model of the

plasma spray process since they allow for heat losses in the coating and substrate between successive passes of the plasma torch. The model to be described here thus accounts for the particular plasma spray geometry used in experimental deposition of thermal barrier coatings, outlined in chapter 3, and employs standard finite difference heat flow numerical techniques, confined to the coating thickness dimension for simplicity, to predict heat flow through the system as a whole. The final temperature distribution on completion of spraying may then be used to determine room temperature residual stress levels.

4.2 Prediction of transient temperature distributions in thermal barrier coatings during and after plasma spraying.

Conceptually, a model of the system under consideration can be described by figure 4.1.

(i) Heat is tranferred from the plasma torch to the coating/substrate by conduction from the hot gas stream, radiation from the incandescent plasma flame and by conduction from heated particles which impact with the surface. The heat flux from the plasma torch and rate of impact of heated particles is expected to vary with time at any point on the substrate as a consequence of the relative movement of workpiece and plasma spray torch.

(ii) Heat will by conducted through the system and lost to the surroundings by conduction and re-radiation. The rate of heat transfer may then be affected by such factors as material properties and coating thickness and the nature and degree of any air cooling which may be applied during deposition.

The problem of modelling such a system can then be broken down into three distinct areas.

(i) Calculation of time dependant boundary conditions surrounding the model coating system.

(ii) Calculation of system temperature distributions as a function of time.

(iii) Calculation of time dependant modification to the model coating system thickness dimension i.e. arrival of new particles.

The model considers heat flow through a point in the centre of a flat testpiece, attached to a rotating turntable, which is traversed under the plasma flame such that a coating is built up. The point under consideration is considered, in heat flow terms, in the thickness dimension only for simplicity of calculation and because the highest temperature gradients are expected to be generated in this direction. In-plane heat flow is assumed to be minimal as adjacent areas in the testpiece are likely to remain at approximately similar temperatures, bearing in mind that the heat flux from the plasma torch is large and spread over a

large area of the testpiece when in contact with it.

4.3 Calculation of time dependant boundary conditions surrounding the model coating system.

Although the plasma torch is fixed and the turntable system rotated/traversed under it, it is helpful in visualising the path of the torch over the table surface if the opposite is assumed i.e. the table is fixed and the plasma torch is moved. The effective path is then spiral and is illustrated in figure 4.2. On the first half of a coating cycle, the torch spirals toward the centre of the turntable at a constant tangential linear velocity but at an increasing angular and radial velocity. For the second half, where the torch moves out from the centre of the table, the tangential linear velocity is again maintained and the angular and radial components are reduced. For a fixed point on a testpiece on the table surface, the direct heat flux then cycles alternately between a maximum and minimum value on each table revolution at the points of closest and furthest approach respectively, with the maximum value varying as a function of spiral radius. This latter effect is caused by the temperature/intensity variation with distance from the core of the plasma flame, and is illustrated in figure 4.3, after [23]. The important time variant boundary conditions which must then be calculated are radiative heat flux, plasma

gas temperature and heat transfer coefficient as seen by the reference point on the surface of the testpiece. As the finite difference method calculates temperatures at discrete time intervals, it is therefore only necessary to input the boundary data calculated at such relevant points in time.

4.3.1 Calculation of reference point position and velocity with time.

Calculation of boundary conditions at any point in time may be achieved by relating plasma flame parameters to expressions which describe the effective position and speed of the plasma torch relative to the centre of the turntable , given a set of initial conditions, tangential linear velocity and time step size.

The turntable/traverse system employs stepper motors driving 15:1 reduction gearboxes. Each motor shaft rotates through 360° after 200 input pulses. The angular rotation of both the turntable and traverse shaft per motor step is then given by:

$$\text{Angular Rotation / Motor Step, } d\theta = \frac{360}{200 \times 15} = 0.12^{\circ}\,\text{Step}^{-1}$$

and the linear traverse per step by:

$$\text{Linear Traverse / Motor Step, } dl = \frac{0.12 \times 4}{360} = 1.333 \times 10^{-3}\,\text{mm.step}^{-1}$$

To maintain a constant relative linear velocity between a point on the turntable surface directly below the plasma flame axis and the torch itself, requires the angular velocity to be continuously varied as the spiral radius changes (due to traversing), figure 4.4. The required angular speed may be determined using the following relationship:

$$V = r\omega \qquad 4.1$$

where v = tangential linear velocity (ms)

and r = radius of point (m)

w = angular velocity (rad.s^{-1}).

Unfortunately, limitations of the computer used in controlling the actual apparatus meant that the angular velocity of both turntable and traverse drive shafts could only be updated every 200 motor steps (24° of turntable rotation or 2.667 x 10^{-1} mm of traverse). To reduce errors in circumferential speed and sample position to a minimum, an effective, constant angular velocity, w_i , was calculated which allowed the same circumferential and radial distance to be covered in the same time period as if the shaft angular speeds had been continuously updated. This is illustrated in figure 4.5. For the model to be consistent with the practical apparatus, the value of w , may be calculated for each constant velocity segment of shaft rotation

from the following relationships, using the nomenclature of figure 4.5.

To cover the same circumferential distance in the same time:

$$V_c(t_2 - t_1) = \int_{t_1}^{t_2} V_i \, dt \qquad 4.2$$

i.e. the areas under the lines in figure 4.5c and figure 4.5f must be equal.

Now, $V_i = mt + c$

where $m = \dfrac{V_1 - V_2}{t_2 - t_1}$

and $c = V_2$

$$\therefore \int_{t_1}^{t_2} V_i \, dt = \int_{t_1}^{t_2} (mt + c)\, dt$$

ie. $$V_c(t_2 - t_1) = \frac{1}{2}\frac{(V_1 - V_2)}{(t_2 - t_1)}(t_2 - t_1)^2 + V_2(t_2 - t_1)$$

$$V_c = \frac{V_1 + V_2}{2} \qquad 4.3$$

Substituting equation 4.1 into equation 4.3 gives:

$$\omega_i = \frac{2V_c}{r_1 + r_2} \qquad 4.4$$

The speed errors which occur in v_i are small in view of the low traverse rates employed. For a given discrete time step size, Δt , the number of such whole time steps at each angular velocity may be calculated, with any small fractional part being added to the total time at the next velocity, using equation 4.5:

$$\text{Number of Time Steps, } n = \frac{t}{\Delta t} \qquad 4.5$$

where t = time taken to rotate through 200 steps

and Δt = discrete time step size chosen for heat flux calculation.

For a given starting turntable radius, angular position and relative linear velocity, boundary conditions of the corrected constant velocity segments and total number of discrete time steps per segment, it is then possible to calculate the position, direction and velocity of the plasma torch axis relative to angular and turntable centre datums after any given time interval throughout the spray cycle. This is illustrated in figure 4.6.

4.3.2 Calculation of net radiative heat flux from plasma torch to sample reference point.

The heat flux arriving at the surface of a sample exposed to a plasma flame is adequately described by equation 4.6, after [112]:

$$\text{Heat Flux, } q_r = \frac{I_T S}{2\pi L^2} \qquad 4.6$$

where I_T = total intensity of argon plasma radiation (W)

and S = surface area of sample (m^2)

L = distance from plasma flame (m).

The total intensity of argon plasma radiation, I_T, may be calculated using equation 4.7, again after [112]:

$$\text{Total Intensity, } I_T = IA\alpha \qquad 4.7$$

where I = intensity of argon plasma radiation ($Wm^{-2}Sr^{-1}$)

and A = surface area of emitter (plasma flame)

α = solid angle of emission (sr).

If it is assumed that the plasma flame can be approximated by a cone with uniform emission over its surface, then the emitter area may be estimated from the plasma flame length and the diameter of the torch exit nozzle, using equation 4.8:

$$\text{Surface Area of Flame, } A = \pi r\sqrt{r^2+h^2}$$

$$\text{Surface Area of Flame, } A = \pi r\sqrt{r^2+h^2} \qquad 4.8$$

where r = radius of exit nozzle (m)

and h = length of plasma flame (m).

Substituting values of known parameters and rearranging equation 4.6, the radiation heat flux per unit area

falling on the surface of the sample is then given by:

$$\text{Heat Flux / Unit Area, } \frac{q_r}{S} = \frac{29.618}{L^2} \qquad 4.9$$

where L = distance from plasma flame (m)

and I = 10^6 $Wm^{-2}sr^{-1}$

r = 3.25×10^{-3} m

h = 5.0×10^{-2} m.

Radiative heat loss from the surface of the testpiece or coating was estimated from standard relationships based on Stefans' law.

4.3.3 Calculation of gas temperature and convection heat transfer coefficient at surfaces of testpiece.

Measurements of gas temperature in a typical argon-hydrogen plasma flame, carried out in [23], suggested that gas temperature values may be adequately described by a Gaussian function of the form:

$$\text{Gas Temperature, } T = T_o \exp[-C(v^2)] \qquad 4.10$$

where $C = \frac{4 \ln(2)}{H_t^2}$

H_t = function width at half maximum temperature

and T_o = maximum temperature of plasma gas (°C)

r = radial distance from plasma flame axis (m)

A curve fit of experimental data in [23], adjusted to suit the argon-hydrogen plasma flame used in the

current investigation, produced the following formulae for maximum gas temperature, equation 4.11, and function width at half maximum temperature, equation 4.12, as a function of axial spray distance:

$$\text{Maximum Temperature, } T_o = 0.35\left(11451\exp^{(-16.97L)}\right) \quad 4.11$$

where L = axial spray distance (m).

$$\text{Function Width, } H = 6.5012\times10^{-2}\exp(14.72\,L) \quad 4.12$$

The minimum gas temperature outside the plasma gas plume and at the rear face of the sample is fixed at 20

A theoretical treatment of plasma gas heat transfer coefficient in [117] again suggests that values for a plasma flame can be described by a Gaussian function of the form:

$$H = H_o\exp\left[-C(r^2)\right] \quad 4.13$$

where H_o = maximum heat transfer coefficient ($Wm^{-2}K^{-1}$)

and r = radial distance from the flame axis (m)

$C = 4\ln(2)/H_h^2$

H_h = Function width at half maximum heat transfer coefficient.

A curve fit of theoretical data in [117] produced equation 4.14, which describes the variation of maximum

heat transfer coefficient with spray distance:

$$\text{Maximum Coefficient}, H_o = 482.28 - (2428.5L) \quad 4.14$$

where L = spray distance (m).

The variation of function width with spray distance was again estimated from equation 4.12.

Outside the plasma gas plume and at the rear face of the sample, the heat transfer coefficient is maintained at a fixed value commensurate with the air cooling conditions, if any, employed.

Using equations 4.11, 4.12 and 4.14 and the relative positions of plasma torch and sample reference point it is then possible to estimate gas temperatures and heat transfer coefficients for the model system throughout the coating cycle.

4.4 Calculation of system temperature distributions as a function of time.

The complexity of the plasma spray deposition process in terms of heat transfer is such that an analytical solution, even for the one dimensional system under consideration , is extremely difficult to achieve. An alternative approach is to solve the problems of transient heat transfer by using a numerical technique. Here, the differential relationships that describe the system are transformed into finite difference equations which can then be solved using a computer. A

characteristic of this technique is that temperatures are calculated at discrete points, described by the nodes of a mesh, at finite time intervals. The mesh and time step size are usually optimised to provide the required accuracy and system stability over a reasonable computation time.

4.4.1 Generation of system model equations.

As already mentioned, the finite difference technique provides for the calculation of temperatures at a number of discrete points in a body subject to a thermal gradient. The points at which temperatures are calculated are called nodes and generally lie at the intersections of a superimposed mesh or grid, figure 4.7. Using the approach described in reference [134], the basic equations of heat transfer are approximated by finite difference equations, derived from a consideration of an energy balance in a control volume surrounding a node and assuming that the temperature profile between nodal points may be approximated by a straight line. For the node illustrated in figure 4.8, the energy conducted across the control volume towards the node i, j, from node i-i, j may be obtained from Fourier's law:

$$_{i-1,j}Q_{i,j} = \frac{-k\Delta y\,(T_{i,j} - T_{i-1,j})}{\Delta x} \qquad 4.15$$

In the steady state, the algebraic sum of conduction towards any nodal point, plus the rate of internal enargy generation, must be zero:

$$i\text{-}1,j\,Q_{i,j} + i,j\text{-}1\,Q_{i,j} + i+1,j\,Q_{i,j} + i,j+1\,Q_{i,j} + \dot{q}_i \Delta x \Delta y = \phi \qquad 4.16$$

where q_i = rate of internal energy generation (Wm^{-2})

Assuming a square mesh, equation 4.16 reduces to:

$$T_{i-1,j} + T_{i,j-1} + T_{i+1,j} + T_{i,j+1} - 4T_{i,j} + \dot{q}_i \frac{\Delta x^2}{k} = \phi \qquad 4.17$$

Equation 4.17 is a finite difference equation which is satisfied at every point on the grid and can be solved as part of the set of simultaneous equations describing the system.

The energy balance approach may be further extended to solve time varying problems, since the net heat conducted into a control volume around a node causes a temperature change. For the one dimensional system illustrated by the distance/time grid in figure 4.9, the energy balance on a nodal point is described by equation 4.18:

$$i\text{-}1,j\,Q_{i,j} + i+1,j\,Q_{i,j} = \frac{\Delta(m C_p T)}{\Delta t} \qquad 4.18$$

This can be simplified to:

$$\text{Future Temperature, } T_{i,j+1} = F_o T_{i-1,j} + (1-2F_o)T_{i,j} + F_o T_{i+1,j} \qquad 4.19$$

where F_o = $\alpha \Delta t / \Delta x^2$

and α = $\alpha \Delta t / \Delta x^2$

Equation 4.19 is Thermal Diffusivity equation which may then be used to predict 'future' temperatures providing the initial temperature is known and the boundary temperatures are known for all times.

Equation 4.19 however is unstable for values of $F_o > 0.5$, leading to solutions which oscillate numerically about the true value. If the present and future temperatures are considered, then the tendency to oscillate is reduced, allowing larger time steps between calculations. Using the Crank-Nicholson semi-implicit method, equation 4.19 is then modified to include the temperatures at both the present and future:

$$\frac{T_{i,j+1} - T_{i,j}}{\Delta t} = f\left\{\frac{\alpha}{\Delta x^2}\left(T_{i+1,j+1} + T_{i-1,j+1} - 2T_{i,j+1} + \dot{q}_I \frac{\Delta x^2}{K}\right)\right\}$$

$$+ (1-f)\left\{\frac{\alpha}{\Delta x^2}\left(T_{i+1,j} + T_{i-1,j} - 2T_{i,j} + \dot{q}_I \frac{\Delta x^2}{K}\right)\right\} \qquad 4.20$$

where f = weighting factor (=0.5).

Equation 4.20 may be rewritten in a more general form:

$$A_i T_{i-1}^{+} + B_i T_i^{+} + C_i T_{i+1}^{+} = D_i \qquad 4.21$$

where T_n^+ = future temperature at n^{th} node

and $A_i = -F_o$

$B_i = 2 + 2F_o$

$C_i = -F_o$

$$Di = (2-2F_o)T_{i,j} + F_o T_{i-1,j} + F_o T_{i+1,j} + F_o \frac{\Delta x^2}{2k}\left(\dot{q}_{I_j} + \dot{q}_{I_{j+1}}\right)$$

The coefficients of equation 4.21 describe the behaviour of an internal node point in a single material. A thermal barrier system generally contains more than one material with consequent internal boundaries. Further, their surfaces are subject to convective and radiative heat transfer to and from the surroundings. So that the entire system may be accurately described, the coefficients of equation 4.21 are modified to account for the particular conditions at certain nodes, although the general form is retained. The alternative situations which must be considered are then:

(i) Surface nodes subject to convection and radiation

(ii) Internal material boundaries

(iii) Nodes with unequal control volume dimensions either side.

4.4.2 Finite difference equations describing the behaviour of surface nodes subject to convection and radiation.

Applying the energy balance technique, after [134], to the left hand boundary node illustrated in figure

4.10, results in the relationship described by equation 4.22.

$$f\dot{Q}_w + {}_1\dot{Q}_w + \dot{Q}_{int} + \dot{Q}_{rad} = M C_p \frac{dT}{dt} \qquad 4.22$$

where $\dot{Q}_{int}$ = rate of internal energy generation

and $\dot{Q}_{rad}$ = net rate of radiative heat transfer to the surface

and $${}_f\dot{Q}_w = -h\,\Delta y\,\Delta z\,(T_{w,j} - T_{f,j})$$

h = heat transfer coefficient.

Substituting as before and applying the Crank-Nicholson method leads to a general relationship of the form of equation 4.21, but with modified coefficients which account for the convective and radiative heat transfer processes:

$$\text{i.e. } A_i T_{i-1}^{+} + B_i T_i^{+} + C_i T_{i+1}^{+} = D_i$$

where $A_i = 0$

and $$B_i = 1 + F_o + B_o F_o$$

$$C_i = -F_o$$

$$D_i = B_o F_o (T_{f,j} + T_{f,j+1}) + (1 - F_o - B_o F_o) T_{w,j} + F_o (T_{1,j}) + F_o \frac{\Delta x^2}{2k}\left(\dot{q}_{I,j} + \dot{q}_{I,j+1}\right) + F_o \frac{\Delta x}{k}\left(\dot{q}_{r,j} + \dot{q}_{r,j+1}\right)$$

$$B = h\Delta x/k \quad \text{(Biot Number)}$$

$$\alpha = k/\rho c_p \quad \text{(Thermal Diffusivity)}$$

$$F_o = \alpha \Delta t/\Delta x^2 \quad \text{(Fourier Number)}$$

A similar equation may also be derived for a right hand boundary, but with coefficients Ai and Ci transposed.

4.4.3 Finite difference equation describing the behaviour of an internal node at a boundary between dissimilar materials.

An energy balance on the control volume surrounding a node at the boundary between two materials, illustrated in figure 4.11, produces the following relationship:

$$ {}_{s-1}\dot{Q}_{s} + {}_{s}\dot{Q}_{s+1} + \dot{Q}_{int_A} + \dot{Q}_{int_B} = MC_p\frac{dT}{dt} \qquad 4.23 $$

Again, the general equation 4.20 is satisfied but this time the coefficients are modified to include the differing properties of the materials either side of the boundary:

$$ A_i T_{s-1}^{+} + B_i T_s^{+} + C_i T_{s+1}^{+} = D_i $$

where $A_i = -F = \dfrac{F_{o_A} F_{o_B}}{F_{o_B} + R F_{o_A}}$

and $R = K_B / K_A$

and $B_i = FR + F + 1$

$C_i = -FR$

$D_i = F T_{s-1} - T_s (FR + F - 1) + FR T_{s+1} + \dfrac{\Delta x}{4}\left(\dot{q}_{I_A} + \dot{q}_{I_{A+}} + \dot{q}_{I_B} + \dot{q}_{I_{B+}} \right)$

4.4.4 Finite difference equation describing the behaviour of an internal node with unequal control volume dimensions either side.

Where the control volume is of differing thickness either side of a node, such as at the boundary between areas with different node spacings, figure 4.12, energy balance considerations produce the general relationship of equation 4.21 but with the coefficients modified to account for differing material thickness:

$$A_i T_{i-1}^{+} + B_i T_i^{+} + C_i T_{i+1}^{+} = D_i$$

where $A_i = -F_{o_1}$

and $B_i = 2 + F_{o_1} + F_{o_2}$

$C_i = -F_{o_2}$

$$D_i = (2 - F_{o_1} - F_{o_2}) T_{i,j} + F_{o_1} T_{i-1,j} + F_{o_2} T_{i+1,j} + \frac{(F_{o_1} \Delta x_1^2 + F_{o_2} \Delta x_2^2)}{2K} \cdot (\dot{q}_{I_{i,j}} + q_{I,j+1})$$

$F_{o_1} = \alpha \Delta t / \Delta x_1^2$

$F_{o_2} = \alpha \Delta t / \Delta x_2^2$

4.4.5 Calculation of temperature distribution.

Each nodal point of the system is described by a linear algebraic relationship of the form given by equation 4.21. Calculation of the temperature distribution after a given time increment is achieved by collecting together this set of simultaneous

equations and solving for temperature. In matrix form, the set can be described as follows.

$$\begin{bmatrix} A_1 & B_1 & C_1 & & & \\ & A_2 & B_2 & C_2 & & \\ & & A_3 & B_3 & C_3 & \\ & & & & & \\ & & & A_n & B_n & C_n \end{bmatrix} \begin{bmatrix} T_1^+ \\ T_2^+ \\ T_3^+ \\ \\ T_n^+ \end{bmatrix} = \begin{bmatrix} D_1 \\ D_2 \\ D_3 \\ \\ D_n \end{bmatrix}$$

Terms A_1 and C_n are zero at the system boundaries and terms in D are always defined since the current temperature profile and present and future boundary conditions are known. The resulting coefficient matrix is tridiagonal and the temperature solution can be simply obtained by Gaussian elimination.

An important feature of this technique is that it readily lends itself to rapid solution using a computer. Each node type is specified in the computer program by a code number in an array, with the order reflecting the appearance of the system as a whole, figure 4.13. As calculation proceeds, the correct coefficients, A_i', B_i', C_i' and D_i' are determined from definitions of each node type, minimizing the amount of data stored. This simplicity of system specification also allows the behaviour of different combinations and dimensions of thermal barrier coating to be investigated under varying boundary conditions with the minimum of program alteration.

4.5 Calculation of time dependant modification to the model coating system thickness dimension by particle deposition.

The method of determining temperature distributions in model coating systems, described in the previous section, applies strictly to fixed boundary dimensions. In order that the plasma spray deposition process be modelled accurately, consideration must be given to the arrival of new, hot particles at the surface and their effect on the resulting temperature distribution.

The mechanism whereby the boundary dimensions are increased in the model is illustrated in figure 4.14, with reference to the computer representation of the coating system. Before the arrival of a new particle, the node array has the appearance of figure 4.14a, with a node spacing corresponding to one third of the thickness of a 'splat' or impacted particle. After deposition has occurred, the node array is extended by the extra elements corresponding to the thickness of a new 'splat' and the gas boundary is transferred to the outer edge of the new particle, figure 4.14b. The temperature distribution before and after deposition is illustrated in figures 4.15a and b respectively. To simplify the calculation procedure, the temperature profile throughout a new particle is assumed to be constant at the moment of impact, and to correspond to a typical particle impact temperature, say 3000K.

Further, the particle is assumed to have solidified immediately upon impact into its final dimensions and no contribution from latent heat of fusion is considered. To prevent numerical oscillations of the system arising from the step changes in temperature at the particle boundary, the time steps over which temperatures are calculated are reduced to 1% of the normal value until the particle has cooled. The problem then is reduced to determining the location of the reference point when deposition is occuring and the number and probable arrival times of each particle during the coating cycle.

4.5.1 Determination of reference point location within plasma flame deposition zone.

Particle deposition may only occur when the reference point on the surface of the testpiece lies within a certain distance from the plasma jet axis, assuming of course that coating material is being injected into the flame. For simplicity the limiting distance is assumed to be a circle of radius r_s, surrounding the axis of the flame, which does not vary with spray distance. Figure 4.16 illustrates the spiral path of the plasma flame, centre point described by radius r_ℓ and angle θ, past the reference point, radius r_e and angle α from turntable centre and angular datums respectively. If the effective separation of reference point and plasma

flame axis is r_n and the limiting deposition or spray radius is r_s, then material will be deposited whenever r_n is less than r_s.

From a consideration of the geometry of figure 4.16, r_n may be calculated using equation 4.24:

$$r_n = \sqrt{(r_e \sin\alpha - r_l \sin\theta)^2 + (r_e \cos\alpha - r_l \cos\theta)^2} \qquad 4.24$$

For any time step within a corrected segment at constant angular (w_i) and radial (v_i) velocity, the value of θ and r_l may be calculated at the beginning and end of each step using equations 4.25 and 4.26:

$$\theta = \theta_o + n\, w_i\, dt \qquad 4.25$$

where θ_o = angle at start of segment

and n = number of time steps

dt = time step duration (s)

w_i = angular velocity ($rads^{-1}$)

$$r_l = r_o - f_r(m-1) - n\, v_i\, dt \qquad 4.26$$

where r_o = starting radius at beginning of spray traverse (m)

and f_r = traverse feed rate ($mrev^{-1}$)

m = number of whole table revolutions

n = number of time steps of size dt

v_i = radial velocity (ms^{-1}).

As the position of the reference point is fixed with respect to the turntable datums, r_n may then be calculated at the beginning and end of each time step within the plasma spray plume.

4.5.2 Calculation of number and probable arrival times of coating particles during deposition.

The rate at which material is deposited within the spray radius r of a plasma flame has been shown to follow a Gaussian distribution and for a straight path through such a plume, illustrated in figure 4.17, the amount of material deposited per pass at a distance x from the centre is given by equation 4.27, after [135]:

$$dx = \sqrt{\frac{1}{2\pi}} \cdot \frac{\eta G_s}{\gamma V_h \sigma} \cdot \exp - \frac{(x - \bar{x})^2}{2\sigma^2} \qquad 4.27$$

where V_h = horizontal velocity (ms^{-1})

and G_s = powder feed rate (kgs^{-1})

γ = density of deposited layer (kgm^{-3})

σ = standard deviation of plume

$\bar{x}$ = position of plume centre (m)

η = material deposit efficiency.

Effectively, equation 4.27 calculates the integrated area under the deposition rate distribution, illustrated in figure 4.17.

To calculate the amount of material deposited in a single time step along a spiral path is however more

complicated. At the start of a time step, the value of $r_n = r_{n_1}$ and the horizontal velocity, v_{h_1} is the resolved product of the radial velocity, v_i and angular velocity, w_i. Similarly at the end of the time step, the values of r_n and v_h are r_{n_2} and v_{h_2}. The amount of material deposited during the time step is then the area under the distribution in figure 4.18, which is corrected for radius and velocity variation. As the time increments are small in relation to the residence time under the plume, it is acceptable to assume average values of $r_{n_{Av.}}$ and $v_{h_{Av.}}$ during the time step illustrated in figure 4.19, simplifying the calculation procedure:

$$r_{n_{Av.}} = \frac{r_{n_1} + r_{n_2}}{2} \qquad 4.28$$

$$V_{h_{Av}} = \sqrt{(r_{n_{Av}} . w_i)^2 + v_i^2} \qquad 4.29$$

Substituting the values of $r_{n_{Av.}}$ and $v_{h_{Av.}}$ into equation 4.26 gives the average height of the deposition rate distribution, $Zr_{Av.}$ at $r_{n_{Av}}$:

$$Zr_{Av.} = \frac{1}{2\pi} . \frac{\eta G_s}{\gamma V_{h_{Av.}}} . \exp -\frac{(r_{n_{Av}})^2}{2\sigma^2} \qquad 4.30$$

The amount of material deposited in a given time step, dt is then described by equation 4.31:

$$\text{Thickness Deposited}, T = V_{h_{Av.}} \cdot dt. \; Zr_{Av.} \qquad 4.31$$

The above relationship, however, implies a semi-continuous deposition rate, at least during the passage through the plasma flame. In reality, particles arrive at the surface of the coating at discrete intervals, increasing coating dimensions by distinct steps equivalent to the average thickness of a solidified 'splat'. The latter effect is achieved in the model by summing the thickness deposited per time step, until an amount of material equivalent to the thickness of a splat has been accumulated. At that point in time, then, the model system dimensions are increased to mimic deposition of a particle and the time step number recorded. The effect of such intermittent deposition on coating thickness as a function of deposition time compared with the semi-intermittent rate of equation 4.31 is illustrated in figure 4.20.

4.6 Plasma spray process simulation computer programs.

The descriptive equations outlined in previous sections were incorporated into three computer programs.

The first, written in BASIC for a BBC microcomputer

and entitled 'FINITE,' was fairly elementary in that it employed static material and thermal boundary conditions and accounted only for conductive and convective heat transfer. Despite its simplicity, it was configured to investigate the following aspects of coating manufacture and behaviour:

(i) The effect of material property variation on insulation effectiveness.

(ii) Optimum positioning of air cooling during spraying.

(iii) Factors affecting the cooling rate of ceramic particles after impact with the substrate.

The remaining programs, written in FORTRAN 77 for a Honeywell mainframe computer, were designed to more fully simulate the plasma spray process by incorporating algorithms for position and time dependant thermal and material boundaries. Radiative heat transfer was also considered but no allowance for the relatively minor contribution from heat of solidification was incorporated. The first of these two routines, entitled 'SPRAY', generated data at given time intervals for plasma flame temperature, radiation heat flux, heat transfer coefficient and the number and arrival time of each deposited particle for a given set of input 'spray' parameters. This data was stored in a file to be used in conjunction with the second program, 'HEAT', which calculated heat transfer in the model

coating system using this boundary information. The output from this second program was a temperature distribution throughout the coating and substrate thickness at given time intervals.

The latter programs were configured to investigate the effects of important plasma spray process parameters on temperature distributions in model coatings. Finally, residual stresses were calculated for the model coatings on returning to room temperature.

4.6.1 The effect of material property variation on insulation effectiveness.

The effect of material property variation on insulation performance was investigated by systematic modification of individual parameters, about a set of median values, for an aluminium substrate and zirconia coating. The average data were chosen to be typical of currently available literature values and are given in table 4.1.

Each insulation model was subjected to a static thermal gradient and heat transfer conditions similar to those expected in an operating, advanced diesel engine, summarised in table 4.2.

Parameter variation was restricted to value ranges quoted in current literature, or which might be expected to be achieved through process modification,

and in every case the values of material properties were assumed to be constant over the entire temperature range. Unless otherwise stated, parameters used to configure the models were the median data. Output from the model was in the form of a through thickness temperature profile, plotted at 25 second intervals as a 3-dimensional grid. Assessment of insulation effectiveness was then achieved by comparison of output data with the median plot.

4.6.1.1 Coating thickness.

Coating thickness, currently limited in practice to several mm., is expected to increase to provide useful insulation properties. Ceramic coatings of 1mm and 5mm were therefore modelled to examine not only the effect of thickness variation about the median value of 3mm but to determine temperature gradients between coating and substrate.

4.6.1.2 Coating thermal conductivity.

Processing and material properties, together with experimental uncertainty in practical thermal conductivity measurements have resulted in literature values which may vary one order of magnitude about the median value for this investigation.

To determine the effect of such uncertainty, 3mm coatings were modelled with thermal conductivities of

$0.1Wm^{-1}K^{-1}$ and $1.0Wm^{-1}K^{-1}$ for comparison with the median value.

4.6.1.3 Coating specific heat capacity.

Depending on the type and proportion of stabiliser material, the specific heat capacity of thermal barrier coatings may vary significantly. To assess the sensitivity of coating specific heat capacity on insulation performance, 3mm coatings of zirconia were modelled with specific heat capacities of $400JKg^{-1}K^{-1}$ and $600JKg^{-1}K^{-1}$ for comparison with the standard.

4.6.1.4 Coating density.

Material processing and stabiliser composition may affect coating density. This aspect of insulation behaviour was subsequently investigated although no allowance for commensurate changes in conductivity was included. 3mm zirconia coatings were modelled with densities of $3000Kgm^{-3}$ and $5000Kgm^{-3}$ and compared with the median value.

4.6.1.5 Substrate material.

Ceramic coatings are intended to be applied to metallic materials other than aluminium. In the event that substrate material properties other than expansion coefficient are important, 3mm thick zirconia coatings were modelled with both steel and copper substrates for

comparison. The combination of these three materials was chosen because each possessed a particularly prominent material property, not found in the other two. Typical properties of each metal are given in table 4.3.

4.6.2 Determination of the optimum position of air cooling jets during spraying.

Forced air cooling is commonly employed during the manufacture of industrial ceramic coatings to reduce temperatures and improve quality and durability. While the benefits are well known, the siting of cooling jets has often been decided on by past experience and the constraints of component geometry. In an attempt to determine the most efficient site for an air blast, a model of a 1mm zirconia coating on a 10mm aluminium substrate was configured using the parameters in tables 4.1 and 4.2. The coating and substrate were initially at a temperature of 500°C, surrounded by air at 25°C, and were allowed to cool to room temperature by natural convection or with simulated back, front or front and back face cooling.

This was achieved in the model by raising the heat transfer coefficient at a particular face from a still air level of $20Wm^{-2}K^{-1}$ to $75Wm^{-2}K^{-1}$.

As before, through thickness temperatures were plotted on a 3-dimensional grid but at 50 second

intervals.

4.6.3 Factors affecting the cooling rate of ceramic particles after impact with the substrate.

During deposition of a thermal barrier coating, the conditions under which molten or semi-molten ceramic particles impact with the substrate must vary considerably. For example, the substrate temperature will rise progressively as spraying proceeds, and the rate of heat flow away from impacted particles will vary according to the temperature and conductivity of the underlying material. This latter point is particularly important because particles are initially deposited onto a cool, high conductivity metal substrate, but as the coating thickness builds up, subsequent particles impact with relatively hot, low conductivity zirconia material. Ceramic particles were therefore modelled to simulated conductive and convective cooling after impact with either plain metallic or underlying ceramic material of different thicknesses. Other important factors such as thermal conductivity of zirconia particles, particle temperature at impact and long-term cooling rate were also investigated.

4.6.3.1 Effect of underlying zirconia particles.

The simple model was configured with median material property values, described in tables 4.1 and 4.2, and utilised a 10mm thick aluminium substrate in still air.

Measurements of solidified particle thickness from S.E.M. micrographs showed that typical dimensions were of the order of 2μm and this value was selected for the model. Cooling of an impacted particle on plain metal or one, two or three underlying particles was investigated. The substrate and underlying ceramic material were initially at 20°C and the particle at 2000°C. No radiative heat loss or heat of solidification calculations were included in the simulation. Through thickness temperatures were plotted on a 3 dimensional grid, at 20us intervals, in an attempt to determine initial rapid cooling rates.

4.6.3.2 Zirconia particle thermal conductivity.

The range of experimentally derived zirconia thermal conductivity values were incorporated into an earlier simulation to determine their effect on insulation effectiveness. Such parameter variation was also likely to affect initial rapid cooling of impacted particles. The model described in the previous section, for a particle impacting onto a metal substrate, was therefore reconfigured with zirconia conductivities of $0.1 Wm^{-1}K^{-1}$ and $1.0 Wm^{-1}K^{-1}$ for comparison with the median

value included in that simulation.

4.6.3.3 Zirconia particle temperature.

The probability of all impacting particles having the same temperature is somewhat remote because of differences in particle size and trajectory through the plasma flame. The initial model of a single particle with average properties, impacting with a metallic substrate, was again utilized but in this instance particle temperatures of 2000°C, 3000°C and 4000°C were chosen for comparison. Through thickness temperatures were again plotted on a 3 dimensional grid but the timeplot interval was reduced to 1.0 μs to improve resolution.

4.6.3.4 Long-term cooling of an impacted particle.

Cooling rates of impacted particles are initially rapid due to the large temperature difference between them and the substrate. Once the temperatures of ceramic and metal have equalised, cooling must become less rapid and is likely to be controlled by the rate of heat flux from the low conductivity zirconia particle.

Timescales employed in previous simulations in this section were too short to investigate longer term cooling of impacted particles and so the initial model was reconfigured with a time plot interval of 0.1s to

investigate complete cooling of a single particle. To prevent model oscillation, due to the large time steps involved, the initial temperature profile of particle and substrate was set up to be that which existed at the end of the initial rapid cooling phase simulated in section 4.6.3.1 for a single particle.

4.6.4 Prediction of temperature profiles in coating and substrate during plasma spraying.

Within the limitations of the model, an attempt was made to simulate real coating conditions as closely as possible by incorporating actual material and process parameter data into both computer programs. This was considered to be of great importance in obtaining meaningful results for comparison with experimentally derived data.

Material properties for zirconia coatings rather than bulk data were used and where appropriate were defined by temperature dependant relationships within the programs.

No data was available for the variation of specific heat of zirconia coatings with temperature and so this was measured for powders and coatings of materials A and B using the technique described in chapter 3.

Spray parameters used to configure program 'HEAT' were exactly those used to define the spraying conditions of some coatings deposited during the

experimental work described in chapter 3. The accuracy of the model could then be assessed by direct comparison with practical results. Specific parameters investigated were:

(i) Effect of air cooling.

(ii) Spray distance.

(iii) Workpiece/sprayhead relative velocity.

(iv) Substrate material.

4.6.4.1 Effect of air cooling.

Air cooling has been previously shown to be important in altering residual stress. The complex model was therefore configured to investigate this effect. Model coatings of zirconia were deposited over 0.1mm of bondcoat onto a 3mm aluminium substrate, using the properties and parameters listed in tables 4.4 and 4.5, and either uncooled or with combined front and back face cooling. The latter was simulated by raising the local heat transfer coefficient at either face to $50Wm^{-2}K^{-1}$, from a still air value of $20Wm^{-2}K^{-1}$.

The remaining coating parameters are summarised in table 4.6. Deposit efficiency was obtained from practical measurements described earlier in chapter 3.

4.6.4.2 Spray distance.

Practical thermal barrier coatings may be significantly affected by workpiece/sprayhead separation or spray distance because input heat flux from the plasma torch is strongly position dependant. The complex model was therefore configured for varying spray distances in an attempt to duplicate this effect. Two simulations were performed, using identical conditions and parameters to those employed in the previous air cooled model, but with the spray distance increased from 75mm to either 100mm or 125mm.

4.6.4.3 Workpiece/sprayhead relative velocity.

This parameter was thought to be especially important because residence times of coating and substrate under the plasma flame are directly related to the relative speeds of torch and workpiece. The model was thus configured to investigate the effects of workpiece/sprayhead relative velocity on temperature profile. Two speeds, $0.4ms^{-1}$ and $0.3ms^{-1}$, were modelled for comparison with the air-cooled simulation in section 4.6.4.1. All other input parameters were retained.

4.6.4.4 Substrate material.

Practical applications of thermal barrier coatings will require them to be applied to a range of metallic materials with predictable results. It has been previously shown that substrate properties may affect the magnitude of residual stresses generated in thermal barrier coatings. The model was configured for those substrate materials used in practical investigations of the same effect, described in chapter 3. Using exactly similar spray conditions to those used in section 4.6.4.1 for air-cooled deposition on aluminium, 3.0mm thick substrates of copper and mild steel were simulated.

4.7 Calculation of residual stress from model coating temperature distributions. Residual stress in the model coating system was calculated from a 'final' temperature distribution on completion of the deposition process. The choice of 'final' distribution was made on the basis of it being that which existed in the coating at the maximum substrate temperature during the final spray pass. The reasons for this choice were:

(i) Initial rapid cooling of particles to the underlying substrate temperature would be at such a rate as to suppress material flow, causing tensile stress and finally stress relief by microcracking when the elastic strength of the ceramic was

exceeded.

(ii) Continually rising substrate and ceramic temperatures during spraying would result in tensile stress relief by microcracking and sliding in the coating layer.

(iii) Impact of subsequent particles would raise the temperature of underlying material, again causing stress relief by cracking.

(iv) Coooling of the final coating from the maximum substrate temperature achieved during the last spray pass would tend to develope compressive stress which is more easily supported by ceramic materials. Shear stresses between adjacent layers at different temperatures, developed on cooling, would be accommodated by sliding and limited cracking.

Residual stress was calculated at the bondcoat/ceramic interface and at the ceramic front surface by determining the differential contraction between that point and the substrate on cooling to room temperature. For the purposes of calculation, the substrate was assumed to be massive and rigid compared to the coating, so that minimal coating stress relief by substrate bending occurred, figure 4.21. Further, differential contraction was assumed to be accompanied only by elastic deformation of substrate and coating materials. The residual strain, due to differential contraction between coating and substrate, at a height

z in the coating, and in an arbitrary in-plane direction, x, was determined using equation 4.32:

$$\text{Residual Strain, } {}_z\varepsilon_x = \alpha_c({}_zT_c - T_\phi) - \alpha_s(T_s - T_\phi) \qquad 4.32$$

where α_c = thermal expansion coefficient of coating

and α_s = thermal expansion coefficient of substrate

${}_zT_c$ = temperature of coating material at ht. z (°C)

T_s = Substrate bulk temperature (°C)

T_ϕ = Room temperature (°C).

Residual stress was then estimated by substituting values of ${}_z\varepsilon_x$ into equations 3.5 - 3.7 and using appropriate values of the elastic constants for zirconia coating materials.

Chapter 5 - Results.

5.1 Introduction.

Detailed results of both the practical and theoretical investigations, described in chapters 3 and 4 respectively, are presented in the following sections. The information has been logically associated into three areas related to each of the original aims of this study. These are:

(i) Practical measurements of coating strain/stress under varying deposition conditions.

(ii) Theoretical data derived from mathematical models of heat transfer within coating systems.

(iii) X-Ray diffraction analysis of zirconia coating materials subject to heat treatment.

Experimental material or physical property data, measured using the techniques described in chapter 3, is presented at the appropriate point within the context of each part, and microstructural information, where relevant, is associated with the particular properties of individual thermal barrier coatings.

5.2 Practical measurements of coating strain/stress under varying deposition conditions.

5.2.1 Morphology and chemical homogeneity of powder coating materials.

Both metallic and ceramic powder materials were examined using a scanning electron microscope, and their typical morphologies are illustrated in plates 2.1a to c. The bond coat alloy powder, plate 2.1a, whose composition was described earlier, was rounded and fairly coarse, and typical of atomised nickel base powder materials. A separate aluminium constituent was not easily distinguishable although fragments of organic material, presumably binder, were clearly visible. Partially stabilized zirconia powder A, illustrated in plate 2.1b, was manufactured by fusing, crushing and grinding. Consequently it was fairly coarse, with a wide size range, and angular or shard-like in nature. Powder B, illustrated in plate 2.1c and manufactured by sintering and spray drying, appeared completely different in size and shape, being fine and rounded, with a fairly narrow size range. Each of the spheroidal particles was clearly made up of an agglomerate of much finer particles.

X-Ray diffraction analysis of powders A and B revealed further characteristic features which made the materials easily distinguishable. Sections of each trace, between 24^{o} and 36^{o} of 2θ, are reproduced in figures 5.1a and b. Powder A had achieved a high degree of stabilization and consisted entirely of retained

tetragonal and cubic phases with no free yttria. Powder B, in contrast, contained a high proportion of monoclinic together with retained tetragonal and cubic phases and a very small amount of free yttria. The proportion of monoclinic phase and morphological evidence suggested that high temperature sintering during manufacture of the latter material was less extensive than for material A.

5.2.2 Powder feed rate calibration data and optimisation of particle melting.

Calibration of the powder feed unit was carried out for both metallic and ceramic powder materials and the corresponding graphs for both bondcoat and ceramic materials are given in figure 5.2. Feed rate was in each case linearly related to %RPM and reproducible to within ± 2 $gmin^{-1}$.

Subsequently, deposit and melting efficiency were evaluated for both ceramic powders. Calibration curves of weight deposited/per unit length of spray pass, at constant relative speed and material feed rate, for both variable pressure and flow conditions, are given in figures 5.3a and b for powder A and figures 5.4a and b for powder B.

Particle melting efficiency was investigated using a scanning electron microscope. Optimum melting conditions on a microscopic scale were found to conform

with maxima in material deposition rates. Examples of both optimum and poorly melted particles of powders A and B are shown in plates 5.1a and b and plates 5.2a and b respectively.

Close examination of the deposition data showed that deposit efficiency was strongly material dependant. For a given material feed rate under optimum melting conditions, powder B was deposited between three and four times more efficiently than powder A and was much less sensitive to injection parameters.

Deposit efficiency was also found to vary strongly with sprayhead/workpiece separation or spray distance. The results are summarised in figure 5.5 for distances between 50mm and 110mm and provided an accurate reference for later investigations.

5.2.3 Dependance of residual stress on substrate plate size, measurement orientation and ceramic powder type.

Graphs showing the values of linear and curvature strain, measured at the surfaces of the ceramic layer from test bars cut from orthogonal directions in 100mm square plates after removal of substrate and bond coat, are reproduced in figures 5.6a and b.

Linear strains were compressive i.e. samples extended in length when the substrate was removed. Curvature-related strain in a flattened, free coating was tensile at the front face and compressive at the

rear face.

Regardless of the deposition conditions employed, linear strain values measured in the ceramic layer in a direction transverse to the spray path were about 80% of their corresponding values in the longitudinal i.e. tangential to the spray path direction. Curvature related strain values were apparently unaffected by the measurement orientation.

A reduction in magnitude of both linear and curvature related strain was noted as workpiece/sprayhead relative velocity was increased from $0.3ms^{-1}$ to $0.5ms^{-1}$.

Errors in linear strain measurement were typically $\pm 0.01mm$ between adjacent measurements on the same sample and between similar samples. For the smallest strain measured, about $2x10^{-3}$, over a gauge length of 70mm, this represented a maximum error of $\pm 7\%$.

Curvature strain was determined by measuring the radius of curvature of the free coating profile using curve fitting. Errors in the latter technique were estimated to be about $\pm 2\%$. It should be noted, however, that corresponding errors in larger radii of curvature were offset by the inverse relationship with curvature related strain.

Intermediate values of linear strain, generally about 10% less than the final value, were recorded after removal of the substrate but with the bond layer still attached. Curvature strain measured on ceramic layers

with bondcoats attached was often of opposite sign to when it was removed, i.e. the exposed ceramic surface was convex rather than concave. Under these conditions, the bond coat layer was seen to act as a thin stiff skin, capable of supporting tensile stress. The thickness dimension of the bondcoat layer, in comparison to the substrate was so small, however, that its effect on residual stress in the ceramic layer was considered minimal when compared to the relatively more massive substrate, and as such its contribution was subsequently ignored.

Further measurements of curvature and linear strain in the ceramic layer were undertaken on test bars sectioned from 100mm by 25mm testpieces. The values are also shown in figures 5.6a and b. Linear strain related data was in close agreement with that obtained from the longitudinal direction in larger 100mm$^{\square}$ plates, while curvature strain was reduced at the lower velocity.

Comparison of the data in figures 5.6a and b showed that, within experimental error, the values obtained for each ceramic material were nominally the same and in all cases both curvature and linear strain were reduced at higher workpiece/sprayhead relative velocity.

Residual stress was determined at the front and rear faces of each ceramic coating. The transverse strain component required for calculating biaxial ceramic

layer stresses developed in narrow testpieces was obtained by scaling to 80% of the longitudinal value in line with the larger plate data. The calculated residual stresses are shown in figure 5.7a and b.

In-plane residual stress in each coating was compressive, regardless of deposition parameters, leading to tensile residual stress perpendicular to the surface. In-plane stress measured at the front or exposed face of ceramic coatings was less compressive than that developed at the coating/substrate interface.

Within experimental error, residual stresses determined in equivalent coatings of materials A and B were similar although the former appeared more sensitive to workpiece/sprayhead relative velocity.

Some variation between large and small plates was noted, related to differences in measured curvature strains, but a reasonable similarity was obtained and so the smaller plates were therefore adopted, together with the 80% scaling factor for determination of transverse linear strain for subsequent investigations.

Microstructural examination showed that coatings were lamellar in nature, with good adhesion between particles. No major structural defects were noted, although all samples contained evidence of microcracking through and between 'splats' of ceramic, and included porosity, plate 5.3. Coatings manufactured from powders A and B were indistinguishable except the

former contained occasional part melted particles.

5.2.4 Dependance of residual stress on the time delay between coating cycles.

Measured values of residual strain in the ceramic layer after removal of both substrate and bond coat are plotted in figure 5.8. At each workpiece/sprayhead relative velocity, values of linear strain were significantly reduced when samples were allowed to cool between coating cycles although microstructural examination showed no evidence of layering in the ceramic, plates 5.4a and b. At $0.2ms^{-1}$, the difference between curvature strain values was similarly affected, but at $0.5ms^{-1}$, there was little difference. Again, the marked effect of relative velocity on measured strain was noted, with significant reductions at $0.5ms^{-1}$, regardless of deposition technique.

Residual stresses were calculated as before, based on measurements from 100mm by 25mm testpieces. The results are given in figure 5.9. In-plane stress was compressive for all samples, but less so at the front face. Examination showed that intermittent deposition and/or increased workpiece/sprayhead relative velocity significantly reduced the values of residual stress developed in these coatings.

5.2.5 Dependence of residual stress on ceramic coating thickness.

Measurements of curvature and linear strain in the ceramic layer obtained from each sample after removal of both substrate and bondcoat are given in figure 5.10. At 0.2mm of ceramic, curvature strain was a maximum, and it steadily decreased as thickness increased. Similarly, linear strain was a maximum at 0.2mm but thereafter a reduced, nominally constant value was observed.

Values of residual stress were calculated and are given in figure 5.11. In-plane stress was compressive regardless of coating thickness but was reduced at the front face. As thickness increased, front and back face in-plane stress values converged towards a common value.

Microstructural examination revealed typical coating structures although all coatings greater than 0.2mm thick contained instances of cracking, parallel and perpendicular to the coating plane. Horizontal cracking was initially confined to the boundary between complete coating layers, but as thickness increased, additional cracks were noted between half-layers deposited in alternate traverse directions. Vertical cracks were regularly spaced and propagated through the section from the free surface towards the bondcoat. Horizontal cracks appeared to originate at the surfaces of

vertical cracks but rarely propagated completely between successive sites. Examples of uncracked (0.2mm) and extensively cracked (1.24mm) coatings are shown in plates 5.5a and 5.5b respectively.

Free coating samples of 1.24mm thick ceramic, despite containing cracks, were sufficiently robust to allow measurement of thermal expansion coefficient. The resulting data are shown in figure 5.12. An average thermal expansion coefficient of $10.8 \times 10^{-6} K^{-1}$ was recorded for both heating and cooling cycles.

5.2.6 Dependance of residual stress on workpiece sprayhead relative velocity at two different spray distances.

Measured values of linear and curvature strain in the ceramic layer after removal of both substrate and bondcoat are shown in figures 5.13 and 5.14, corresponding to a spray distance and ceramic layer thickness of 65mm and 0.3mm, and 110mm and 0.2mm respectively.

Curvature related strain values were found to increase steadily at a spray distance of 110mm as relative velocity and the number of spray passes increased. This effect, however, was not apparent at a distance of 65mm where nominally similar values were obtained. In contrast, regardless of speed, linear strain values, at both spray distances, showed a marked

dependance of measured strain on velocity, with the smallest values being recorded at the highest relative speeds. No strain data was available from samples produced at $0.1ms^{-1}$ and 65mm separation because testplates were substantially melted during coating deposition. Another important feature of these data were the significant increases in both linear and curvature related strain when coatings were deposited at a spray distance of 65mm.

Values of residual stress derived from measured strain data at 65mm and 110mm separation are given in figures 5.15 and 5.16 respectively.

In each case, in-plane residual stress was compressive and reduced at the front face compared with the rear. At 65mm spray distance this front/rear difference was larger than for equivalent coatings deposited at 110mm, particularly at lower relative velocity. The majority of this increased stress gradient was attributable to increased compressive stress at the substrate/coating interface.

Microstructural examination revealed that coatings manufactured at 65mm spray distance and at relative velocities of 0.2 and $0.3ms^{-1}$ contained occasional horizontal cracks. However cracking was not extensive and generally confined to the boundary between complete coating layers. No such cracking was found in any of the coatings deposited at 110mm spray distance.

Examples of cracked and uncracked coatings are given in plates 5.6a and b repectively.

5.2.7 Dependance of residual stress on spray distance under constant deposition conditions.

The data presented in the previous section suggested a marked dependance of curvature related residual strain on sprayhead/workpiece separation distance at low relative velocity. To further investigate this aspect, additional coatings were produced at $0.2ms^{-1}$ relative velocity and 90mm spray distance, under exactly similar conditions. Nominal ceramic coating thicknesses of 0.24mm were recorded. Strain data measured on the additional coating set after removal of both substrate and bond coat are shown in figure 5.17 together with corresponding data for $0.2ms^{-1}$ coatings taken from figures 5.13 and 5.14.

Examination of the complete data set suggested that at $0.2ms^{-1}$ relative velocity, both linear and curvature related strain were inversely related to spray distance.

Residual stresses were calculated and plotted with equivalent values from the previous set in figure 5.18. As spray distance increased, the difference between front and rear in-plane stress was reduced although front face stresses were not significantly altered. Again the majority of the reduction in the front/rear

stress gradient was associated with decreased stress at the substrate/coating interface.

Microstructural examination revealed no instances of cracking in the additional coating samples.

5.2.8 Dependance of residual stress on air cooling conditions during deposition.

Measurements of curvature and linear strain were taken from samples produced under various air cooling conditions and the results are given in figure 5.19.

Air cooling, when applied from any position, was found to be effective in reducing compressive linear strain, but had no noticeable effect on curvature related strains except at $0.1ms^{-1}$ with combined air cooling. Where air cooling was applied from one side of the sample only, this was found to be most effective directed at the front face, i.e. on the coated surface. The most significant reductions in strain were noted when combined front and back face cooling was employed, although this was only slightly more effective than front face cooling alone.

Measured values of substrate temperature for non-cooled, back, front, and front and back face cooled samples are shown in figures 5.20, 5.21, 5.22 and 5.23 respectively.

Substrate average back face temperature during deposition was reduced most effectively when combined

front and back face cooling was applied, although once more this was only slightly more effective than front face cooling alone. On average, combined cooling achieved a reduction of about 150°C compared with non-cooled testpieces. Examination also showed that average substrate temperatures were achieved more rapidly at higher workpiece/sprayhead relative velocity.

The effectiveness of air cooling was highlighted in comparisons between the maximum and minimum temperatures recorded during each spray cycle. Cooling tended to limit the peak temperature achieved by the substrate as the torch more closely approached the measurement location during a spray cycle, again with reductions of about 150°C over uncooled samples when air was directed at both faces. Similarly, temperature reductions between complete spray cycles of approximately 100°C were recorded, compared with uncooled samples where ranges of about 50°C were more common. As with previous data, workpiece/sprayhead relative velocity was inversely related to measured strains, although the effect on linear strain was reduced by air cooling.

Calculated values of residual stress, corresponding to figure 5.19, are given in figure 5.24.

In-plane residual stresses were compressive, with a reduction at the front face compared to the rear.

Examination showed that air cooling was not particularly effective in reducing in-plane residual stress, despite significant reductions in substrate temperature. The greatest reductions were obtained at $0.1ms^{-1}$ relative velocity with combined cooling. The effect of workpiece/sprayhead relative velocity on residual stress was again noted.

Microscopical examination showed samples produced at $0.1ms^{-1}$ with front and back face cooling contained vertical crack networks, originating at the top face and propagating toward the bond coat, plate 5.7a. All other samples were free of cracks of this type and exhibited typical coating microstructures, plate 5.7b.

5.2.9 Dependance of residual stress on the presence of a bondcoat during deposition.

Measured values of curvature and linear strain in the ceramic layer after removal of the substrate are shown in figure 5.25 together with the corresponding data for bondcoated testpieces from figure 5.19. Values of compressive linear strain at each relative velocity were decreased slightly by omission of the bondcoat. Curvature related strain in the ceramic layer was apparently unaffected under any deposition conditions by the presence or otherwise of a bondcoat.

Corresponding values of residual stress were calculated and are shown in figure 5.26.

In-plane residual stress was compressive and reduced at the front face compared to the rear. Within the limits of experimental error, the presence of a bondcoat had a small effect on ceramic coating residual stress when air cooling was employed but the effect of relative velocity was unaltered.

As before, microstructural examination revealed vertical crack networks in samples prepared at $0.1ms^{-1}$ with back and front face air cooling. The remaining samples showed no differences between the structure of ceramic coatings either with or without bond layers.

5.2.10 Dependance of residual stress on substrate material properties and thickness.

Measurements of linear and curvature strain were taken from testbars after both substrate and bondcoat had been removed using a suitable etch.

The relationships between measured strain and substrate thickness are shown in figure 5.27 for each material, and between measured strain and substrate expansion coefficient for a given substrate thickness in figure 5.28. No data was available for aluminium and copper testbars in range 1 because significant permanent deflections of the substrates were found after coating. Examination of figures 5.27 and 5.28 showed that for each plate thickness range linear strain increased significantly as the magnitude of

substrate-ceramic thermal expansion coefficient mismatch increased. Further, a reduction in linear strain was noted for each substrate material as plate thickness increased. A similar relationship was noted between curvature strain values and increasing substrate thickness, but there was little correlation between substrate/ceramic expansion mismatch and curvature related strain.

Residual stresses were calculated from the strain data and are shown in figure 5.29, plotted against substrate/ceramic thermal expansion coefficient mismatch for each substrate thickness.

In-plane stress at the front face of zirconia coatings, deposited on steel substrates of thickness range 1 and 2, was tensile and compressive at the rear face. Coatings deposited on aluminium, copper and range 3 steel substrates were compressive at the front face with increased compressive stress at the rear face. In general, in-plane residual stresses were less compressive when coatings were deposited onto thicker substrates and the differences between front and rear face values were also reduced. Values of residual stress obtained were also greatly dependant on the magnitude of the ceramic-substrate expansion coefficient mismatch, being larger when the mismatch was greater.

Microstructural examination revealed vertical crack

networks in the ceramic layer of samples deposited on all substrates in thickness range 1 and on steel substrates in thickness range 2.

Cracking originated at the free surface and had propagated into the section towards the bond layer. Examples of such cracking are shown in plates 5.8a and b. Coatings deposited on copper substrates were characterised by a layer of black copper oxide beneath the bond coat, plate 5.9. The remaining samples exhibited typical coating microstructures and were defect free.

5.2.11 Dependance of residual stress on coating thickness in industrial coatings up to 3mm thick, deposited on aluminium and mild steel substrates.

Measurements of linear and curvature strain were taken on testbars after removal of substrate and bondcoat. The data are presented in figure 5.30 for aluminium substrates and in figure 5.31 for steel substrates.

Several data points were not available because the coatings proved so weak as to delaminate or disintegrate on sectioning. In general free coating sections removed from both substrates appeared weaker as the original particle size decreased and coating thickness increased.

On aluminium substrates, figure 5.30, curvature

strain was greatest in 1mm coatings manufactured from powder C2, and in general the magnitude decreased as coating thickness increased, reducing to zero in 2mm and 3mm coatings of powder C3. Linear strain, in contrast, was generally less in coatings manufactured from powder C2 and was greatest in 1mm coatings of powder C1. Recorded values of linear strain attained a maximum value at 2mm thickness before reducing sharply at 3mm coating thickness.

For steel substrates, figure 5.31, curvature strain in every case was zero. Linear strain, at a given coating thickness, was similar for each powder type and again a maximum value was recorded for 2mm coatings.

A comparison of figures 5.30 and 5.31 showed that linear strain values were considerably reduced on steel substrate samples compared with their aluminium counterparts. This result was similar to that noted previously for much thinner coatings. Further, regardless of substrate, measurements of strain were only possible over the entire coating thickness range for samples manufactured from the most coarse powder, C3. Data for powder C1, the finest, were only available for 1mm coatings.

Values of residual stress were calculated and corresponding values for aluminium and steel substrates are shown in figures 5.32 and 5.33 respectively. On aluminium substrates, in-plane residual stresses were

compressive for 1mm coatings of materials C1 and C3, with the rear face values being more so than those at the front face. In contrast, front face values for material C2 were tensile and rear face values compressive. At 2mm thick, the stress gradient between compressive stresses at the front and rear faces of coatings of C3 had reduced to zero and that for material C2 had become more compressive. At 3mm thick, no residual stress was measured in coatings of material C3.

On steel substrates, in-plane residual stress in 1mm coatings in general was compressive, small in value and no difference existed between front and back face values. Thicker coatings exhibited similar characteristics.

Visual examination of the surface of coated testpieces showed that as coating thickness increased beyond 1mm, the surface adopted an 'orange peel' or uneven cellular appearance characterised by small ridges of mean spacing of about 2-3mm, however no cracking was evident.

Microstructural examination showed that every sample, except those of 1mm thickness prepared on aluminium substrates using powder C2, were extensively microcracked. Generally, 1mm thick coatings exhibited vertical crack networks that originated at the free surface and which penetrated approximately 90% of the

coating thickness. These were regularly spaced at intervals of between 1 and 2mm. Horizontal microcracking, emanating from vertical cracks, was concentrated on the boundaries between layers deposited on consecutive, complete coating cycles, and generally extended between 0.1 and 0.5mm either side. Where cracking occurred in 1mm thick coatings, it appeared to be similar in nature regardless of substrate composition, but samples prepared from powder C2 on aluminium were not cracked and those on steel less extensively so. Examples of the latter two coatings are shown in plates 5.10a and b, together with an example of more typical cracking in plate 5.10c.

All 2mm and 3mm coatings were found to contain extensive microcracking, but there was no apparent difference in extent between those deposited on aluminium and steel substrates. 'Ridging' of the surface previously noted on visual examination was found to occur at positions where vertical microcracks reached the free surface. Of great significance, however, were easily observable differences between the extent of propagation and vertical spacing of horizontal microcracks. As the thickness increased from 1mm to 3mm, so the extent of horizontal propagation increased, often with cracks developing over several millimetres leading to complete separation between vertical crack sites. Coatings prepared from powder C1

contained the most extensive arrays of propagated cracks while those manufactured from powder C3 contained the least. In the former, propagation was found not only on the boundaries between layers deposited on consecutive complete coating cycles, but on sublayer boundaries associated with forward and reverse traverse directions of the spray rig. While a few sublayer cracks were found in coatings of powder C2, extensive propagation was confined to complete cycle layer boundaries. Finally, extensive propagation in coatings of powder C3 was often confined to every third or fourth interlayer boundary, with only partial propagation in the intervening layers. Examples of these extensive crack networks are shown in plates 5.11a,b,c for 3mm coatings deposited on steel substrates using powders C1, C2 and C3 respectively.

Free coating test bars, manufactured for this particular study, were of sufficient thickness to allow measurement of their elastic modulus using the dynamic resonance technique. Data obtained from all of the available test bars is shown in figure 5.34. The highest recorded values were those obtained from 1mm thick bars manufactured from powder C2, with steel substrate samples having slightly higher modulii than their aluminium counterparts, despite the latter being crack free. Similar 1mm coatings of powders C1 and C2, while maintaining the differences between substrates,

attained much lower modulii, probably reflecting the extent of microcracking in their structures. Thicker coatings continued to show further reductions in strength, with extensively microcracked 3mm coatings of powder C3 attaining approximately 25% of the modulus of equivalent 1mm coatings.

5.3 Theoretical data derived from mathematical models of heat transfer within coating systems.

5.3.1 Use of models.

Computer program 'FINITE' (simple model) was employed to investigate the consequences of material property variations on insulation effectiveness, the optimum positioning of air cooling during coating deposition and finally to model the rapid cooling of 'splats' of ceramic material.

Programs 'SPRAY' and 'HEAT' (complex model) were used to predict substrate and coating temperatures during coating deposition, ultimately allowing the determination of residual stresses in model coating systems.

5.3.2 The effect of material property variation on the performance of thermal barrier coatings.

5.3.2.1 Effect of coating thickness.

The 3-dimensional output data plots for simulations of 1mm, 3mm and 5mm coatings, are shown in figures 5.35a to c. Through thickness temperature profiles, from the left hand boundary at 800°C to the right hand boundary at 20°C, are displayed at increasing time from the start of the simulation towards the back of the plot.

Predictably, temperature differences across the coating increased with coating thickness, but the gradient was reduced for 5mm coatings. Maximum surface and substrate temperatures were reached in all cases after about 225 seconds. Final substrate temperature, maximum coating front face temperature and temperature drop across the coating were measured from the plats and are shown in figure 5.36. Coating surface and substrate temperatures were changed by similar amounts as thickness increased, and the greatest improvement in insulation was achieved by increasing the coating thickness from 1mm to 3mm. Thicker insulation was also seen to have important consequendes for expansion mismatches between substrate and coating. At the metal/ceramic interface, temperatures were reduced, thereby lowering expansion mismatch stress, and the

exposed ceramic face was seen to be about twice as hot as the substrate material for both 3mm and 5mm coatings, virtually mullifying the twofold difference in expansion coefficient mismatch between substrate and ceramic.

5.3.2.2 Effect of coating thermal conductivity.

Temperature profiles obtained from simulations with increasing zirconia conductivity are shown in figures 5.37a to c respectively.

Through thickness temperature gradients were considerably reduced as conductivity increased, although maximum surface and substrate temperatures were achieved after approximately 225 seconds as before. Corresponding plots of final substrate and coating surface temperature and their difference are shown in figure 5.38, and serve to highlight the effect of increasing conductivity. In particular, through thickness temperature gradients for the highest conductivity coating were reduced to approximately one quarter of that achieved at a conductivity of $0.1 Wm^{-1}K^{-1}$.

5.3.2.3 Effect of coating specific heat capacity.

Temperature profiles are shown for each simulation in order of increasing heat capacity in figures 5.39a to c.

An initial assessment showed them to be almost identical in terms of maximum substrate and ceramic surface temperatures. Detailed examination, however, highlighted the fact that the time taken to achieve both peak surface and substrate temperature was increased with larger values of heat capacity. The results are summarised in figure 5.40 and illustrate the more sluggish response with higher heat capacity coatings.

5.3.2.4 Effect of coating density.

Temperature profile data are shown in figures 5.41a to c for each simulation in order of increasing coating density.

Detailed study of these plots showed them to be virtually identical in every respect. An important factor with regard to this result is that no account was taken of the decrease in conductivity which must occur when ceramic material is replaced by very low conductivity air.

5.3.2.5 Effect of substrate material.

Temperature profiles for models of median coatings on copper, aluminium and steel substrates are shown in figures 5.42a to c respectively.

Measurements of ceramic surface and substrate/ceramic interface temperatures revealed no differences in the temperature drop across the insulating layer, although absolute values for copper were about 5°C and 20°C lower than aluminium and steel respectively. Final substrate temperature gradients, however, reflected the conductivity of the metallic materials and these are summarised in figure 5.43. There was no apparent effect on time to peak surface or substrate temperature.

5.3.3 Investigation of the optimum position for air cooling jets during coating deposition.

Through thickness temperature profiles for a model coating, cooling by natural convection or with simulated back, front or combined air cooling, are shown in figures 5.44 a to d respectively. Profiles are displayed with increasing time from the start of the simulation towards the front of the plot.

It was immediately apparent that the greatest temperature reduction in a given time was achieved by combined front and back face cooling, however the effect of directing the air blast at the ceramic surface alone was only marginally less effective. In

contrast, back face cooling achieved only minimal reductions in temperature compared with the uncooled case. Of particular interest was the observation that any front face cooling increased the temperature gradient across the coating layer and altered the balance of expansion mismatch between substrate and ceramic.

5.3.4 Factors affecting the cooling rate of ceramic particles after impact with the substrate.

5.3.4.1 Effect of underlying zirconia particles.

Through thickness temperature profiles, for simulations of a hot zirconia particle impacted with a substrate which has either none, one, two or three existing particles, are shown in figures 5.45a to d respectively. As in the previous section, later profiles are shown towards the front of the plot for clarity.

Impact of the first particle with a plain metal substrate produced a very rapid initial temperature drop of some 510°C in 20μs (2.55×10^{7} °Cs^{-1}), after which the cooling rate was considerably reduced. In fact, the timescale employed in the simulation was so short that subsequent cooling from about 1490°C was slow enough for the particle and substrate temperature to be considered 'constant'. The substrate was heated only in

a very narrow range next to the particle and the ultimate cooling rate was controlled by the convective heat transfer rate and thermal conductivity of the ceramic material.

When an insulating, pre-existing 'splat' of zirconia was present underneath the impacting particle, conditions were considerably altered. A temperature drop of about 1100°C was experienced in 55μs (2.0×10^{7} °Cs^{-1}), reaching a mean temperature of 900°C, after which the particle cooled much more slowly. Again the substrate was heated in a narrow region next to the existing zirconia partice. In contrast, the underlying particle was rapidly heated to about 900°C because of its poor conductivity.

Where two and three existing particles were present, 'constant' temperatures of about 680°C and 565°C were reached after 85μs and 105μs respectively, and the underlying material was again rapidly heated. The values of average cooling rate and 'constant' temperature for each simulation are summarised in figures 5.46 and 5.47 respectively, and clearly illustrate the effect of underlying material on cooling rate.

An important consequence of the modification of 'constant' temperature by underlying material, figure 5.47, is that zirconia particles will be very rapidly cooled to temperatures below the tetragonal-monoclinic

transformation range only when several um of ceramic material are allready present. Early particles will have 'constant' temperatures above the transformation temperature and will cool relatively slowly through it, possibly resulting in the formation of monoclinic material at the metal/ceramic interface.

5.3.4.2 Effect of zirconia thermal conductivity.

Temperature profiles are reproduced in figures 5.48a to c, with the simulations ordered by increasing thermal conductivity of the impacting zirconia particle.

Examination showed that in each case, the 'constant' temperature was similar at 1490°C, with the formation of monoclinic phase again a distinct possibility. However, as conductivity increased, the time taken to reach the 'constant' temperature rapidly decreased. Values of average particle cooling rate are reproduced in figure 5.49 and showed that average rates to the 'constant' temperature increased almost linearly with zirconia thermal conductivity.

5.3.4.3 Effect of zirconia particle temperature.

Temperature profiles are shown in figures 5.50a to c, with the simulations displayed in order of increasing particle temperature. The interval between profiles was reduced to improve resolution.

It was apparent that the form of each plot was similar, although 'constant' temperatures were increased with higher starting temperatures and achieved at slightly different times. Average cooling rates and 'constant' temperatures were derived from the temperature plots and are shown in figures 5.51 and 5.52 repectively, for each particle temperature.

Examination of figure 5.51 showed that particle average cooling rate rose exponentially as initial temperature increased. In practice, cooling rates would be expected to be even higher, due to radiative heat loss, although in turn this would be limited by ceramic conductivity. Figure 5.52 showed that 'constant' temperature increased linearly with particle temperature, with subsequent implications for cooling through the tetragonal-monoclinic transformation range.

5.3.4.4 Determination of cooling rate from the 'constant' temperature.

Temperature profiles are shown in figure 5.53 for a single particle cooling from the 'constant' temperature. The time interval between profiles was increased to 0.1s to emphasise that the 'constant' temperature is simply a result of the high resolution of earlier simulations.

The average cooling rate to 500^{o}C, below which no further transformation was considered to take place,

was calculated to be approximately $3.9x10^{3}\,^{\circ}Cs^{-1}$ and was probably sufficient to prevent monoclinic phase forming. The substrate was also subject to a heat 'pulse' up to several hundred $^{\circ}C$ over a period of about 2 seconds, but this was somewhat unrealistic because the model assumed that there was no 3 dimensional heat conduction, or alternatively that a 2μm layer of ceramic was simultaneously deposited over the whole surface of a large plate.

5.3.5 Prediction of temperature profiles in coating and substrate during deposition and calculation of residual stress in model systems.

5.3.5.1 Material property data.

Specific heat capacity data for powders and coatings of materials A and B were measured and the corresponding data are shown in figures 5.54a and b. The results from a coating of material B were curve fitted to obtain a temperature dependant relationship for inclusion in the model.

5.3.5.2 Effect of air cooling.

Output data from the program 'SPRAY', which effectively generated the input conditions to the heat transfer model in program 'HEAT' from the spray parameters, is shown in figures 5.55a to e.

Figure 5.55a describes the variation in plasma gas temperature over the point of interest on the substrate surface during 20 revolutions i.e. one traverse towards the centre of the turntable. Data for the return pass was identical except that it was reversed. Figure 5.55b similarly describes the heat flux due to radiation from the flame to the point of interest during the spray cycle. The data in figures 5.55a and 5.55b was effectively unchanged by the presence or otherwise of air cooling. In contrast, figures 5.55c and d describe the gas heat transfer conditions at the point of interest and show how air cooling prevented the effective heat transfer coefficient from flame to surface or surface to air from falling below a certain fixed value, figure 5.55d. Finally, figure 5.55e describes how coating thickness increased in a stepwise fashion as individual particles arrived at the surface during spraying. Due to restrictions in the amount of processor time available and the extraordinarily large number of calculations involved in running each simulation, it was only possible to model one traverse of the plasma torch i.e. over 20 complete table revolutions from the edge to the centre of the table. Consequently, thicknesses deposited were very thin compared to practical coatings, but were expected to display similar trends.

Output data from the program 'HEAT' is summarised in

figures 5.56a and b and 5.57a and b for the uncooled and cooled models respectively.

The graphs illustrate the maximum and minimum temperatures achieved during each spray pass at two locations in the coating thickness. The first site, figures 5.56a and 5.57a, was at the surface of the substrate on the bondcoat/substrate interface line. The temperature at this position and in all subsequent simulations was very similar to that at the bondcoat/ceramic interface and so the latter values were not displayed. Figures 5.56b and 5.57b show the minimum and maximum temperatures at the front face of the ceramic layer. The position of the latter was therefore moved at the arrival of each new particle, but was chosen because the maximum ceramic temperatures were found there. Further, the 'maximum' ceramic temperature quoted in each case was that value obtained after a period of rapid cooling and was the temperature existing at the maximum substrate temperature during each cycle. The reasons for this latter choice have already been described in chapter 4.

Considering the uncooled case first, substrate temperatures, described by figure 5.56a, were subject to a thermal cycle, up to about 400°C and cooling down to about 50°C, each time the plasma torch passed over the point of interest. During later cycles, the centre of the plasma flame was more closely approached and so

the thermal cycle was shifted to higher temperatures. From the eighth pass onwards, ceramic particles were deposited on the substrate surface, with important results. Maximum substrate temperatures per cycle were reduced by the thermal barrier effect and minimum substrate temperatures were raised by reductions in heat loss, due to the insulating coating, and emissivity. A further small contribution due to heat conduction from the hot particles probably raised temperatures initially, but would have become less important as the layer thickness was built up. Maximum and mimimum substrate temperatures were observed to alter only during those passes when particles were deposited. Later passes, when no coating material was laid down, retained approximately similar temperature ranges although some overall reduction occurred as the point of interest moved further from the flame centre. The insulation effect of the layer was such that at the end of the traverse, maximum substrate temperatures were reduced to about 350°C and minimum temperatures raised to about 250°C. Ceramic front face temperatures for the uncooled case, figure 5.56b, behaved in an identical manner with temperature ranges reduced as the insulation layer was built up and 'maximum' and minimum values virtually identical to those experienced at the substrate/bondcoat interface.

Air cooling was seen to have no effect on the form of

either substrate or coating face temperature data. Changes were noted, however, in the absolute values of temperature. Cooled substrate and coating minimum temperatures, figures 5.57a and b were consistently 30°C to 40°C lower than their uncooled counterparts. In contrast, maximum temperatures in both substrate and coating were similar to uncooled data until the onset of ceramic deposition when a reduction of about 30°C was achieved.

Residual strain, developed in the model coating on cooling from the maximum substrate temperature during the final spray pass, was calculated for both simulations. Coating thicknesses were generally very thin (10s of micrometres) and as such through thickness temperature gradients were negligible, thus preventing assessment of strain differences between front and back coating faces. The data were subsequently transformed to residual stress using an elastic modulus for zirconia coatings of 30GPa and a Poissons ratio of 0.25. Values of residual strain and stress are summarised in table 5.1.

Despite large differences in thickness between equivalent practical coatings and the model, a similar effect of air cooling was noted in that it gave a small reduction in residual stress both parallel and perpendicular to the coating plane.

5.3.5.3 Effect of spray distance.

Output data from program 'SPRAY' is reproduced in figures 5.58a to d and 5.59a to d for 100mm and 125mm spray distances respectively.

Direct comparison with equivalent data for 75mm spray distance, figures 5.57a,b,d and e showed that with increasing spray distance maximum plasma gas temperature, heat transfer coefficient, radiation heat flux and material deposited per traverse were all decreased. Also minimum gas temperature was raised at longer spray distances because the plume radius was enlarged. Significant trends are summarised in figures 5.60a to d.

Substrate and coating front face temperature range values are shown in figures 5.61a to b and 5.62a to b for 100mm and 125mm spray distances respectively.

A comparison with figure 5.57a, spray distance 75mm, showed that the form of figures 5.61a and 5.62a were similar in that maximum and minimum substrate temperatures tended to converge as the coating layer was deposited. With increasing spray distance however, maximum substrate temperatures were reduced. Minimum substrate temperatures were also raised but to a lesser extent. Also the substrate cyclic temperature range throughout the process was reduced as was the final substrate temperature.

Ceramic front face temperatures, figures 5.61b and

5.62b, were similar in form to those at 75mm, figure 5.57b, and their values decreased with larger spray distance, mimicking their substrate temperatures. Overall temperature reductions due to the coating layer were maximised at 75mm separation distance because they were thickest.

Values of residual strain/stress were calculated and are given in table 5.2, together with comparable data from table 5.1.

Calculated in-plane and perpendicular residual stresses are shown in figure 5.63, for the range of spray distances involved, and illustrate the inverse relationship between stress and spray distance. If constant thickness coatings had been simulated, substrate temperatures at longer spray distances would probably have been further reduced because the coatings would have been thicker.

5.3.5.4 Effect of workpiece/sprayhead relative velocity.

Output data from the program 'SPRAY' is reproduced in figures 5.64a to d and 5.65a to d for $0.4ms^{-1}$ and $0.3ms^{-1}$ relative velocities respectively.

Comparison with similar input data for the $0.5ms^{-1}$ model, figures 5.55a,b,d,e, showed that apart from coating thickness, parameters were similar in magnitude except that the timescales were increased. Coating

thickness was greater at lower velocity because the residence time under the plasma flame, during which deposition took place, was longer per spray pass.

Maximum/minimum substrate and ceramic front face temperatures are shown in figures 5.66a,b and 5.67a,b for velocities of $0.4ms^{-1}$ and $0.3ms^{-1}$ respectively, for comparison with $0.5ms^{-1}$ data in figures 5.57a and b.

Before coating deposition occurred, substrate maximum temperatures were raised at lower velocities because of increased flame residence times. Similarly, minimum temperatures were lowered because of increasing time periods between spray passes. During and after deposition, equal substrate maximum and minimum temperatures were attained regardless of relative velocity, presumably because increased heat input at lower velocity was offset by thicker insulating layers.

Ceramic front face temperatures were representative of their respective substrates with final values again being similar regardless of relative velocity.

Residual strains/stresses were calculated for each velocity and the results are shown in table 5.3 together with comparison data from table 5.1.

The data did not show the same trend as practical coatings i.e. decreased strain/stress with increased relative velocity. The model, however, was not directly comparable with practical coatings in that only one traverse of the sprayhead was simulated and

consequently very thin 'coatings' were produced. The cause of practical variations in stress, in this instance, may well be associated with later stages of the coating process which were not modelled here.

5.3.5.5 Effect of substrate material.

Output data from the program 'SPRAY' for these particular simulations was identical to that described by figures 5.57a to b and d to e.

Maximum and minimum substrate and coating front face temperatures are shown in figures 5.68a and b for copper and 5.69a and b for mild steel.

A comparison of substrate temperatures in figures 5.57a, 5.68a and 5.69a for aluminium, copper and mild steel respectively, showed that minimum temperatures on each cycle were very similar. Maximum temperatures, before coating deposition, were highest in aluminium substrates and lowest in copper substrates, with the difference averaging 25°C. During coating, this difference was reduced until at the end of the traverse each substrate had a similar maximum substrate temperature.

Ceramic front face temperatures reflected those of their substrates and attained similar final maximum temperatures.

Residual strains/stresses were calculated as before and the results are given in table 5.4, together with

substrate thermal expansion coefficients used and comparable data for aluminium from table 5.1.

Calculated values of residual stress were plotted against expansion coefficient and the graph is shown in figure 5.70. Examination showed that in the absence of temperature differences between the coatings, residual stress was directly related to expansion mismatch between coating and substrate.

5.4 X-ray diffraction analysis of zirconia coating materials subject to heat treatment.

5.4.1 Visual analysis of diffractometer traces.

5.4.1.1 Low-angle data.

Diffraction data obtained from the angular range 27° to 34° of 2θ was termed low-angle data. Sections of the output traces obtained from as-supplied powder, as-sprayed and representative heat-treated free coatings are reproduced in figures 5.71a to c and 5.72a to c for materials A and B respectively.

Material A contained no monoclinic phase reflections in either powder or sprayed coating and none were detected during the subsequent heat-treatment program. In contrast, Material B displayed two relatively intense monoclinic {111} type reflections in the starting powder form which were not completely removed

by the plasma spray process. Later heat treatment did not affect the intensity of these residual peaks or their relative intensity compared to that of the combined cubic+tetragonal reflections. The integrated intensity of monoclinic {111} type and cubic+tetragonal (111) reflections was measured for material B and the data are given in table 5.5.

5.4.1.2 High-angle data.

Diffraction data obtained from the angular range 72° to 77° of 2θ was described as high-angle data. Digitised versions of the diffractometer output traces, after removal of background intensity, are shown in figures 5.73a to h for material A and figure 5.74a to h for material B.

Figure a in each case describes the reflections obtained from the starting powder. Subsequent diagrams illustrate and compare data obtained on rapid cooling from a particular heat treatment temperature with that of the as-sprayed material.

The high angle traces were composed of between two and five overlapping reflections attributed to tetragonal, transformable (t) and non-transformable (t'), and cubic phases. Each particular reflection was in turn the sum of the diffracted intensities of copper K_{α_1} and K_{α_2} radiation. While individual peaks were often not resolved, it was possible to draw general

conclusions about phase transformations and to identify the onset of microstructural changes.

Material A in starting powder form consisted of cubic and a majority of retained tetragonal phases, with no evidence of free yttria. Rapid cooling through the cubic phase field, figure 2.6, after plasma spraying resulted in an almost complete 'displacive' transformation to non-transformable tetragonal (t') phase which was subsequently retained to room temperature. Heat treatment in the tetragonal plus cubic phase field at 1100°C or higher, for comparitively short periods, was sufficient for some of the t' phase to break down into cubic and low-yttria transformable tetragonal (t) phases. Subsequent rapid cooling after heat treatment prevented further transformation of low-yttria tetragonal (t) phase to monoclinic material. At 1400°C, structural changes were sufficiently rapid that after two hours at this temperature, the majority phase was cubic on return to room temperature.

In contrast, Material B in starting powder form principally contained cubic material, with some monoclinic phase identified in low angle data and a very small amount of free yttria. Plasma spraying produced a coating that contained a majority of non-transformable tetragonal (t') phase with smaller proportions of cubic, transformable tetragonal (t) and

monoclinic phases. No free yttria, however, was found. Heat treatment in the tetragonal plus cubic phase field at 1000°C or higher again caused some t' phase to break down, increasing the proportions of cubic and low-yttria transformable tetragonal (t) phase. Rapid cooling after heat treatment was sufficient to prevent the formation of additional monoclinic material. At 1400°C, structural changes were again rapid, with a majority of cubic phase being formed and retained on cooling to room termperature.

Output traces for each material were further examined to determine the exposure required at each heat treatment temperature for a noticeable structural change to occur. The results are summarised in figures 5.75 and 5.76 for coatings of materials A and B respectively, and show that the latter was slightly less stable at high temperatures. The diagrams effectively defined a safe operating envelope for use of these thermal barrier coatings where structural stability is required.

5.4.2 Determination of coating phase composition.

Phase compositions were calculated for both powders and free coatings by determining the integrated intensity of particular reflections and using that data to solve equations 2.13a to c.

Where necessary, high angle traces with overlapping

reflections were deconvoluted into separate peaks using the computer program 'X-RAY'. An example of a deconvoluted trace is shown in figure 5.77. Superimposed on the original data points are the individual composite K_{α_1} and K_{α_2} reflections which make up the original trace. Output data giving the angular positions of individual and composite peaks, peak width at half maximum intensity (PWHM), maximum intensity and integrated intensity are also given. Each trace was analysed several times to assess the range of output data values obtained by the curve fitting process. In general variations of about 5% were encountered in calculated integrated intensities but where traces had low signal to noise ratios, the difference was increased to about 15%.

The intensity of (004) transformable tetragonal (t) phase reflections, in all samples of material A and for samples of material B heat treated below 1300°C, was so small that it was not possible to reliably separate them from close, relatively more intense (004) t' reflections. Consequently, diffracted intensity in that region of the trace was assumed to originate wholly from the latter reflection when separation proved difficult. Errors from this assumption were expected to be quite small in terms of total diffracted intensity and phase composition.

A summary of the compositions of starting powder and

as sprayed coating are given in table 5.6 for both materials.

Starting powder of material A was found to consist of a high proportion of non-transformable tetragonal (t') phase, with the remainder of cubic and transformable tetragonal (t) material. Plasma spraying converted virtually all of the material to non-transformable tetragonal (t') phase.

In contrast material B starting powder contained a larger proportion of cubic and non-transformable tetragonal (t') phase, together with a significant proportion of monoclinic material. The latter was drastically reduced after plasma spraying and the proportion of non-transformable tetragonal (t') phase was increased to nearly twice that of cubic. Subsequent heat treatment at termperatures of up to 1000^{o}C for 100H produced no noticeable changes in the proportions of the phases in coatings of either material using this technique. This was at variance to evidence from visual examination of traces which showed that small changes had occurred after 50 hours at 1000^{o}C in coatings of material B. This apparent insensitivity was accounted for by the variation in deconvoluted data produced by the curve fitting process. Such variation was not due to errors in the deconvolution program but was related to the fact that iterative input parameters had finite step sizes.

At temperatures above 1000°C, consistent changes in phase composition were noted for heat treated free coatings of both materials. The ranges of calculated phase compositions are shown for material A in figures 5.78a,b to 5.81a,b, and for material B in figures 5.82a,b to 5.85a,b, after heat treatments in the range 1100°C to 1400°C. Diagram a for each heat treatment temperature illustrates the proportions of monoclinic, total tetragonal and cubic phases, while diagram b illustrates the relative proportions of transformable (t) and non-transformable (t') tetragonal phase.

Except at 1100°C for coatings of material B, the proportions of cubic and transformable tetragonal phases increased with heat treatment time and temperature, at the expense of non-transformable tetragonal (t') phase. The apparent increase in t' in coatings of material B heat treated at 1100°C may have been caused by chemical inhomogeneity in the samples tested.

The rate of transformation of t' in coatings of material A, as heat treatment temperature/time increased, was higher than in corresponding coatings of material B. This latter effect was attributed to the greater departure from equilibrium of the original structure of as-sprayed coatings of material A compared with equivalent coatings of material B. Also the rate of formation of cubic phase in coatings of material A

was about twice as fast as that for transformable tetragonal phase. In contrast, both rates were similar in coatings of material B. Finally, despite large differences in as-sprayed coating compositions, heat-treatment for two hours at 1400°C was sufficient to bring the final phase compositions of coatings of materials A and B to similar values.

5.4.3 Determination of coating lattice parameters.

Analysis of diffractometer traces from heat treated coating samples provided other important information in addition to integrated intensity data. The location of each reflection was described in terms of angular position, and the results are given in figures 5.86 and 5.87 for heat treated coatings of A and B respectively.

Examination showed that the positions of each reflection, while subject to variation due to deconvolution errors, remained fairly constant despite the fact that significant changes in microstructural phase composition had occurred. Even at temperature/time combinations where partial changes had occurred, significant continuous variation in the angular location of phases was not found. Further, the appearance of transformable tetragonal (t) phase, was at distinct positions which were maintained regardless of heat treatment temperature. These observations suggested that bulk diffusion over significant

distances had not occurred, rather that phase transformation from non-transformable tetragonal (t') phase to cubic plus tetragonal (t) material had occurred by nucleation and growth of low-yttria tetragonal (t) phase.

Standard structural relationships, [136] , were used to determine the lattice parameters of cubic, transformable (t) and non-transformable tetragonal (t') phases from angular position data. Maximum and minimum lattice parameters were determined from extreme values of angular position for each phase regardless of heat treatment temperature and are summarised in table 5.7.

The lattice parameters of each phase were very similar in coatings of materials A and B. Finally, data from table 5.7 for materials A and B is shown in figures 5.88a and 5.88b respectively, superimposed on data described in reference [137] for similar materials. Close agreement between the results of this study and the published data was obtained.

Chapter 6 - Discussion.

6.1 Introduction.

The penultimate chapter of this work is given over to a discussion of experimental and theoretical results.

A qualitative model, describing the origin and nature of residual stress in zirconia thermal barrier coatings is outlined first, followed by a discussion of experimental and theoretical results within that context. Subsequently, the effect of material properties on insulation effectiveness is considered and the structure and stability of zirconia coating materials are discussed. Finally, the design of an optimum thermal barrier coating is outlined based on current knowledge and techniques.

6.2 Qualitative model for the origin and nature of residual stress in thermal barrier coatings.

A simple elastic model of a ceramic coating, attached as a single slab at high temperature onto a cold substrate, predicts a high uniform tensile stress in the ceramic layer on cooling to room temperature, figure 6.1. The data described in chapter 5 shows that in general, for a high expansivity substrate like aluminium, the opposite is in fact true i.e. that a compressive stress is developed. Moreover, the stress singularity is replaced by a distribution which varies

with depth in the coating. It is obvious then that a number of other considerations must be taken into account to explain this apparent stress reversal.

In general, thermal barrier coatings are deposited onto metallic substrates which start at room temperature or at a preheat temperature of several hundred degrees centigrade. Regardless of the actual value, the first ceramic particles which impact the surface solidify at say 2700°C and cool rapidly to the substrate temperature with little opportunity for deformation. For typical zirconia particles cooling to room temperature, a contraction strain of about 2.7% is developed which they cannot support and shrinkage cracking must result. The net effect is that the first impacted particles are attached to the surface and subjected to a small tensile stress equivalent to their remanent elastic strength. Subsequent passes of the plasma torch and the arrival of new, molten zirconia particles have a number of important effects. Heat input from the plasma flame raises the temperature of both coating and substrate. Where the latter is aluminium, its expansion coefficient is about twice that of zirconia and because the substrate is more massive than the coating, it expands, subjecting the coating to a tensile stress which is accommodated by further cracking and perhaps yielding of the substrate if temperatures are high enough. To a certain extent,

this tensile stress will be offset by heating of the coating, in turn leading to its own expansion. Also the arrival of new molten particles tends to heat those underneath causing further expansion. The new particles bond with the existing ones to form a microcracked lamellar layer, capable of deformation by cracking and sliding. The process continues with the arrival of each new layer of zirconia particles and the substrate and coating temperature rise as spraying proceeds. As coating thickness increases however, the thermal barrier effect of the coating layer tends to limit the amount of heat which can pass through to the substrate. A consequence of this is that relative expansion of the substrate is reduced with each new layer of zirconia. Because substrate expansion is accomodated by cracking and sliding of the semi-compliant coating, the only tensile stress supported by the coating is its composite elastic strength. Another consequence of the thermal barrier effect is that the temperature of later layers of ceramic is raised, simply because heat from impacted particles and the plasma flame cannot be conducted away as easily.

On completion of spraying the temperature profile through a typical coating is as shown in figure 6.2, with the front face of the coating at an elevated temperature compared to that at the metal/ceramic interface. Because the process has essentially resulted

in a coating which is either stress free or weakly in tension on completion of spraying, the maximum (but not necessarily the final) substrate temperature is termed the stress-free temperature. The stress distribution through the coating on completion of spraying is described by figure 6.3. The ceramic is, perhaps, subjected to a weak tensile force which tends to reduce at the hotter outer surface due to temperature gradients. At the interface, the substrate may, in turn, be subjected to compressive stress causing yielding, depending on the substrate material and temperature.

Subsequent cooling to room temperature then leads to differential contraction between the high expansion aluminium substrate and relatively low expansion coating. Because the substrate is more massive it's contraction will be dominant and the coating is subjected to a compressive residual stress. Maximum stresses are developed at the ceramic/substrate interface because their temperatures are similar. Towards the front of the coating, temperatures are higher, leading to greater contraction of the ceramic. Because each ceramic layer is prevented from contracting by underlying material and ultimately the substrate, tensile stresses are developed progressively, reaching a maximum at the hotter, exposed surface. The effect of these superimposed

tensile stresses is to reduce the compressive residual stress towards the front of the coating. The final stress distribution is then described by figure 6.4. If the temperature gradient is sufficiently high in the coating, or it is cooled excessively compared to the substrate, or the expansion coefficient of the substrate is low then the overall stress distribution may become tensile towards the exposed surface, figure 6.5, leading to tension and shear cracks on cooling.

If the strain developed on cooling from, say, 500°C to room temperature is considered, then a maximum value of about 0.6% is envisaged for an aluminium/zirconia coating. In practice this value is often much less and so sources of compliance in the system may be operative. Within the coating, the same mechanism which allows deformation in tension i.e. cracking and particle sliding must also be operative. Similarly, the substrate is at an elevated temperature and so yielding may occur in the surface layers to further reduce stress levels. Practical thermal barrier coatings also contain bondcoat layers which are known to deform easily at elevated temperatures, and these materials are concentrated at the site of maximum stress.

6.3 Discussion of experimental and theoretical results with respect to the development of residual stresses in thermal barrier coatings.

6.3.1 Relationship of experimentally measured strain to qualitative model predictions.

Before discussing specific aspects of these results in terms of the model outlined above, it is worthwhile examining the strain measurement technique in relation to the general model of coating deposition. The practical technique measures two types of strain in free coatings, curvature and linear-related. The former is generally the physical manifestation of the final temperature gradient in the coating layer before cooling and can be explained as follows. The outer layers of coating material are deposited and cool to the temperature of the underlying material, building up a flat coating of uniform dimension, containing a temperature gradient. Subsequent cooling to room temperature results in the outer layers attempting to contract further than underlying material, leading to the development of tensile stress. In fact, the outer layers are shorter at room temperature than those at the substrate/ceramic interface, and upon removal of the constraining substrate by chemical etching, the free coating relaxes and curves to equilibrium. Subsequent measurement of coating curvature allows the

front/back strain differential to be calculated. The technique does of course assume that material properties are uniform through the coating thickness, (microstructural examination has not shown otherwise), and that the temperature gradient through the coating is linear. If the latter were not true, then measured curvature would be that which existed when internal forces in the coating were balanced rather than zero. Again, however, this would not be expected to result in significant errors. Linear-related strain is measured on a flattened free coating, essentially with tensile and compressive forces applied to remove curvature. The measured value of linear strain is then assumed to be that which exists at the mid point between front and back face. This linear strain in fact originates in the differential contraction between coating and substrate on cooling from the 'stress-free' temperature after spraying. The total strain is the algebraic sum of differential contraction at the metal/coating interface and that due to the through thickness temperature gradient at the mid-point of the coating thickness. An important assumption in the measurement technique is that the act of flattening a brittle, ceramic coating, i.e. applying tensile and compressive stress to it, does not damage the coating. An important point here is that the attached coating is generally always subject to an overriding compressive stress, which is removed

in practice with the substrate. Practical examination of free coatings shows that induced damage due to flattening does not occur. In fact, considering the brittle nature of the materials employed, the ceramic coatings are remarkably resilient.

6.3.2 Substrate plate size and material type.

Initial practical investigations were concentrated on determining the most efficient plate size for manufacture of coating testpieces, bearing in mind the cost of materials and the requirements for accurate measurement of residual strain in orthogonal directions within the plate.

Considering curvature-related strain first of all, this was found to be uniform in larger plates regardless of measurement orientation. The implication of this is that through thickness temperature gradients in the coating layers were uniform. Similar values were found in smaller plate sizes, particularly at higher relative velocity, suggesting that through thickness temperature gradients were common to both plate sizes. Any variation may have been due to experimental error, or differences in the behaviour of alternative plate sizes under certain deposition conditions.

Linear-related strain in larger plates was found to vary with measurement orientation, being higher in a direction tangential to the spray path. This was not

entirely unexpected because the heating effect of the plasma torch is concentrated on this line, with the edges of the plate subjected to reduced flame temperatures at the edge of the plume. Perhaps more surprising was the similarity between narrow and wide plate linear strains in the spray direction. Given that the larger plate must have had a greater heat sink effect due to conduction, the only explanation which can be offered is that the narrow plate was subjected to less direct heating by the plasma flame, by virtue of its orientation, and the two effects therefore cancelled out. The direct implication of this result is that both plate sizes must have experienced similar temperature distributions during the spray process and together with the similarity in curvature-strain data, suggests that the adoption of smaller, more economic plates was justified.

Powder materials A and B, despite having been manufactured using different techniques and containing different phase structures, gave similar values of residual stress in comparitive tests under two different sets of deposition conditions. Apparently, then, residual stress in thermal barrier coatings is relatively insensitive to material manufacture. Consideration of this fact in terms of the model suggests broad agreement, although if the conductivity and/or porosity of a coating were significantly reduced

by the material type, this might have adverse effects on through thickness temperature gradients and compliance during deformation.

6.3.3 Time delay between successive coating cycles.

The effect of allowing the coating system to cool to room temperature was not constant over the range of relative velocities employed. At low speed ($0.2ms^{-1}$, 2 coating runs), intermittent deposition reduced both linear and curvature-related strain compared with continuously sprayed samples. The implication of this result in terms of the model is that both substrate and coating back/front temperature gradient were reduced when coatings were deposited intermittently. At higher velocity ($0.5ms^{-1}$, 5 coating runs), substrate temperature was again reduced since linear strain and therefore differential contraction was lower than for equivalent continuously deposited coatings. However, the temperature gradient between coating front and back for intermittent samples was similar to coatings deposited at $0.2ms^{-1}$. In contrast, the gradient in continuously deposited coatings was reduced to a comparable level. From the point of view of the model, the effect of intermittent deposition in these coatings is relatively easy to explain. While it lowers both substrate temperature and coating temperature gradient, on subsequent reheating the thermal barrier effect of

existing material is small because the coating is thin. Thermal gradients are not then aggravated by intermediate cooling in the same way as they would be in a thick coating where the thermal barrier effect is more pronounced. The fact that temperature gradient is not lowered at higher relative velocity may be a consequence of the coating having achieved a limiting gradient.

6.3.4 Coating thickness.

Thermal barrier coatings were manufactured in stages of increasing thickness to determine the effect on residual stress.

The behaviour of the coatings with increasing thickness was in line with predicted effects expected from the qualitative model. Linear strain was found to decrease slightly as coating thickness increased, suggesting that substrate temperatures were slightly reduced by the thermal barrier effect. Also, testpieces were allowed to cool briefly while coatings of intermediate thickness were removed.

Curvature-related strain was also reduced as coating proceeded, suggesting that front-back temperature gradients were lowered. In fact, the opposite was probably true, since intermediate cooling between thicker layers would tend to aggravate the temperature gradient between existing and newly arrived material

(because of the thermal barrier effect). This apparent departure from expected results can be explained quite simply by examination of the microstructural evidence. As the thickness, and therefore front/back temperature gradient increased, so did the accompanying level of tensile and shear stress in the coating. Above a certain level, the coating was unable to support the tensile stress and fracture occurred, leading to stress relief (and a reduction in the room temperature free coating curvature).

It is apparent from the sequence of cracking that initially, vertical tensile fracture is most favourable, presumably because the resolved stresses are highest in the coating plane. However, as thickness continued to build up, stress relief by horizontal shear fracture becomes more favourable. The obvious sites for this to occur are vertical free surfaces i.e. the faces of vertical tensile cracks. Undoubtedly, the weakest points on the surfaces of such cracks are the boundaries between complete, consecutive coating layers, where large mismatch strains must occur on deposition. Once these sites have become exhausted as a source of stress relief, the next most favourable must become operative. It is apparent from the microstructural evidence that these sites lie on the boundaries between coating layers deposited in the same run but in different directions of sprayhead traverse.

The implication from these observations is that for shear crack formation, the most likely sites for crack nucleation lie on the boundaries between coating layers which have the longest time delay between their deposition. This is not altogether surprising since the greatest temperature differences, and therefore contraction strains and associated damage, must occur between existing and newly arrived material.

6.3.5 Workpiece/sprayhead relative velocity.

Experimental results, under a variety of deposition conditions, have demonstrated that at constant intermediate spray distance, powder feed rate and final coating thickness, compressive residual stress in zirconia thermal barrier coatings deposited on aluminium substrates is reduced when relative velocity is increased. This result is particularly important because it demonstrates that residual stress in such coatings may be modified in a controlled manner simply by altering one spray parameter. While the benefits of such a simple modification are clear, the mechanism by which it is achieved is somewhat less obvious. Consideration of the qualitative model described earlier suggests that reductions in both linear and curvature related strain (and therefore residual stress) must be achieved by reductions in both stress-free substrate temperature and front/back

coating temperature gradient respectively. However, factors which are likely to influence coating and substrate temperatures such as deposit efficiency, final coating thickness, total manufacturing time or total flame exposure time are unaltered with increased relative velocity, provided the number of traverses are increased accordingly. That substrate final temperatures are altered with relative velocity is confirmed by other experimental observations. In particular, measurements of substrate temperature were taken continuously during the manufacture of a series of equivalent zirconia coating at different relative velocities. Initial temperature rises were rapid and similar, regardless of relative speed. As the thickness of zirconia material was built up, the rate of temperature rise was reduced, presumably by the thermal barrier effect of existing material. Of greater importance was the observation that average rates of temperature rise for testpieces coated at lower velocity were greater than for those deposited at higher speeds. The heating effect on the substrate during each traverse was clearly visible as a temperature 'pulse', which decreased as the torch moved to its extremes of travel. The magnitude of this heat pulse was greater at lower velocity, as expected, because traverse rates were lower, but two important factors emerged. First, the apparent cooling rate of

the substrate between pulses was increased at higher velocity, allowing a greater substrate temperature reduction per unit time. Secondly, over equivalent time periods, e.g. 1 traverse at $0.1ms^{-1}$, or 5 traverses at $0.5ms^{-1}$, the maximum temperature experienced was greater at lower velocity. The latter point is of particular importance since according to the model, the stress-free substrate temperature is the maximum value reached during the spray cycle, and therefore affects the magnitude of linear strain on cooling. Higher substrate temperatures experienced during spraying at lower velocity would then be expected to increase the magnitude of compressive linear strain, as experienced in practice.

Attempts to duplicate the variable heating effect in the spray process model were not successful because only one traverse was simulated. Despite this limitation, rapid and similar initial substrate temperature rises were simulated at these different relative speeds, and the peak temperatures attained were directly comparable to those measured in practice.

The reduction in substrate cooling rate and raised substrate temperatures at lower relative velocity may be explained if the manner in which coatings are deposited is considered. At low relative velocity, thick layers of material are deposited with consequent relatively low surface to volume ratios. As a result,

the amount of heat which can be lost from the surface by radiation and convection is relatively low, and therefore a relatively large proportion will have to be conducted away into the substrate. If several thick layers are deposited, then progressively later ones will be subject to a thermal barrier effect, limiting conduction of heat away from the coating and aggravating thermal gradients within it.

In addition, because the plasma torch is resident over the coating for a significant period of time, a relatively static thermal gradient is more likely to be established causing considerable heating of both coating and substrate, and allowing maximum heat transfer rates to be esbablished.

In contrast, thinner coatings deposited at much higher relative velocity have, for a given final thickness of coating, a greater surface to volume ratio, also the number of such coating layers in a given thickness is increased. Heat loss from the coating surface is then much more efficient, allowing more heat to be lost to the surroundings. Also, because many more coating layers are deposited, at higher velocity, a relatively larger proportion will be deposited with thin layers of underlying material, altering the efficiency of the thermal barrier effect. A consequence of these two effects is that less heat will be conducted to the substrate. Further, as

residence times of the plasma torch are considerably reduced, static thermal gradients are less likely to be established, limiting substrate and coating heating effects.

The ultimate temperature distribution in the substrate and coating is then a fine balance between heat loss from surfaces, thermal barrier effects of underlying material and establishment or otherwise of efficient input heat fluxes from the plasma torch.

Improved substrate cooling at higher relative velocity may be simply related to the mechanics of the spray apparatus. Each sample is attached to a moving turntable, and as rotational speeds are increased, so an increased air flow over the samples may cool them more efficiently.

Because heat input from the plasma flame is reduced and heat loss from coating layers is improved at higher relative velocity, large thermal gradients between the front and back faces of the coating are less likely to be established. An important consequence is that curvature-related residual strains will tend to be reduced at higher relative velocity, once more agreeing with experimentally derived data.

At short (65mm) spray distances, although linear strain continues to vary as expected with relative velocity, values of curvature strain are similar regardless of speed and are large in value. The

implication of this result is that the temperature gradient developed across the coating during spraying has reached a limiting value.

Microstructural evidence, however, suggests that stress relief by shear cracking on inter-layer boundaries occurs at lower relative velocities, holding the amount of room temperature curvature observed to a limiting value, equivalent to the maximum shear stress supportable by the coating during deposition. Similarly, very large values of linear strain at low velocity suggest that substrate heating was pronounced. (Samples deposited at $0.1ms^{-1}$ were melted during spraying.) At longer spray distances (110mm), the effect of relative velocity on linear strain, and therefore stress-free substrate temperature, is less pronounced and generally reduced, presumably because input heat flux from the plasma torch is lower. In contrast, for the results described in figure 5.14, curvature-related strain actually increased as relative velocity was raised. A reasonable explanation for this apparent reversal in trend may be that relatively thin coatings deposited at long spray distances are able to cool efficiently and have low input heat fluxes from the plasma torch, regardless of relative velocity. The only remaining factor to consider then is the thermal barrier effect of underlying material. At low velocity this may not exist and at higher speeds may be

instrumental in developing a thermal gradient through the coating thickness. On repeated passage of the plasma torch at higher relative velocity the opportunity would then exist for enhanced curvature strain on cooling to room temperature.

6.3.6 Spray distance.

Another important parameter which has been demonstrated to have a profound effect on residual stress in zirconia thermal barrier coatings deposited on aluminium is spray distance or torch/workpiece separation length.

Experimental data has shown that for a given powder feed rate, both linear and curvature related strain components decrease, with a consequent reduction in compressive residual stress. An important factor in these results is that as distance was increased, so coating thickness was reduced in line with deposit efficiency. From the viewpoint of the qualitative description of residual stress origins in thermal barrier coatings, the experimental results suggest that both substrate stress-free temperature and coating front/back temperature gradients are reduced with increasing spray distance. Also, at lower relative velocities and short spray distances, the shear stress developed in these coatings is such that stress relief by cracking occurs, limiting the maximum curvature

observed under these conditions. This conclusion is entirely consistent with the factors discussed in the previous section. As spray distances increase, then input heat flux must decrease lowering substrate temperatures. Because deposit efficiency decreases with distance, coating layers are thinner, improving cooling behaviour, and reducing the thermal barrier effect on both coating temperature gradient and substrate temperatures. If equivalent thickness coatings had been produced it is anticipated that reductions in residual stress would still have occurred, primarily due to a reduction in the effects of input heat flux on substrate temperature.

Output data from the spray process model, despite being limited in terms of simulation time, correctly predicted that residual stress developed as a result of differential contraction were compressive, and would reduce with increased spray distance. In fact the values of stress predicted were comparable with those determined on real coatings.

6.3.7 Air cooling during spraying.

Air cooling during plasma spraying is often used to improve the quality and performance of the final product. Experimental results, derived from air cooled testpieces, have shown that cooling is capable of reducing the compressive residual stress distribution

in zirconia thermal barrier coatings, deposited onto aluminium substrates at a range of relative velocities.

The most effective conditions for air cooling were achieved at low relative velocity using both combined front and back, or front face cooling. Back face cooling or higher relative velocity reduced the effectiveness. In general, where changes to residual stress patterns occurred, linear strains were affected most significantly, while curvature-related strain was the most difficult to influence.

In terms of the qualitative model, reduced linear strain suggested that stress-free substrate temperatures had been lowered when air cooling was applied, whereas curvature-related strain was related to the coating front/back temperature gradient, and this apparantly was little changed. Substrate temperatures were recorded continuously during spraying of air-cooled coatings and examination shows that particularly at low relative velocity, combined cooling or front face cooling were most effective in reducing substrate temperature, in complete agreement with results from actual testpieces. Back face cooling was also seen to be the least effective method of reducing coating and substrate temperatures.

The conclusion to be drawn from these results is that despite the fact that cooling jets were aimed at the coated surface, they were able to cool the substrate

more effectively than if they were aimed at it directly! Three possible routes for air cooling the coating and substrate have been identified and a consideration of each allow an assessment of which method is most effective under a particular set of deposition conditions.

The first possibility relies on the fact that cooling air will become combined with the hot gases from the plasma flame, lowering their temperature. The effect of this dilution process is that input heat flux to the coating is reduced, thus lowering both coating and substrate temperatures. Previous discussions of the effect of relative velocity on residual stress identified that input heat flux is most important at lower relative velocity. Therefore, the dilution effect on input heat flux would be most effective at low speeds.

The remaining possibilities were demonstrated by the investigation of air cooling jet siting using the simple heat transfer model. Once more this method predicted that combined cooling would be most effective, although only slightly more efficient than front face cooling alone. Each route relies on forced convection i.e. air cooling, removing heat from either the coating or substrate directly. The difference between them is the efficiency with which this can be achieved. The substrate may cool by convection fairly

readily because of its high conductivity. Back face cooling improves this process slightly but does little to remove heat from the low conductivity zirconia coating. To achieve this it is necessary to set up a thermal gradient through the hot, relatively thick substrate, to remove heat by conduction. Because the substrate mass is much larger than that of the coating, this process requires a considerable amount of time to remove sufficient heat. Effectively, the cooling medium is isolated from the coating over short time intervals by a sluggish layer of hot metal. Cooling of the substrate is also limited by the presence of the thermal barrier coating i.e. it insulates one surface.

In contrast, when the coating is air cooled, heat loss from the entire system is dramatically increased. First, heat is removed directly from the hot, low conductivity coating, lowering its temperature. Second, because the coating is cooling, the insulation effect on the coated surface of the substrate is reduced, so heat loss from the substrate becomes more efficient as well.

Because air cooling was uniformly distributed over the surface of the turntable, it is difficult to envisage any relative velocity dependance on convective cooling efficiency. As such then this mechanism must be considered to be velocity independent and uniform over the range studied.

Of the mechanisms described, dilution of the plasma flame is the only one which is affected by relative velocity and as such may explain the greater efficiency of cooling at low relative velocity. Forced air-cooling, either of the coating, or less efficiently of the substrate, would then be expected to provide a uniform contribution to cooling over the entire velocity range. Back face cooling might, however, become slightly more effective if very long time scales were employed. Ultimately then, air cooling would be achieved by a combination of the above mechanisms, depending on the particular cooling conditions employed.

Microstructural examination of coatings deposited at $0.1ms^{-1}$ with combined cooling showed that they contained tensile cracks emanating from the front face. Because the coatings were quite thin and deposited under maximum cooling conditions, it was unlikely that they had developed excessive through thickness temperature gradients. Examination of the simple heat transfer model simulations however shows that combined air cooling was particularly effective at inducing reverse temperature gradients through the thickness of ceramic coatings. If sufficient air cooling was applied, tensile stresses could be induced at the front face, leading to cracking. That cracking was not extensive or obtained in front face cooled samples (with slightly

reduced temperature gradients) suggests that it was a marginal effect.

Simulation of the effect of air cooling was also attempted using the spray process model. The model was configured to investigate the effect of combined cooling compared with the uncooled case at high relative velocity. This velocity was chosen because the effects of flame dilution by cooling air were expected to be minimal in reality. Further the model possessed no direct mechanism for simulating the effects of dilution at lower speed anyway.

Despite the limited thickness of coating simulated in the model, output data was extremely encouraging, in that it correctly predicted substrate and residual stress reductions when air cooling was employed. Once more, the calculated values of residual stress were directly comparable with those obtained from actual testpieces.

6.3.8 Presence of a bondcoat.

Equivalent testpieces, deposited under identical conditions over a range of relative velocities, were found to have slightly reduced linear residual strain components when bond-layers were omitted. Curvature-related strain was unaffected by the presence or otherwise of a bond coat.

This phenomena may be explained if the effect of

bond-coat layers on residual stress in thermal barrier coatings is first considered. During the process of removal by chemical dissolution to produce free zirconia coatings, an intermediate stage is reached where the substrate has been removed and the bondcoat layer is still attached. As described previously, the bond-coat is seen to act as a thin, stiff skin on the underside of the coating, capable of changing the sense of curvature from concave to convex i.e. the bond coated side is shorter than the outer face. Also on removal of the bond layer, linear strains are generally found to increase by about 10%. The implication from these observations is that the free length of the bond-coat layer is intermediate between that of the substrate and ceramic, and that it was in tension relative to the zirconia layer. If the contribution of the bond layer to the through thickness stress distribution on completion of spraying is now included in figure 6.4, a modified stress profile results, figure 6.6. Because the bondcoat layer is metallic, it is more likely to be able to withstand a higher tensile stress than the ceramic.

Subsequent cooling to room temperature must then result in a stress distribution of the form shown in figure 6.7. (It is assumed that the thermal expansion coefficient of the bond layer is intermediate between that of aluminium and zirconia.) If the intermediate

bondcoat layer has no effect on residual stress in the coating and substrate, then the relative difference between them is maintained. However, the stress discontinuity at the weak ceramic/bondcoat interface is considerably reduced compared with the ceramic/aluminium case, with important consequences for subsequent thermal cycling. Because part of the stress discontinuity across the ceramic metal interface is supported by the stronger bond layer, this would be expected to decrease the stress applied to the surface layers of the aluminium substrate on cooling. As a result, the amount of yielding which would be expected to occur in the substrate surface layer would decrease, increasing the compressive stress developed in the coating. Against this increase, some deformation of the bond layer might also occur and its presence would tend to reduce the substrate temperature, because it is less conductive, tending to reduce compressive stress in the ceramic layer. The net effect then is quite small, but leads to marginal reductions in linear strain.

Tensile microcracks were once more found in the front face of coatings deposited at $0.1ms^{-1}$ using combined air cooling. It can only be assumed that their origin was again related to enhanced cooling of the front face compared to the substrate, resulting in the generation of tensile stress.

6.3.9 Substrate material properties and thickness.

Experimental observations of residual strain in identical zirconia thermal barrier coatings deposited onto various substrate materials have highlighted two important effects. First, measured values of linear strain were found to become rapidly more compressive as the expansion coefficient mismatch between coating and substrate increased. No equivalent effect was noted, however, for curvature related strain. The second important result was that both linear and curvature-related strains were found to decrease as substrate thickness was increased.

Both of thse effects are readily explained by the qualitative model for the origin of residual stress in zirconia thermal barrier coatings. Linear strain is seen to originate in the differential contraction which occurs between substrate and coating on cooling from the 'stress-free' temperature. Obviously as the expansion mismatch is increased, so will be the differential contraction. Variations in conductivity and specific heat capacity of a substrate would then be expacted to deviate from a linear dependance of linear-related strain on expansion coefficient mismatch. The properties of the substrate, for a reasonable coating thickness, would not however be expected to alter the temperature gradient through the coating significantly. Hence, curvature-related strains

appear independant of substrate material.

Where thinner, low expansion steel substrates were used, front face residual stresses were found to be tensile, while back face stresses were compressive. This effect is explained quite simply because the linear compressive strain component, arising out of substrate-coating expansion mismatch, was less than the tensile curvature-related strain component at the front face. The presence of tensile stress in such coatings was confirmed by optical examination of polished sections. Tensile microcracks were observed at the front face, propagating into the section.

When thicker substrates were utilised, the value of both linear and curvature related strains were reduced for each material investigated. Linear strain, which is related to substrate expansion, was reduced because for a given heat input, the temperature rise of a larger substrate mass was correspondingly reduced. In a similar manner, the greater heat sink effect of a thicker substrate would tend to reduce coating temperature and front/back temperature gradient in thinner, more conductive coatings, leading to reduced curvature-related strains.

For the thickest steel substrate, reductions in curvature-related strain were sufficient to prevent tensile residual stress at the front face of the coating on cooling. This was reflected on

micro-structural examination where no cracks were found. Thin substrates of aluminium and copper were subject to significant permanent deformation on cooling. This was assumed to have been caused by the inability of each substrate to support significant tensile stresses developed at the metal/ceramic interface as a result of differential contraction. Because significant yielding must have taken place, any measurements of residual stress would have reflected this and so the results were omitted.

Microstructural examination of sections from those buckled substrates showed that each coating contained tensile cracking at the front face. This was because the lack of compression by the substrate had allowed the coatings to be subjected to tensile stresses on cooling.

An attempt to simulate the effect of substrate material on residual stress in thermal barrier coatings was made using the plasma spray process simulation model. Because only one complete traverse was modelled, the magnitude of substrate temperatures and coating thicknesses was somewhat less than achieved in practice. Despite these limitations, the simulation was able to predict correctly that residual stress at the metal/ceramic interface was compressive for all substrates and that the magnitude would increase with increasing substrate/coating thermal expansion

mismatch.

6.3.10 Thick zirconia coatings deposited using industrial spray parameters.

Thick zirconia coatings (1,2,3mm) were deposited using materials and spray process parameters supplied by an industrial collaborator onto aluminium and steel substrates. As the thickness of the coatings on either substrate increased, it became impossible to measure strain in free coatings of all but the most coarse powder because the ceramic was extremely brittle.

Residual stress and microstructural examination data together provide sufficient information to consistently describe the behaviour of these coatings in terms of the qualitative model for residual stress origin.

Each of the coatings was produced without any form of air cooling and as such this would be expected to lead to high through thickness temperature gradients in the coatings and tensile cracking on cooling to room temperature. Microstructural examination confirmed that in every 1mm thick coating, except those manufactured from powder C2 on aluminium substrates, that verical crack networks were present. Samples manufactured from powder C2 on steel substrates appeared less extensively cracked than their counterparts. The implication from this result is that material C2 produced coatings of this thickness which were stronger

and tougher. Examination of residual stress data for aluminium substrate 1mm coatings shows this to be true since the front face of coatings of material C2 were subject to tensile residual stress and yet were not cracked. Equivalent coatings of materials C1 and C3, although subject to front face compression, had presumably achieved this state by stress relief cracking. Similar 1mm thick coatings on steel substrates were cracked regardless of composition although C2 coatings were less extensively so. Each would, however, be expected to develop higher tensile stress on cooling because of reduced coating/substrate expansion mismatch. Therefore, cracking of apparently tougher 1mm thick coatings of powder C2 on steel substrates may be attributed this latter factor.

Thicker coatings (2,3mm) deposited on either substrate exhibited a different dependence of coating material on apparent toughness. As the powder became more coarse, so the extent of horizontal cracking increased. Once more the cause of these cracks could be attributed to the high front/back temperature gradient developed during plasma spraying. The appearance of planar, shear cracks suggested that stress relief by tensile, through thickness cracking had become exhausted. Shear cracking, where it occurred, appeared to propagate from the free surfaces of vertical tensile cracks (where shear stresses would be highest) along

the boundaries between coating layers, as observed in thicker coatings in section 6.3.4. These latter sites would be expected to be weak because they must themselves have been subject to high shear stress on the arrival of a new coating layer.

The apparent transition in crack mechanism from tensile to shear cracking may be attributed to a number of contributing factors:

(i) Once fracture has occurred, the local stress must build up once more to a level where further tensile fracture may occur. This implies that the coating thermal gradient must continually increase.

(ii) The achievement of a limiting thermal gradient in the coating as the thickness builds up prevents the induced tensile force from exceeding a given level. This tensile force is distributed over a continually increasing cross section, leading to a reducing tensile stress.

(iii) Within the 'islands' of uncracked coating, shear stress effects at their edges prevent the local tensile stress from exceeding the tensile fracture strength.

(iv) The microcracked nature of the coating material making up these 'islands' allows deformation or stress reduction.

(v) The many vertical crack surfaces provide a greater number of sites from which shear cracks can

propagate, making this stress relief mechanism more favourable.

The extent to which the material suffered from shear cracking increased as the powder particle size decreased. Again, cracking was increasingly concentrated on less favourable, lower time delay boundaries as stress relief cracking exhausted the weakest sites. A possible explanation for the apparent material sensitivity may be in the density of the coating. As particle size increases, generally so does the proportion of included porosity. A less dense coating may then be more compliant and therefore more resistant to cracking.

Comparison of residual stress data with microstructural observations shows two further effects. First, the extent of shear cracking appears to be unrelated to the substrate material type, implying that its origin lies solely in the coating temperature gradient. Second, once horizontal cracking between vertical crack networks becomes extensive, front/rear face residual stress differences reduce to zero, although substrate/coating expansion mismatch is still effective in subjecting the coating to compressive residual stress, albeit at a limiting value. Extensive crack propagation may then also explain the extreme brittleness of some thicker, free coatings.

Finally, measurements of elastic modulus on free

coatings have shown that its value was a maximum for 1mm coatings of material C2, in line with its apparent resistance to crack propagation. Subsequent crack initiation and propagation in thicker coatings must then be responsible for reductions in the effective modulus.

6.4 The effect of material properties on coating performance.

The effect of material and coating properties on thermal barrier coating performance was investigated on both micro- and macro-scopic scales using the simple heat transfer model described in chapter 4. The results of these simulations are now considered in the context of their effects on thermal barrier coatings for use in insulated diesel engines.

6.4.1 Coating thickness.

While coating thickness is a geometrical rather than material property of an insulation system, it nevertheless has an important bearing on the use of thermal barrier coatings. Temperature gradients across model coating systems were seen to increase with coating thickness, suggesting that the required insulation effect may be achieved by simply depositing a coating of the required thickness (ignoring residual stress considerations of course). Comparison of steady

state temperatures, however, showed that as coating thickness increased, ceramic surface temperature increased at a greater rate than substrate temperature decreased. As an illustration of the consequences of this result, maximum steady state surface and substrate temperatures in figure 5.36 were converted to strain and both interface mismatch strain, coating surface strain and coating strain gradient were derived. (The substrate was assumed to be rigid with no bondcoat deformation.) The data for each coating thickness are given in table 6.1.

As coating thickness increased, insulation was found to be beneficial under static thermal gradients in reducing metal/ceramic mismatch strain and the through thickness strain gradient in the coating.

Because of differences in expansion between substrate and coating, surface layers of thinner coatings were subjected to tensile stress while 5mm thick coatings experienced a smaller compressive stress. Expansion mismatch stresses at the substrate/coating interface were tensile in all cases, with the largest value experienced in 1mm coatings. In general, interfacial stresses were greater than those experienced at the coating surface and such large stresses must be accommodated by yielding in the substrate and bond layer or shear failure would occur. The small compressive stress developed at the surface of 5mm

coatings might be considered beneficial but when the maximum transient temperature differences experienced between front and rear faces of the coating on heating are considered, compressive stress developed at the exposed face of the coating may be sufficient to cause spalling of the insulating layer. To assess this effect, maximum transient temperature differences between the front face of the coating and substrate on heating were derived from model data described by figures 5.35a-c, and were converted to equivalent thermal mismatch strains given in table 6.2. For the particular set of heating conditions employed in the simulation, 1mm coatings of zirconia on aluminium substrates would be expected to suffer a small tensile stress at the exposed surface and a much larger tensile stress at the metal/ceramic interface, at the point of maximum transient temperature difference. As coating thickness, and therefore transient temperature difference increased, so the front face of the coating became increasingly compressive, while the interfacial stresses were reduced. Higher heating rates would be expected to further exaggerate transient stress levels.

Transient stress for both thin and thick coatings is then seen to be harmful. If bondcoat deformation rates in thin coatings are not high enough, then interfacial shear failure or through thickness cracking may occur. As coating thickness increases, compressive stress

levels may be sufficient to cause coating spallation, particularly if bondcoat temperatures are low enough to prevent adequate deformation. Further if bondcoat oxidation prevents reverse deformation on cooling transients then large compressive stresses may be developed in all coating thicknesses, leading to interfacial shear failure or spallation at the end of the thermal cycle as well.

The requirement for effective insulation to reduce heat loss is then seen to be in direct conflict with the requirement to resist coating failure on startup. As coating thickness increases, so do both transient and static compressive thermal stress, with the former increasingly likely to result in spallation at high heating rates. The problem is not solved by reducing coating thickness either. At intermediate thickness where the coating is subject to tensile stress in the steady state, tensile interfacial or compressive surface stresses developed on rapid heating may be sufficient to cause failure if bond coat deformation is not rapid enough to allow stress relief. Thin coatings may not be subjected to compressive stress at any point in their thermal cycle but may contain through thickness cracking and be subject to interfacial shear, depending on the bond coat. Some consequences of this state will then be that enhanced oxidation and corrosion of coating, bondcoat and substrate may occur,

hot spots will be developed at the base of cracks where insulation is least and fuel ingress may lead to explosive failure of the coating on ignition.

The problem of transient compressive thermal stress causing spallation will of course be exacerbated by compressive residual stress although interfacial shear would be reduced. If the residual stress state is unknown or ignored, a coating which has been designed to operate successfully under well described conditions may fail inexplicably on its initial thermal cycle, simply because total compressive stress had exceeded the spallation strength of the coating or interfacial shear stresses had become too high.

6.4.2 Coating thermal conductivity.

On a macroscopic scale, modelling has shown that reductions in thermal conductivity of thermal barrier coating materials i.e. improving their insulation effectiveness, have important consequences for their practical use. As thermal conductivity is decreased, the temperature gradient across a given coating thickness increases, but of greater importance, front face temperatures rise at a greater rate than substrate temperatures decrease. The consequences of this behaviour were discussed in the previous section and suggest that for a given coating thickness, lower conductivity coatings will be subject to additional

transient tensile and compressive stress and steady state compressive stresses. Also an enhanced temperature gradient would be expected to increase the shear stress developed through the coating thickness.

On a microscopic scale, the effect of lower particle conductivity would also be felt. Simulation has shown that lower conductivity coating particles undergo less rapid initial cooling rates with two important consequences. First, the amount of time available for material flow before solidification occurred would be increased, allowing improved bonding and flow to minimise shrinkage cracking. Second, initial cooling rate and 'constant' temperature would be altered such that monoclinic phase would be more likely to form.

6.4.3 Coating specific heat capacity and density.

Of the two coating material properties considered in this section, only the former was found in simulations to have any effect on coating performance. Density variation of coating materials, by virtue of stabiliser composition at constant conductivity rather than conductivity changes associated with included porosity, was found to have no effect on insulation performance in model thermal barriers. In contrast, specific heat capacity of ceramic materials was found to have an important effect on transient heating rates of otherwise equivalent coatings. Final temperature

distributions were, however, identical.

As zirconia heat capacity was increased, so the time taken to achieve a static thermal gradient in the coating and substrate was also increased. This result would be expected to have two important consequences for coating behaviour. Of greatest significance, a reduction in heating rate would be expected to lower transient thermal stress during the heating cycle. Also, longer timescales during thermal transients in either direction would be expected to reduce required deformation rates in bondcoat layers, making them more effective in reducing mismatch stress at the ceraic/metal interface.

6.4.4 Substrate material.

Modelling of identical thermal barrier coatings deposited on various substrates was particularly instructive in that it highlighted the importance of two important substrate material properties. For the intermediate thickness coatings simulated, each achieved a similar temperature distribution over a similar timescale. From the temperatures of both substrate and coating, steady state and maximum transient mismatch strains were derived for each substrate (assuming it was rigid and bondcoat deformation did not occur) and these data are given in tables 6.3 and 6.4 respectively.

Examination of the data then shows that substrate/coating thermal expansion mismatch has important effects on induced stresses. In the steady state, substrates with intermediate expansion mismatch would be expected to develop the most easily supportable stress distributions in the absence of bondcoat deformation, with relatively small tensile and compressive stresses developed at the interface and coating surface respectively. Where the mismatch is low, high surface compressive stress may result in spallation. At the other extreme, high interfacial stress may lead to shear failure if sufficient stress relief by bondcoat deformation does not occur.

Transient behaviour in coatings of this thickness would tend to favour those materials with high mismatch particularly, because bondcoat deformation would be less likely to occur. As expansion differences are reduced, front face compressive stress may be sufficient once more to cause spallation. The second important substrate property is that of thermal conductivity. Where the conductivity of the metallic material is low, thermal gradients would develop through the substrate thickness, leading to differential expansion and possible buckling of the substrate. If this occurred, coatings might be subjected to high tensile stress leading to through thickness cracking.

6.4.5 Cooling of coating particles.

Cooling of impacted coating particles was investigated, both in terms of initial temperature and presence of existing particles, to determine the effect on cooling rates and the liklihood of monoclinic phase formation. For a single particle impacting with a plain aluminium substrate, both initial cooling rate and 'constant' temperature at the end of the rapid cooling phase were found to increase as particle temperature increased. Two competing considerations were identified which might affect the final phase structure of the particle. If initial cooling rates are raised, the liklihood of the diffusional cubic to transformable tetragonal reaction occuring is reduced in favour of the displacive cubic to non-transformable tetragonal reaction. However, as the onset temperature of slow cooling is also raised, the possibility of a destructive tetragonal to monoclinic reaction occuring is more likely for any transformable tetragonal material present. This is simply because that material is more likely to cool slowly through the important transformation temperature range and hence the reaction is less likely to be suppressed. One positive outcome of higher 'constant' temperature on impact is that flow in the particle is more likely to occur before solidification, reducing mismatch strain and probably improving inter particle bonding. Longer term cooling

of a single particle suggested that the substrate may be subjected to a heat pulse of a few seconds duration. While this is unlikely for a single particle impacting on a large high conductivity substrate, the situation may conceivably occur when a coating is rapidly deposited over the whole surface. The resultant expansion of the substrate would then be expected to cause significant damage within the ceramic layer. As the mismatch is at a maximum on impact of the first particle, (subsequent particles are increasingly shielded from the substrate by the thermal barrier effect), the damage caused would be localised at the site of maximum expansion mismatch during subsequent thermal cycling.

Modelling of an impacted particle with progressively increasing numbers of cool, underlying 'splats' highlighted other important effects. Because of the insulation effect of underlying particles, perhaps not surprisingly, initial cooling rates were greatest in the first particle to impact with the substrate. Subsequent material then cooled at progressively reduced initial, average rates, and 'constant' temperatures were also reduced with important implications for formation of non-transformable tetragonal (t') and monoclinic phases. Later particles were then less likely to form t' but suppression of the monoclinic transformation was more likely because the

constant temperature may well be below the transformation range. As the number of underlying particles increased, so the reheating effect on existing material is reduced. This would be expected to be beneficial in two ways. First expansion mismatches between coating layers would be reduced and second, the liklihood of reheating into the tetragonal to monoclinic transformation temperature range is reduced. In contrast, reduced heating would be expected to lower interparticle bond strengths.

In summary, it is apparent that the greatest damage and liklihood of formation of monoclinic material occurs with high temperature particles impacting on a bare substrate, although formation of transformable tetragonal phase itself is less likely.

6.5 Structure and stability of thermal barrier coating materials.

6.5.1 Structure of zirconia powders and as-deposited coatings.

Morphological differences between zirconia powders A and B, of ostensibly similar chemical composition, were undoubtedly responsible for variations in melting and deposit efficiency. Powder A, consisting of a wide size range of irregular particles, proved difficult to melt and deposit efficiently. Microstructural examination

showed occasional large part-melted particles of this material in coated testpieces. The wide size range also made it difficult to attain optimum injection conditions for all particles, resulting in a low deposit efficiency. In contrast, powder B, consisting of rounded agglomerates of fine particles confined to a relatively narrow size range, was melted more easily and efficiently and little unmelted material was observed. Despite improved deposition and melting properties, material B was found to be less satisfactory in terms of phase composition that material A. The as-supplied powder contained approximately 20% monoclinic phase and a very small amount of free yttria, presumably because sintering during manufacture was incomplete, and despite efficient melting during spraying, about 4% of the former phase was retained into the coating. The presence of monoclinic material was somewhat disconcerting because of its destructive effects during thermal cycling. The remaining constituents of coatings of material B were a majority of non-transformable tetragonal (t') phase together with cubic phase and a lesser proportion of transformable (t) tetragonal phase. Material A, in contrast, contained no monoclinic phase either before or after deposition. The majority phase after plasma spraying was again t', in greater proportion that in coatings of B, and with small,

roughly equal proportions of t and cubic phases. The lack of monoclinic phase before and after deposition may be attributed to efficient sintering during manufacture. Coatings of material A, despite poor deposit and melting efficiency, were considered preferable because of the absence of the destructive monoclinic/tetragonal phase transformation, at least initially, on subsequent thermal cycling.

6.5.2 Phase stability of heat treated zirconia coatings.

Usual observations of structural changes in heat treated thermal barrier coatings of materials A and B suggested that the former was generally more stable over the range of temperatures studied. For periods up to 100 hours, at temperatures up to 1000°C, the phase composition of coatings of material A was unchanged, and that of material B only slightly at the extreme. It is relatively safe to assume then that operation within these constraints would be entirely predictable in terms of phase changes, provided no other mechanism such as corrosive leaching of stabiliser were active.

As heat treatment temperatures were raised above 1000°C, significant structural changes were noted in free coating samples, for exposive times of less than 100H. At 1400°C, the highest temperature, such changes were noted after 30 minutes. Of the two materials,

coatings manufactured from material A appeared to retain their structural stability for longer periods than equivalent coatings of material B, except at 1400°C where changes were comparitively rapid in either case. The apparent greater stability of coatings of material A is attributed to the higher degree of chemical homogeneity and stabilisation prior to and after deposition. This is evidenced by the lack of monoclinic phase and small proportions of retained tetragonal (t) and cubic phases. Subsequent transformation by nucleation and growth would then be expected to be more difficult to initiate, conferring greater stability. Evidence gained from structural analysis suggests, however, that once transformation had begun, the rate of formation of equilibrium tetragonal (t) and cubic phases was higher in coatings of material A. This was only to be expected because the structure of coatings of material A consisted almost entirely of tetragonal (t') phase, and while more homogeneous, they were further from their equilibrium composition than equivalent coatings of material B. The driving force for transformation was therefore less in coatings of the latter. Further evidence for this effect is provided by the observation that the rate of formation of cubic phase in coatings of material A was about twice as fast as that for tetragonal (t) phase. In equivalent coatings of material B, the rates were

approximately similar.

Lattice parameter measurements from each of the tetragonal and cubic phases found in as sprayed and heat treated coatings were derived from high angle diffractometer traces. Within experimental error, lattice parameters were found to be relatively invariant with heat treatment temperature, even when structural transformations were occuring. That similar lattice parameters for each phase were obtained in each sample is of little interest because the recorded values were simply those attained during rapid cooling of the structure. Of greater importance, however, is the observation that where structural transformations were only partially completed, continuous ranges of phase composition were not detected. Two possible causes for this effect may be envisaged. Either the analysis technique is too insensitive to detect a range of phase compositions, or the amount of material of intermediate composition is too small to be detected. The former is characterised by scatter in deconvoluted data and a certain proportion was observed, although probably not enough to completely mask the effect of continuous composition variations.

Alternatively, diffusion in ceramic materials is known to be difficult and tetragonal precipitates are observed to form at intragranular sites with consequent relatively short diffusion distances, suggesting that

their formation is accompanied by a minimum of material of intermediate composition.

6.6 Design considerations for an optimum thermal barrier coating system.

Development of a successful zirconia thermal barrier coating system for aluminium substrates is possible provided the following requirements are met:

(i) Zirconia and bondcoat materials have stable and predictable behaviour throughout the operating cycle and coating lifetime.

(ii) Thermal gradients in the zirconia coating are minimised during the entire spray process.

(iii) Residual stresses in the zirconia coating are carefully controlled to reduce thermal stress and prevent failure during thermal cycling.

(iv) Transient and static thermal stress levels do not exceed the capabilities of the coating materials during the operating cycle.

The important parameters necessary to satisfy each requirement are summarised below.

6.6.1 Choice of coating materials.

Considering the zirconia coating first, pre-reacted materials enjoying a high degree of stabilisation are to be favoured. Their use is more likely to achieve structural stability at high temperatures and reduce

occurrences of the damaging monoclinic phase. A thorough evaluation of phase stability above and beyond the operating temperature and lifetime is obviously of paramount importance in determining the suitability of a candidate zirconia material.

Bondcoat materials should also be chosen carefully. Their ability to resist oxidation and corrosion at all temperatures should be considered, together with their ability to deform freely over the thermal cycle, under relatively low loads. The latter point is of particular importance for the substrate/coating combination chosen because the bondcoat layer must be able to relieve significant mismatch strains.

6.6.2 Minimisation of thermal gradients in zirconia layers during deposition.

If gross tensile and shear cracking is to be avoided during manufacture of thicker thermal barrier coatings, temperature gradients through the coating thickness must be carefully controlled. Results have shown that this may be achieved by air cooling, directed most effectively at the front face, during spraying. Avoidance of tensile cracking through the thickness on cooling after spraying may then be achieved by preventing the front face from cooling at a faster rate than the substrate, for example by reducing the air blast. thermal gradients during spraying may also be

minimised by adjustment of spray parameters, such that less heat is input to the coating. Increased workpiece/sprayhead relative velocity, spray distance and cooling time between layers of ceramic have all been shown to be effective in reducing coating front/back temperature gradient, although if the latter is too long, the boundaries between layers may become points of weakness.

6.6.3 Control of residual stress.

Investigation has shown that residual stress in zirconia coatings for the target substrate is generally compressive. This factor may be usefully employed in reducing tensile stress developed during thermal cycling, if the residual stresses can be controlled to produce the required distribution. Experience has shown that plasma spray parameters (in the absence of different substrate materials) are effective in altering residual stress and may be used to achieve the required level. Compressive residual stress can be reduced i.e. made more tensile, by employing air cooling, increasing workpiece/sprayhead relative velocity, spray distance, time delay between coating cycles and the thickness of the substrate. All of these parameters, except air cooling, are effective in reducing the front/back coating residual stress gradient as well. Interaction of compressive residual

stress with thermal transient and static stress is considered more fully in the next section, but suffice to say at this stage that large compressive stress distributions are to be avoided, particular in thicker coatings, because thermal transient stress may lead to spallation.

6.6.4 Control of transient and static thermal stress.

For a given set of material properties, the response of a zirconia thermal barrier coating to a thermal cycle depends on the thickness of the insulating layer and the presence of residual stresses.

During a rapid thermal transient for the 1mm thick model coating described earlier, the equivalent stress distribution is described by the sum of both transient and residual stresses, figure 6.8a. (Heating of the front face of the coating will have modified the room temperature residual stress distribution, raising compression at the front face.) If the compressive stresses developed are large enough, then spalling may result.

Once the static temperature gradient is established, the equivalent stress distribution without bond coat deformation is described by figure 6.8b. Again, residual stresses have been considerably modified by heating of the substrate and coating. The equivalent distribution illustrates that large tensile stresses

are developed in the coating and large shear stresses across the ceramic/substrate interface. Failure would then be expected to occur at the weaker location. Where a deformable bondcoat is present, the situation is considerably modified, leading to an equivalent distribution described by figure 6.8c. the presence of such a layer is then paramount in ensuring that the coating survives a thermal cycle.

Subsequent slow cooling from the static temperature accompanied by reverse bondcoat deformation would be expected to restore the coating system to the equivalent stress distribution described by figure 6.8a.

Rapid cooling preventing bondcoat deformation, or significant bondlayer oxidation would produce an equivalent stress distribution described by figure 6.8d. (Note that residual compressive stress is restored on cooling.) The large compressive stress distribution so developed would then be expected to result in spallation or interfacial shear failure, the latter site having been identified as probably the weakest area in the zirconia coating. Whereas in 1mm coatings, the combination of compressive residual and transient tensile stress effectively reduces the chances of failure, the same cannot be said for 5mm thick coatings. A rapid thermal transient in a 5mm thick model coating, would be expected to produce an

equivalent stress distribution described by figure 6.9. The combination of compressive residual and transient stresses must exceed the fracture strength of the coating leading to failure on the first thermal excursion, either by spallation or interfacial shear fracture, unless some form of compliance can be introduced into the system. Bondcoat deformation would be even less effective than in 1mm coatings because substrate temperatures would be lowered by the insulation effect of the coating.

Compliance may be introduced into the coating in the form of vertical crack networks, developed specifically during manufacture, leading to room temperature coatings with segmented microstructures. At room temperature, the appearance of the coating is described by figure 6.10a, with cracks separating islands of ceramic material attached to the substrate. During the heating transient, compressive strain is absorbed by the crack networks, figure 6.10b, preventing failure. In the steady state, the crack networks would tend to close at the outer face of the coating because expansion would be maximised at this location, figure 6.10c.

Material properties may be used to modify the response of zirconia coatings to thermal stress. Reduced porosity and therefore increased conductivity, while reducing insulation effectiveness, must reduce

both transient and static thermal stress. Also, coatings with high specific heat capacity should also be effective in reducing thermal transients because they take longer to achieve the final temperature distribution.

From these considerations, it is apparent that control of thermal stress is extremely important in achieving viable thermal barrier coatings. It is necessary to take into account the complete operating cycle of the coating system, the required degree of insulation and then tailor the properties of the coating accordingly while taking full account of residual stress distributions which exist in the system.

Chapter 7 - Conclusions.

7.1 Conclusions.

A consideration of the results and discussions described previously has identified a number of conclusions which can be drawn from this work.

(i) Residual stresses developed in zirconia thermal barrier coatings can be estimated reliably using the chemical dissolution technique described earlier.

(ii) Residual stress in the system studied i.e. zirconia on aluminium, originates in the differential contraction which occurs between coating and substrate on cooling, and is generally compressive.

(iii) The magnitude of the stress so determined depends on the measurement location in the thickness dimension. Residual stress at the exposed face of the coating is generally less compressive than that at the metal/ceramic interface. The origin of this variation lies in the through thickness temperature gradient which exists in the coating on completion of spraying.

(iv) Bondcoat layers have little effect on residual stress in zirconia coatings but do reduce the stress discontinuity at the interface between ceramic and substrate.

(v) Of the two zirconia materials studied, the material type had apparently no effect on residual stress in otherwise identical coatings.

(vi) Plasma spray parameters are effective in changing the magnitude and gradient of residual stress in thermal barrier coatings. Air cooling, increased time delay between coating cycles, workpiece/sprayhead relative velocity, spray distance, substrate thickness and coating thickness were all effective in making residual stress less tensile.

(vii) Tensile and shear cracks developed in thicker thermal barrier coatings were caused by excessive through thickness temperature gradients.

(viii) Residual stresses, developed in otherwise identical coatings deposited on different substrates, exhibit residual stresses which are directly related to the thermal expansion mismatch between coating and substrate.

(ix) The mathematical model of the plasma spray process, while limited in the thickness of coating simulated, was capable of correctly predicting changes in coating residual stress with air cooling, spray distance and substrate material.

(x) Modelling of transient heating of thermal barrier coatings has identified that increasing coating thickness and decreasing coating conductivity and specific heat capacity increase the liklihood of spallation on heating transients. Static tensile stresses were increased with reduced coating thickness and increased thermal conductivity and

substrate/coating thermal expansion mismatch. Static and transient thermal stresses were generally more tensile at the ceramic/metal interface than at the coating surface.

(xi) Modelling of rapidly cooled coating particles identified that impact of the first particles with the substrate, especially those with higher temperatures, was more likely to result in the formation of monoclinic phase and that contraction damage would be maximised at this location.

(xii) X-ray diffraction analysis of zirconia coatings identified that fully sintered zirconia materials were less likely to contain monoclinic phase after deposition and were more homogeneous.

(xiii) Analysis of heat treated coatings showed that those manufactured from pre-reacted materials were more stable at high temperature than equivalent coatings of part-reacted powder.

(xiv) Lattice parameter measurements demonstrated the absence of continuous ranges of phase composition in part-reacted zirconia coatings.

7.2 Suggestions for further work.

A number of possibilities exist for further investigation, including:

(i) Manufacture of thicker thermal barrier coatings on representative substrates using the design objectives

discussed in chapter 6.6, and subsequent analysis of residual stress distributions.

(ii) Development of apparatus to thermally cycle such coating/substrate combinations in a manner similar to that experienced in an operating diesel engine.

(iii) Analysis of the particular contribution of the bond layer to stress relief during thermal cycling, in particular relating to the effects on residual stress during the lifetime of such systems.

(iv) Analysis of heat-treated samples of alternative coating materials to determine their stability and phase transformation behaviour.

(v) Analysis of heat-treated samples using transmission electron microscopy to determine the fine structure of the transformations involved.

(vi) Allow the plasma-spray process model programs to run to completion, thus improving the applicability of the solutions obtained.

(vii) Develop three-dimensional simulations of the spray process, using finite element techniques, so that the model may improve its accuracy and usefulness in simulating actual component geometries.

Appendix.

Deconvolution of composite X-ray diffraction traces.

Diffraction traces obtained from zirconia coatings, in the range 72° to 77° of 2θ, may contain intensity data from as many as five separate reflections from three different phases. Overlapping of the intensity profiles or peaks from each reflection may serve to distort their shape/size and shift their observed angular position. In order that accurate analysis of phase composition may be carried out, it is therefore necessary to separate or deconvolute the composite trace into the component peaks due to each reflection.

The method described here attempts to replicate the original trace by summing an equivalent number of model intensity profile functions. An accurate simulation is obtained by systematically varying each of the function parameters by a small amount until the least squares difference between the original and simulated traces is minimised i.e. a non-linear least squares method is used. Each parameter is varied in turn about the current value by one iterative step size and the current value is only changed permanently if the increment/decrement produces a reduction in the sum of squares difference. The best fit is deemed to have been obtained when iterative variation of all of the current function parameter values produces an increase in the

sum of squares difference.

Once the original trace has been duplicated, each of the reflection peaks contained in it are described by the equivalent intensity profile functions which make up the simulated trace. It is then a simple matter to calculate the integrated intensity of each of the component peaks.

The success of this technique depends on a number of factors:

(i) The similarity between the actual reflection data and the model intensity profile function chosen to describe it.

(ii) The step size chosen for iterative variation of function parameters.

(iii) The presence of sufficient information in the composite trace to fix the number of original component peaks and therefore the number of profile functions used in the simulation.

(iv) Operation of the diffractometer in such a manner as to achieve maximum resolution.

(v) A high signal to noise ratio for the original trace.

Examination of the literature shows that the function most commonly used to describe a reflection intensity profile is the Gaussian distribution, [126,129,137]. In practice however, this distribution is too broad near the peak and too narrow at the tails, [138]. The

Pearson type VII distribution has been shown to be more accurate, [138], and the modified-Lorentzian form has been used successfully [131,132]. The form of this function was incorporated into the analysis program and is given below:

$$I = \frac{I_o}{[1 + C(2\theta - 2\theta_o)^2]^2} \qquad A1$$

$$C = \frac{4(\sqrt{2} - 1)}{H^2}$$

where I = Intensity at angular position 2θ

I_o = Maximum intensity at peak centre ($2\theta_o$)

2θ = Current angular position

$2\theta_o$ = Position of the peak centre

and H = Peak width at half maximum intensity

Iterative adjustment of the profile function parameters was confined to the position of the peak centre, $2\theta_o$, maximum intensity, I_o, and the peak width at half maximum intensity, H.

The apparatus used in this investigation employed Ni-filtered copper K_α radiation. The use of such an X-ray source results in a double intensity maxima, from the K_{α_1} and K_{α_2} components, for a given reflection, figure A1. The resulting peak is itself a distorted convolution of the two components, figure A2, and must be accounted for in the calculations. This is achieved in practice by calculating the intensity profile of a composite $K_{\alpha_1}/K_{\alpha_2}$ reflection, using the K_{α_1} peak as a reference. For the purposes of this analysis, the

maximum intensity of the K_{α_2} reflection was taken to be 50% of that of the corresponding K_{α_1} reflection. The wavelengths of each component are well documented, allowing the angular position of the K_{α_2} reflection to be derived from that of the corresponding K_{α_1} reflection using the following relationship.

$$\theta_{\alpha_2} = \sin^{-1}\left(\frac{L_{\alpha_2}\sin\theta_{\alpha_1}}{L_{\alpha_1}}\right) \qquad \underline{A2}$$

where L_{α_1} = Wavelength of K_{α_1}, 1.540562 A.

L_{α_2} = Wavelength of K_{α_2}, 1.544390 A.

θ_{α_1} = Bragg angle/2 for K_{α_1}

and θ_{α_2} = Bragg angle/2 for K_{α_2}

The peak width at half maximum intensity, H, for the K_{α_2} reflection was assumed to the same as that for K_{α_1}. Iterative adjustment of the profile function parameters was therefore confined to those describing the K_{α_1} reflection.

Finally, the practical diffractometer trace contains background noise which must be either removed or accounted for. In this analysis, the former was achieved by preprocessing the raw data to remove its contribution completely. The benefit of removing it before deconvolution is that the number of function parameters are minimised.

The choice of function parameter iterative step size is also of great importance and ultimately

represents a trade off between accuracy of fit and computation time. For example, if the step size is large, the best fit is more likely to lie between two successive parameter values, although the solution will be arrived at more quickly. Conversely, if the step size is small, then a more accurate fit is obtained at the expense of increased computation time. The scope for increased error or computation time is compounded with each additional reflection (up to a maximum of five in this case). In order to simplify the situation, the iterative step size for equivalent function parameters in different reflections was made the same. In contrast the step size adopted for each type of parameter was chosen to reflect its overall effect on the model function value.

If the original trace contains insufficient detail to specify the number of component reflections, then deconvolution becomes extremely difficult. The problem is not one of accuracy since if sufficient reflections are assumed, then a perfect fit to the original data may be obtained, although it may bear no relation to the true situation. In this instance the problem is described as ill-posed and an accurate solution cannot be obtained. This effect may be minimised by operating the diffractometer under conditions of maximum resolution to minimise the

amount of peak overlap. Specifically, this implies the use of narrow collimator slits and slow scanning to achieve maximum peak separation. The choice of reflection for analysis is also of great importance since the higher the value of 2θ, the greater the resolution.

Assuming that sufficient information is available to achieve a realistic analysis, the accuracy with which the original trace can be simulated depends on the amount of signal noise present in the trace. If a high noise level is present then important profile information may be masked to such an extent that a poor fit is obtained. Attaining a high signal to noise ratio depends on the counter/detector in the diffractometer receiving a maximum diffracted intensity. Unfortunately, this is at variance with the requirements for maximum resolution, particularly at higher values of 2θ where intensity is reduced. To a certain extent, this effect may be counteracted by increasing the counting time during the diffractometer scan, or employing multiple scan averaging techniques. Once again, the trade-off between accuracy and time must be optimised.

References.

1. Bryzik,W. and Kamo,R. 'TACOM/Cummins adiabatic engine program'. Paper SAE 830314, Society of Automotive Engineers Inc., 1983.

2. Kamo,R. and Bryzik,W. 'Cummins/TACOM advanced adiabatic engine program'. Paper SAE 840428, Society of Automotive Engineers Inc., 1984.

3. French,C.C.J. 'Ceramics in reciprocating internal combustion engines'. Paper SAE 841135, Society of Automotive Engineers Inc., 1984.

4. Kamo,R., Woods,M., Yamada,T. and Mori,M. 'Thermal barrier coating for diesel engine piston'. Paper ASME 80-DGP-14, American Society of Mechanical Engineers, 1980.

5. Kamo,R. and Bryzik,W. 'Ceramics for adiabatic turbocompound engine'. In: Army Materials Conference Series Vol.6; 'Ceramics for High Performance Applications III-Reliability', pp187-216, Plenum Press, 1983.

6. Marmach,M., Servent,D., Hanninck,R.H.J., Murray,M.J. and Swain,M.V. 'Toughened PSZ ceramics-their role as advanced engine components'. Metal Powder Report. 39, [1], pp7-12, 1984.

7. Woods,M.E. and Oda,I. 'PSZ ceramics for adiabatic engine components'. Paper SAE 820429, Society of Automotive Engineers Inc., 1982.

8. Kamo,R., Cheng,C. and Williamson,A.S. 'Advanced materials for improving diesel engine performance and emissions'. In: Proceedings of 1st Conference on 'Advanced Materials for Alternative Fuel Capable Directly Fired Heat Engines', Castine, Maine, 31st Jul-3rd Aug 1979, pp832-865. U.S Dept. of Energy.

9. Timoney,S. and Flynn,G. 'A low friction, unlubricated SiC diesel engine'. Paper SAE 830313, Society of Automotive Engineers Inc., 1983.

10. Walzer,P., Heinrich,H. and Langer,M. 'Ceramic components in passenger-car diesel engines'. Materials and Design, 7, [2], pp75-80, March-April 1986.

11. Parker,D.A. 'Ceramics technology-application to engine components'. Proc. Instn. Mech. Engrs., 199, [A3], pp135-150, 1985.

12. Kvernes,I. and Fartum,P. 'Use of corrosion-resistant plasma sprayed coatings in diesel engines'. Thin Solid Films, 53, pp259-269, 1978.

13. Guillemot,J.M., Dehaudt,P. and Ducos,M. 'Diesel engine combustion chamber insulation by ceramic plasma spraying'. In: 'Advances in Thermal Spraying'; Proceedings of the 11th International Thermal Spraying Conference, Montreal, Canada, Sept 8-12, 1986, pp513-521.

14. Carr,J. and Jones,J. 'Post densified chromia coatings for adiabatic engine'. Paper SAE 840433, Society of Automotive Engineers Inc., 1984.

15. Gasthuber,H. 'Plasma sprayed, zirconia based coating systems for automotive application'. In: Proceedings of 'Advanced Materials Research and Developments for Transport, Ceramic Coatings for Heat Engines', Strasbourg, France. Nov. 26-28, 1985, pp297-304. MRS-Europe.

16. Kvernes,I., Solberg,J.K. and Lillerud,K.P. 'Ceramic coatings on diesel engine components'. In: Proceedings of 1st Conference on 'Advanced Materials for Alternative Fuel Capable Directly Fired Heat Engines', Castine, Maine, 31st Jul-3rd Aug 1979, pp233-257. U.S Dept. of Energy.

17. Grosshans,G. and Guillemot,J.M. 'Insulation of the combustion chamber of marine diesel engines-theoretical and practical aspects'. In: Proceedings of 'Advanced Materials Research and Developments for Transport, Ceramic Coatings for Heat Engines', Strasbourg, France. Nov 26-28, 1985, pp305-312. MRS-Europe.

18. Tovell,J.F. 'Ceramics and the reciprocating internal combustion engine'. Materials and Design, 5, pp215-220, Oct/Nov 1984.

19. Scott,K.T. 'Plasma sprayed ceramic coatings'. Ceramic Surfaces and Heat Treatments. In: British Ceramic Proceedings, 34, pp195-206, Aug 1984.

20. Ingham,H.S. and Shepard,A.P. METCO Flame Spray Handbook, Vol. III, 'Plasma Flame Process'. METCO Inc., Long Island, New York, 1965.

21. Gerdeman,D.A. 'Arc plasma technology in materials science'. Publ. Springer Verlag, 1972.

22. Vardelle,A., Vardelle,M., McPherson,R. and Fauchais,P. 'Study of the influence of particle temperature and velocity distribution within a plasma jet coating formation'. In: 'General Aspects of Plasma Spraying', Proceedings of the 9th International Thermal Spraying Conference, The Hague, May 19-23, 1980, pp155-161.

23. Vardelle,A., Vardelle,M. and Fauchais,P. 'Influence of velocity and surface temperature of alumina particles on the properties of plasma sprayed coatings'. Plasma Chemistry and Plasma Processing, 2, [3], pp255-291, 1982.

24. Fauchais,P., Vardelle,A., Vardelle,P., Coudert,J.F. and Lesinski,J. 'Correlation of the physical properties of sprayed ceramic coatings to the temperature and velocity of the particles travelling in atmospheric plasma jets: measurements, modelling and comparison'.Thin Solid Films, 121, pp303-316, 1984.

25. Vardelle,A., Vardelle,M., Lombard,D., Gitzhofer,F. and Fauchais,P. 'Plasma spraying of zirconia stabilized with yttria or calcia; correlation of the spraying conditions to the thermophysical properties of the deposits'. In: Proceedings of 'Advanced Materials Research and Developments for Transport, Ceramic Coatings for Heat Engines', Strasbourg, France. Nov. 26-28, 1985, pp85-95. MRS-Europe.

26. Vardelle,M.,Vardelle,A. and Fauchais,P. 'Influence of the percentage of hydrogen and of the size and injection velocity distributions on the momentum and heat transfer between plasma jets and ceramic powders during plasma spraying process'. In: 'Advances in Thermal Spraying'; Proceedings of the 11th International Thermal Spraying Conference, Montreal, Canada, Sept 8-12, 1986, pp379-386.

27. Ducos,M. and Reitz,V. 'Coating properties and characteristics; optimization of the operation of a plasma generator for thermal spraying'. In: 'Advances in Thermal Spraying'; Proceedings of the 11th International Thermal Spraying Conference, Montreal, Canada, Sept 8-12, 1986, pp187-196.

28. Marijnissen,G. 'The influence of the powder characteristics of zirconia on the spraying process'. In: 'Advances in Thermal Spraying'; Proceedings of the 11th International Thermal Spraying Conference, Montreal, Canada, Sept 8-12, 1986, pp251-259.

29. Stecura,S. 'Effects of plasma spray parameters on two-layer thermal barrier coating life'. NASA report TM81724, 1981.

30. Hendricks,R.C. and McDonald,G. 'Effects of arc current on the life in burner rig thermal cycling of plasma sprayed zirconia-yttria'. Cer. Eng. Sci. Proc., pp737-743, Sept/Oct 1982.

31. Bennett,A. 'Properties of thermal barrier coatings'. Materials Science and Technology, 2, pp257-261, Mar 1986.

32. Stecura,S. 'Effects of yttrium,aluminium and chromium concentrations in bond coatings on the performance of zirconia-yttria thermal barriers'. Thin Solid Films, 73, pp481-489, 1980.

33. Miller,R.A., Argewal,P. and Duderstadt,E.C. 'Life modelling of atmospheric and low pressure plasma-sprayed thermal-barrier coating'. Cer. Eng. Sci. Proc., 5, [7-8], pp470-478, 1984.

34. Heuer,A.H. and Ruhle,M. 'Phase transformations in zirconia containing ceramics:1, the instability of c-zirconia and the resulting diffusion controlled reactions'. Advances in Ceramics Vol 12, Science and Technology of Zirconia II, pp1-13, 1985. Eds. Heuer,A.H., Claussen,N. and Ruhle,M. American Ceramic Society Inc.

35. Ruhle,M. and Heuer,A.H. 'Phase transformations in zirconia containing ceramics:2, the martensite reaction in t-zirconia'. Advances in Ceramics Vol 12, Science and Technology of Zirconia II, pp14-32, 1985. Eds. Heuer,A.H., Claussen,N. and Ruhle,M. American Ceramic Society Inc.

36. Subbarao,E.C. 'Zirconia-an overview'. Advances in Ceramics Vol 3, Science and Technology of Zirconia, pp1-23, 1981. Eds. Heuer,A.H. and Hobbs,L.W. American Ceramic Society Inc.

37. Stubican,V.S. and Ray,S.P. 'Phase equilibria and ordering in the system ZrO2-CaO'. J. Am. Cer. Soc., 60, [11-12], pp534-537, 1977.

38. Grain,C.F. 'Phase relations in the ZrO2-MgO system'. J. Am. Cer. Soc., 50, [6], pp288-290, 1967.

39. Scott,H.G. 'Phase relationships in the zirconia-yttria system'. J. Mat. Sci., 10, pp1527-1535, 1975.

40. Porter,D.L. and Heuer,A.H. 'Microstructural development in MgO-partially stabilised zirconia (Mg-PSZ)'. J. Am. Cer. Soc., 62, [5-6], pp298-305, 1979.

41. Garvie,R.C., Hanninck,R.H. and Pascoe,R.T. 'Ceramic steel?'. Nature, 258, pp703-704, 1975.

42. Porter,D.L. and Heuer,A.H. 'Mechanisms of toughening partially stabilised zirconia (PSZ)'. J. Am. Cer. Soc., 60, [3-4], pp183-184, 1977.

43. Lange,F.F. 'Transformation toughening'. J. Mat. Sci., 17, pp225-262, 1982.

44. Evans,A.G. 'Toughening mechanisms in zirconia alloys'. Advances in Ceramics Vol 12, Science and Technology of Zirconia II, pp193-211, 1985. Eds. Heuer,A.H., Claussen,N. and Ruhle,M. American Ceramic Society Inc.

45. Hanninck,R.H.J. and Garvie,R.C. 'Sub-eutectoid aged Mg-PSZ alloy with enhanced thermal up-shock resistance'. J. Mat. Sci., 17, pp2637-2643, 1982.

46. Lanteri,V., Heuer,A.H. and Mitchell,T.E. 'Tetragonal phase in the system ZrO2-Y2O3'. Advances in Ceramics Vol 12, Science and Technology of Zirconia II, pp118-130, 1985. Eds. Heuer,A.H., Claussen,N. and Ruhle,M. American Ceramic Society Inc.

47. Miller,R.A., Smialek,J.L. and Garlick,R.G. 'Phase stability in plasma sprayed zirconia-yttria'. Advances in Ceramics Vol 3, Science and Technology of Zirconia, pp241-255, 1981. Eds. Heuer,A.H. and Hobbs,L.W. American Ceramic Society Inc.

48. Kvernes,I. 'Coating of diesel engine components'. Coatings for High Temperature Applications, pp361-394, 1983. Ed. Lang,E. Applied Science Publishers.

49. Lugscheider,E., Eschnauer,B., Hauser,B. and Agethen,R. 'Influence of different plasma spray processes and various types of stabilised zirconia on the morphology of thermal barrier coatings'. In: 'Advances in Thermal Spraying'; Proceedings of the 11th International Thermal Spraying Conference, Montreal, Canada, Sept 8-12, 1986, pp261-268.

50. Mantkowski,T.E., Rigney,D.V., Froning,M.J., and Jayaraman,N. 'Characterisation of ZrO2-Y2O3 thermal spray powder systems'. In: Proceedings of 'Advanced Materials Research and Developments for Transport, Ceramic Coatings for Heat Engines', Strasbourg, France. Nov. 26-28, 1985, pp41-56. MRS-Europe.

51. Gitzhofer,F., Lombard,D., Vardelle,A.&M., Martin,C. and Fauchais,P. 'Thermophysical properties of zirconia coatings sprayed with calcia or yttria: influence of spraying parameters and heat treatment'. In: 'Advances in Thermal Spraying'; Proceedings of the 11th International Thermal Spraying Conference, Montreal, Canada, Sept 8-12, 1986, pp269-275.

52. Nicholl,A.R. 'Protective coatings and their processing-thermal spray'. In: Proceedings of Conference on 'High Temperature Materials and Coatings', Finland, June 24-29, 1984.

53. Fauchais,P., Coudert,J.F., Vardelle,A., Vardelle,M. and Lesinski,J. 'Diagnostics under thermal plasma conditions'. In: Proceedings of Materials Research Society Symposium, [30], pp37-51.

54. Wuest,G., Keller,S., Nicholl,A.R. and Donelly,A. 'Plasma spray deposition efficiencies'. J. Vac. Sci. Technology A, 3, [6], pp2464-2468, 1985.

55. Steffens,H.D. and Fischer,U. 'Processing of ceramic coatings'. In: Proceedings of 'Advanced Materials Research and Developments for Transport, Ceramic Coatings for Heat Engines', Strasbourg, France. Nov. 26-28, 1985, pp71-83. MRS-Europe.

56. Grisaffe,S.J., Levine,S.R. and Clark,J.S. 'Thermal barrier coatings'. NASA Tech. Memo. TM78848, 1978.

57. Shiembob,L.T., Stewart,O.L. and Bill,R.C. 'Development of sprayed ceramic seal system for turbine gas path sealing'. Paper ASME 78-WA/GT-7, American Society of Mechanical Engineers, 1978.

58. Berndt,C.C. and McPherson,R. 'The adhesion of flame and plasma sprayed coatings-a literature review'. AWRA report P11-1-78. Australian Welding Research, 6, pp75-85, 1979.

59. Chandler,P.E. 'Improving the bonding of plasma sprayed coatings'. Report TPRD/M/1473/N85, May 1985. Central Electricity Generating Board, U.K.

60. Becher,P.F., Rice,R.W., Wu,C.C. and Jones,R.L. 'Factors in the degradation of ceramic coatings for turbine alloys'. Thin Solid Films, 53, pp225-232, 1978.

61. Siemers,P.A. and Mehan,R.L. 'Mechanical and physical properties of plasma-sprayed stabilized zirconia'. Cer. Eng. Sci. Proc., pp828-840, Sept/Oct 1983.

62. Shankar,N.R., Berndt,C.C. and Herman,H. 'Failure and acoustic emission response of plasma sprayed ZrO2-8wt% Y2O3 coatings'. Cer. Eng. Sci. Proc., pp772-792, Sept/Oct 1982.

63. Berndt,C.C. and Herman,H. 'Anisotropic thermal expansion effects in plasma sprayed ZrO2-8% Y2O3 coatings'. Cer. Eng. Sci. Proc., pp792-801, Sept/Oct 1983.

64. Eaton,H.E. and Novak,R.C. 'A study of the effects of variations in parameters on the strength and modulus of plasma-sprayed zirconia'. Surface and Coatings Technology, 27, pp257-267, 1986.

65. Rangaswamy,S., Herman,H. and Safai,S. 'Thermal expansion study of plasma sprayed oxide coatings'. Thin Solid Films, 73, pp43-52, 1980.

66. Liebert,C.H. 'Emittance and absorbtance of the NASA ceramic thermal barrier coating'. Thin Solid Films, 53, pp235-240, 1978.

67. Morrell,P. and Taylor,R. 'Thermal diffusivity of thermal barrier coatings of ZrO2 stabilised with Y2O3'. High Temperatures, High Pressures, 17, pp79-88, 1985.

68. Pawlowski,L., Lombard,D., Tourenne,F., Kassabji,F. and Fauchais,P. 'Thermal diffusivity of plasma sprayed NiAl, NiCr, NiCrAl, NiCrAlY and NiCoCrAlY coatings'. High Temperatures, High Pressures, 17, pp611-625, 1985.

69. Hendricks,R.C., McDonald,G. and Mullen,R.L. 'Residual stress in plasma sprayed ceramic turbine tip and gas-path seal specimens'. Cer. Eng. Sci. Proc., pp802-809, Sept/Oct 1983.

70. Wilkes,K.E. and Lagedrost,J.F. 'Thermophysical properties of plasma sprayed coatings'. NASA report CR-121144, 1983.

71. Pawlowski,L., Lombard,D. and Fauchais,P. 'Structure-thermal properties relationships in plasma sprayed zirconia coatings'. J. Vac. Sci. Technology A, 3, [6], pp2494-2500, 1985.

72. Kvernes,I., Lugscheider,E. and Fairbanks,J. 'Potential of ceramic coating systems: engineering materials and technical aspects'. In: Proceedings of 'Advanced Materials Research and Developments for Transport, Ceramic Coatings for Heat Engines', Strasbourg, France. Nov. 26-28, 1985, pp13-22. MRS-Europe.

73. McPherson,R. 'The relationship between the mechanism of formation, microstructure and properties of plasma sprayed coatings'. Thin Solid Films, 83, pp297-310, 1981.

74. Chagnon,P. and Fauchais,P. 'Thermal spraying of ceramics'. Ceramics International, 10, [4], pp119-131, 1984.

75. Berndt,C.C. 'Determination of material properties of ceramic coatings'. In: 'Advances in Thermal Spraying'; Proceedings of the 11th International Thermal Spraying Conference, Montreal, Canada, Sept 8-12, 1986, pp149-158.

76. Andersson,C.A. 'Thermal stress fracture of ceramic coatings'. Fracture Mechanics of Ceramics Vol. 6., pp 497-509, 1983. Eds. Bradt,R.C., Evans,A.G., Hasselman,D.P.H. and Lange,F.F. Plenum Publishers.

77. Levine,S.R., Miller,R.A. and Stecura,S. 'Improved performance thermal barrier coatings'. In: Proceedings of NACE 6, Conference on High Temperature Corrosion, Mar 2-6, San Diego, California, 1981, pp621-627. National Association of Corrosion Engineers.

78. Kvernes,I. and Seiersten,M. 'Developments and problems in the use of thermal barrier coatings n metals'. In: Proceedings of NACE 6, Conference on High Temperature Corrosion, Mar 2-6, San Diego, California, 1981, pp615-620. National Association of Corrosion Engineers.

79. Restall,J.E. and Scott,K.T. 'Improved ceramic thermal barrier coatings for heat engines'. In: Proceedings of 'Advanced Materials Research and Developments for Transport, Ceramic Coatings for Heat Engines', Strasbourg, France. Nov. 26-28, 1985, pp93-108. MRS-Europe.

80. Fairbanks,J.W., Demeray,E. and Kvernes,I. 'Insulative, wear and corrosion resistant coatings for diesel and gas turbine engines'. In: Proceedings of 'Surface Engineering and Surface Modification of Materials', Les Arcs, France. July 3-15, 1983, pp524-545.

81. Mullen,R.L., McDonald,G., Hendricks,R.C. and Hofle,M.M. 'Correlation of compressive and shear stress with spalling of plasma sprayed ceramic materials'. Cer. Eng. Sci. Proc., pp810-818, Sept/Oct 1983.

82. Miller,R.A. 'Oxidation-based model for thermal barrier coating life'. J. Am. Cer. Soc., 67, [8], pp517-521, 1984.

83. Watson,J.W. and Levine,S.R. 'Deposition stress effects on the life of thermal barrier coatings in burner rigs'. Thin Solid Films, 119, pp185-193, 1984.

84. Hancock,P. 'Degradation processes for ceramic coatings'. In: Proceedings of 'Advanced Materials Research and Developments for Transport, Ceramic Coatings for Heat Engines', Strasbourg, France. Nov. 26-28, 1985, pp163-179. MRS-Europe.

85. Hendricks,R.C., McDonald,G. and Bill,R.C. 'Some inelastic effects of thermal cycling on ZrO2-Y2O3 materials'. Cer. Eng. Sci. Proc., pp750-757, Sept/Oct 1982.

86. Firestone,R.F., Logan,W.R., Adams,J.W. and Bill,R.C. 'Creep of plasma sprayed ZrO2 thermal barrier coatings'. Cer. Eng. Sci. Proc., pp758-771, Sept/Oct 1982.

87. Hendricks,R.C., McDonald,G. and Mullen,R.L. 'The effect of annealing on the creep of plasma sprayed ceramics'. Cer. Eng. Sci. Proc., pp819-827, Sept/Oct 1983.

88. Meetham,G.W. 'Coating requirements in gas turbine engines'. J. Vac. Sci. Technology A, 3, [6], pp2509-2515, 1985.

89. Kvernes,I., Johnson,M.P. and Burgel,R. 'Performance of thermal barrier coatings for diesel, stationary and aircraft gas turbine components'. In: Proceedings of 'Advanced Materials Research and Developments for Transport, Ceramic Coatings for Heat Engines', Strasbourg, France. Nov. 26-28, 1985, pp247-264. MRS-Europe.

90. Suhr,D.S., Mitchell,T.E. and Keller,R.J. 'Microstructure and durability of zirconia thermal barrier coatings'. Advances in Ceramics Vol 12, Science and Technology of Zirconia II, pp503-517, 1985. Eds. Heuer,A.H., Claussen,N. and Ruhle,M. American Ceramic Society Inc.

91. Miller,R.A., Garlick,R.G. and Smialek,J.L. 'Phase distributions in plasma sprayed zirconia-yttria'. Bull. Am. Cer. Soc., 62, [12], pp1355-1358, 1983.

92. Johner,G. and Schweizer,K.K. 'Flame rig testing of thermal barrier coatings and correlation with engine test results'. J. Vac. Sci. Technology A, 3, [6], pp2516-2524, 1985.

93. Bratton,R.J., Lau,S.K. and Lee,S.Y. 'Evaluation of present day thermal barrier coatings for industrial/utility applications'. Thin Solid Films, 73, pp429-437, 1980.

94. Sumner,I.E. and Ruckle,D. 'Development of improved durability plasma sprayed ceramic coatings for gas turbine engines'. Paper AIAA-80-1193, 1980.

95. Adam,P. and Johner,G. 'Thermal barrier coatings in aircraft engines-status and lines of development'. In: Proceedings of 'Advanced Materials Research and Developments for Transport, Ceramic Coatings for Heat Engines', Strasbourg, France. Nov. 26-28, 1985, pp265-287. MRS-Europe.

96. Vogan,J.W., Hsu,L. and Stetson,A.R. 'Thermal barrier coatings for thermal insulation and corrosion resistance in industrial gas turbine engines'. Thin Solid Films, 84, pp75-87, 1981.

97. Sachs,G. Z. Metallkunde., 19, pp352-357, 1927.

98. Sachs,G. and Espey,G. The Iron Age, 148, pp36, 1941.

99. Szieslo,U. 'Residual stresses within thermal sprayed layers'. In: Proceedings of the 10th International Thermal Spraying Conference, Essen, Germany, 1983, pp222-225.

100. Alekseev,V.V., Loskutov,V.S., Dekhtyar,L.I. and Khanin,A.Y. 'A method of determining residual stresses in plasma coatings'. Industrial Laboratory (trans. from Russian), 49, [11], pp1187-1189, 1983.

101. Barvinok,V.A. et al. 'Residual stresses in plasma coatings deposited on the internal surface of a ring'. Welding Production (trans. from Russian), 28, 5, pp11-13, 1981.

102. Cobb,R.J. Ph.D. Thesis, Nottingham University, 1987.

103. Mathar,J. Arch. Eisen-heutten, 6, pp277-281, 1932.

104. Pantucek,P. and Struth,U. 'Behaviour of thermal barrier and corrosion protective coating systems under combined thermal and mechanical loads (mechanical compatibility problems and potential solutions)'. In: Proceedings of 'Advanced Materials Research and Developments for Transport, Ceramic Coatings for Heat Engines', Strasbourg, France. Nov. 26-28, 1985, pp117-138. MRS-Europe.

105. Bialucki,P., Kaczmar,W. and Gladysz,J. 'Residual stress measurements of plasma sprayed coatings'. In: 'Advances in Thermal Spraying'; Proceedings of the 11th International Thermal Spraying Conference, Montreal, Canada, Sept 8-12, 1986, pp837-844.

106. Hasui,A. and Kitihara,S. 'On the residual stresses in sprayed coatings by plasma-jet'. Proceedings of the NRIM (Tokyo), June 10, 1966.

107. Baxter,C.F. Ph.D. Thesis, Bath University, 1976.

108. Chollet,L., Boving,H. and Hintermann,H.E. 'Residual stress measurement of refractory coatings as a non-destructive evaluation'. J. Materials for Energy Systems, 6, [4], pp293-299, 1985.

109. Tani,N., Ishida,T., Kawano,M. and Kamachi,K. 'X-Ray stress measurement of thermal sprayed coatings at elevated temperatures'. In: 'Advances in Thermal Spraying'; Proceedings of the 11th International Thermal Spraying Conference, Montreal, Canada, Sept 8-12, 1986, pp605-612.

110. Georgopoulos,P., Cohen,J.B. and Herman,H. 'Residual stress measurements of a plasma-sprayed coating system using synchrotron X-ray radiation'. Materials Science and Engineering, 80, ppL41-L43, 1986.

111. Rickersby,D.S., Bellamy,B.A. and Jones,A.M. 'Internal stress and microstructure of titanium nitride coatings'. Surface Engineering, 3, [2], pp138-146, 1987.

112. Pawlowski,L. 'Temperature distribution in plasma sprayed coatings'. Thin Solid Films, 81, pp79-88, 1981.

113. Dallaire,S. 'Influence of temperature on the bonding mechanism of plasma sprayed coatings'. Thin Solid Films, 95, pp237-244, 1982.

114. Pawlowski,L., Vardelle,M. and Fauchais,P. 'A model of the temperature distribution in an alumina coating during plasma spraying'. Thin Solid Films, 94, pp307-319, 1982.

115. Lee,D. 'A finite element modelling of the the low pressure plasma deposition process-II'. Int. J. Mech. Sci., 25, [8], pp553-563, 1983.

116. Tsibin,I.P, Kuznetsov,A.T., Shershnev,A.A, Kokushkin,I.V., Savel'chikova,I.Ya., Entin,E.P. and Mosin,E.F. 'Temperature and stressed and deformed state of refractory materials in plasma spraying'. Refractories (trans. from Russian), 25, [3-4], pp229-236, 1984.

117. El-keddah,N., McKelliget,J. and Szekely,J. 'Heat transfer and fluid flow in plasma spraying'. Metallurgical Transactions, 15B, pp59-70, 1984.

118. Eckold,G., Buckley-Golder,I.M. and Scott,K.T. 'Theoretical analysis of residual stresses in flame sprayed brittle materials'. Ceramics, Composites and Coatings - Recent developments and applications. Cafe Royal, London, Sept. 1987.

119. Apelian,D., Paliwal,M., Smith,R.W. and Schilling,W.F. 'Melting and solidification in plasma spray deposition-phenomological review'. International Metals Reviews, 28, [5], pp271-294, 1983.

120. Chaim,R., Ruhle,M. and Heuer,A.H. 'Microstructural evolution in a ZrO2-12wt% Y2O3 ceramic'. J. Am. Cer. Soc., 68, [8], pp427-431, 1985.
121. Yagi,T., Saiki,A., Ishizawa,N., Mizutani,N. and Kato,M. 'Analytical electron microscopy of yttria partially stabilised zirconia crystal'. J. Am. Cer. Soc., 69, [1], ppC3-C4, 1986.

122. Tremouilles,G., Derep,J.L. and Portier,R. 'Plasma coated metal-zirconia interface'. In: 'Advances in Thermal Spraying'; Proceedings of the 11th International Thermal Spraying Conference, Montreal, Canada, Sept 8-12, 1986, pp445-454.

123. Klug,H.P. and Alexander,L.E. 'X-Ray diffraction procedures for polycrystalline and amorphous materials'. John Wiley and Sons Inc., 1974.

124. Duwez,P. and Odell,F. 'Quantitative analysis of cubic and monoclinic zirconia by X-ray diffraction'. J. Am. Cer. Soc., 32, [5], pp180-184, 1949.

125. Garvie,R.C. and Nicholson,P.S. 'Phase analysis in zirconia systems'. J. Am. Cer. Soc., 55, [6], pp303-305, 1972.

126. Shankar,N.R., Berndt,C.C. and Herman,H. 'Phase analysis of plasma sprayed zirconia-yttria coatings'. Cer. Eng. Sci. Proc., 4, [9-10], pp784-791, Sept/Oct 1983.

127. Shankar,N.R., Herman,H., Singhal,S.P. and Berndt,C.C. 'Neutron and X-ray diffraction of plasma sprayed zirconia-yttria thermal barrier coatings'. Thin Solid Films, 119, [2], pp159-171, 1984.

128. Iwamoto,N., Umesaki,N. and Endo,S. 'Characterisation of plasma sprayed zirconia coatings by X-ray diffraction and Raman spectroscopy'. Thin Solid Films, 127, pp129-137, 1985.

129. Sone,I., Sisson,R.D. and Biederman,R.R. 'Quantitative phase analysis of partially stabilised zirconia-8.5% yttria by a random fitting least chi-squared method'. J. Vac. Sci. Technology A, 3, [6], pp2501-2502, 1985.

130. Evans,P.A., Stevens,R. and Binner,J.G.P. 'Quantitative X-ray diffraction analysis of polymorphic mixes of pure zirconia'. Br. Ceram. Trans. J., 83, [2], pp39-43, 1984.

131. Toraya,H., Yoshimura,M. and Somiya,S. 'Calibration curve for quantitative analysis of the monoclinic-tetragonal ZrO2 system by X-ray diffraction'. Comm. Am. Cer. Soc., C119-121, June 1984.

132. Toraya,H., Yoshimura,M. and Somiya,S. 'Quantitative analysis of monoclinic-stabilised cubic ZrO2 systems by X-ray diffraction'. Comm. Am. Cer. Soc., C183-184, Sept 1984.

133. Standard test method for moduli of elasticity and fundamental frequencies of carbon and graphite materials by sonic resonance. ASTM 17, C747-74, re-approved 1979, pp761-771. American Society for Testing of Materials.

134. Hardisty,H. 'An introduction to heat transfer'. University of Bath, School of Engineering, 1983.

135. Matveishin,E.N. and Kononov,G.V. 'Determination of some parameters of a spray-deposited metal layer'. Sov. Powder Metall. and Met. Ceram., 22, [3], pp191-194, 1983.

136. Cullity,B.D. 'Elements of X-Ray diffraction'. Second Edition, Addison-Wesley Publishing Co. Inc., 1978.

137. Paterson,A. and Stevens,R. 'Phase analysis of sintered yttria-zirconia ceramics by X-Ray diffraction'. J. Mater. Res., 1, [2], pp295-299, March-April 1986.

138. Hall,M.M., Veeraraghavan,V.G., Rubin,H. and Winchell,P.G. 'The approximation of symmetric X-ray peaks by Pearson type VII distributions'. J. Appl. Cryst., [10], pp66-68, 1977.

Table 1·1 Material properties of current metallic and candidate ceramic engine materials, after[3]

Material	Conductivity (k) W/m°C	Density (ρ) kg/m³ x 10³	Specific Heat (Cp) J/kg °C	Temperature Fluctuation Factor √kρCp	Expansion (α) °C⁻¹ x 10⁶	Strength N/m² x 10⁶	Youngs Modulus N/m² x 10⁹	Poisson Ratio	Weibull Modulus	Equivalent Tensile Strength N/m² x 10⁶	Fracture Toughness (Kic)	Fracture for a=10⁻⁴ N/m² x 10⁶	Allowable working Stress (MPa)	Hardness (Brinell) (K-Knoop)
Cast Iron (17)	54.4	7.2	480	13715	12	262 (UTS)	117			262			65	240
Steel (EN32)	50.2	7.87	485	13842	13	586 (UTS)	206	0.27		586			141	450-650
Nimonic (80A)	12.1	8.2	461	6763	13	1100 (UTS)	200			1100			330	200-370
Aluminium (LM27)	155	2.75	915	19749	21	150 (UTS)	71	0.32		150			45	100-150
Hot Pressed Silicon Nitride	25	3.19	710	7524	2.8	840 (3F)	310		15-20	486	5	350	54-108	1800
Reaction Bonded Silicon Nitride	5-10	2.5	710	4213	2.8	220 (3F)	164		15	120	2.3	133-175	14-28	1000
Syalon	18-20	3.2	710	6793	3.0	862 (3F)	288	0.23	10	452	7.7	350	53-106	2000
Reaction Sintered Silicon Carbide	20°C 104 600°C 39	2.98	710 1087	14869 11211	3.4	383 (4F)	332	0.13	10	209	4.9	343	30-60	1860(K)
Alpha Silicon Carbide	20°C 87 600°C 49	3.14	669 1120	13526 13179	4.0	459 (4F)	406	0.14	12.3	276	4.6	322	36-72	2800(K)
Partially Stabilised Zirconia.	2.0	5.78	543	2505	10.6	610 (4F)	200	0.3			9.5 4.6	665 322	49-98	1200(K)
Sprayed Zirconia	1.16	5.20	732	2100	8.0									400
Aluminium Oxide	2·73	3.3	1172	3251	8	380	360	0.27	10		5.85	409	25-50	1600
Sintered Silicon Nitride						742 385			21 12					

Table 2.1 Mechanical properties of plasma sprayed coating materials

Coating Composition (wt%)	Thickness (mm)	Elastic Modulus (GPa)	Poissons Ratio	Adhesive / Bond Strength (MPa)	Strain to Failure (%)	Tensile Strength (MPa)	Reference
7 Y_2O_3						115	51
8 Y_2O_3	0·38	3·4-6·9		30·5-39·8			62,69
12 Y_2O_3	0·38			36·5			61
20 Y_2O_3	2·54	19·8-469				14·5-53	64
						70	51
24MgO	0·4	4·7		22-25		80	48
	0·41	30·3			1·4[tension]		61
	0·41	34·6			0·78[comp.]		61
	1·5	46·2	0·076			33	61
		46	0·36				72
5 CaO						75-150	51

Table 2.1 (continued)

Coating Composition (wt%)	Thickness (mm)	Elastic Modulus (GPa)	Poissons Ratio	Adhesive / Bond Strength (MPa)	Elongation (%)	Tensile Strength (MPa)	Reference
Ni + 22Cr	2·3	198(20°C)					61
+10Al+ 1Y		130(800°C)					
					0	960(600°C)	
					34	365(750°C)	
					275	69 (900°C)	

Table 2·2 Thermal properties of plasma sprayed coating materials

Coating Composition (wt%)	Thickness (mm)	Porosity (%)	Density $x10^{-3}$ (kgm^{-3})	Specific Heat ($Jkg^{-1}K^{-1}$)	Thermal			Emittance / Absorptance	Reference
					Conductivity ($Wm^{-1}K^{-1}$)	Diffusivity (m^2s^{-1})$x10^{-7}$	Expansion (K^{-1})$x10^{-6}$		
$6Y_2O_3$	0·19		6·0			3·0 - 5·5			67
$7Y_2O_3$		6·9-9·6	5·5-5·6			2·8 - 4·0	9·8-10·8		51
	0·3		5·5		1·0 - 1·2	3·1 - 3·6			71
	1·0		5·5		0·8 - 0·95	2·2 - 3·2			71
$8Y_2O_3$	0·28-0·3		5·7 - 5·9			2·0 - 3·0			67
	0·5						10·0		63
	0·6		5·17		0·98-1·09	3·3			61
	1·0		5·2 - 5·4		0·7 - 1·2	2·0 - 3·8			71
$10Y_2O_3$	0·17		5·86			2·5 - 3·5			67
$12Y_2O_3$	0·15-0·19		5·82			1·5 - 3·0			67
	0·15							0·73 - 0·42	66
	0·6		4·43		0·65 - 0·73	2·6 - 2·63			61

Table 2·2 (continued)

Coating Composition (wt%)	Thickness (mm)	Porosity (%)	Density $x10^{-3}$ (kgm^{-3})	Specific Heat ($Jkg^{-1}K^{-1}$)	Thermal			Emittance / Absorptance	Reference
					Conductivity ($Wm^{-1}K^{-1}$)	Diffusivity (m^2s^{-1})$x10^{-7}$	Expansion (K^{-1})$x10^{-6}$		
$12Y_2O_3$			4·97-5·04	445-650	1·9		10·34		70
	0·76							0·6-0·27	66
$20Y_2O_3$		8·2	5·45			2·5-3·5			
							9·8-10·2		70
	0·76-1·7						10·59		65
	1·0	20·0	4·7		0·25-0·4	1·0-1·5			71
24MgO	0·4	2·5-4·0			1·5-2·4		9·0		48
			4·32	640-670	0·78		9·0		72
5CaO		6·9-9·0	5·23-5·25			2·5-5·7	9·0-10·2		51
			4·36-4·4	475-700	0·45		10·25		70
	0·76-1·7						9·53		65
Ni-Cr-Al-Y	0·32		7·0-7·5			35-45	13·5		68

Table 2·3 Characteristics of the available techniques for measuring residual stress in porous ceramic thermal barrier coatings

Test technique	Testpiece relevant to application	Localised test area	Preparation damage to coating	Unintentional modification of properties	Strain/ Depth data	Destructive	Other
Boring out (Sachs)	No	No	No	Yes	Yes	Yes	
Grinding/Turning	Cylinder liner	No	Yes	Yes	Yes	Yes	
Electropolishing	Cylinder liner	No	No	Yes	Yes	Yes	
Gauge / Spray	Yes	No	No	No	Yes	No	Rotation difficult
Hole drilling	Yes	Yes	Yes	Yes	Yes	Yes	
Dissolution	Flat surfaces	No	Removed	No	Surface	Yes	
Strip deflection	Flat surfaces	No	No	No	No	No	Average values
X-Ray diffraction	Yes	Yes	No	No	No	No	Limited depth

Table 2·4 A comparison of the results obtained from alternative formulae for calculating coating composition from integrated intensity X-ray data, after [130].

Equation	% Cubic phase	% Monoclinic phase
Actual composition	60	40
2·9	63·3	36·7
2·12	64·0	36·0
2·14	72·5	27·5
2·15	62·2	37·8

Table 3.1 Chemical composition and particle size analysis of zirconia - 8wt% yttria powder A.

Chemical Analysis	Weight %
Al_2O_3	0.10
CaO	0.06
Fe_2O_3	0.14
MgO	0.34
SiO_2	0.38
TiO_2	0.19
Y_2O_3	7.87
ZrO_2	90.92

Microns	% Passing
176	100.0
125	99.4
88	88.7
62	73.8
44	45.7
31	19.9
22	8.7
16	1.5
11	1.5
7.9	0.6
5.5	0.0

Table 3.2 Chemical composition and particle size analysis of zirconia - 8wt% yttria powder B.

Chemical Analysis	Weight %
Y_2O_3	8.0
ZrO_2	92.0

Particle Size	(μm)
Minimum	20
Average	40
Maximum	80

Table 3.3 Chemical composition and particle size analysis of bondcoat alloy.

Chemical Analysis	Weight %	
	Min	Max
Al	4.5	7.5
Mn		3.0
C		0.3
Si		2.0
Cr	15.5	21.5
Fe		1.5
Organic Solids		3.5
Ni	69.5	

Microns	Weight %
+150	1
+125	10
-45	20

Table 3.4 Coating deposition parameters for zirconia - 8wt% yttria powder materials A and B.

Plasma	
Gun	METCO 3MB, GH nozzle
Voltage (V)	65
Current (A)	500
Pressure (MPa)	Argon = 0.70, Hydrogen = 0.35
Flowrate (Scfm)	Argon = 80, Hydrogen = 15
Distance (mm)	Variable
Cooling	(when used)
Distance (mm)	40, Front and/or Backface
Delivery (lmm-1)	100
Powder Feed	
System	Plasma-Technik Twin 10
Carrier Gas	Argon
	Powder A Powder B
Feed Rate (gmin-1)	90.0 55.0
Pressure (MPa)	0.225 0.25
Flow (lmin-1)	3.5 3.5

N.B. Powder feed rates for each powder chosen to give similar coating thickness.

Table 3.5 Coating deposition parameters for bondcoat.

Plasma	
Gun	METCO 3MB, GH nozzle
Voltage (V)	65
Current (A)	500
Pressure (MPa)	Argon = 0.70, Hydrogen = 0.35
Flowrate (Scfm)	Argon = 80, Hydrogen = 15
Distance (mm)	Variable
Cooling	(when used)
Distance (mm)	40, Front and/or Backface
Delivery (lmm-1)	100
Powder Feed	
System	Plasma-Technik Twin 10
Carrier Gas	Argon
Feed Rate (gmin-1)	40
Pressure (MPa)	0.30
Flow (lmin-1)	3.0

Table 3.6 Etching media for substrate and bondcoat removal.

Substrate	Solution	Molarity (M)	Bondcoat
Aluminium	Sodium Hydroxide	2	Not Etched
Copper	Ferric Chloride	Conc.	Etched
Mild Steel	Hydrochloric Acid	Conc.	Etched

Table 3.7 Summary of surface preparation conditions.

Grit Blasting	
Medium	Coarse Brown Alumina
Air Pressure (psi)	40
Separation (cm)	30
Duration (s)	30
Cleaning/Degreasing	
Method	Ultrasonic
Medium	Methanol
Duration (min)	10
Drying	Hot Air

Table 3.8 Summary of zirconia coating spray parameters.

Set No.	Powder Type	Substrate Material	Substrate Thickness (mm)	Spray Distance (mm)	Relative Velocity (ms^{-1})	No. of Cycles	Coating Thickness (mm)	Bond-coat (Y/N)	Air Cooling Site
1	A,B	Al	3.5	80	0.3	3	0.35	Y	Back
	A,B	Al	3.5	80	0.5	5	0.35	Y	Front
2	A	Al	3.5	110	0.2	2	0.2	Y	Comb.
	A	Al	3.5	110	0.5	5	0.2	Y	Comb.
3	A	Al	3.5	110	0.2	4	0.45	Y	Comb.
	A	Al	3.5	110	0.2	8	0.7	Y	Comb.
	A	Al	3.5	110	0.2	12	0.9	Y	Comb.
	A	Al	3.5	110	0.2	16	1.2	Y	Comb.
4	A	Al	3.5	110,65	0.1	1	0.2,0.3	Y	Comb.
	A	Al	3.5	110,65	0.2	2	0.2,0.3	Y	Comb.
	A	Al	3.5	110,65	0.3	3	0.2,0.3	Y	Comb.
	A	Al	3.5	110,65	0.4	4	0.2,0.3	Y	Comb.
	A	Al	3.5	110,65	0.5	5	0.2,0.3	Y	Comb.
5	B	Al	3.5	80	0.1-0.5	1,3,5	0.35	Y	None
	B	Al	3.5	80	0.1-0.5	1,3,5	0.35	Y	Back
	B	Al	3.5	80	0.1-0.5	1,3,5	0.35	Y	Front
	B	Al	3.5	80	0.1-0.5	1,3,5	0.35	Y	Comb.
[1]	A,B	Al	3.5	80	0.3	3	0.35	N	Back

Table 3.8 Continued.

Set No.	Powder Type	Substrate Material	Substrate Thickness (mm)	Spray Distance (mm)	Relative Velocity (ms^{-1})	No. of Cycles	Coating Thickness (mm)	Bond-coat (Y/N)	Air Cooling Site
6	A	Al,Cu,Fe	1.85-1.51	65	0.2	2	0.3	Y	Comb.
	A	Al,Cu,Fe	3.50-3.24	65	0.2	2	0.3	Y	Comb.
	A	Al,Cu,Fe	11.9-13.2	65	0.2	2	0.3	Y	Comb.
7	C1-C3	Al,Fe	3.5	75	0.5	10	1.0	Y	None
	C1-C3	Al,Fe	3.5	75	0.5	20	2.0	Y	None
[2]	C1-C3	Al-Fe	3.5	75	0.5	30	3.0	Y	None

[1] Samples used for XRD analysis.

[2] Feed rates for powders C1-C3 were adjusted to give 0.1mm of zirconia per spray cycle.

Table 3.9 Typical material properties of substrate materials.

Material	M.Pt. (°C)	Expansion Coeff. ($K^{-1}x10^{-6}$)	Conductivity ($Wm^{-1}K^{-1}$)	Density (Kgm^{-3})	Specific Heat ($JKg^{-1}K^{-1}$)
Aluminium	660	23	180	2800	880
Copper	1080	17	385	8930	385
Steel	1500	12	63	7860	420

Table 3.10 Thickness ranges of substrate materials.

Material	Thickness Range (mm)		
	1	2	3
Aluminium	1.8	3.5	13.1
Copper	1.75	2.9	12.9
Steel	1.5	3.2	11.9

Table 3.11 Preparation method for microstructural examination.

Equipment	Struers Automatic
Mounting Medium	Epoxy Resin
Grinding Medium	Silicon Carbide
Lubricant	Water
Procedure	
120 Grade,	150N, 300rpm, 30 seconds, wash
220 Grade,	150N, 300rpm, 30 seconds, wash
500 Grade,	150N, 300rpm, 30 seconds, wash
1000 Grade,	150N, 300rpm, 30 seconds, wash ,dry
Polishing Medium	Diamond
Lubricant	DP Blue (alchohol based)
Procedure	
6 μ, Pan-W,	150N, 150rpm, 30 seconds, wash, dry
3 μ, Pan-W,	150N, 150rpm, 30 seconds, wash, dry
1 μ, DP Mol,	150N, 150rpm, 30 seconds, wash, dry

Table 3.12 Summary of heat treatment program for coating samples examined by X-ray diffraction.

Treatment Temperature (°C)	Duration (H)
800	20, 50, 100
900	20, 50, 100
1000	20, 50, 100
1100	1, 2, 5, 20
1200	1, 2, 5, 20
1300	1, 2, 3
1400	0.5, 1, 2

Samples received one treatment only, were inserted into furnace at treatment temperature and were rapidly cooled in still air.

Table 4.1 Typical material property data for model substrate and bondcoat.

Material	Thickness (mm)	Density (Kgm^{-3})	Conductivity ($Wm^{-1}K^{-1}$)	Specific Heat ($JKg^{-1}K^{-1}$)
Aluminium	10	2800	180	880
Zirconia	3	4000	0.5	500

Table 4.2 Steady state convective heat transfer conditions in operating engine.

Position	Gas Temperature (°C)	Heat Transfer Coeff. ($Wm^{-2}K^{-1}$)
Ceramic Face	800	100
Substrate Face	20	1000

Table 4.3 Typical material property data for alternative metallic substrates.

Material	Density (Kgm^{-3})	Conductivity ($Wm^{-1}K^{-1}$)	Specific Heat ($JKg^{-1}K^{-1}$)
Steel	7860	63	420
Copper	8930	385	385

Table 4.4 Material property data used in plasma spray process model.

Material	Conductivity ($Wm^{-1}K^{-1}$)	Density (Kgm^{-3})	Specific Heat ($JKg^{-1}K^{-1}$)	Emissivity
Aluminium	180	2800	800	0.3
Steel	63	7860	420	0.4
Copper	385	8930	385	0.4
Bondcoat	75	7500	380	0.7
Zirconia	[1]	4000	[2]	0.65

Where:

$$[1] = 0.651 - (8.465\times10^{-4}Tk) + (1.719\times10^{-6}Tk^2) - (1.420\times10^{-9}Tk^3) + (4.678\times10^{-13}Tk^4)$$

Tk = Temperature in K

$$[2] = 500 + 0.2147Tc$$

Tc = Temperature in °C

Table 4.5 Fixed deposition parameters used in plasma spray process model.

Deposition Parameter		Value
Start Position	- Radius (mm)	165
	- Angle (°)	0
Point of interest	- Radius (mm)	125
	- Angle (°)	0
Centre Position	- Radius (mm)	85
	- Angle (°)	0
Table Revolutions/Direction		20
Traverse Rate/Direction ($mm.rev^{-1}$)		4
Powder Feed Rate (Kgs^{-1})		$1.0x10^{-3}$
Ceramic 'Splat' Thickness (μm)		2

Table 4.6 Zirconia plasma spray parameters for process model.

Spray Parameter	Value
Relative Velocity (ms^{-1})	0.5
Spray Distance (mm)	75
Deposit Efficiency (%)	20

Table 5.1 Calculated values of residual strain and stress, developed in model coatings deposited with and without air cooling.

Cooling Conditions	In-plane Strain ($x10^{-3}$)	In-plane Stress (MPa)	Perpendicular Stress (MPa)
Cooled	-3.06	-122.4	61.2
Uncooled	-3.42	-137.0	68.5

Table 5.2 Calculated values of residual strain and stress, developed in model coatings deposited with increasing spray distance.

Spray Distance (mm)	In-plane Strain ($x10^{-3}$)	In-plane Stress (MPa)	Perpendicular Stress (MPa)
75	-3.06	-122.4	61.2
100	-2.56	-102.0	51.0
125	-1.99	-79.6	39.8

Table 5.3 Calculated values of residual strain and stress, developed in model coatings deposited with increasing workpiece/sprayhead relative velocity.

Relative Velocity (ms^{-1})	In-plane Strain ($x10^{-3}$)	In-plane Stress (MPa)	Perpendicular Stress (MPa)
0.3	-3.06	-122.4	61.2
0.4	-3.06	-122.4	61.2
0.5	-3.06	-122.4	61.2

Table 5.4 Calculated values of residual strain and stress, developed in identical model coatings deposited on different substrate materials.

Substrate Material	Expansion Coefficient ($x10^{-6}\ K^{-1}$)	In-plane Strain ($x10^{-3}$)	In-plane Stress (MPa)	Perpendicular Stress (MPa)
Steel	12	-0.31	-12.4	6.2
Copper	17	-1.52	-60.8	30.4
Aluminium	23	-3.06	-122.4	61.2

Table 5.5 Low-angle, X-Ray relative integrated intensity data from constituent phases of different forms of material B.

Material Form	Monoclinic Intensity	Cubic/Tetragonal Intensity
Powder	20.5	79.5
As-sprayed	4.0	96.0
Heat Treated [1]	4.0	96.0

[1] 1400°C for 2 hours.

Table 5.6 Phase composition of powder and as-sprayed coatings, determined by X-Ray diffraction analysis.

Phase	Average Mole Fraction			
	Material A		Material B	
	Powder	As-sprayed	Powder	As-sprayed
Monoclinic	0	0	0.18	0.03
Cubic	0.26	0	0.48	0.38
Tetragonal (t)	0.11	0	0	0
Tetragonal (t')	0.63	1.00	0.34	0.59

Table 5.7 Angular position and lattice parameters of constituent phases of coatings of materials A and B.

Material A

Reflection	Angular Position (2θ)	Lattice Parameter (nm)	Side
t_{400}	74.46-74.66	50.81-50.93	a_t
t'_{400}	74.15-74.31	51.01-51.11	$a_{t'}$
f_{400}	73.84-74.10	51.14-51.29	a_f
t'_{004}	73.20-73.39	51.56-51.68	$c_{t'}$
t_{004}	-	-	c_t

Material B

Reflection	Angular Position (2θ)	Lattice Parameter (nm)	Side
t_{400}	74.39-74.49	50.91-50.97	a_t
t'_{400}	74.17-74.30	51.02-51.10	$a_{t'}$
f_{400}	73.81-74.05	51.17-51.31	a_f
t'_{004}	73.25-73.56	51.46-51.65	$c_{t'}$
t_{004}	73.03-73.25	51.65-51.78	c_t

Table 6.1 Expansion mismatch strains, developed under steady state conditions in model thermal barrier coatings of increasing thickness. Strain values are relative to the substrate and no allowance for bondcoat deformation or other yielding was included.

Coating Thickness (mm)	Temperature (°C)			Expansion Strain ($x10^{-3}$)			Mismatch Strain ($x10^{-3}$)		Strain Gradient (mm^{-1})
	Subst.	Ceramic Rear	Ceramic Front	Subst.	Ceramic Rear	Ceramic Front	Rear/ Subst.	Front/ Subst.	Front/ Rear
1	295	295	380	6.785	3.186	4.104	3.599	2.681	0.918
3	240	240	440	5.520	2.592	4.752	2.928	0.768	0.720
5	220	220	500	5.055	2.376	5.400	2.684	-0.345	0.605

Table 6.2 Expansion mismatch strains, developed under maximum transient conditions in model thermal barrier coatings of increasing thickness. Strain values are relative to the substrate and no allowance for bondcoat deformation or other yielding was included.

Coating Thickness (mm)	Temperature (°C)			Expansion Strain ($x10^{-3}$)			Mismatch Strain ($x10^{-3}$)		Strain Gradient (mm^{-1})
	Subst.	Ceramic Rear	Ceramic Front	Subst.	Ceramic Rear	Ceramic Front	Rear/ Subst.	Front/ Subst.	Front/ Rear
1	113	113	223	2.608	1.225	2.404	1.383	0.204	1.179
3	81	81	243	1.858	0.873	2.623	0.985	-0.765	0.583
5	38	38	253	0.879	0.413	2.732	0.466	-1.853	0.464

Table 6.3 Expansion mismatch strains, developed under steady state conditions in identical 3mm thick model thermal barrier coatings on different substrates. Strain values are relative to the substrate and no allowance for bondcoat deformation or other yielding was included.

Substrate Material	Temperature (° C)			Expansion Strain ($x10^{-3}$)			Mismatch Strain ($x10^{-3}$)		Strain Gradient (mm^{-1})
	Subst.	Ceramic Rear	Ceramic Front	Subst.	Ceramic Rear	Ceramic Front	Rear/ Subst.	Front/ Subst.	Front/ Rear
Steel	240	240	440	2.880	2.592	4.752	0.288	-1.872	0.720
Copper	240	240	440	4.080	2.592	4.752	1.488	-0.672	0.720
Aluminium	240	240	440	5.520	2.592	4.752	2.928	0.768	0.720

Table 6.4 Expansion mismatch strains, developed under maximum transient conditions in identical 3mm thick model thermal barrier coatings on different substrates. Strain values are relative to the substrate and no allowance for bondcoat deformation or other yielding was included.

Substrate Material	Temperature (°C)			Expansion Strain ($x10^{-3}$)			Mismatch Strain ($x10^{-3}$)		Strain Gradient (mm^{-1})
	Subst.	Ceramic Rear	Ceramic Front	Subst.	Ceramic Rear	Ceramic Front	Rear/ Subst.	Front/ Subst.	Front/ Rear
Steel	81	81	243	0.970	0.873	2.623	0.097	-1.653	0.583
Copper	81	81	243	1.374	0.873	2.623	0.501	-1.249	0.583
Aluminium	81	81	243	1.858	0.873	2.623	0.985	-0.765	0.583

Fuel energy=100%

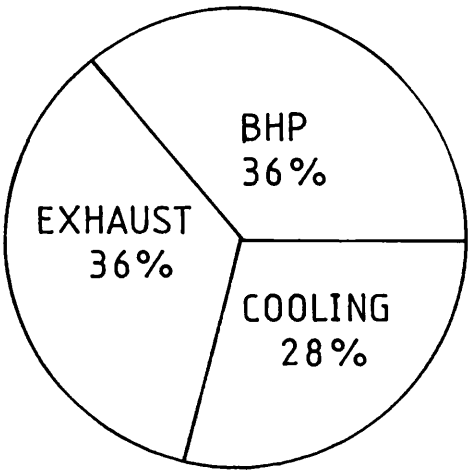

Conventional turbocharged
Diesel engine

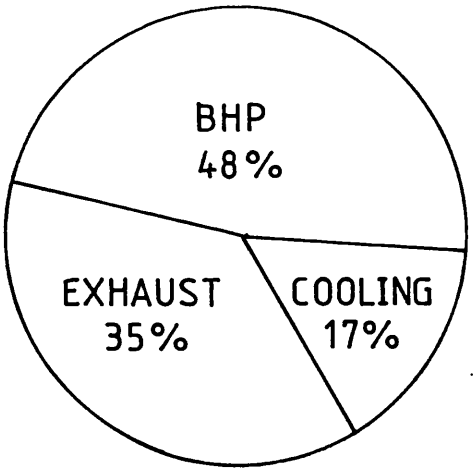

Insulated, turbocharged,
turbocompounded Diesel engine

Figure 1·1 Energy balance diagrams for conventional and insulated, advanced Diesel engines, after [1]

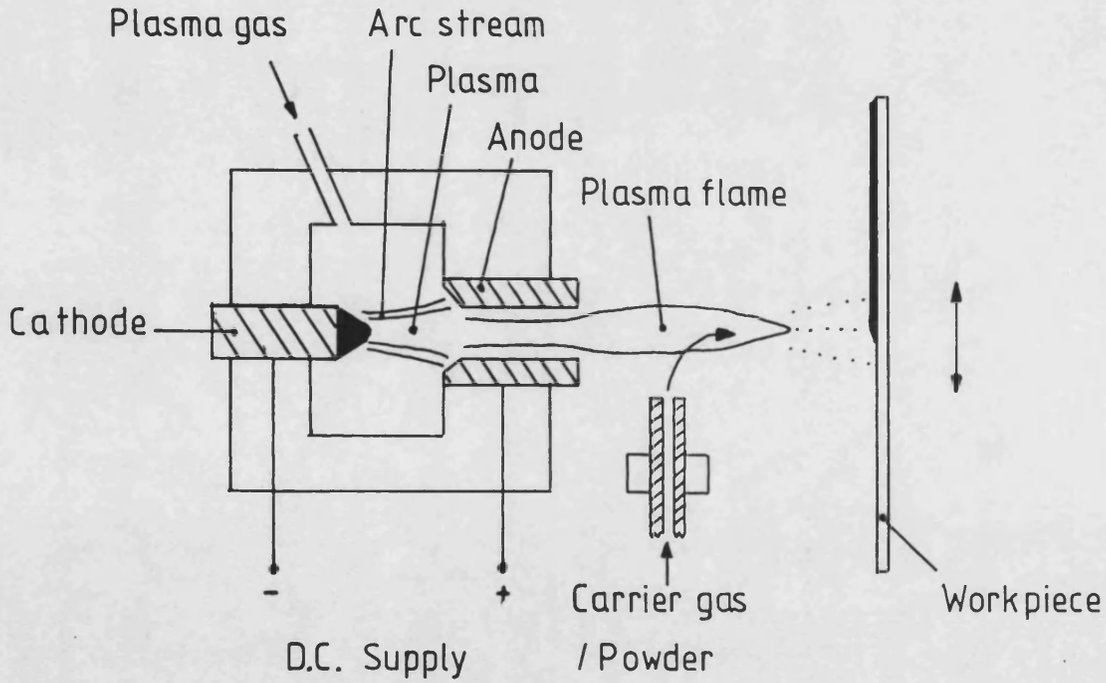

Figure 2·1 Simplified schematic diagram of a plasma spray gun after [20]

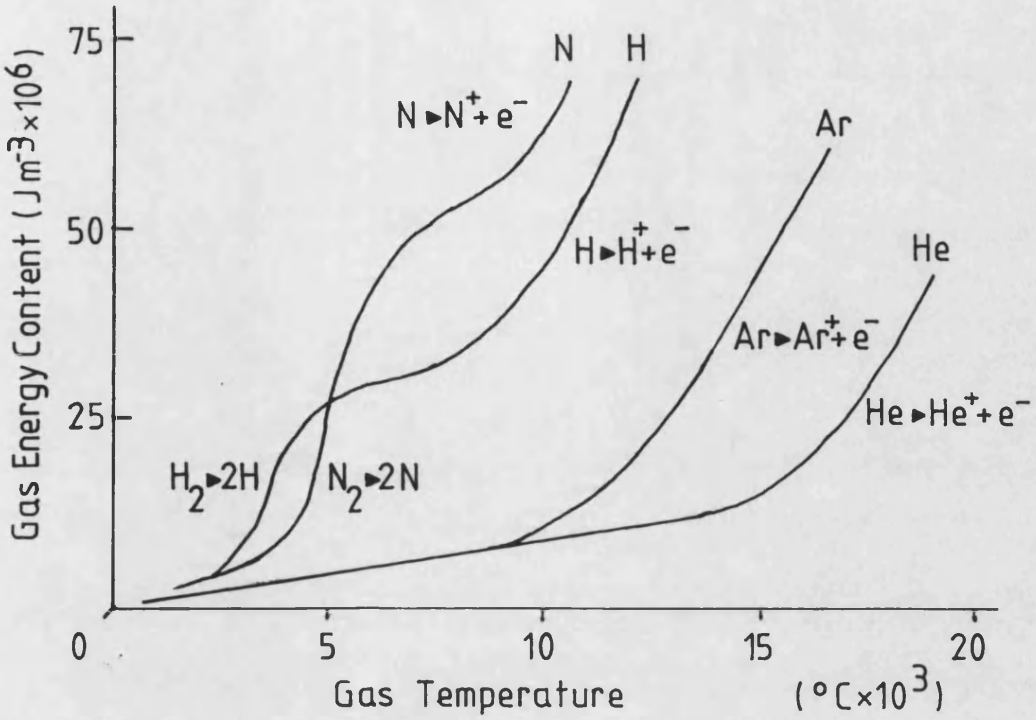

Figure 2·2 Plasma temperature as a function of gas energy content for typical plasma gases, after [20].

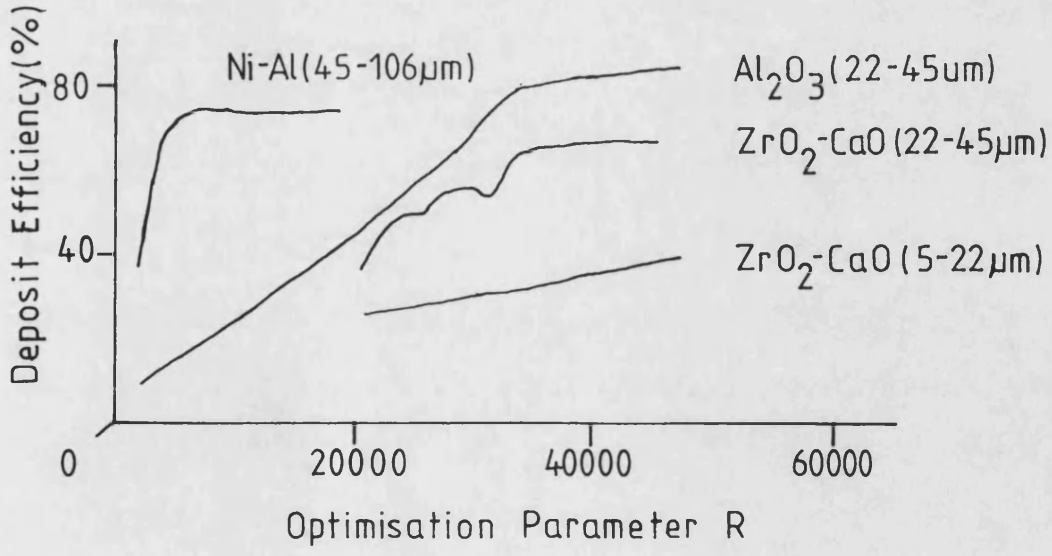

Figure 2·3 Graph illustrating the improvement in deposit efficiency with increasing R parameter, after [27]

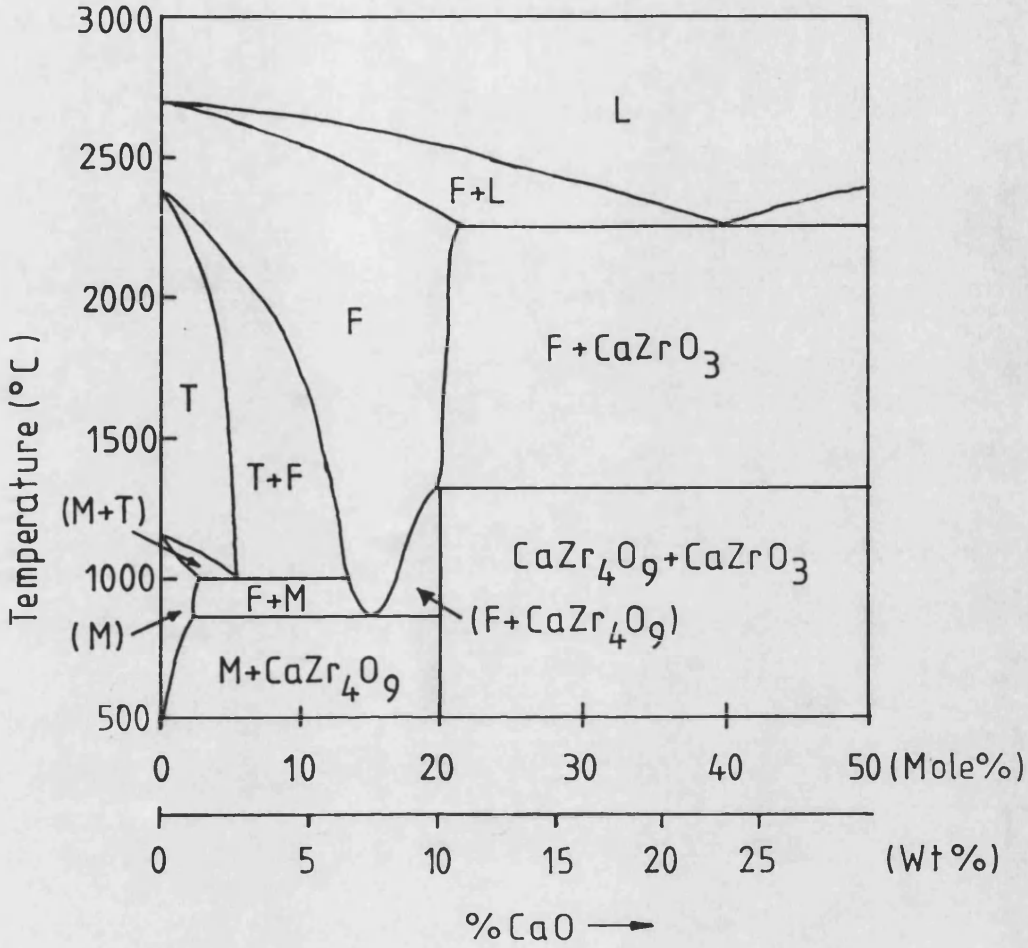

Figure 2·4 ZrO_2-CaO phase diagram, after [37]

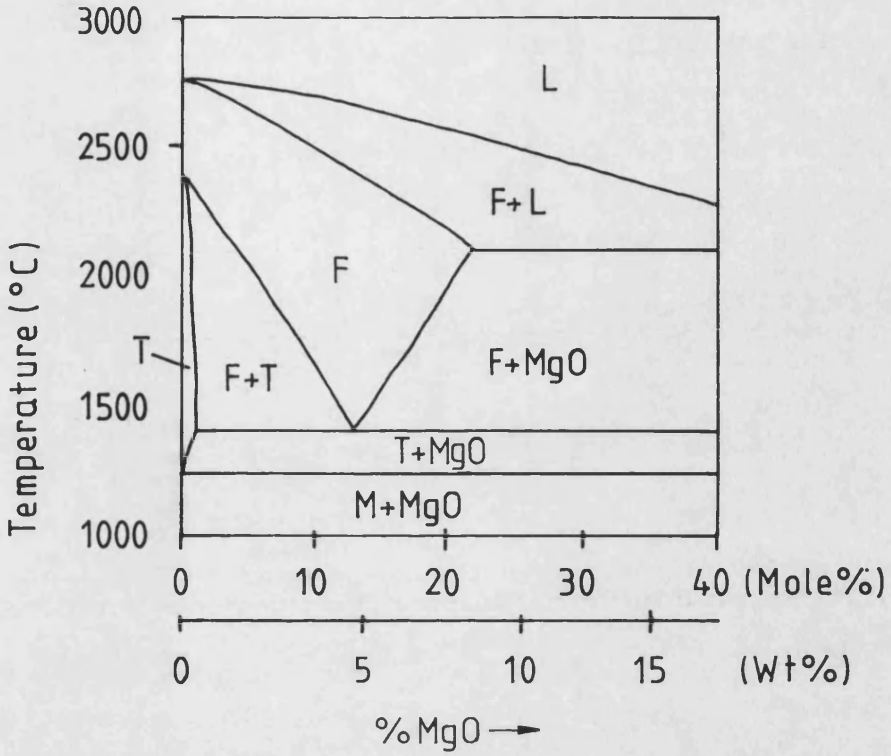

Figure 2·5 ZrO_2-MgO phase diagram, after[38]

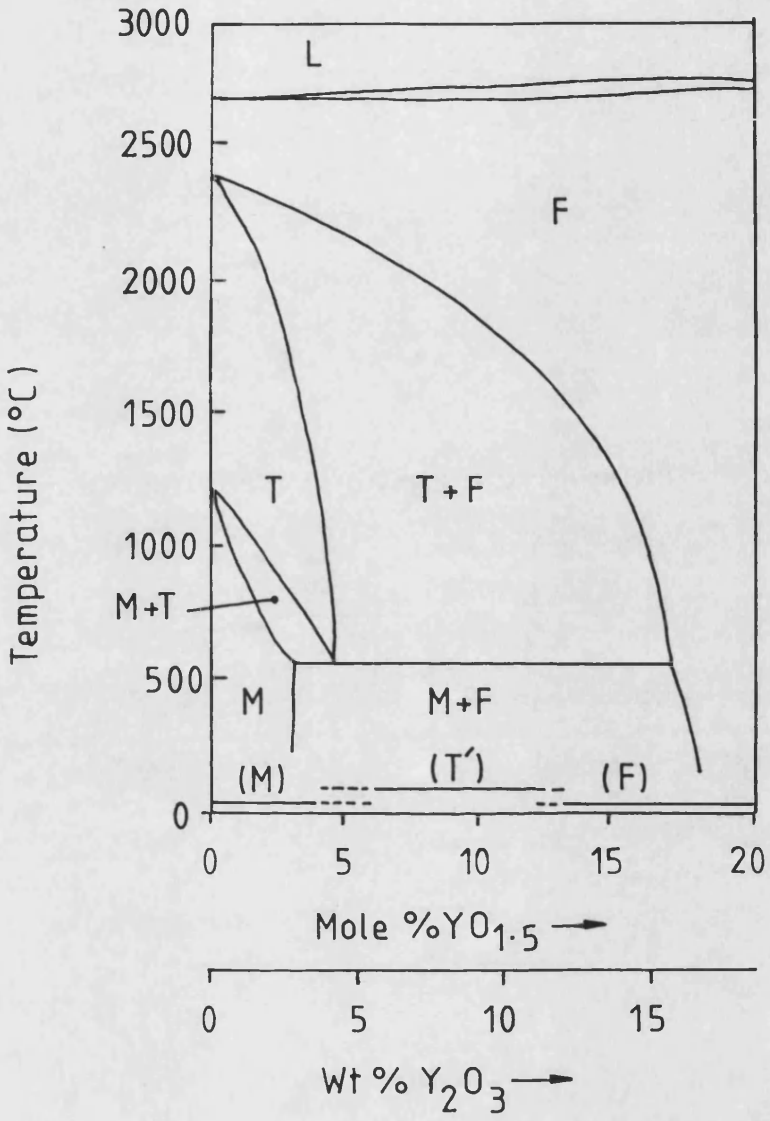

Figure 2·6 ZrO_2-Y_2O_3 phase diagram, after [39]

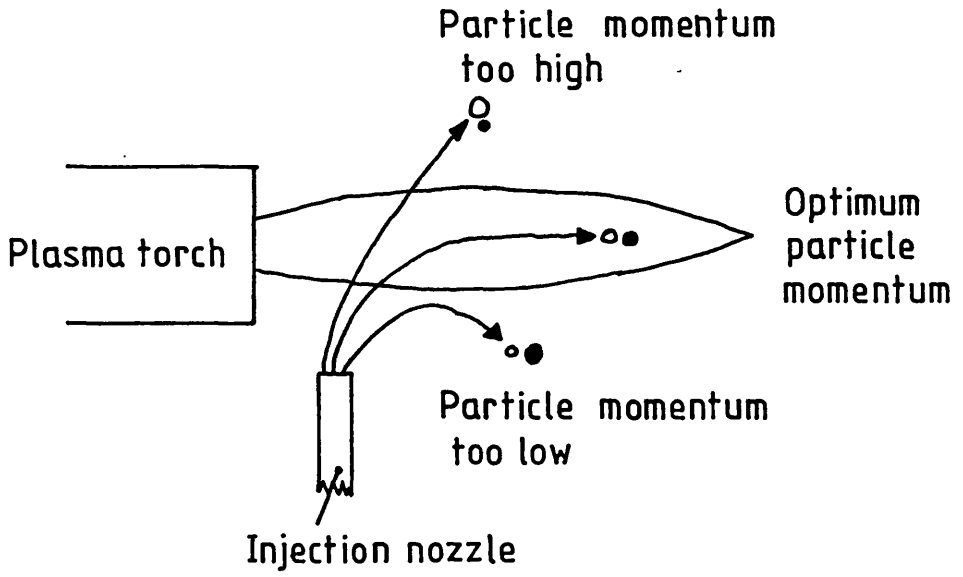

Figure 2·7 Diagram illustrating the effect of particle momentum on trajectory and hence melting efficiency.

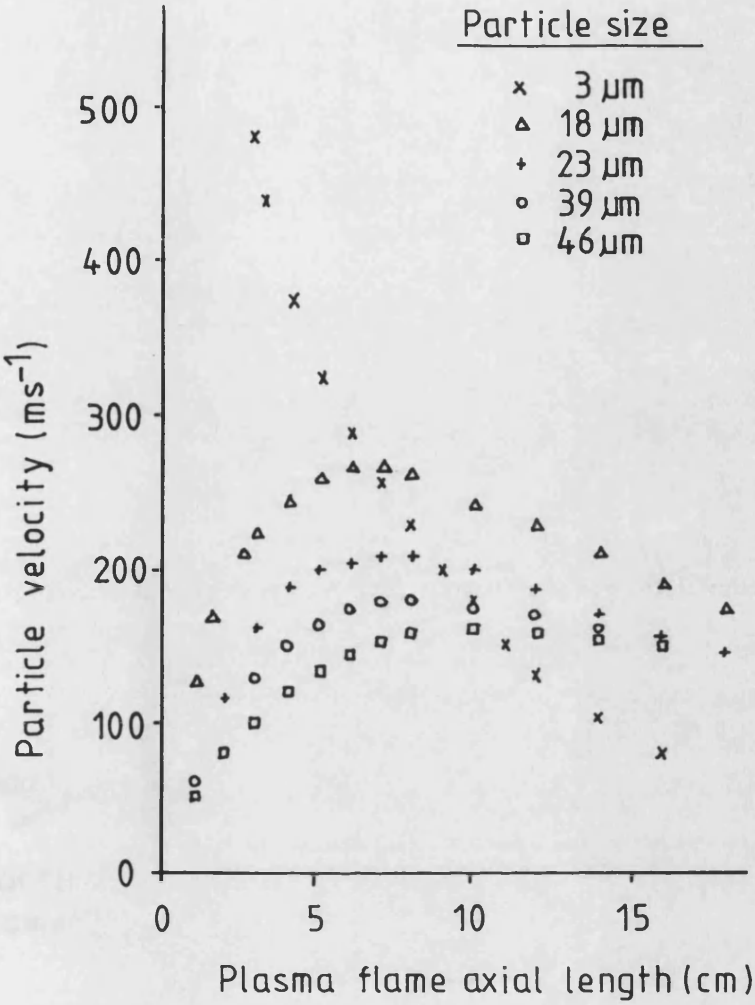

Figure 2·8 Measured velocity of alumina particles of varying sizes along the central axis of a 29kW N_2-H_2 plasma flame, after[23].

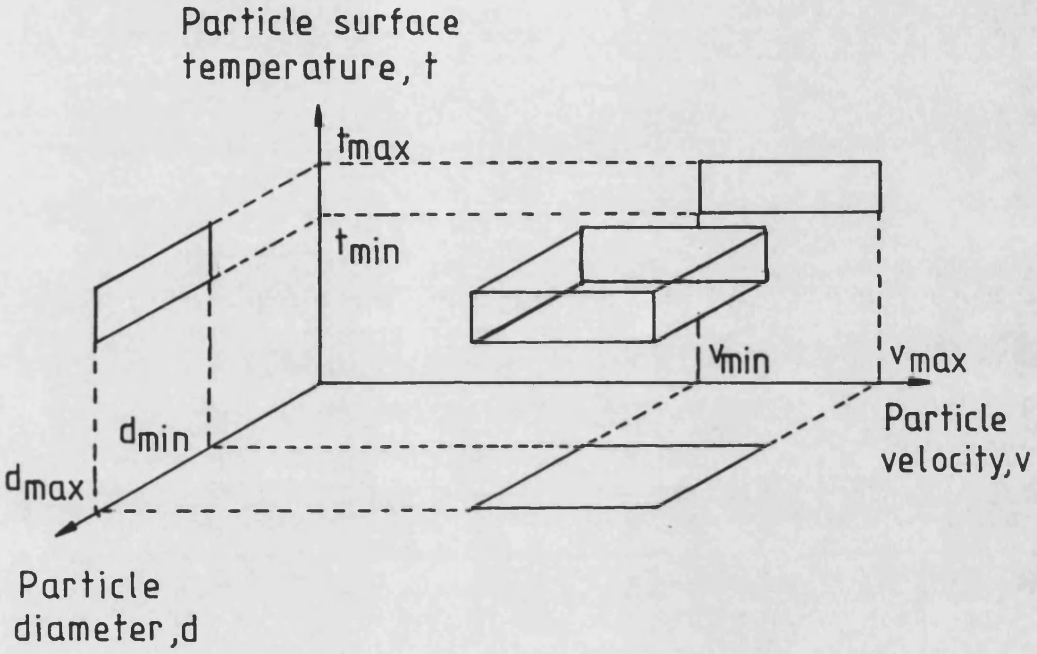

Figure 2·9 Diagram illustrating the conditions necessary for complete melting of powder particles injected into a plasma flame, after [53].

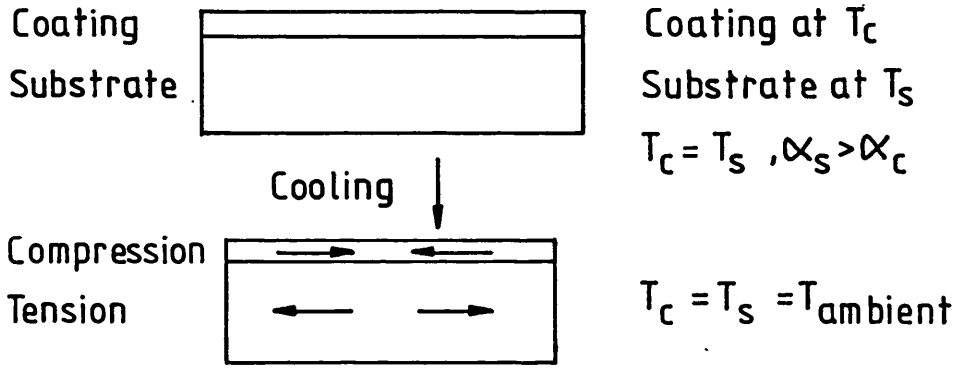

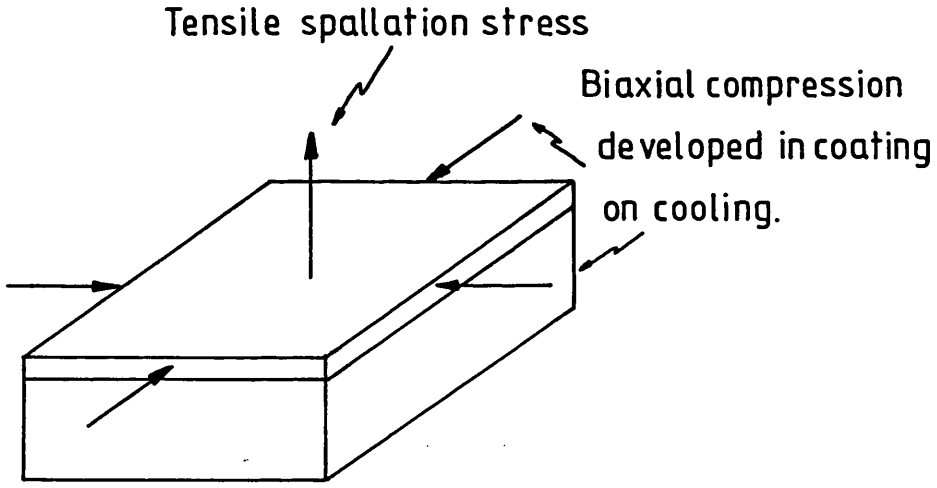

Figure 2·10 Diagram illustrating the development of tensile spalling stresses in thermal barrier coatings deposited on high expansion substrates.

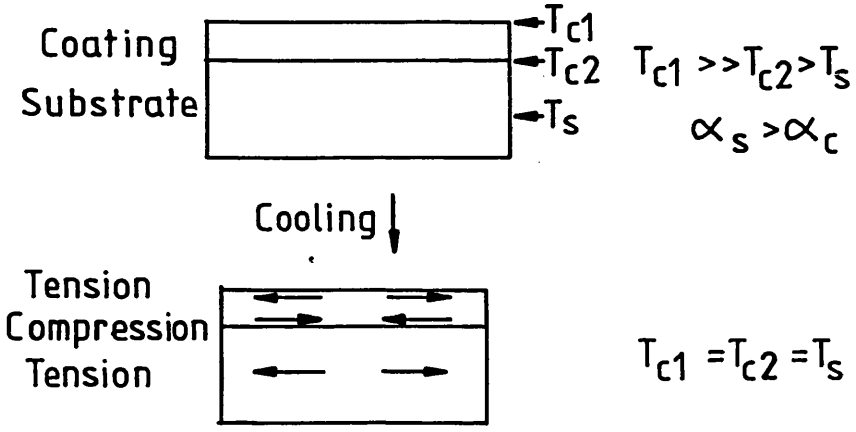

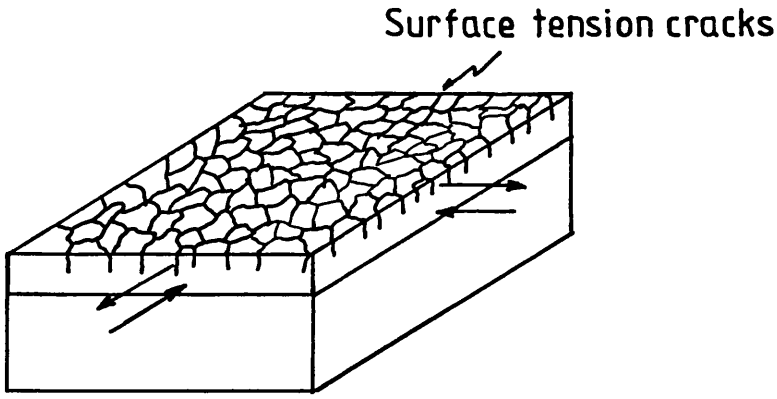

Figure 2·11 Diagram illustrating the development of surface tensile stress and subsequent cracking in thicker coatings subject to large through-thickness temperature gradients during deposition.

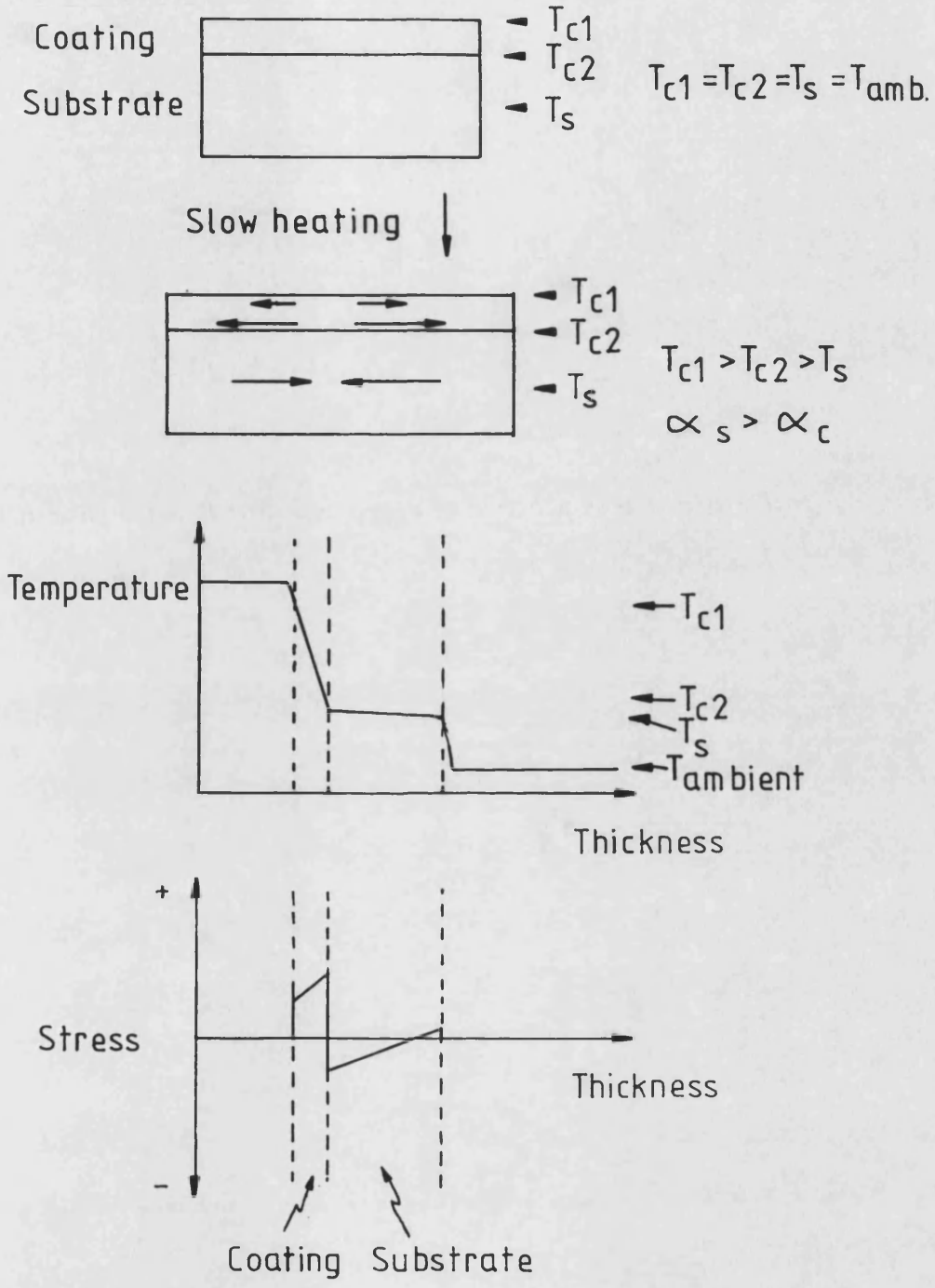

Figure 2·12 Diagram illustrating the stresses generated in a thermal barrier coating slowly heated to its operating temperature.

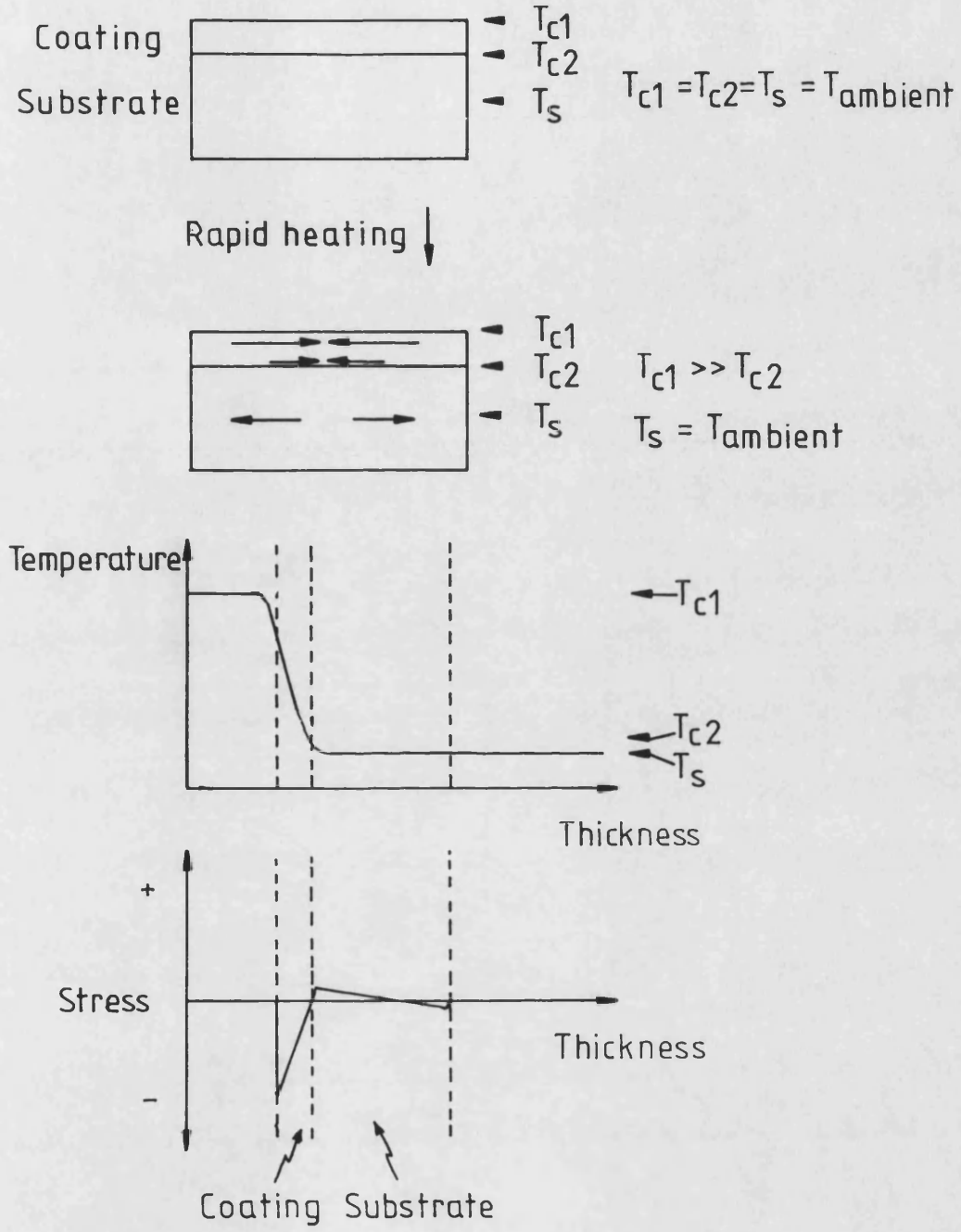

Figure 2·13 Diagram illustrating the stresses generated in a thermal barrier coating subjected to a rapid heating cycle.

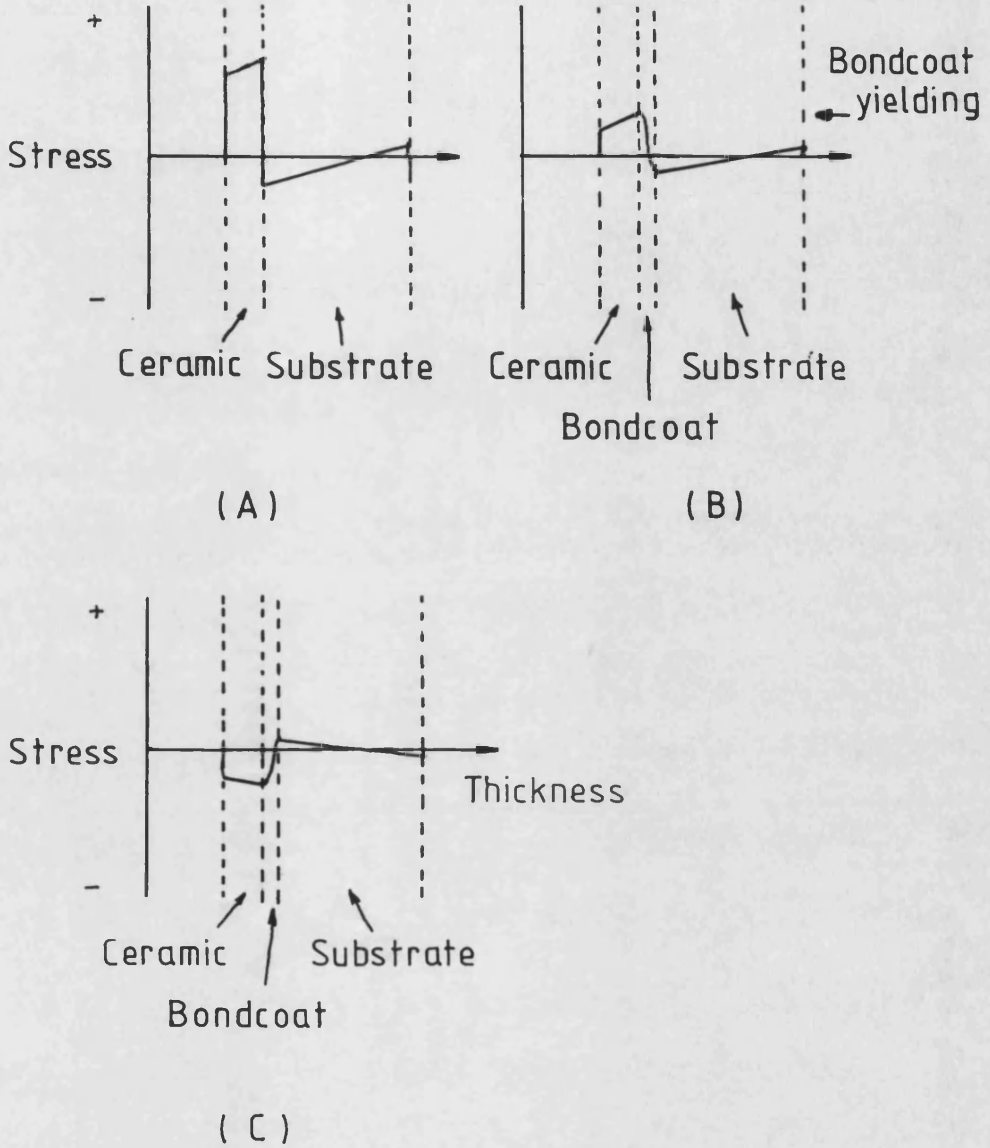

Figure 2·14 Diagrams illustrating the in-plane stresses developed when:

(A) a simple coating on a high expansion substrate is slowly heated.

(B) a two layer coating, similarly heated, undergoes bondcoat plastic deformation.

(C) the bondcoat layer in B is rapidly cooled or oxidised preventing reverse deformation on cooling.

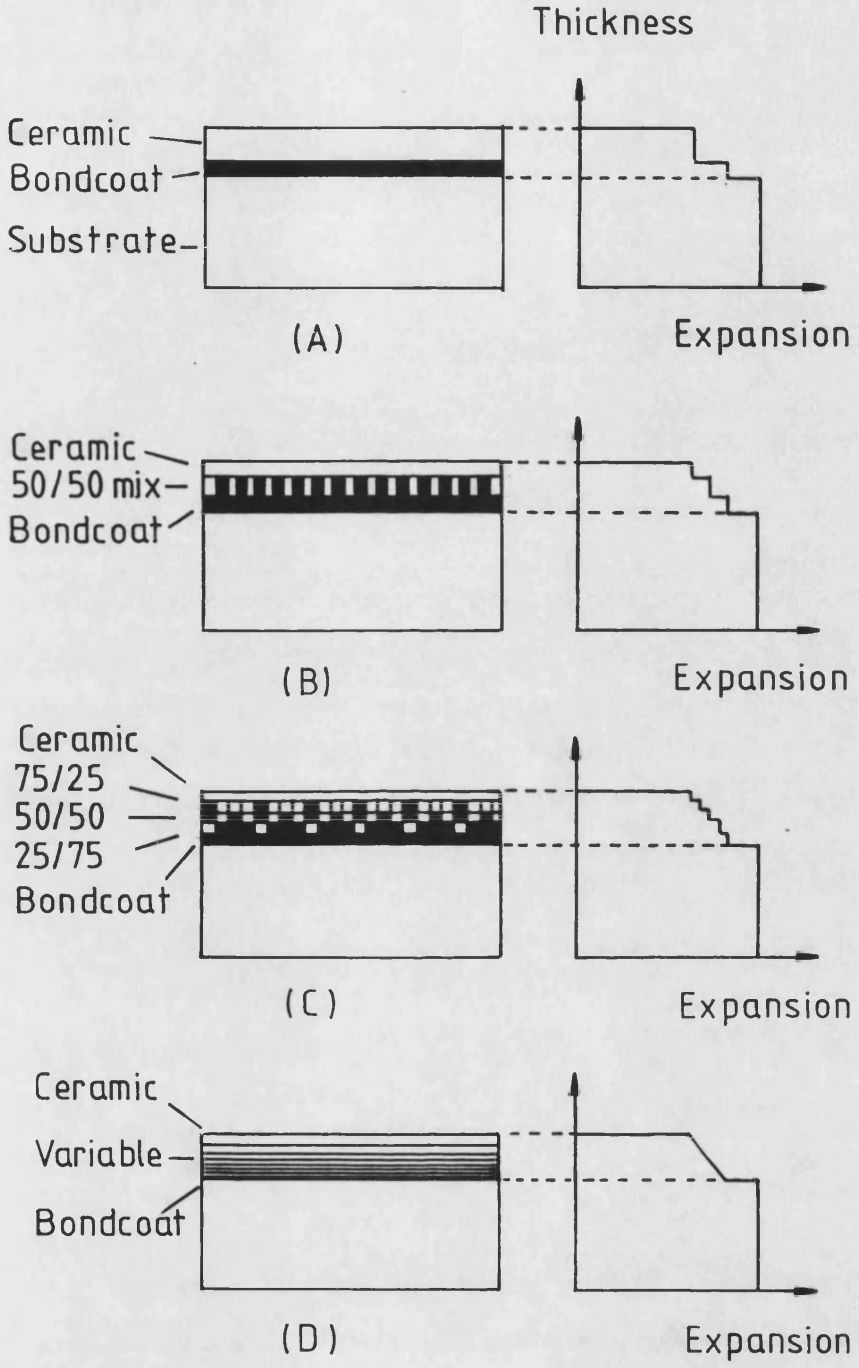

Figure 2·15 Diagrams illustrating the reduction in thermal expansion mismatch achieved when layers of fixed (B,C) and variable (D) intermediate composition are introduced into a simple two layer coating (A).

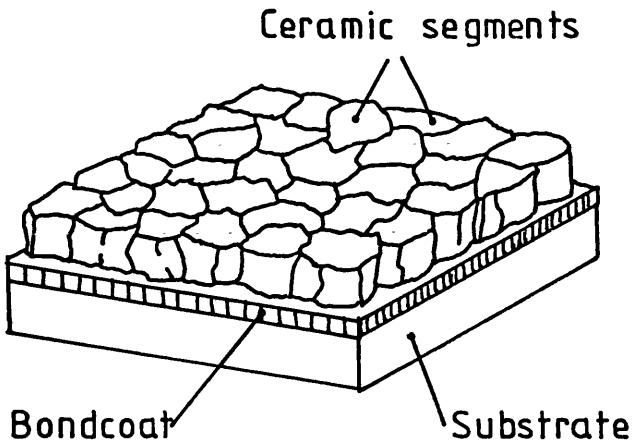

Figure 2·16 Diagram of a segmented thermal barrier coating structure, after [92].

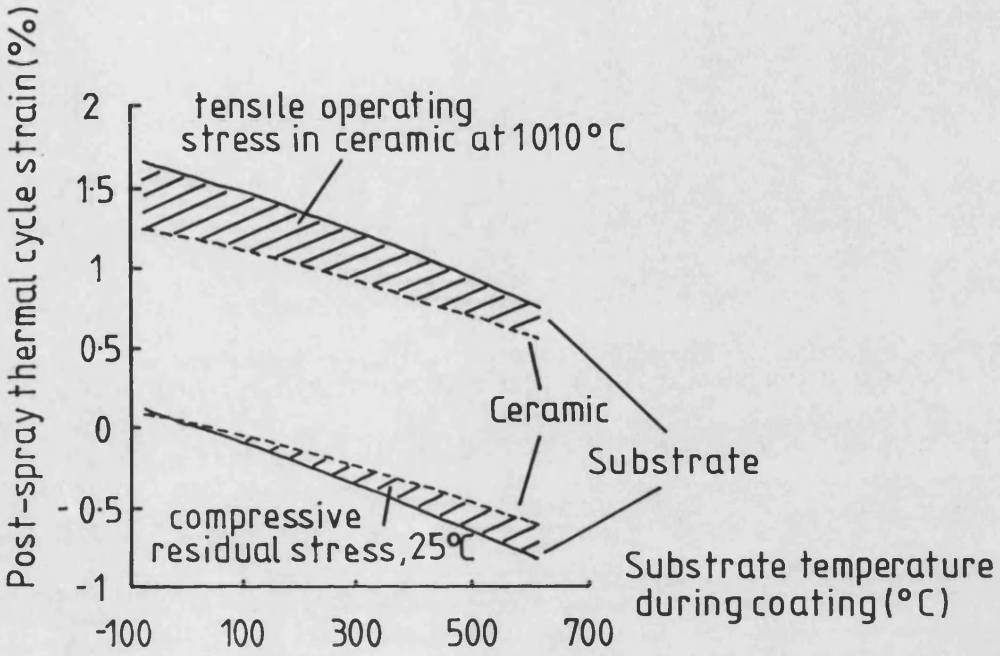

Figure 2·17 Graph showing the variation of interface strain mismatch with substrate temperature during coating, after [94]. The coating was subjected to a thermal cycle up to 1010°C.

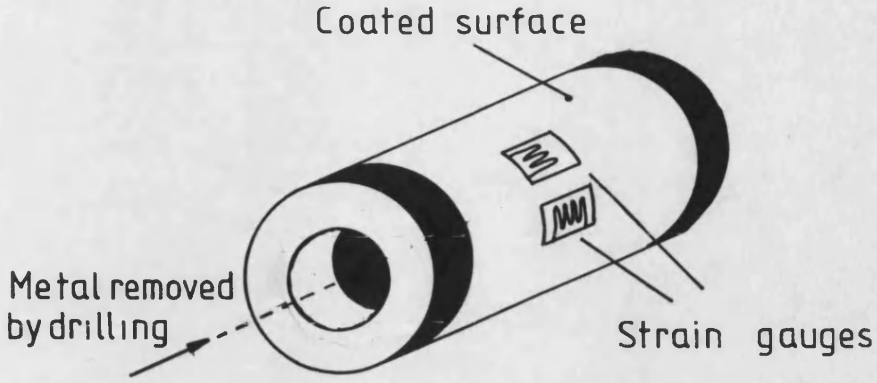

'Boring out' technique

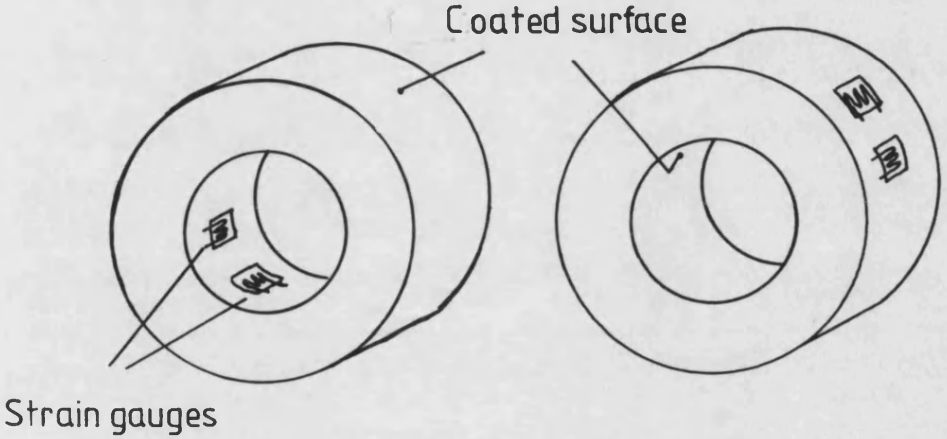

Turning/Grinding

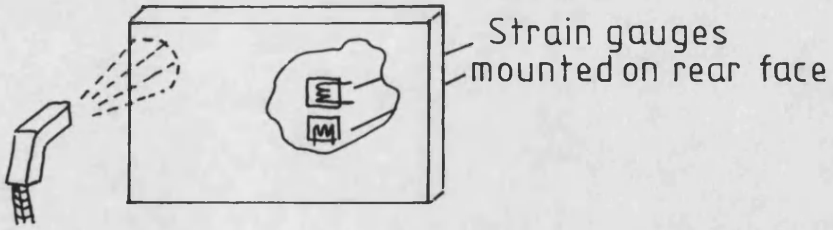

Continuous monitoring

Figure 2·18 Summary of mechanical methods for determining residual stress in coatings

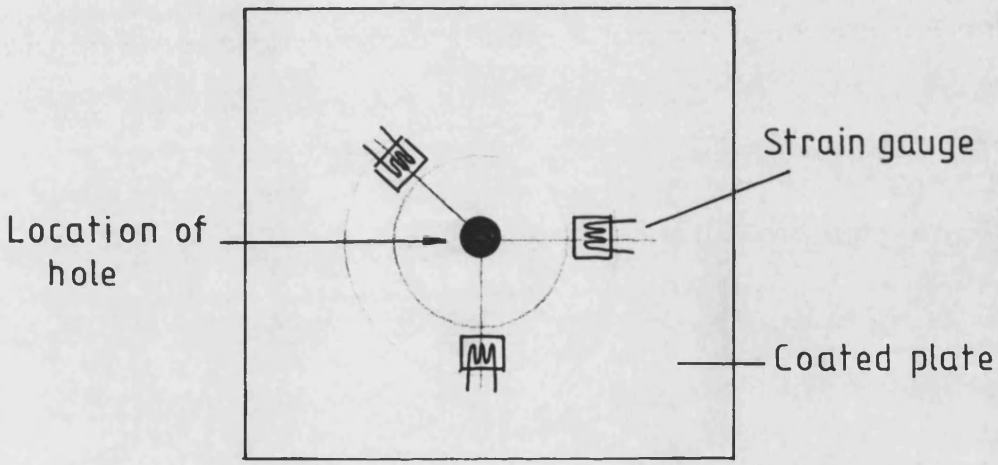

Figure 2·19 Diagram showing the arrangement of strain gauges used to measure coating residual stress in the hole drilling technique.

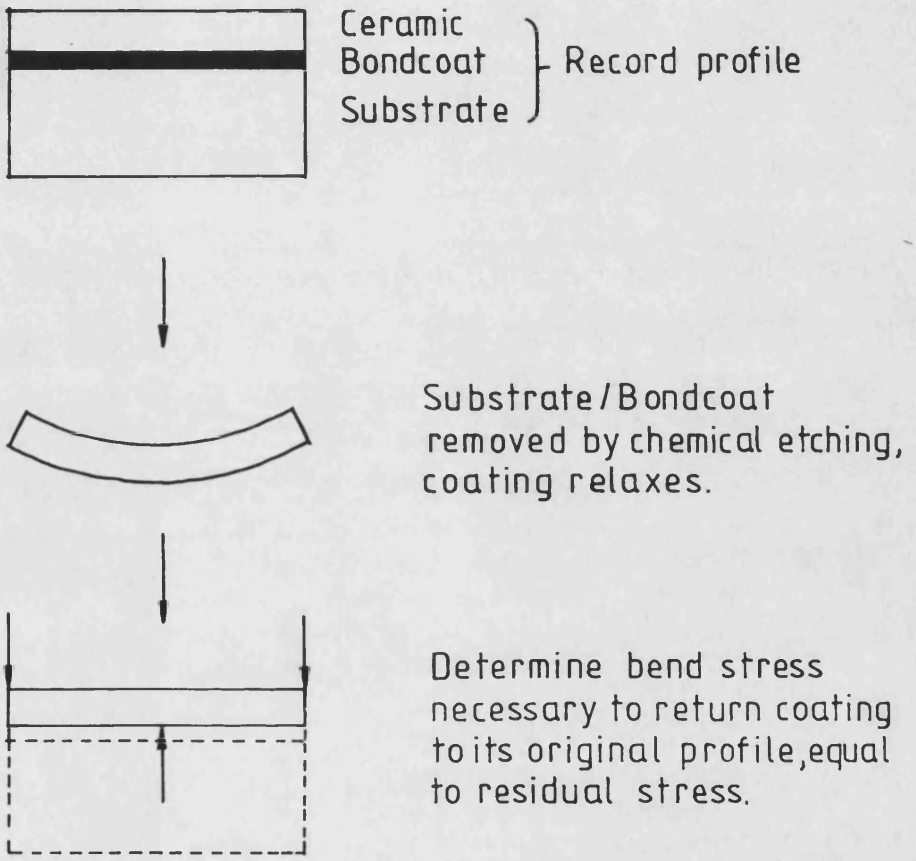

Figure 2·20 Diagram illustrating the chemical etching technique for determining residual stress in inert thermal barrier coatings, described in [69]

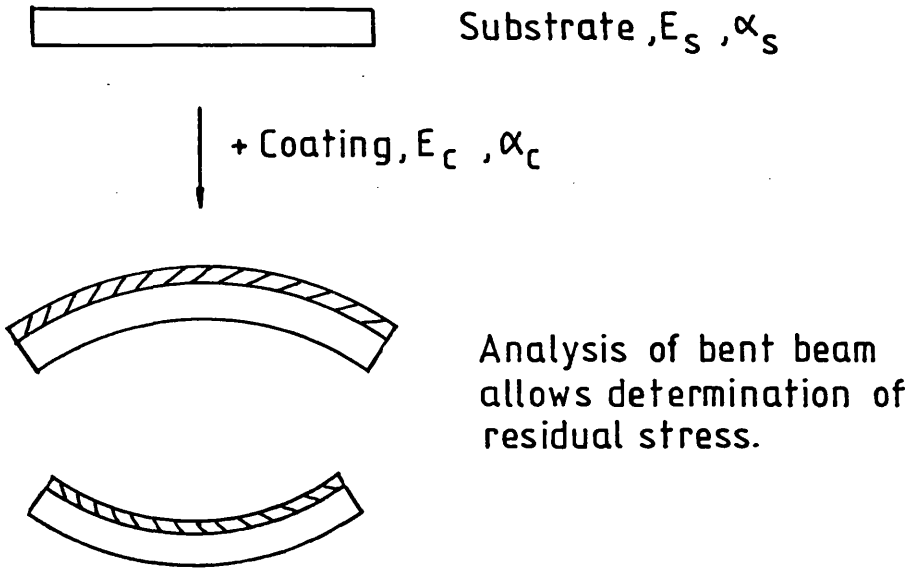

Figure 2·21 Determination of residual stress in coatings deposited on thin substrates.

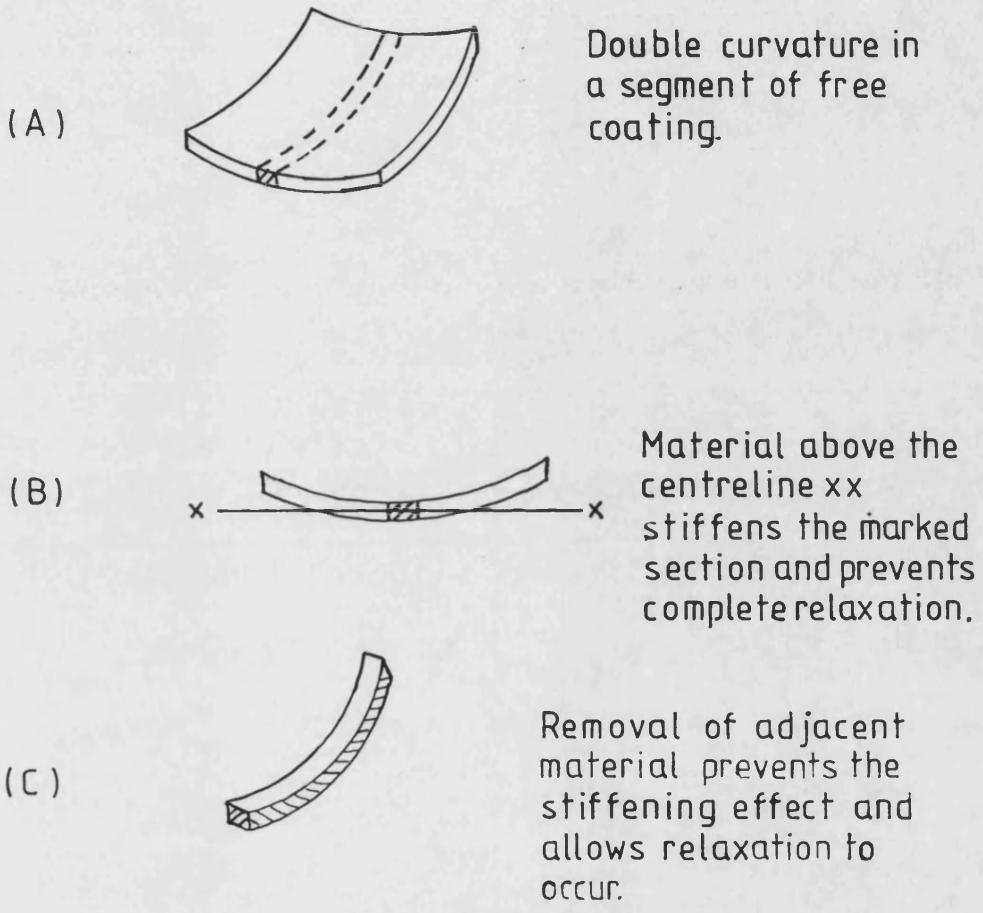

Figure 2·22 Diagram showing the stiffening effect of double curvature in a free coating segment and its effect on coating relaxation,(A,B). Removal of adjacent material by sectioning allows more complete relaxation to occur,(C).

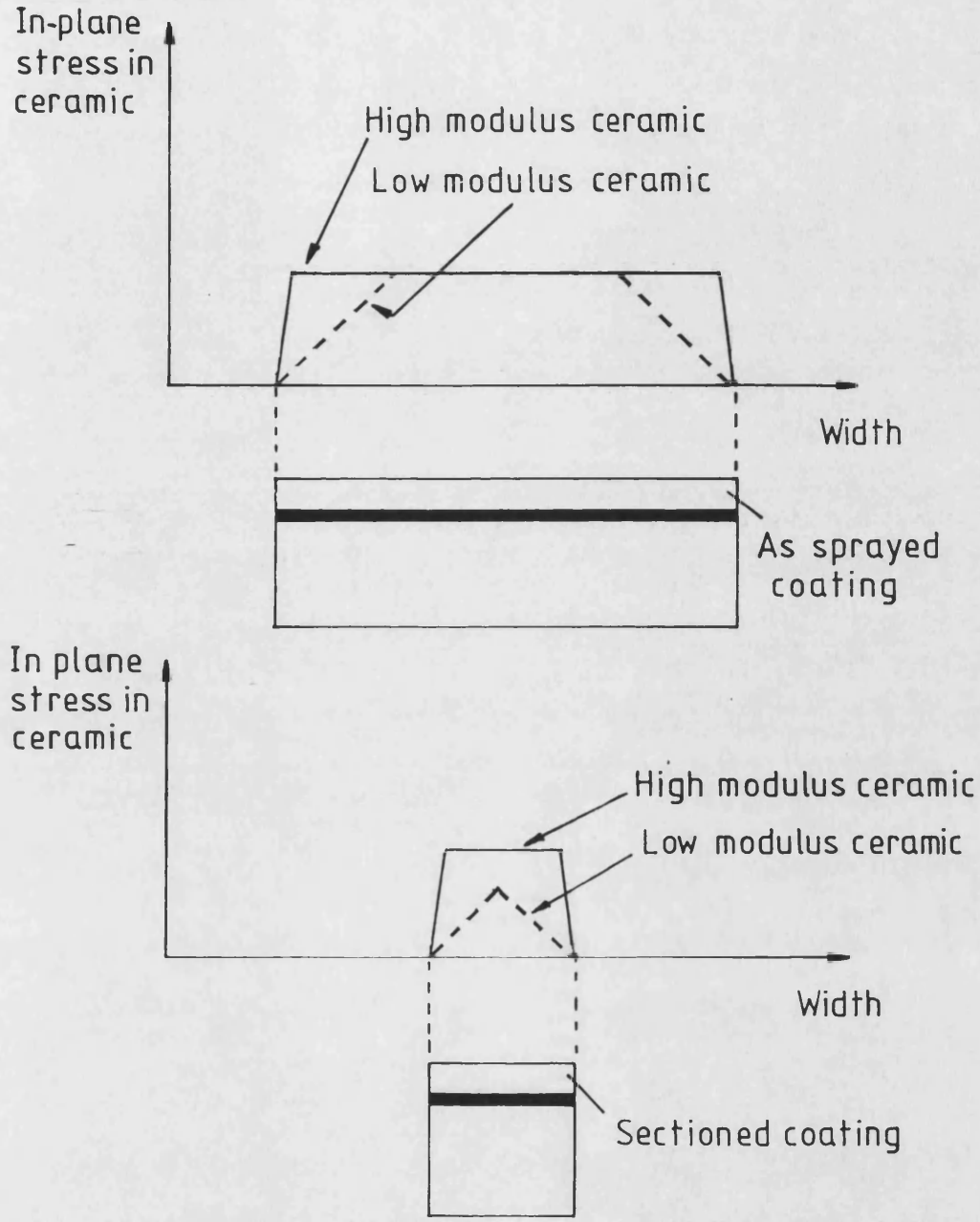

Figure 2·23 Diagram illustrating the effect of ceramic elastic modulus on in-plane stress levels in as-sprayed and sectioned coatings

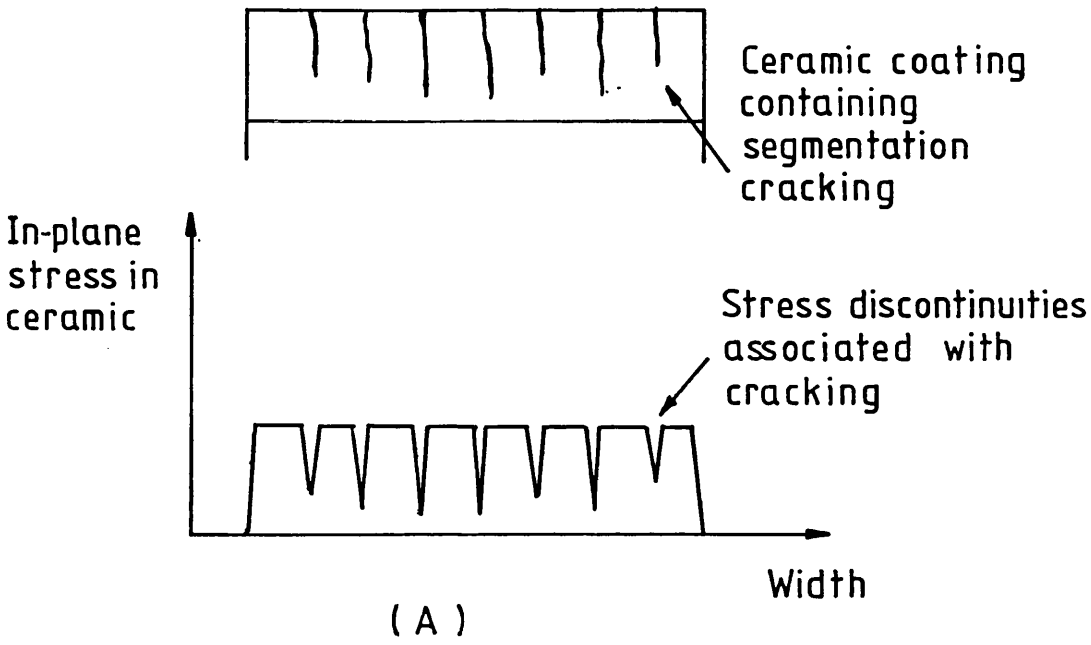

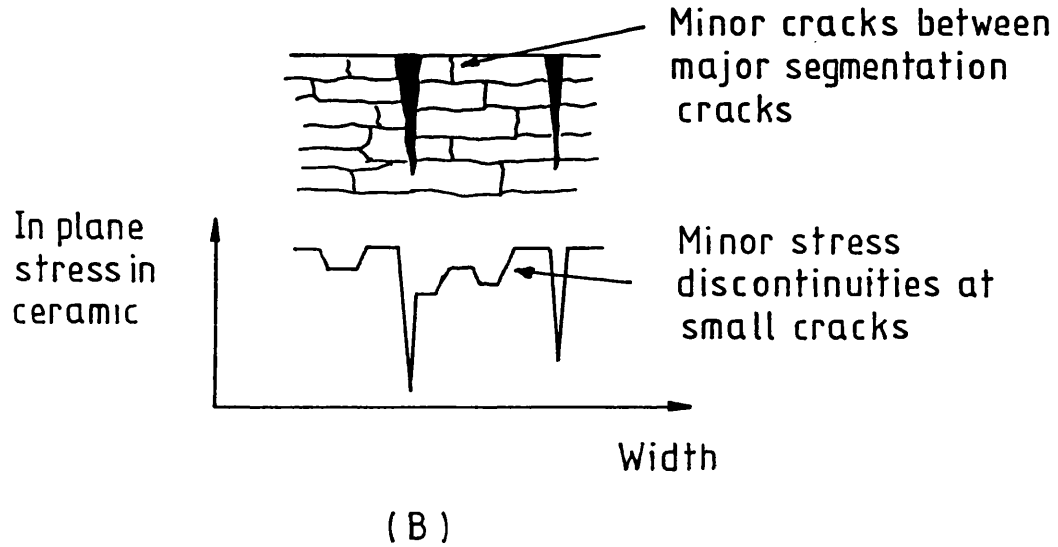

Figure 2·24 Diagram showing the variation of in-plane stress in ceramic coatings containing large,(A), and small,(B), cracks.

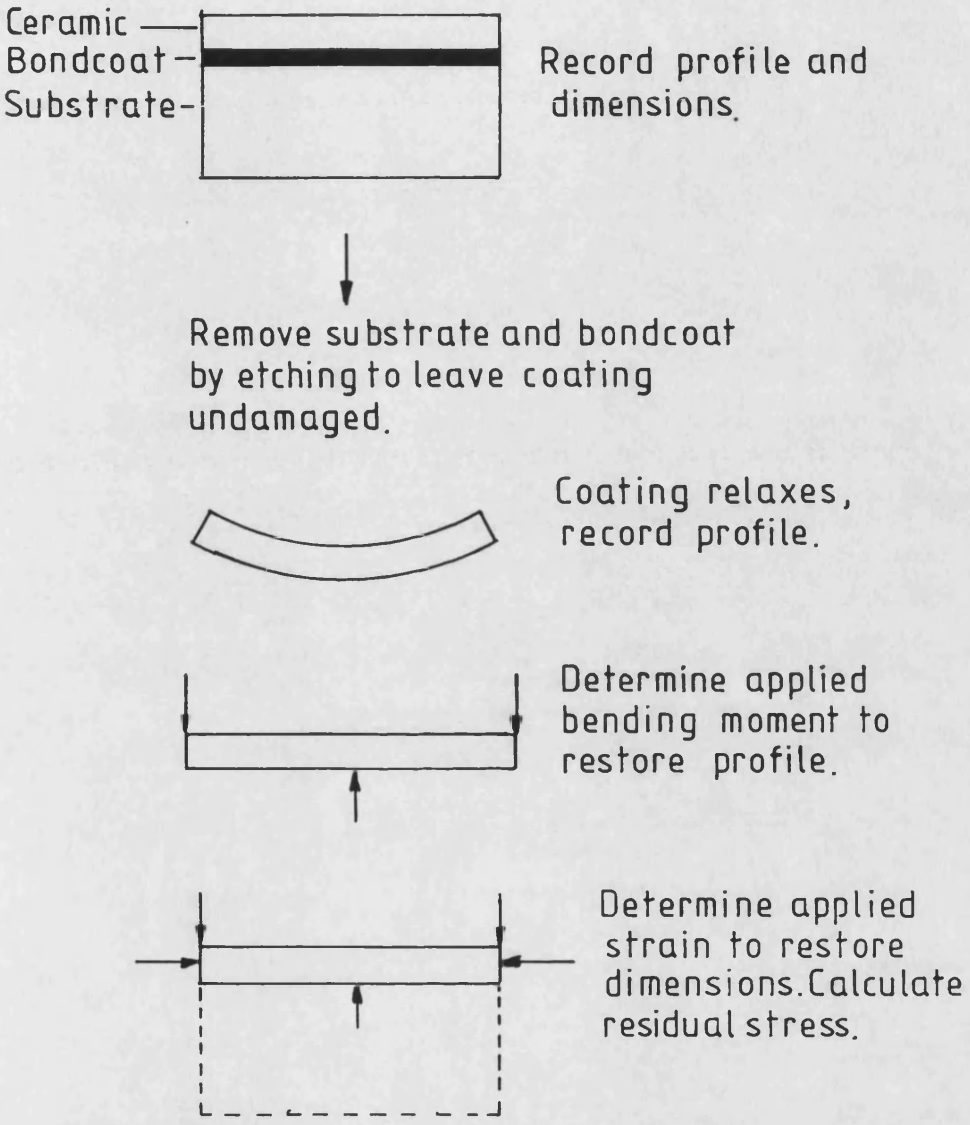

Figure 2·25 Diagram illustrating an improved method, based on chemical etching, for measuring residual stress in ceramic coatings.

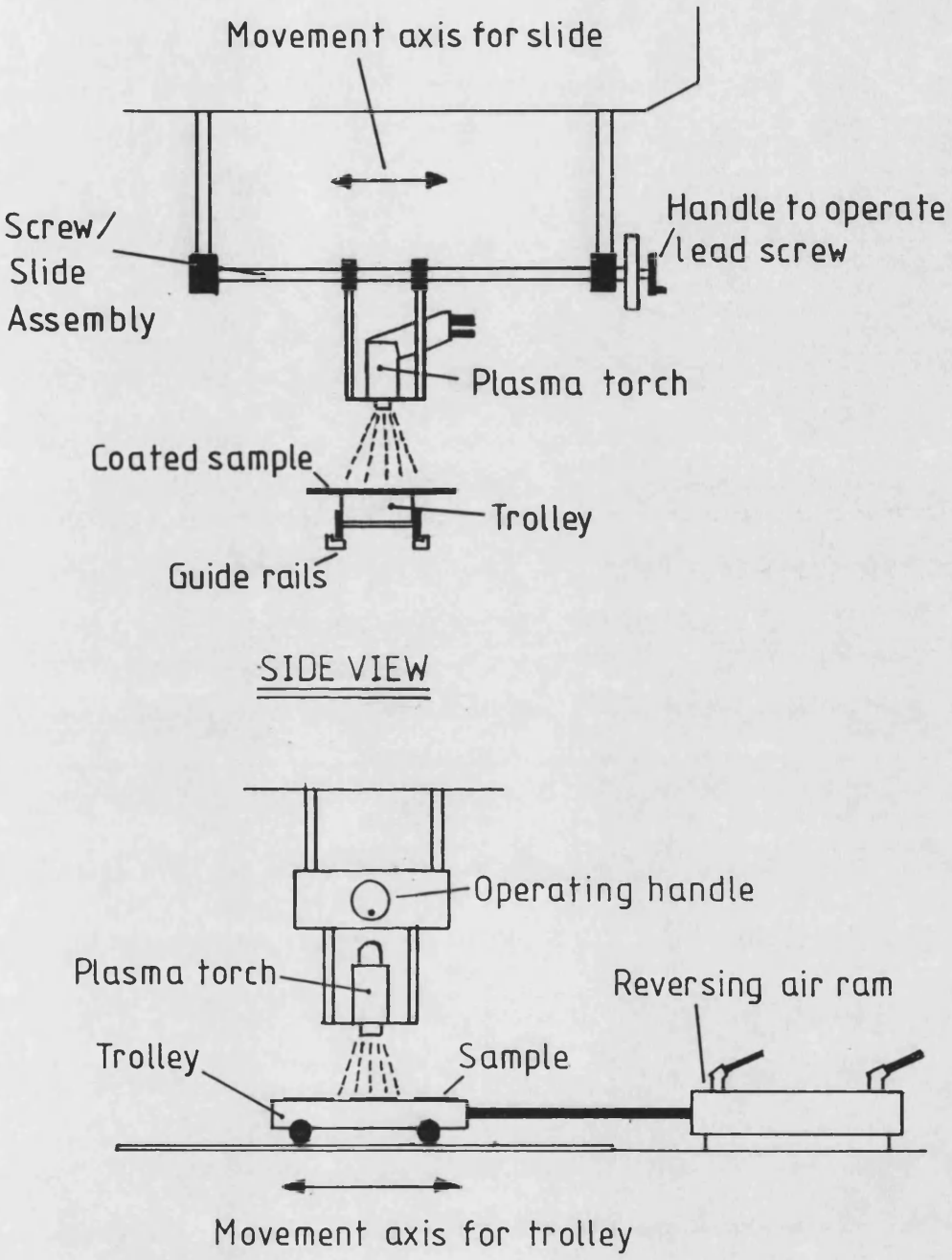

Figure 3·1 Schematic diagram of existing plasma spray system.

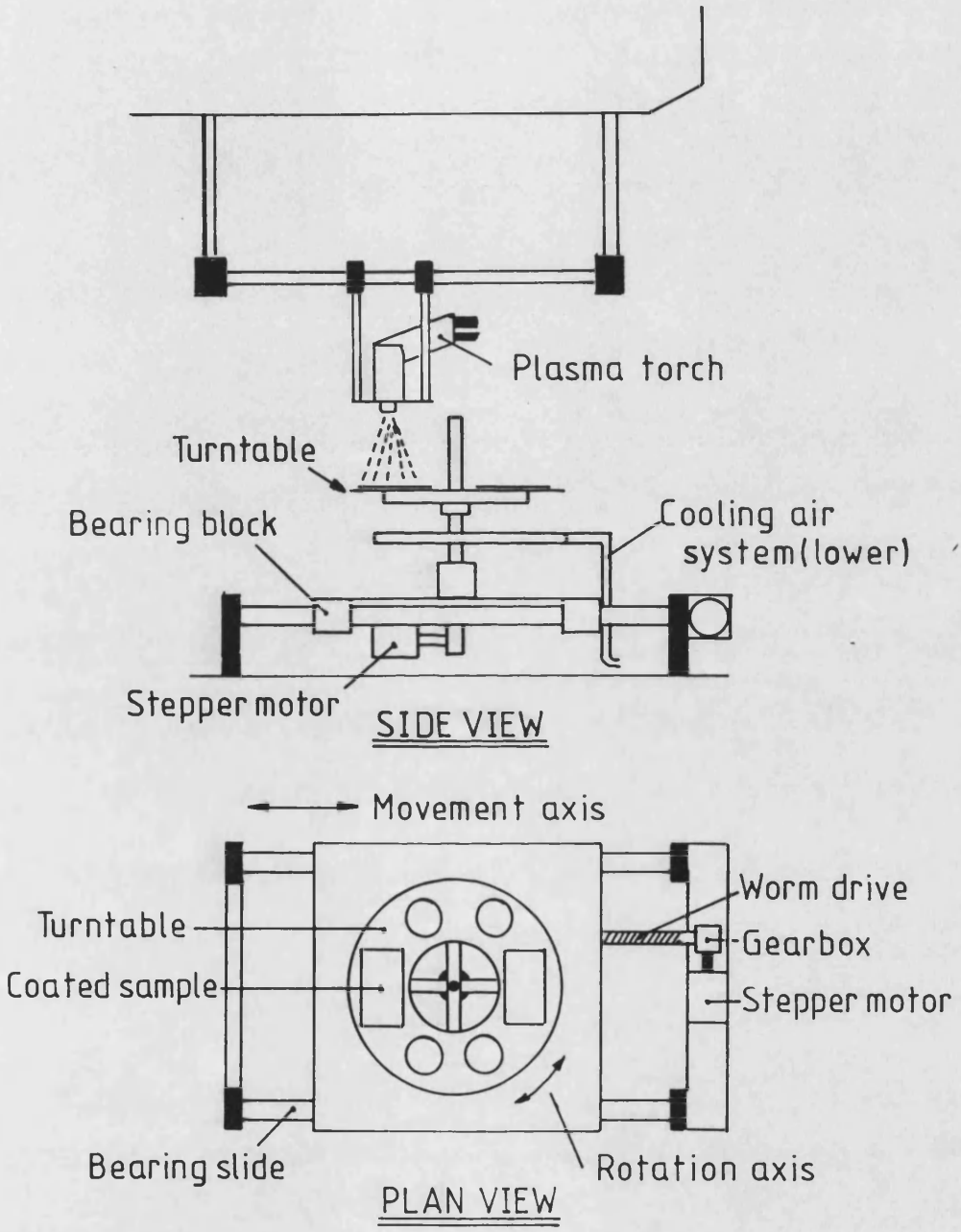

Figure 3·2 Schematic diagram of improved plasma spray system.

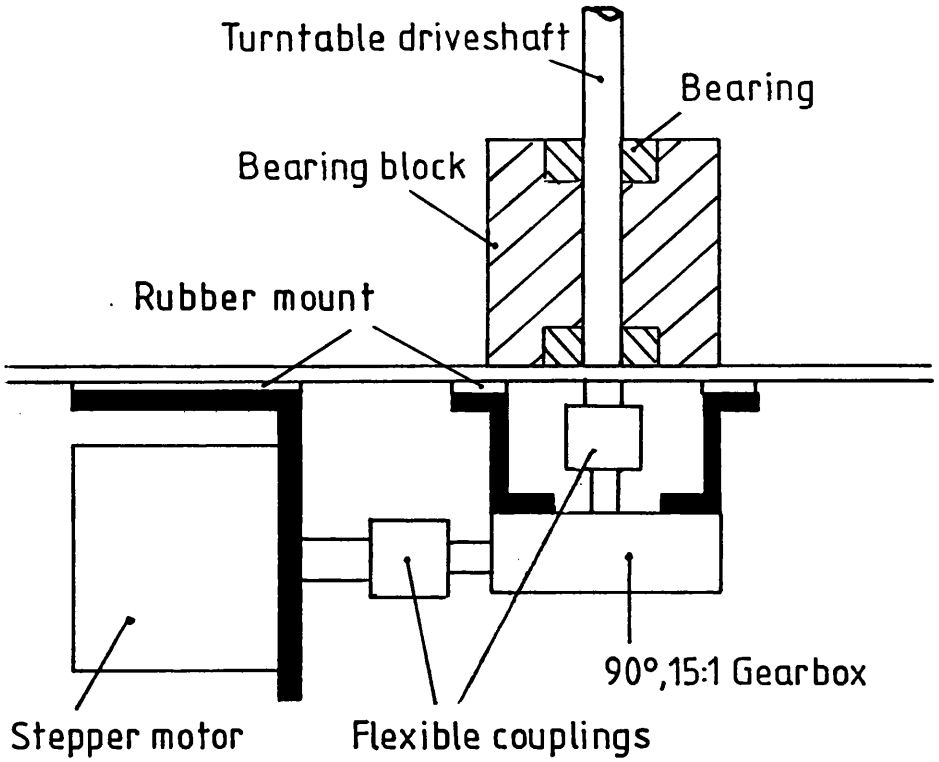

Figure 3·3 Schematic diagram of turntable drive mechanism.

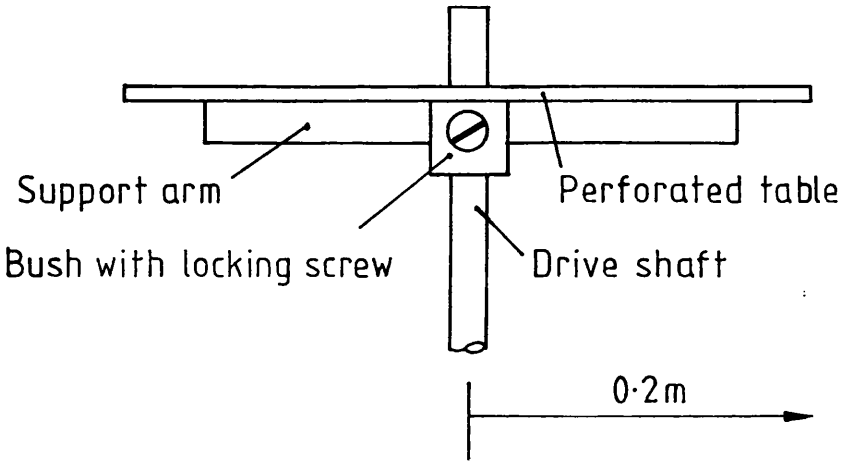

Figure 3·4 Schematic diagram of turntable height adjustment mechanism.

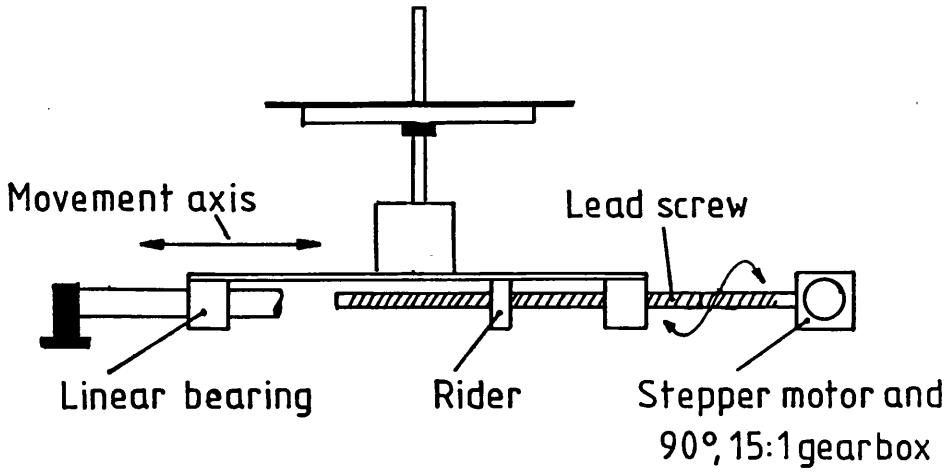

Figure 3·5 Schematic diagram of turntable translation mechanism.

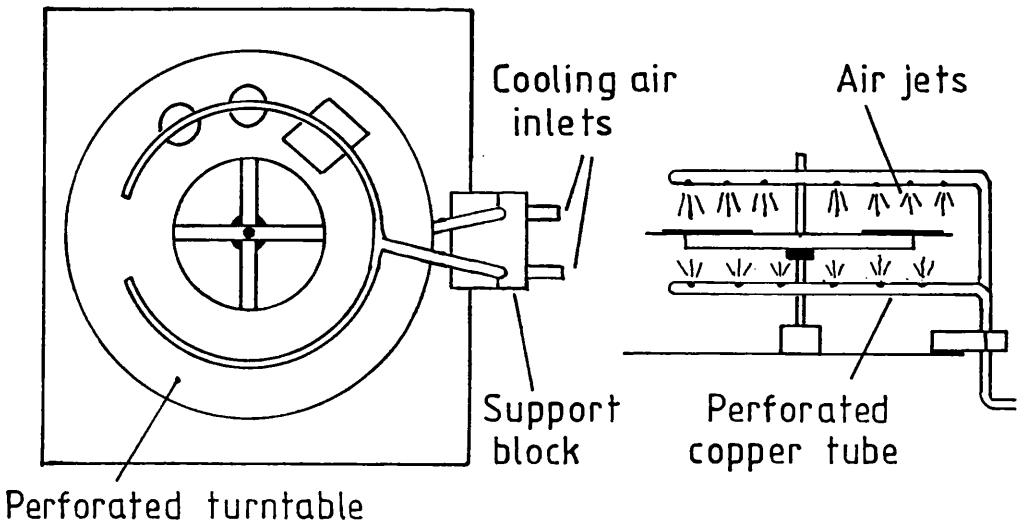

Figure 3·6 Schematic diagram of improved air cooling system.

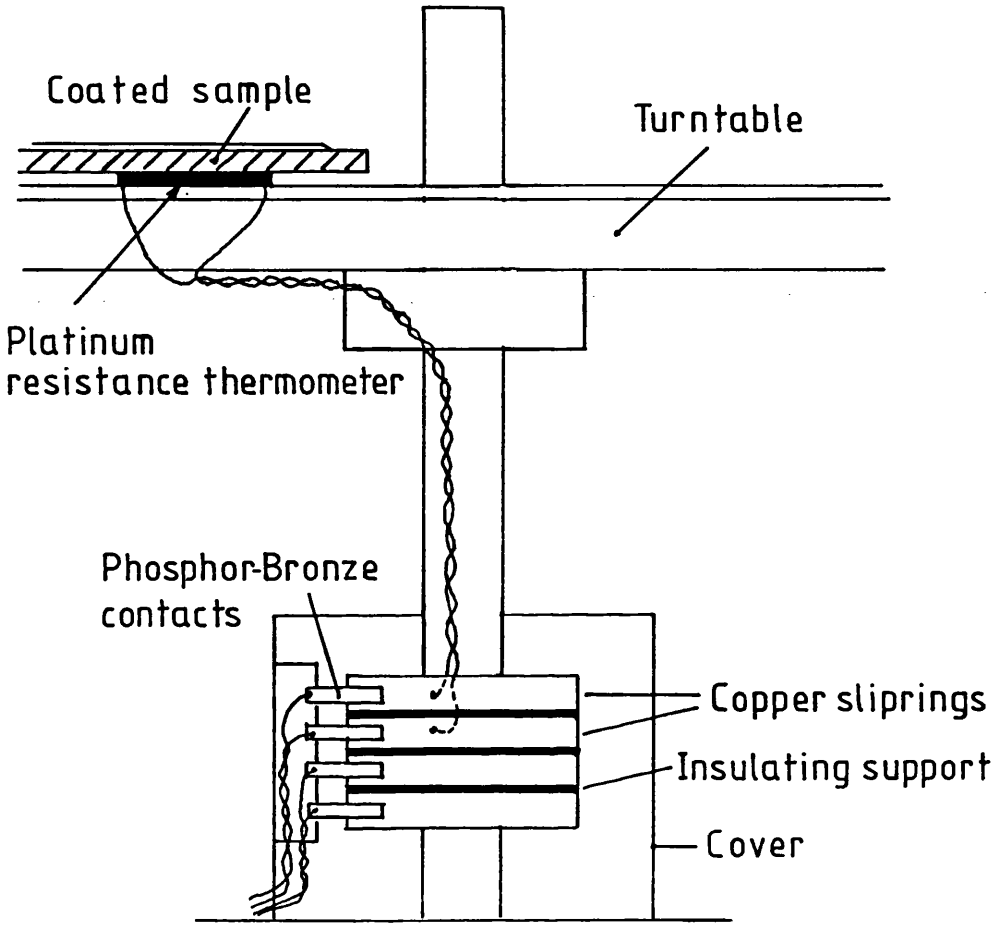

Figure 3·7 Diagram illustrating the testpiece backface temperature monitoring system.

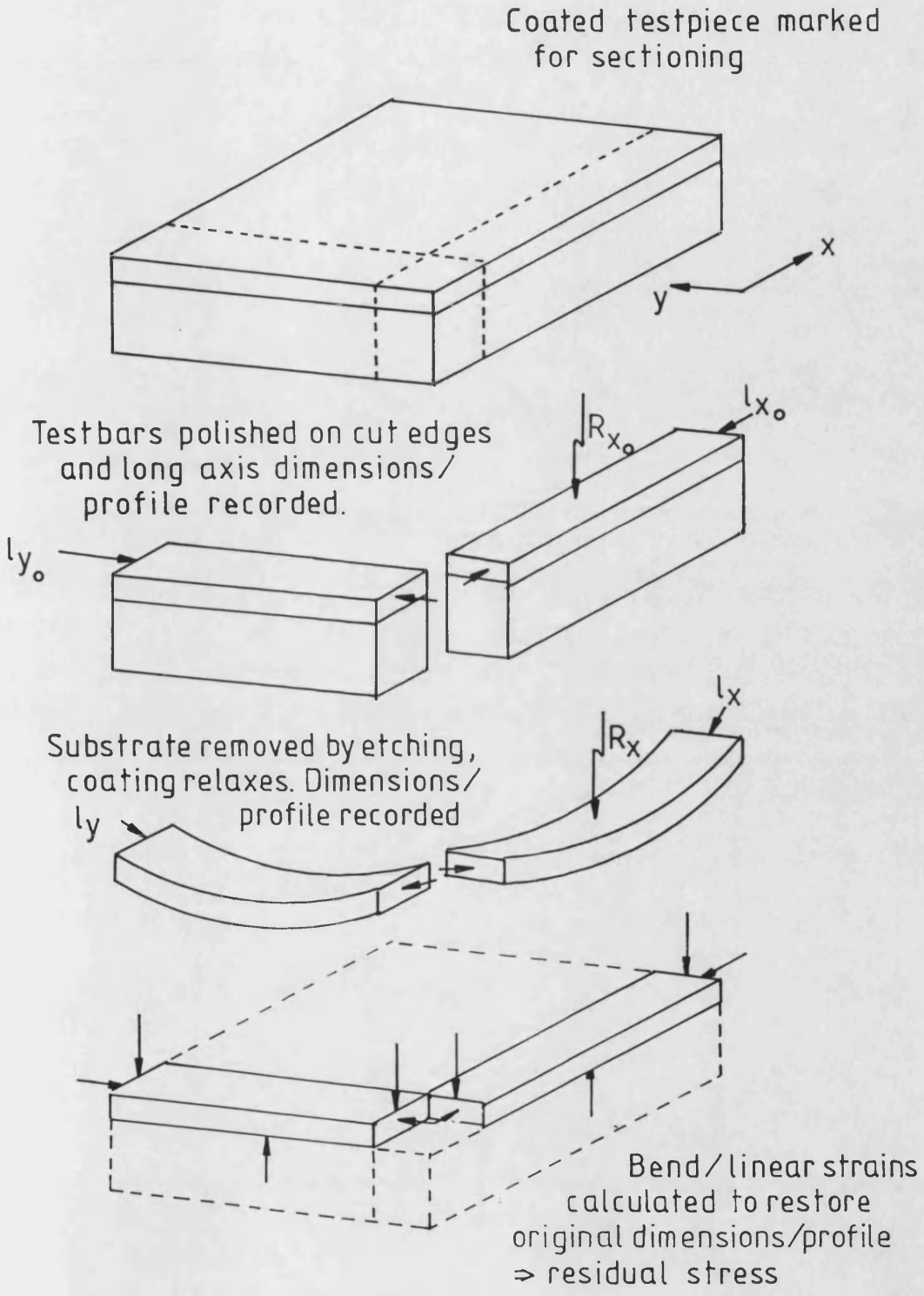

Figure 3·8 Diagram illustrating the steps involved in determining residual stress in thermal barrier coatings.

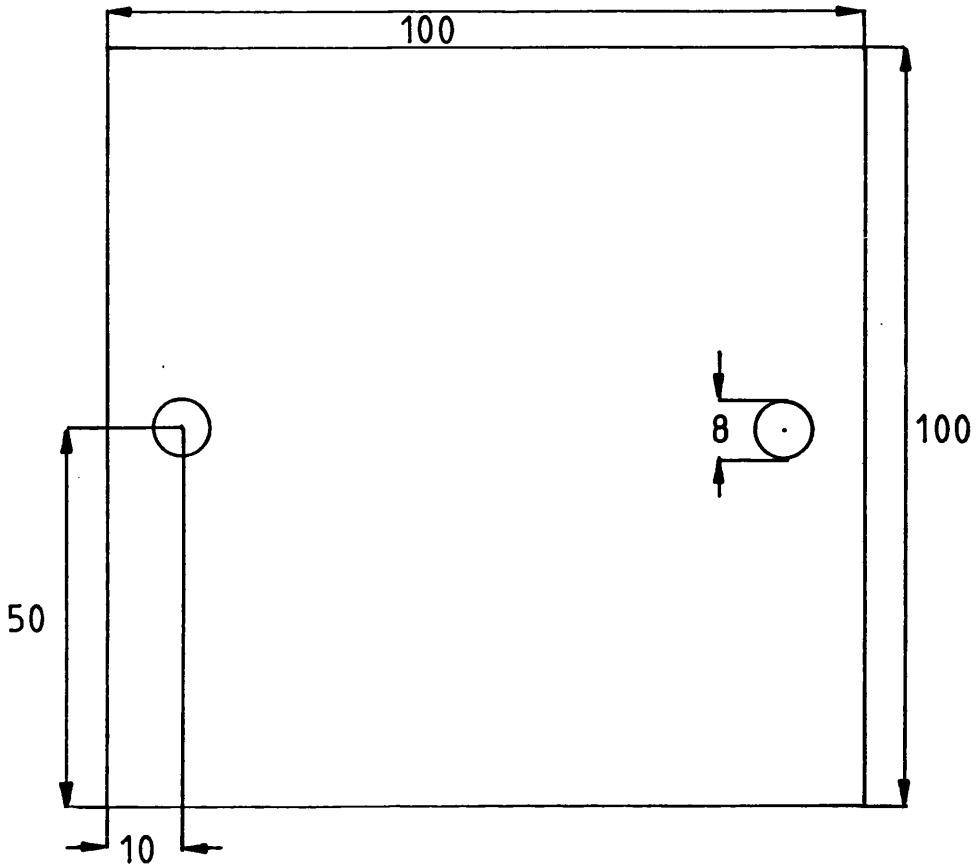

100×100mm Testpiece

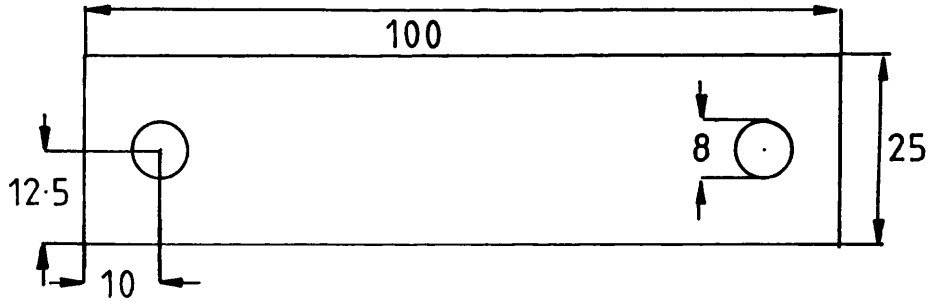

100×25 mm Testpiece

All dimensions in mm

Figure 3·9 Testpiece dimensions

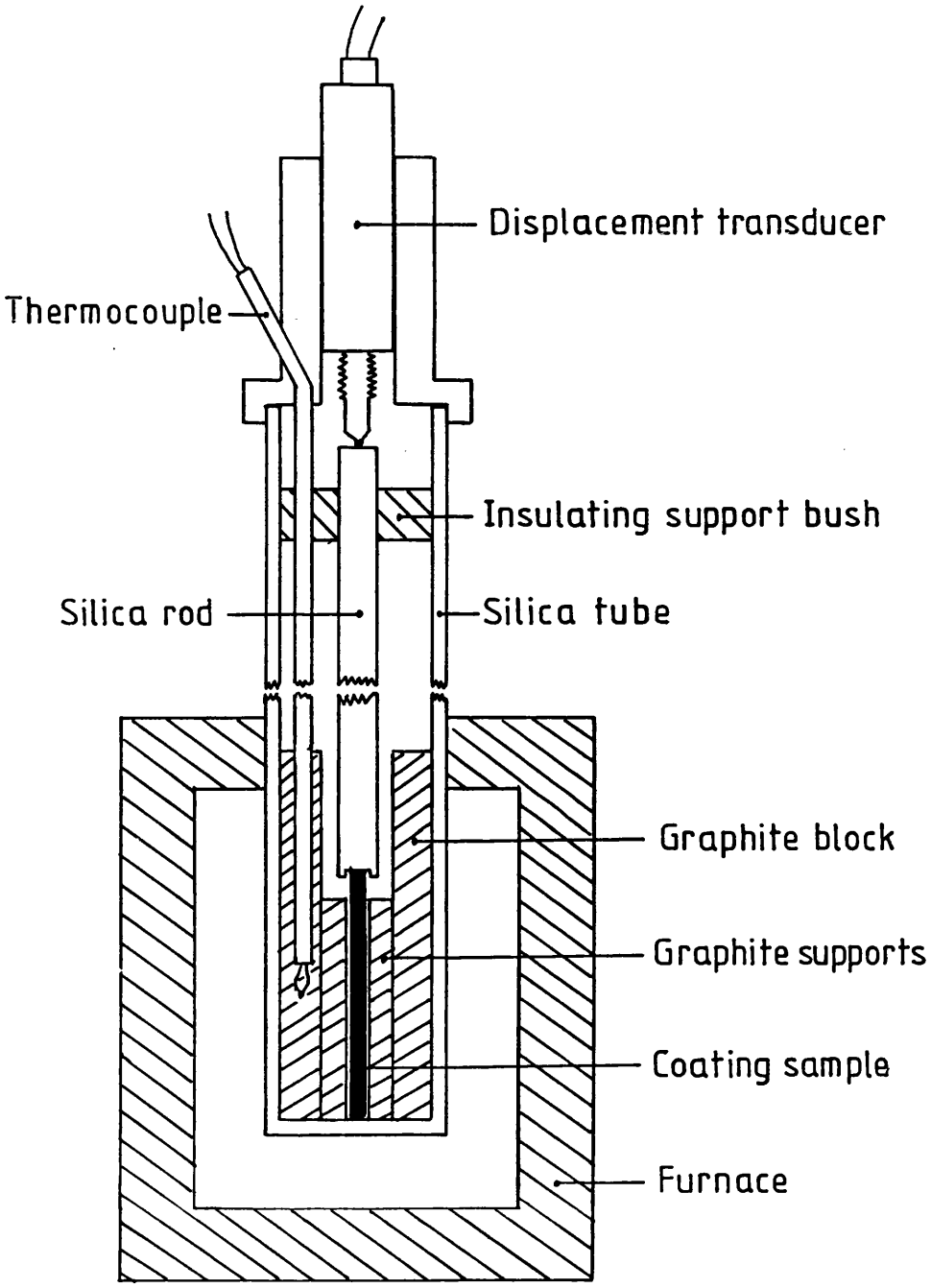

Figure 3·10 Dilatometer apparatus used to measure thermal expansion coefficient of thermal barrier coatings.

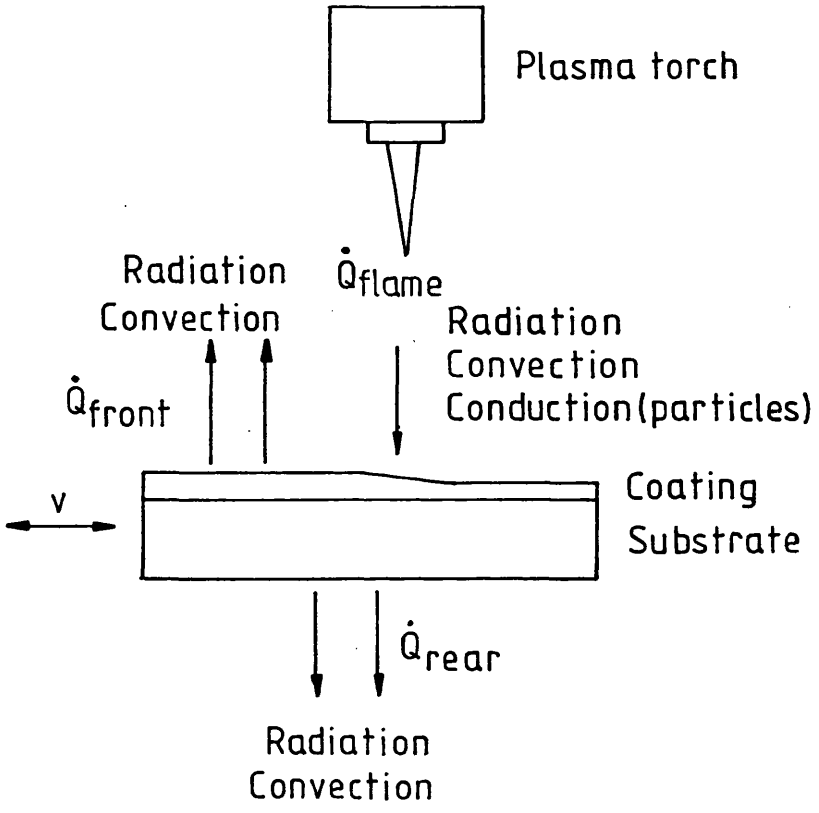

Figure 4.1 Conceptual model of heat flow in a coating system during deposition.

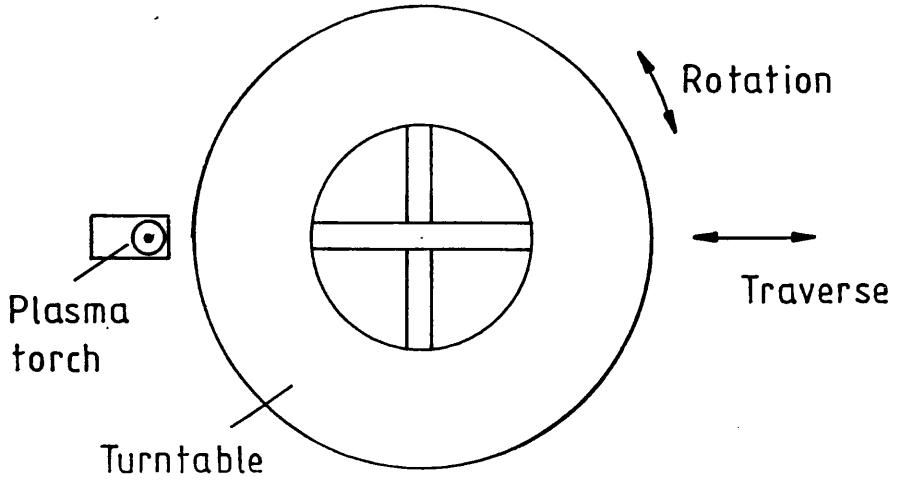

(a)

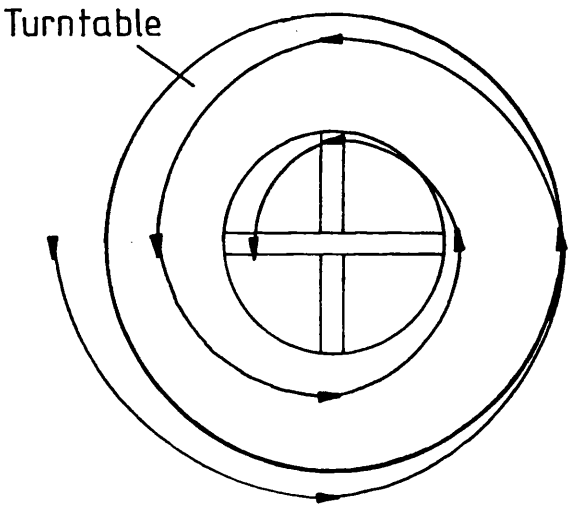

(b)

Figure 4·2 (a) Practical arrangement of fixed plasma torch and turntable system
(b) Effective path of plasma flame over turntable surface.

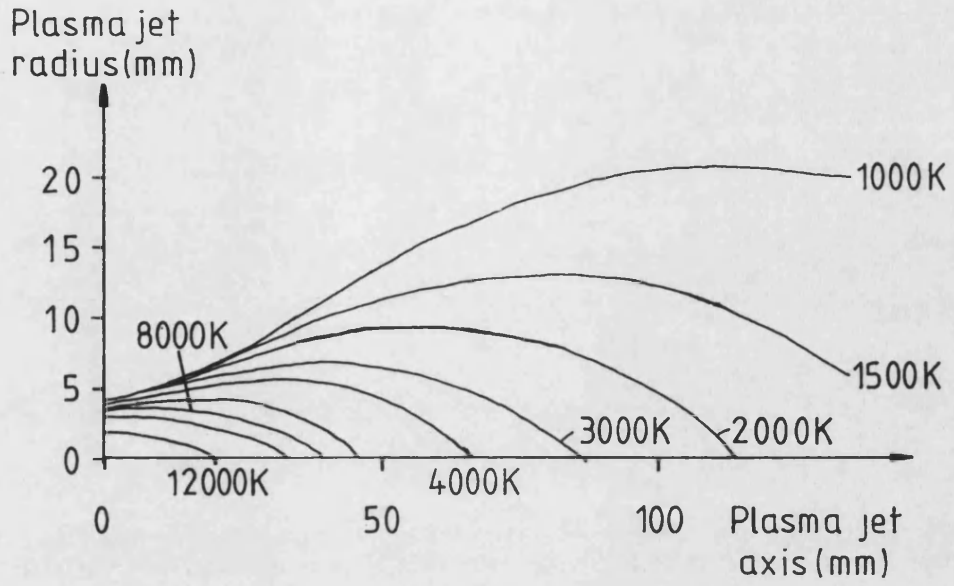

Figure 4·3 Variation of plasma flame temperature with plasma jet radius and axial length in a typical flame, after [23].

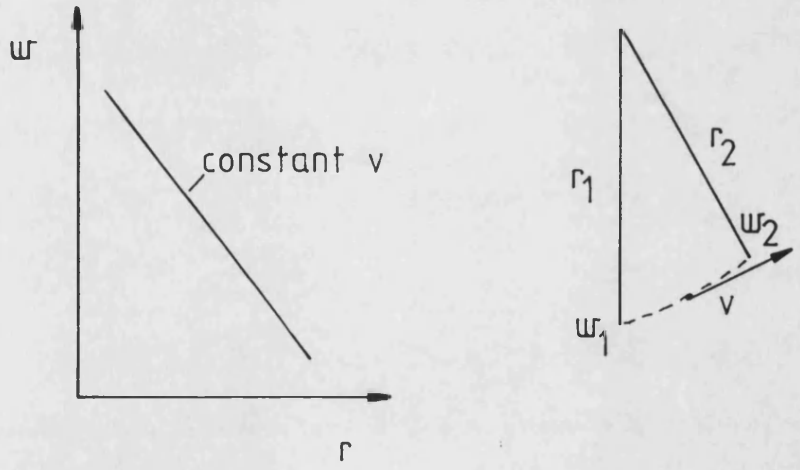

Figure4·4 Diagram illustrating the relationship between radius and angular velocity at a constant linear velocity.

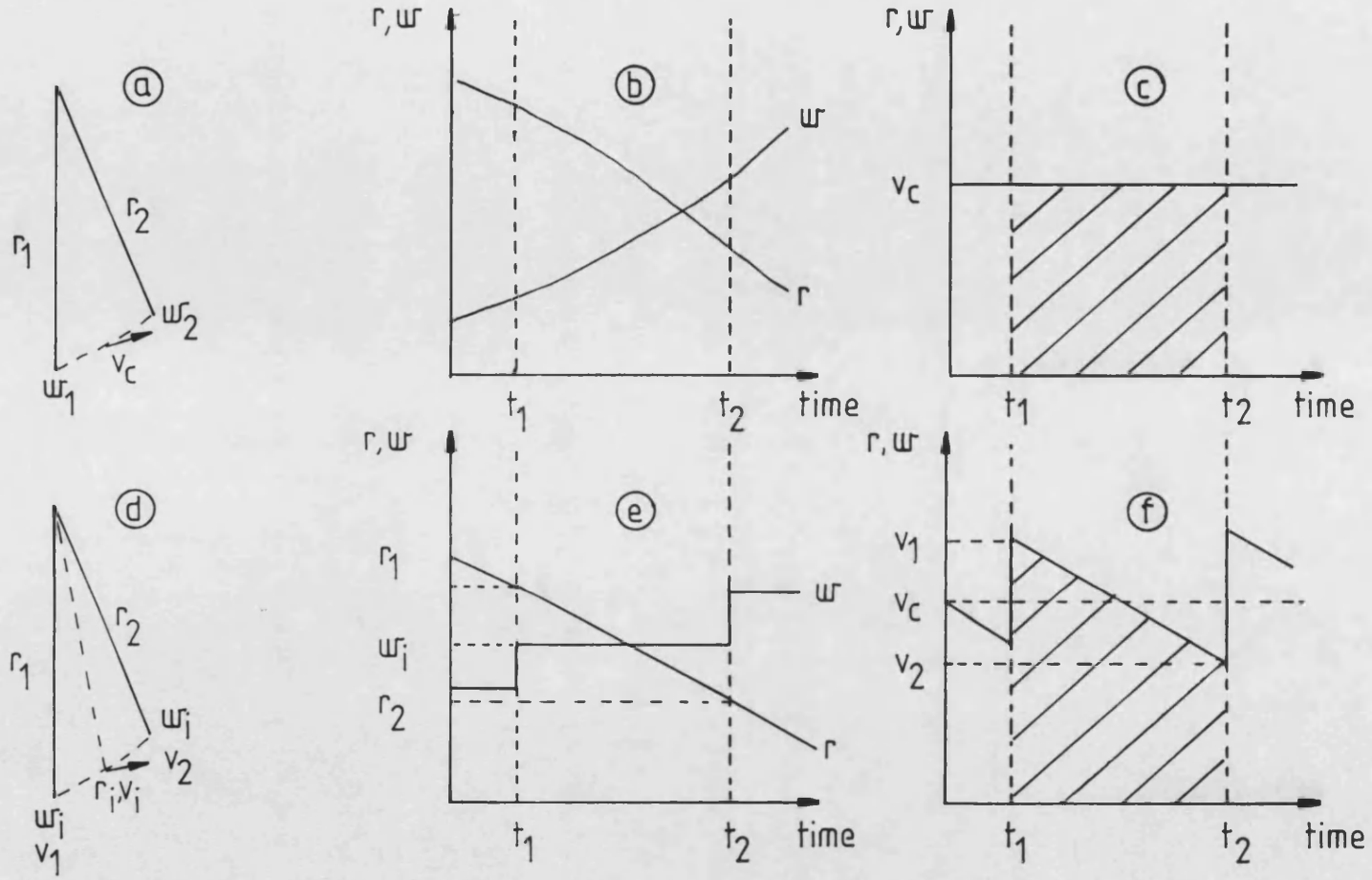

Figure 4·5 Diagram illustrating the differences between theoretical (a,b,c) and practical (d,e,f) control of motor shaft angular velocity.

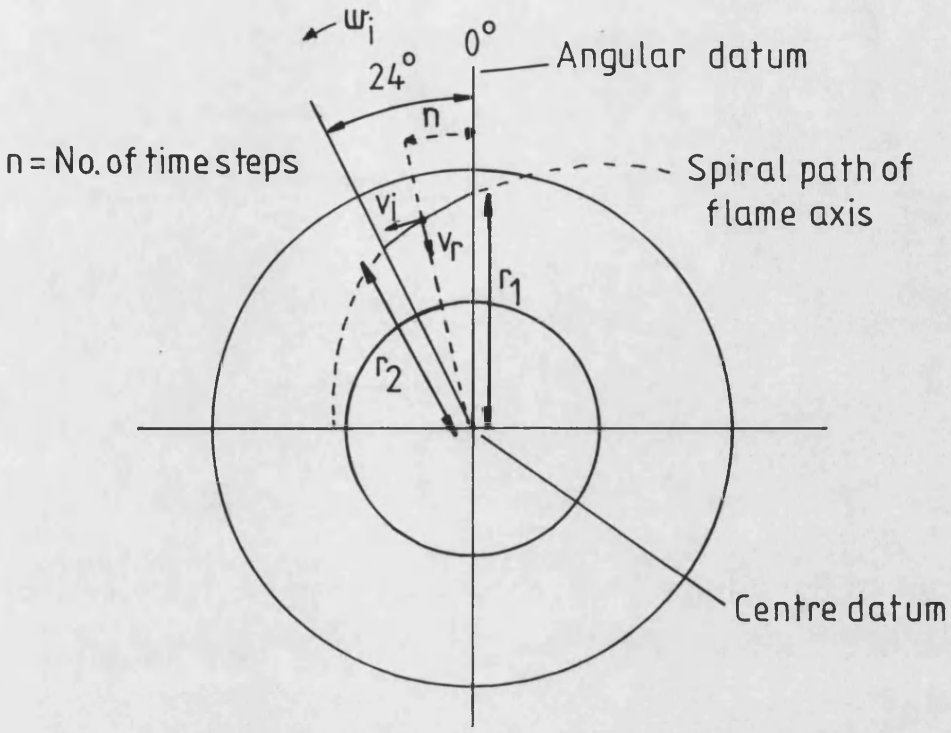

Figure 4·6 Diagram illustrating the important parameters necessary to specify the position and velocity of the plasma torch.

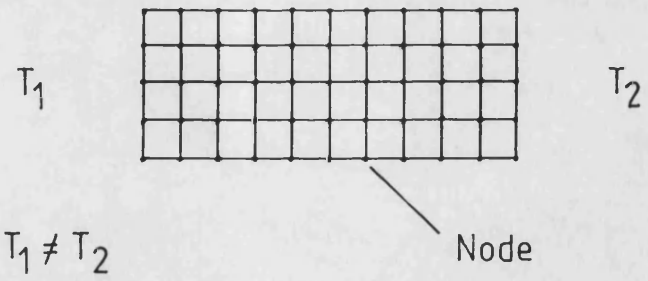

Figure 4·7 Diagram illustrating a mesh of nodes or grid points superimposed on a system subject to a temperature gradient.

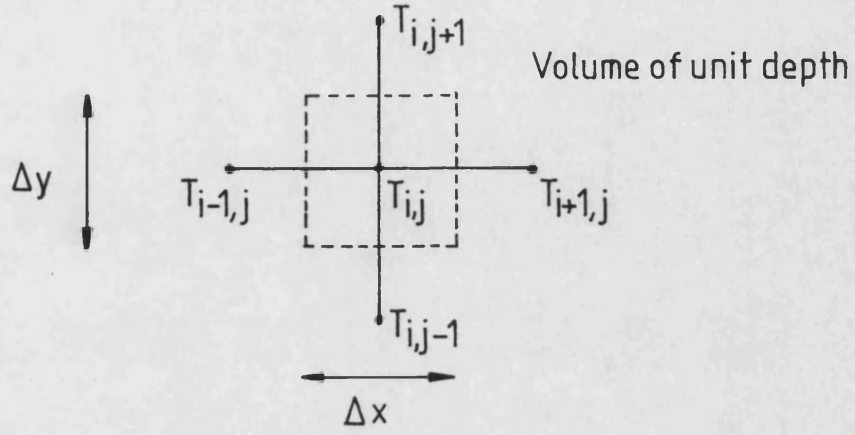

Figure 4·8 The control volume surrounding a node, after [134].

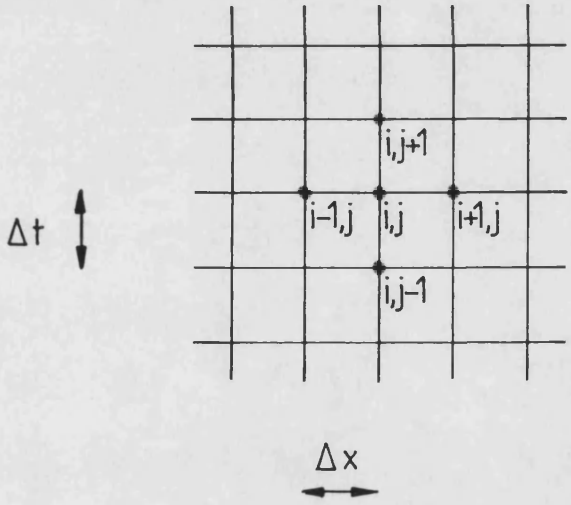

Figure 4·9 Diagram showing the distance/time grid used to develop a time dependant energy balance around the node i,j, after [134].

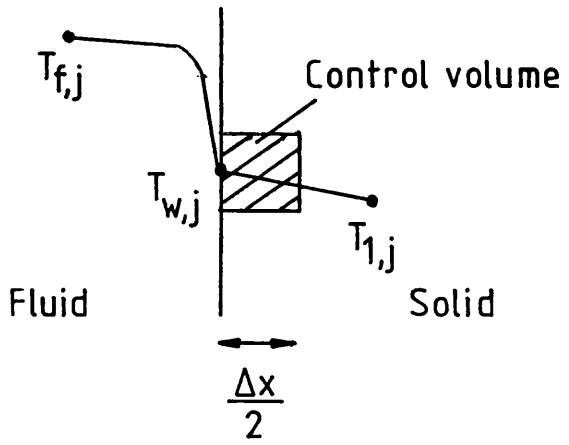

Figure 4·10 Diagram illustrating the arrangement of nodes at a fluid-solid boundary.

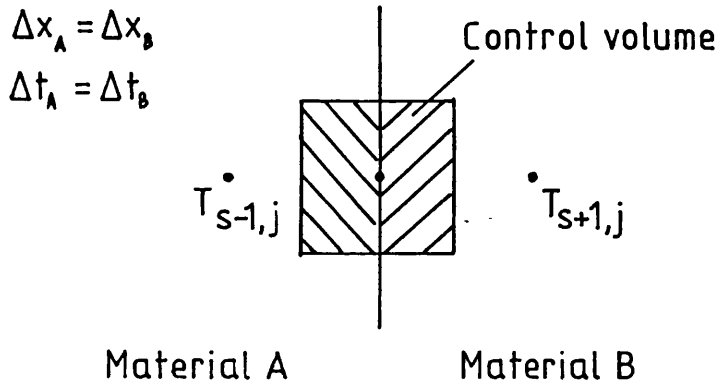

Figure 4·11 Diagram illustrating the arrangement of nodes at a boundary between two materials.

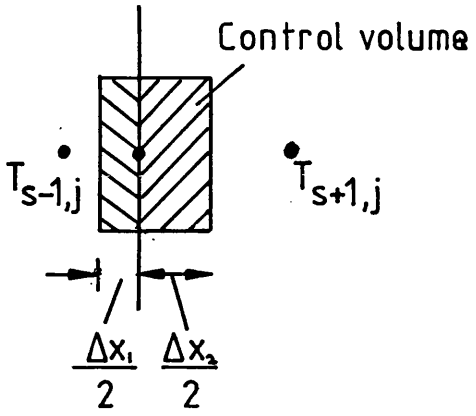

Figure 4·12 Diagram illustrating the arrangement of nodes at the boundary between two areas with different mesh spacings.

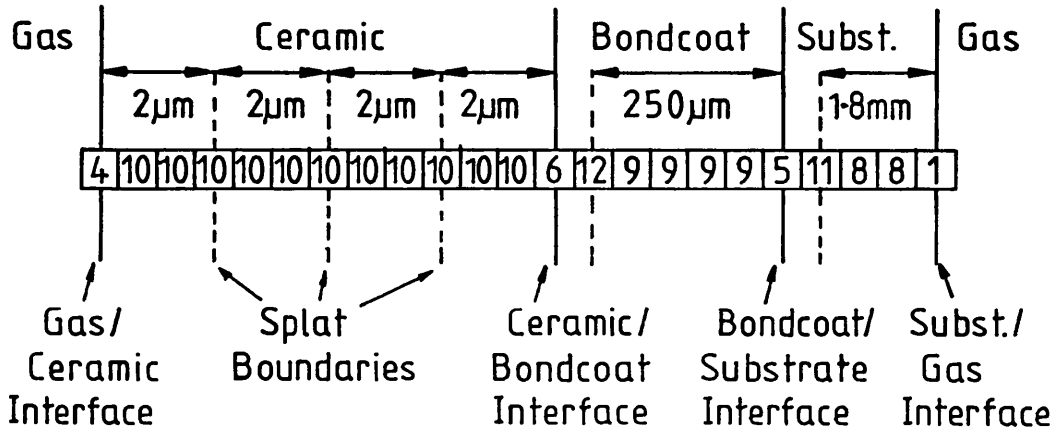

11 & 12 = Size change nodes

Figure 4·13 A simple thermal barrier coating described by a linear array of node codes. Each array element code is used to select the appropriate equations describing the node.

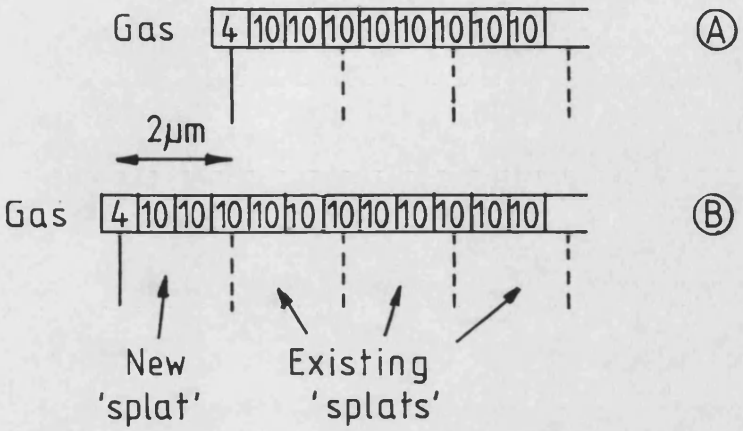

Figure 4·14 Diagram showing the modification to an existing node descriptor array, Ⓐ, when a new particle of ceramic is deposited, Ⓑ.

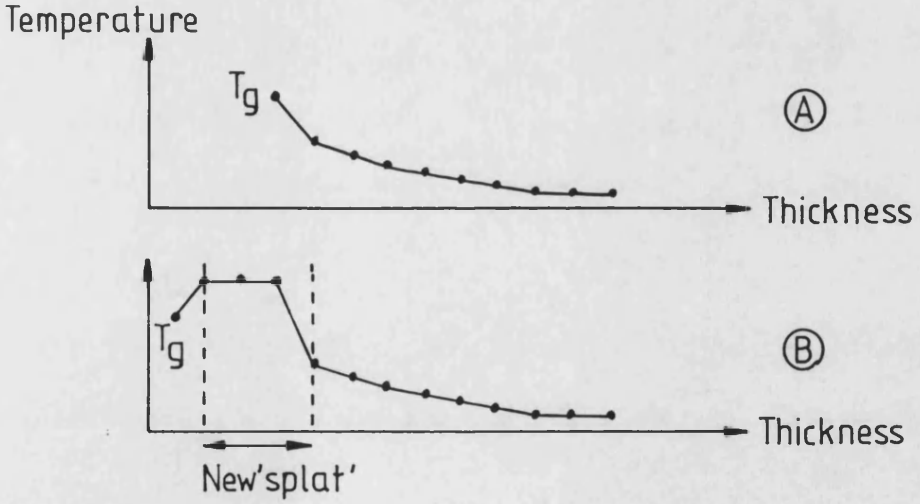

Figure 4·15 The temperature distribution before, Ⓐ, and at the instant a ceramic particle is deposited, Ⓑ, for the node arrays in figure 4·14

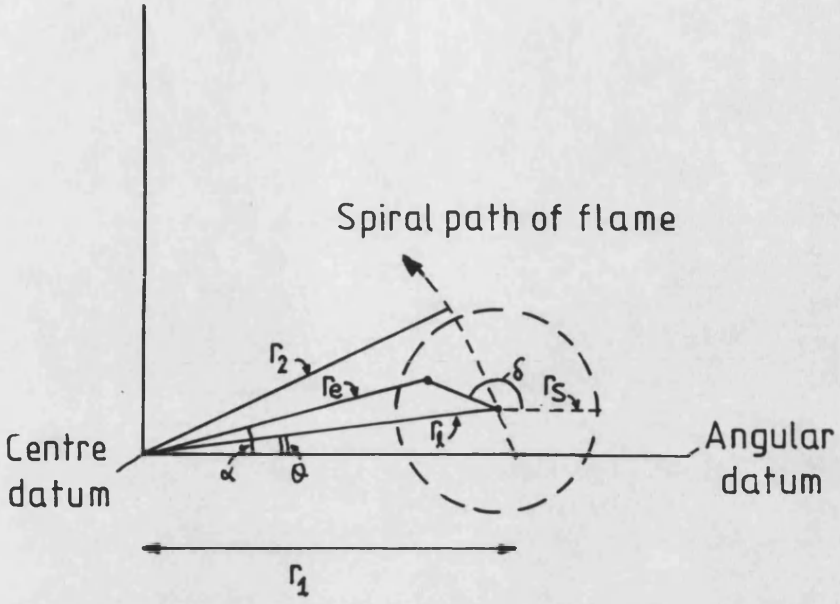

Figure 4·16 The geometrical relationship between flame path and reference point at r_e, α.

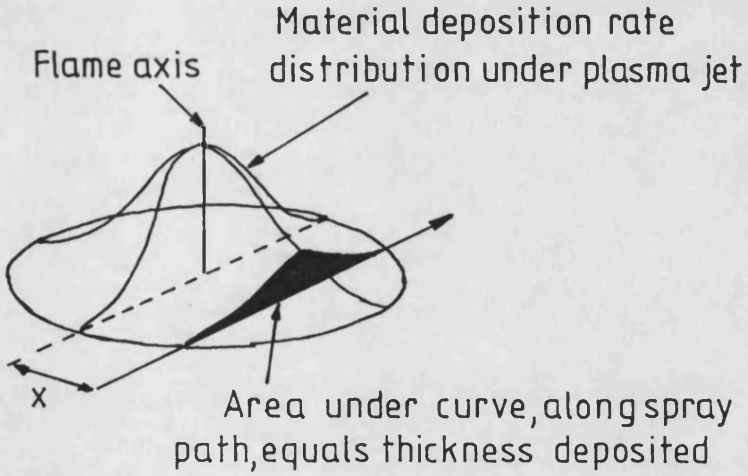

Figure 4·17 Diagram illustrating the variation in material deposition rate with radial distance from the flame axis, after [135].

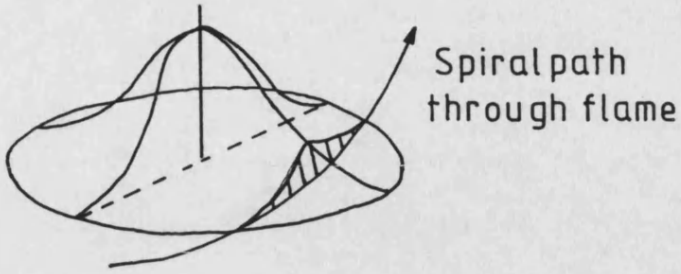

Figure 4·18a Diagram illustrating the spiral path of the reference point through the distribution in figure 4·17.

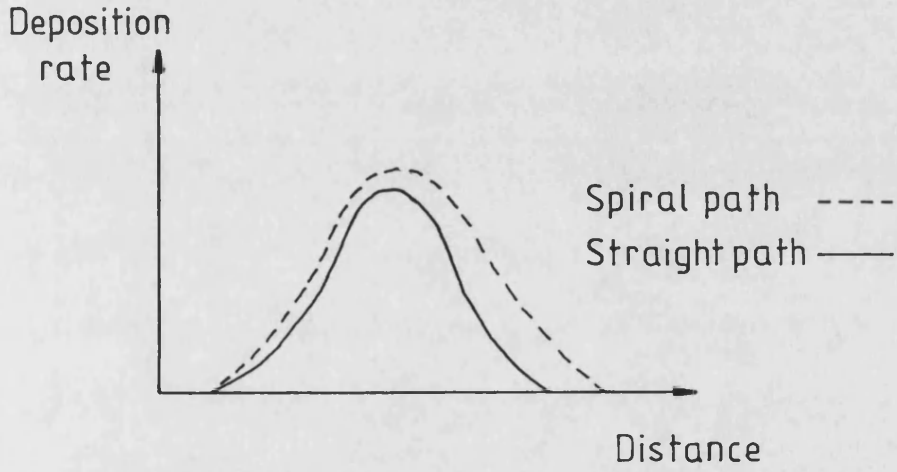

Figure 4·18b Comparitive diagram showing the difference in distribution area for straight and spiral paths beginning at the same location. Note that as the latter continually reduces its radius, the velocity increases and residence time is reduced.

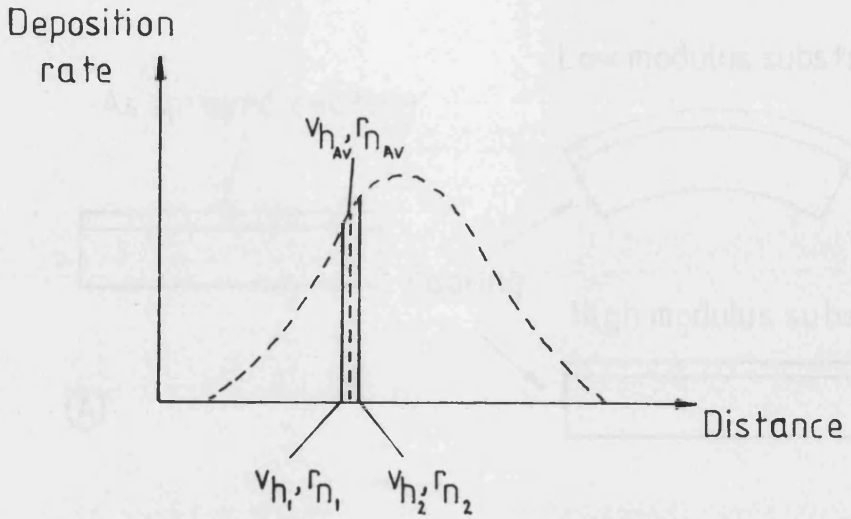

Figure 4·19 Diagram showing the simplification and small error involved in using average values of linear velocity to calculate the thickness of material deposited per time step.

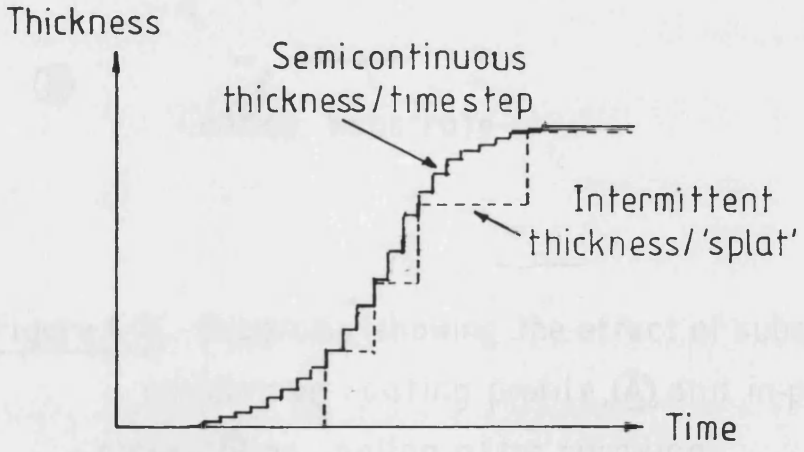

Figure 4·20 Diagram illustrating the technique used to increase the thickness of the model coating by the deposition of uniform 'splats'.

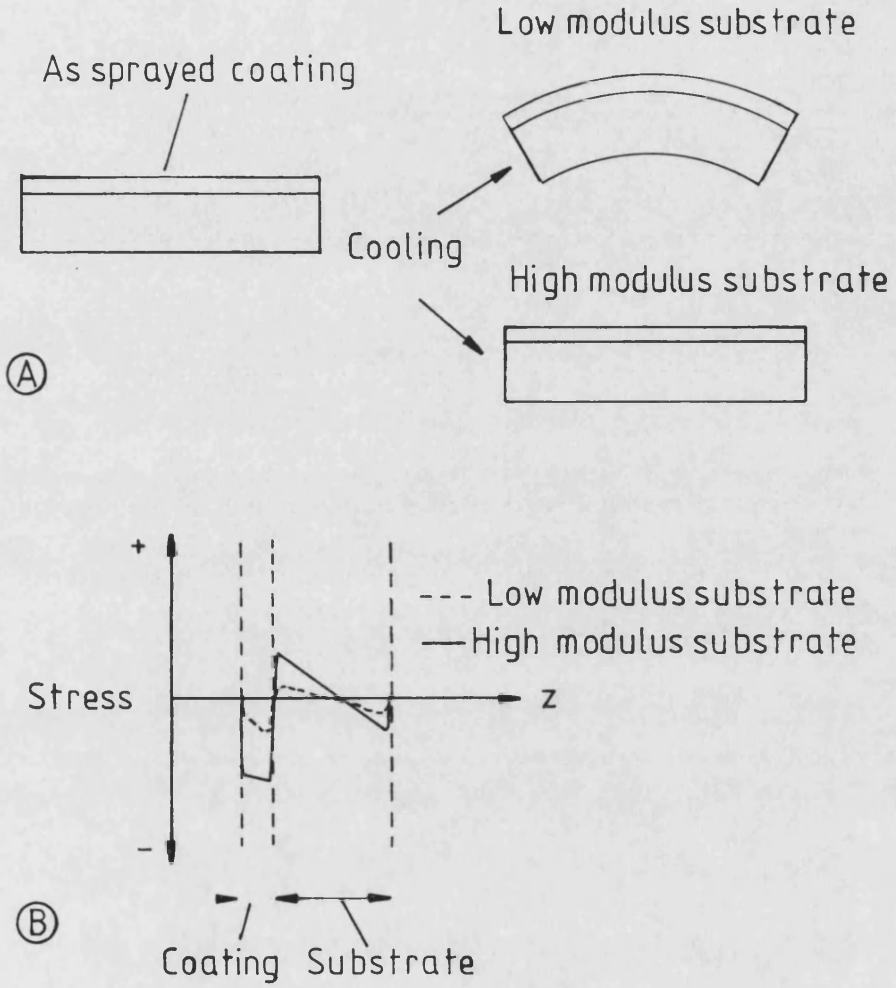

Figure 4·21 Diagrams showing the effect of substrate modulus on coating profile, Ⓐ, and in-plane stress, Ⓑ, on cooling after spraying.

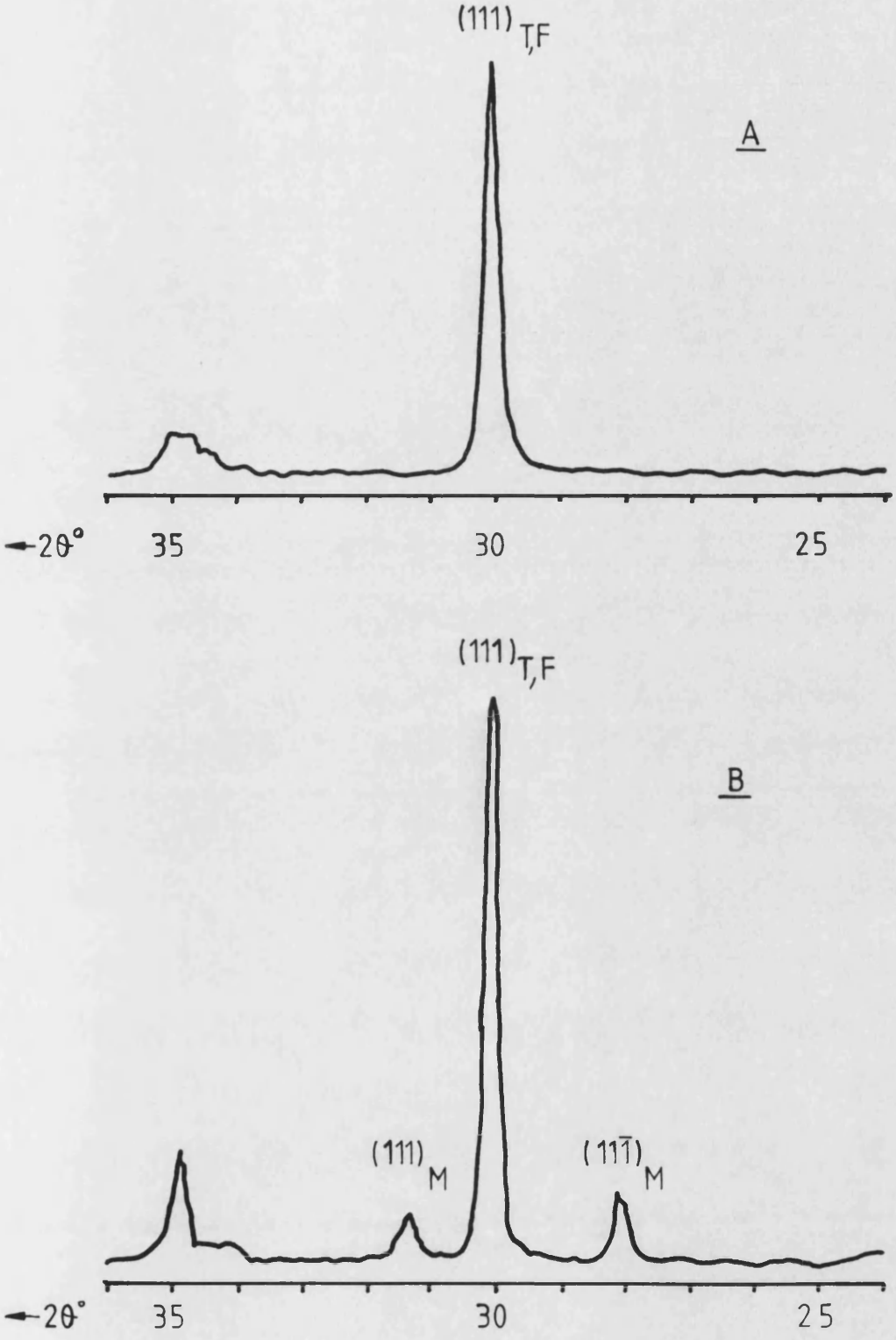

Figure 5·1 X-Ray diffractometer traces from powder A,(A), and powder B,(B), illustrating differences in their phase composition.

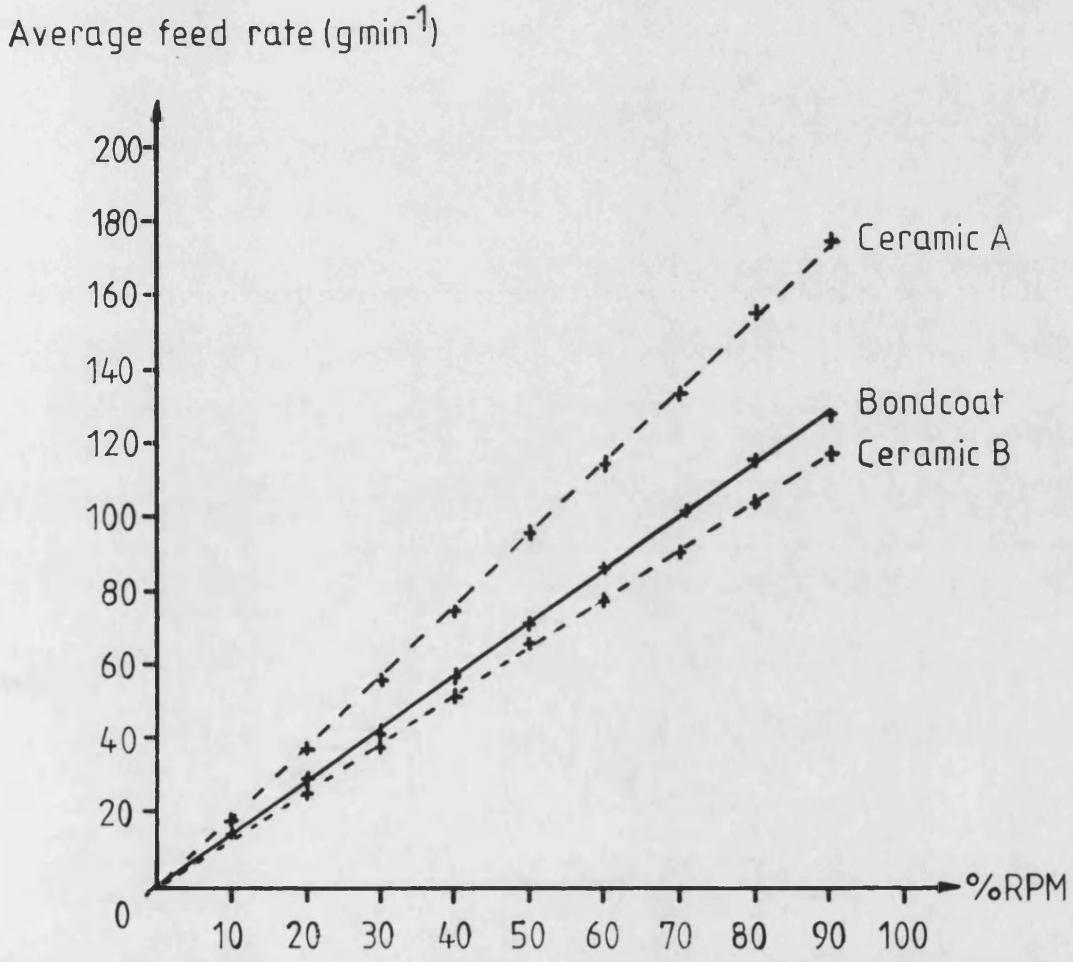

Figure 5·2 Feed rate calibration data for ceramic and bondcoat powder materials.

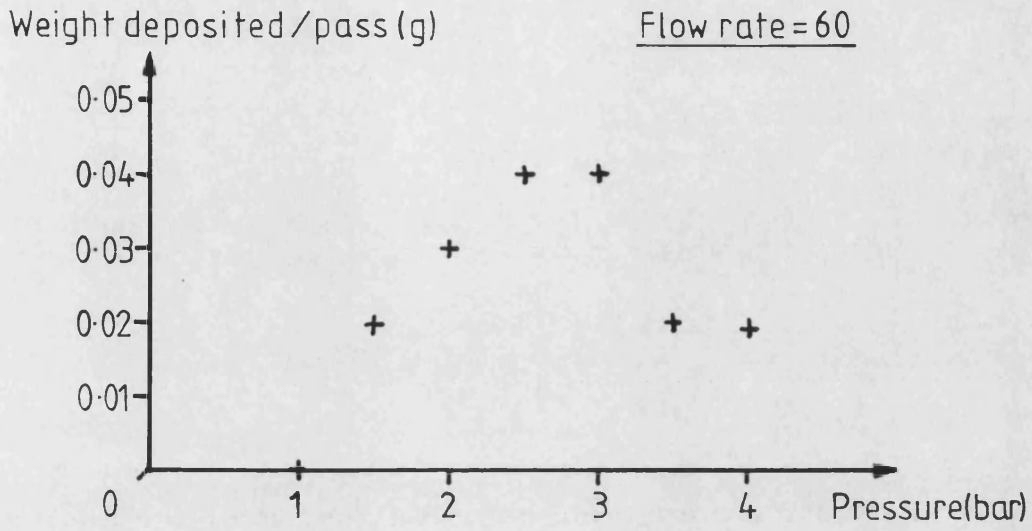

Figure 5·3a Graph showing the variation in deposit efficiency of material A with powder feed gas pressure.

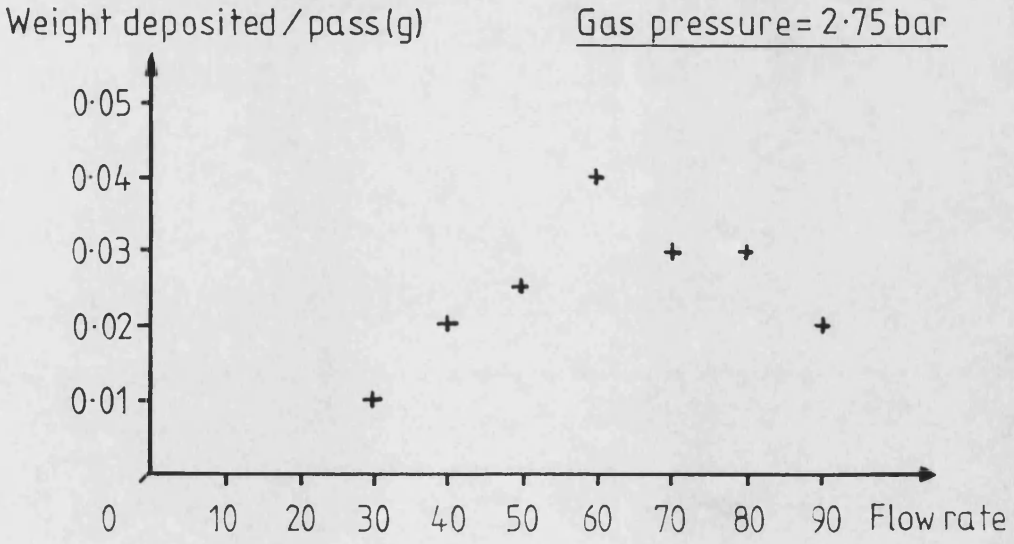

Figure 5·3b Graph showing the variation in deposit efficiency of material A with powder feed gas flow rate.

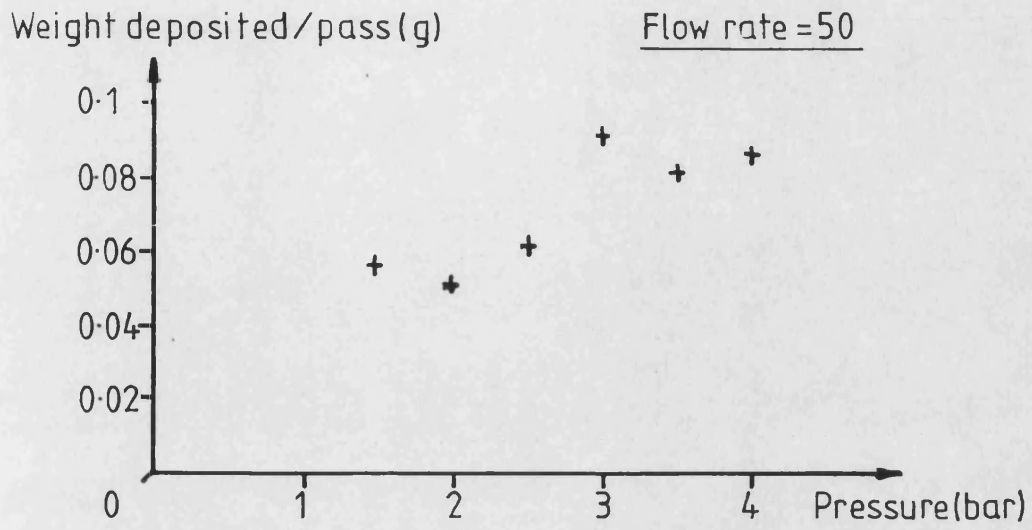

Figure 5·4a Graph showing the variation in deposit efficiency of material B with powder feed gas pressure.

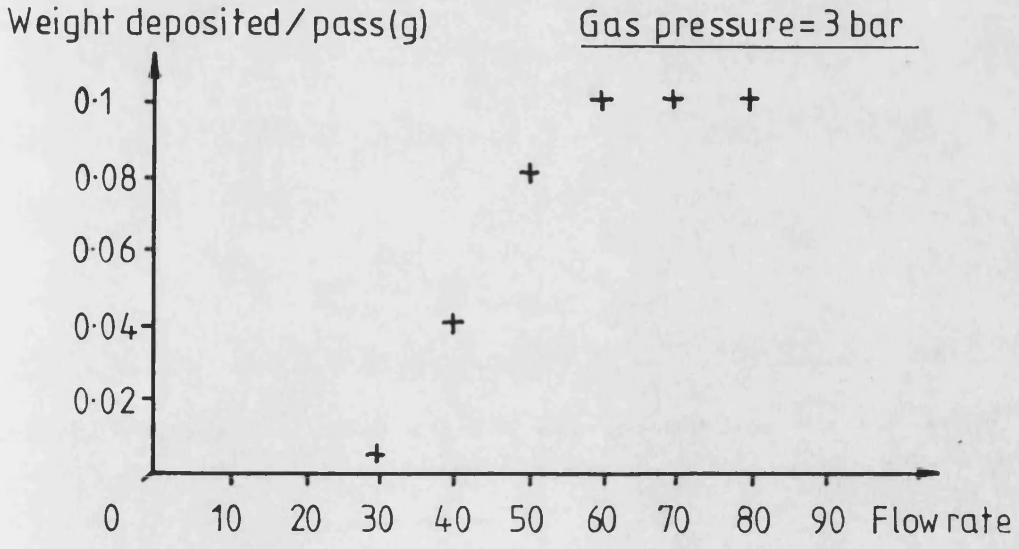

Figure 5·4b Graph showing the variation in deposit efficiency of material B with powder feed gas flow rate.

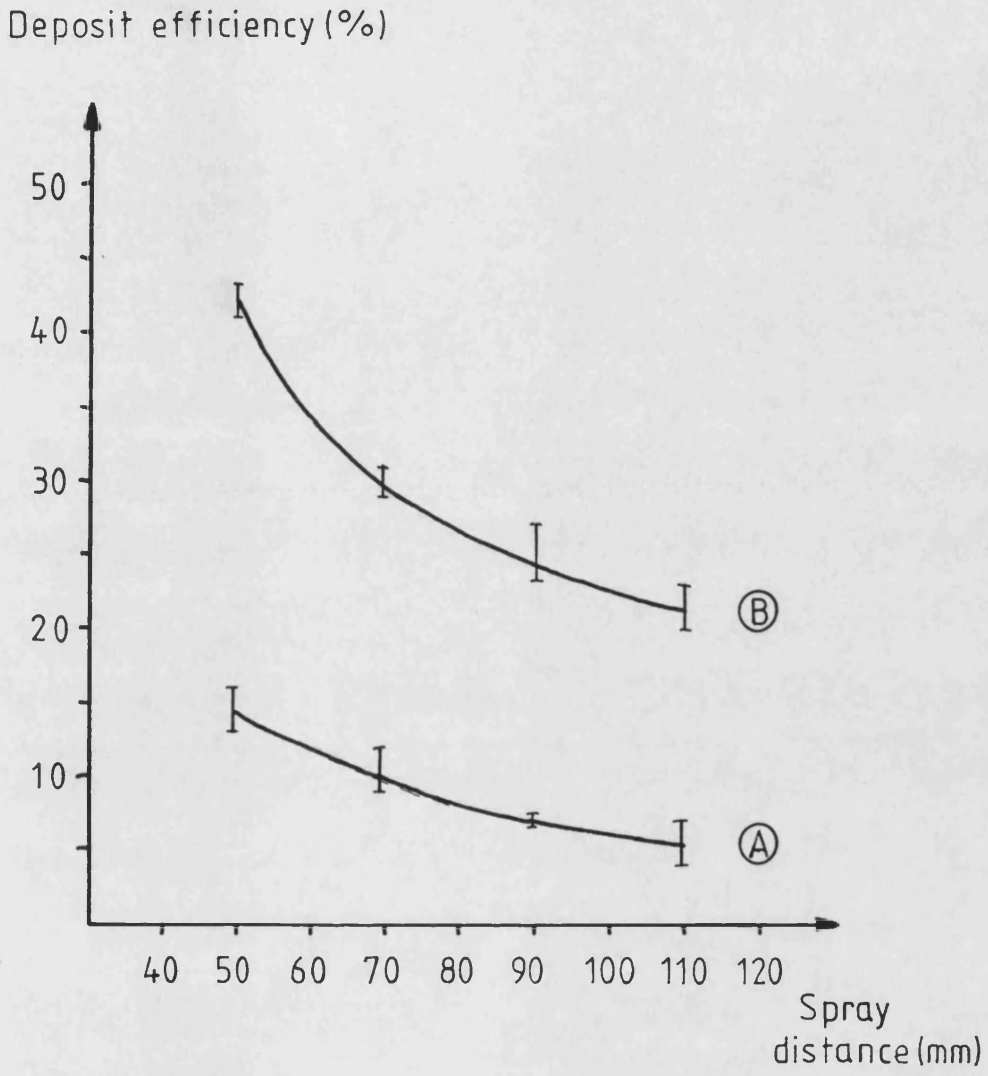

Figure 5·5 Graph illustrating the relationship between ceramic powder deposit efficiency and spray distance for materials A and B

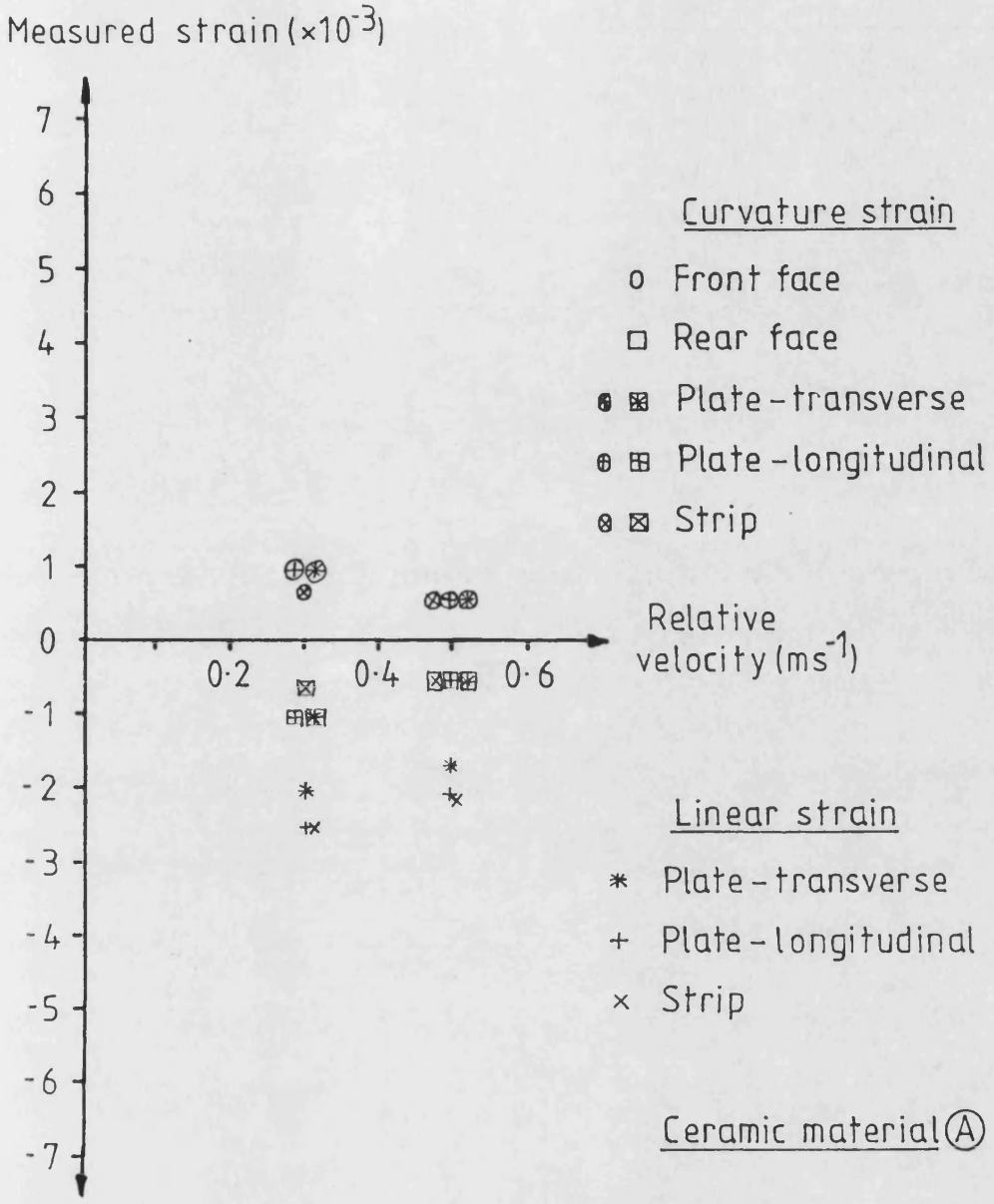

Figure 5·6a Graph illustrating the relationship between measured values of both curvature and linear residual strain and substrate plate size, under varying deposit conditions.

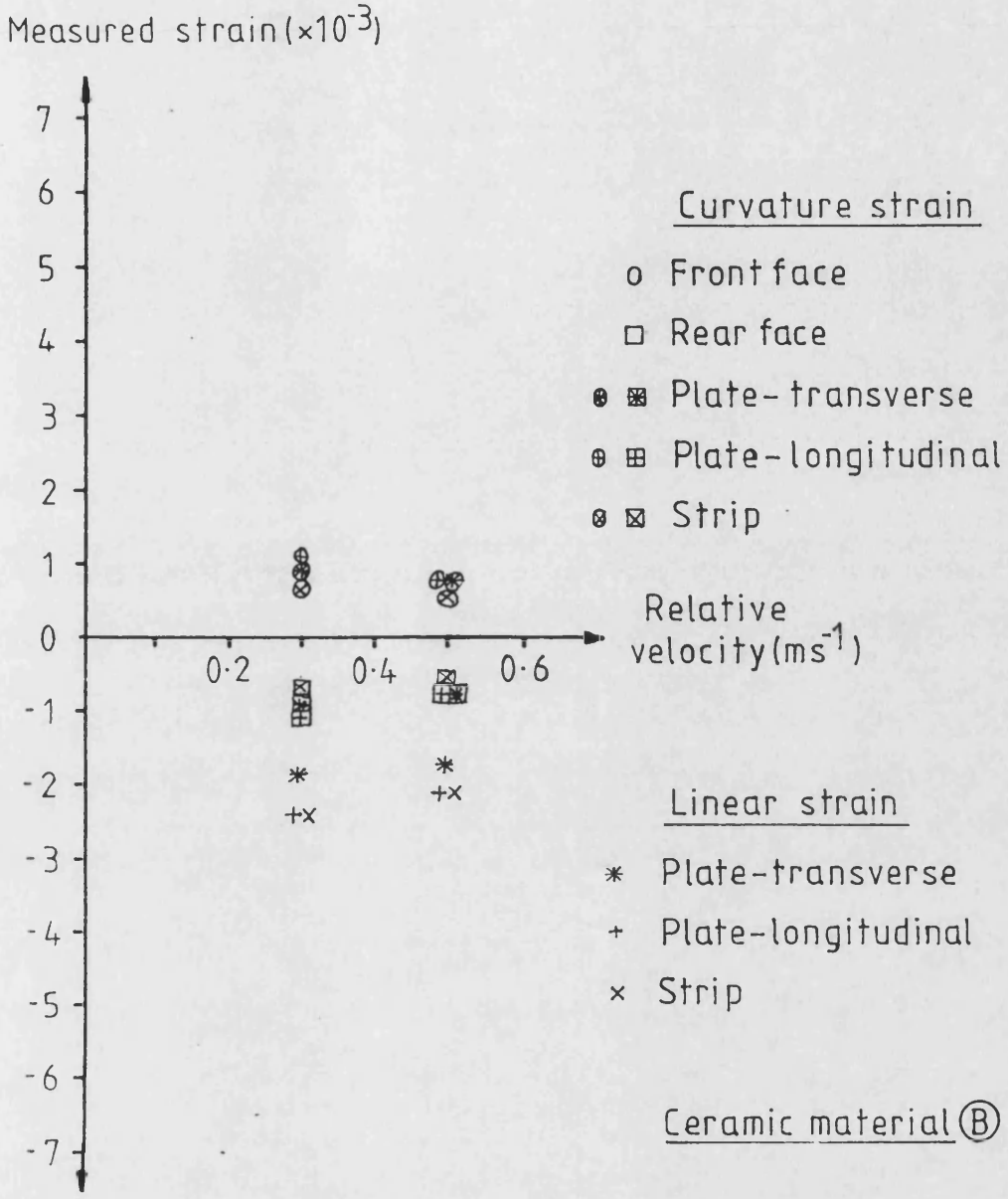

Figure 5·6b Graph illustrating the relationship between measured values of both curvature and linear residual strain and substrate plate size, under varying conditions.

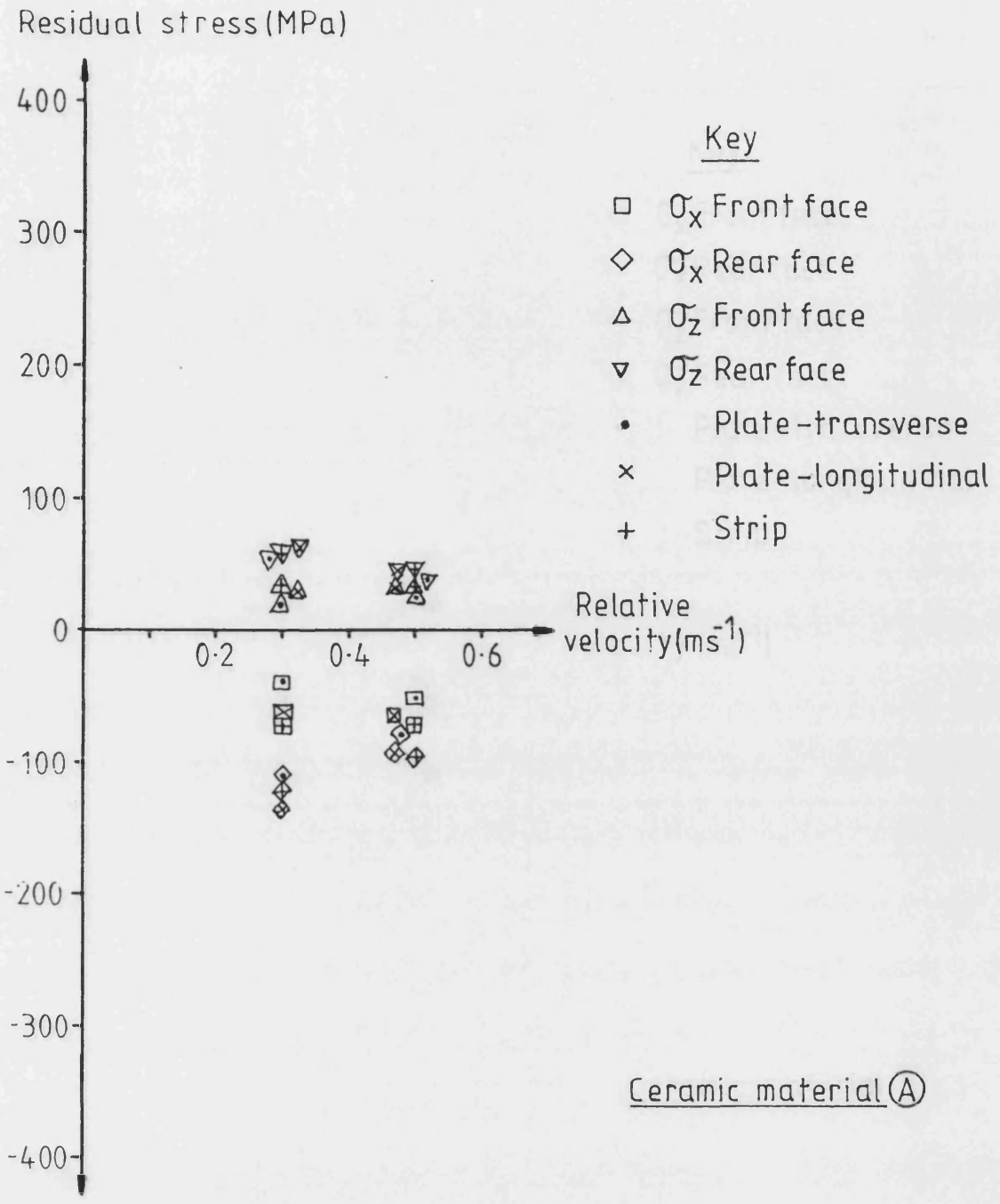

Figure 5·7a Graph illustrating the relationship between coating residual stresses and substrate plate size, under varying deposit conditions.

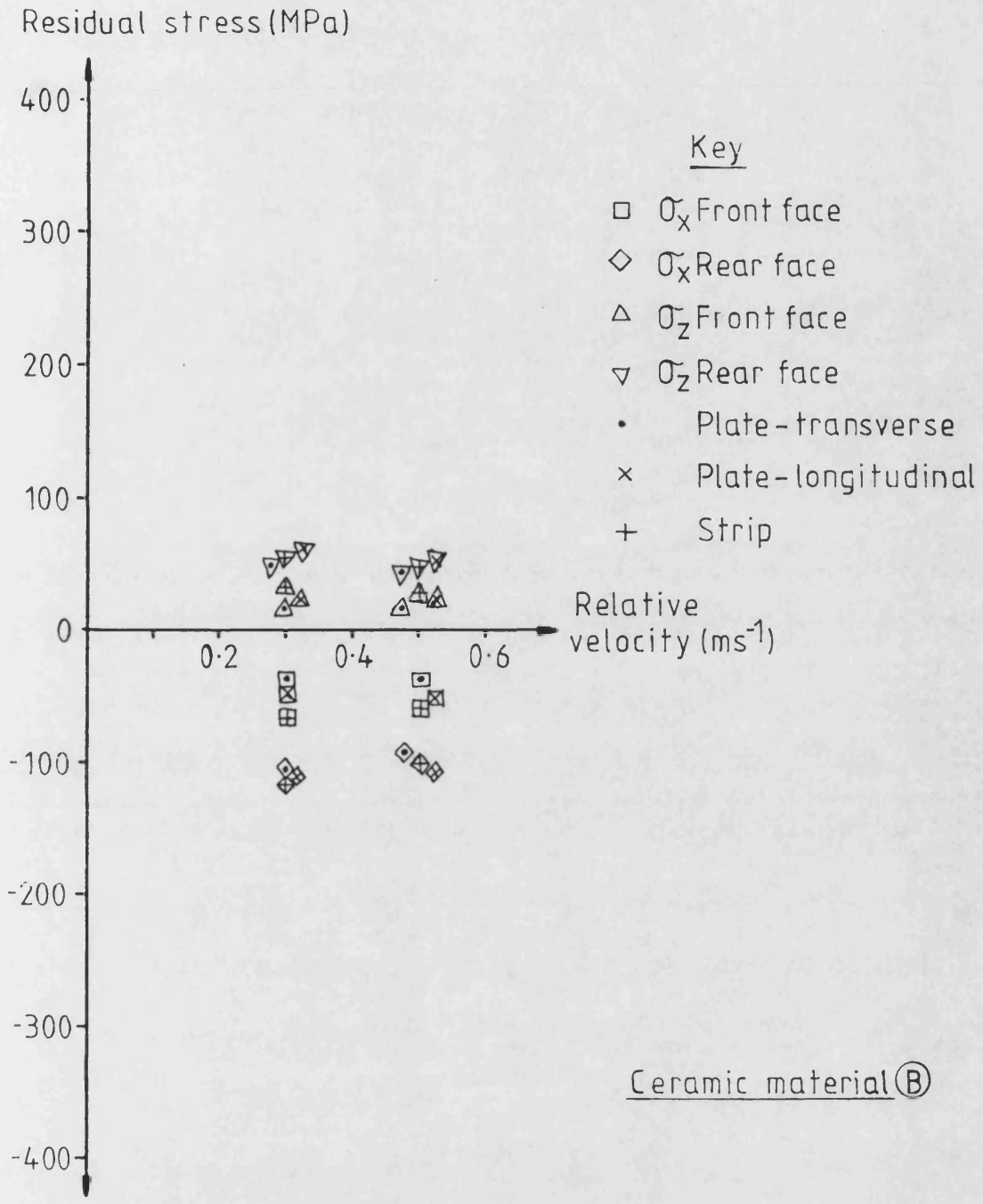

Figure 5·7b Graph illustrating the relationship between coating residual stresses and substrate plate size, under varying deposit conditions

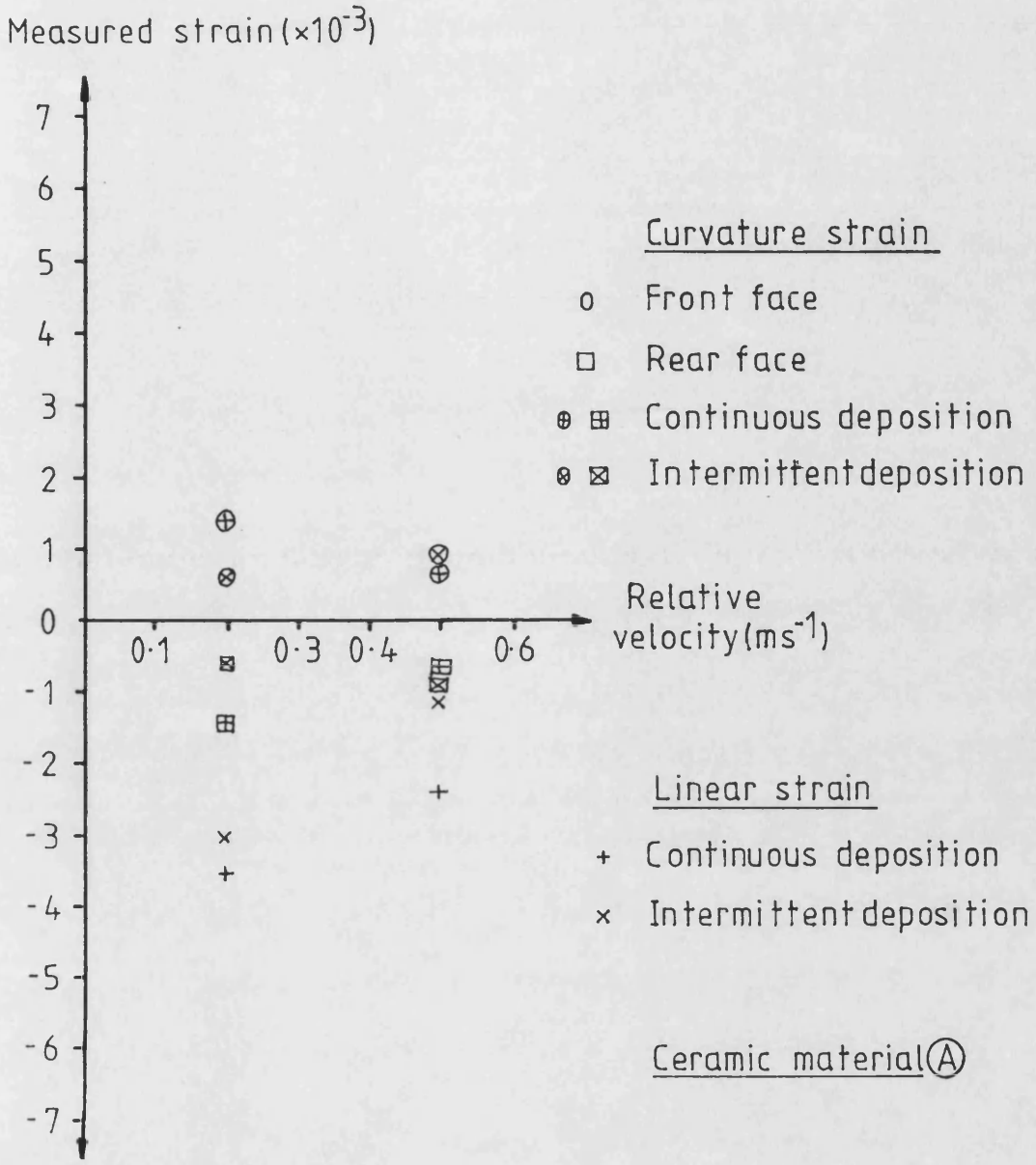

Figure 5·8 Graph illustrating the relationship between measured values of both curvature and linear residual strain and deposition method, under varying conditions.

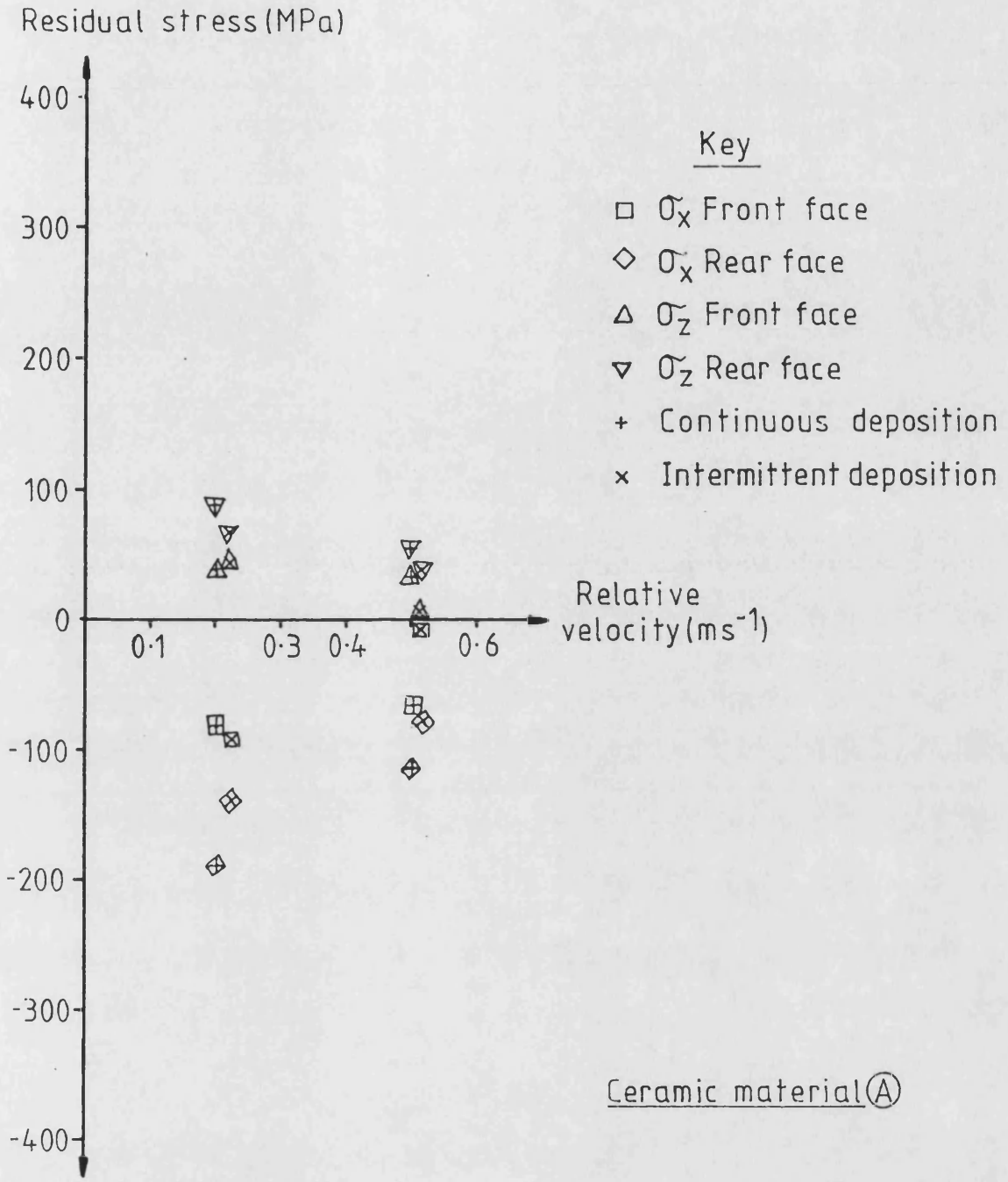

Figure 5·9 Graph illustrating the relationship between coating residual stresses and deposition method, under varying conditions.

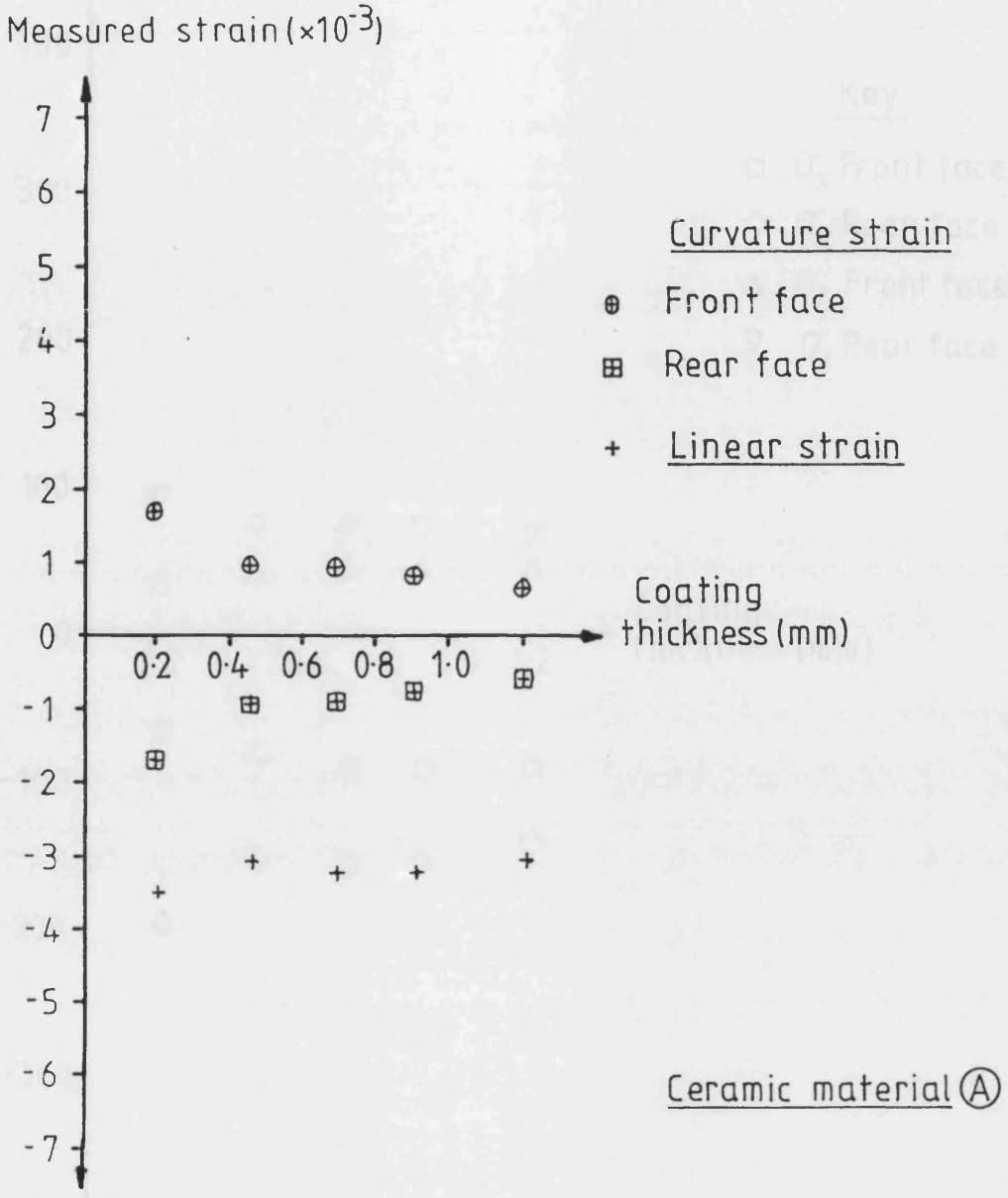

Figure 5·10 Graph illustrating the relationship between measured values of both curvature and linear residual strain and coating thickness.

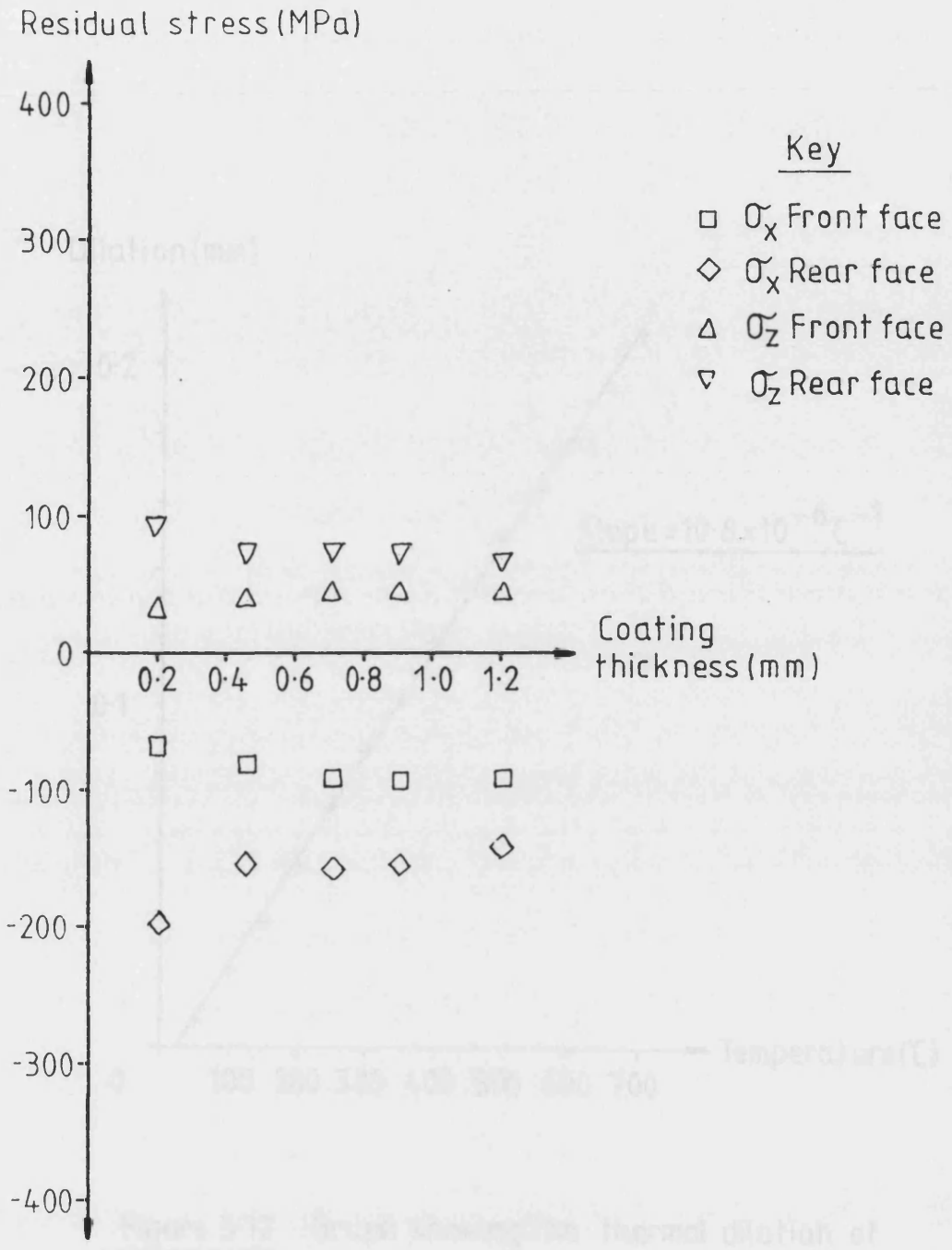

Figure 5·11 Graph illustrating the relationship between coating residual stresses and coating thickness.

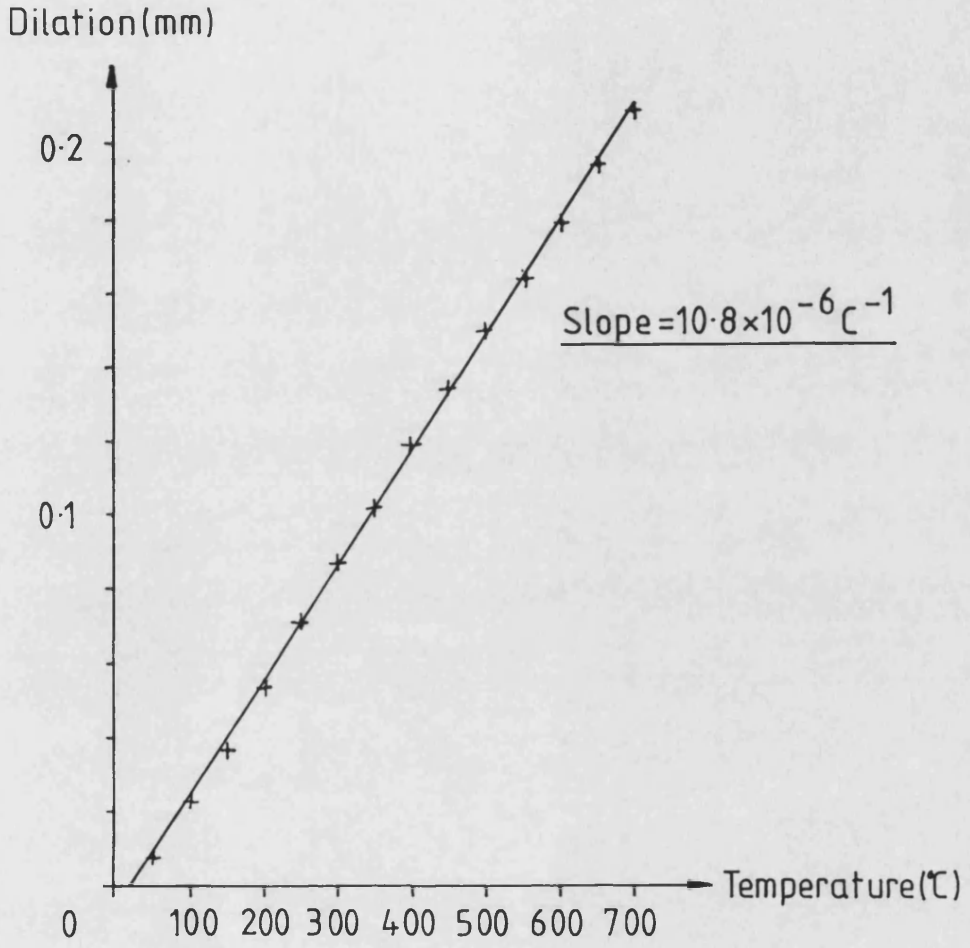

Figure 5·12 Graph showing the thermal dilation of a free coating sample of material A.

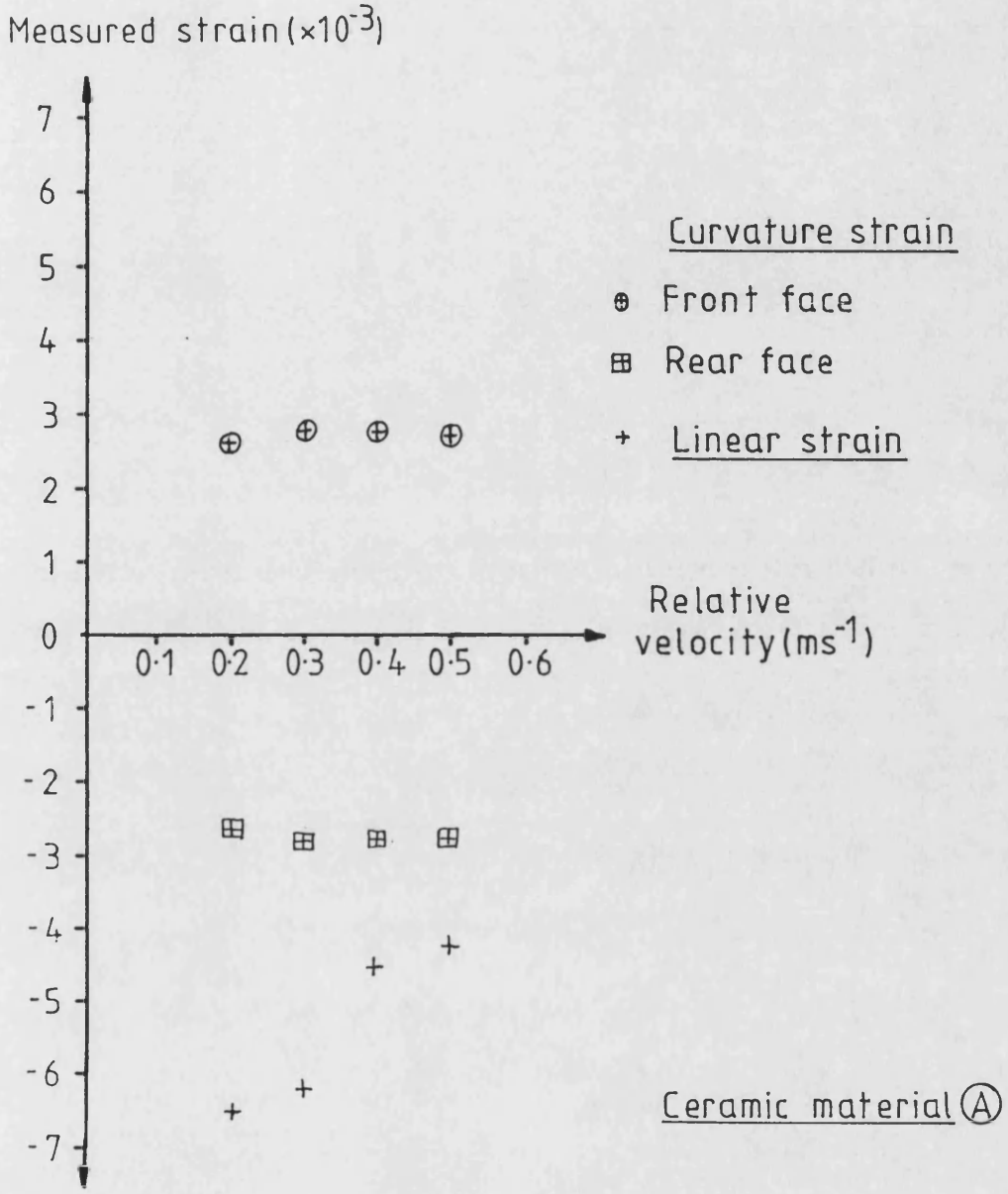

Figure 5·13 Graph illustrating the relationship between measured values of both curvature and linear residual strain and workpiece/sprayhead relative velocity. Spray distance = 65mm.

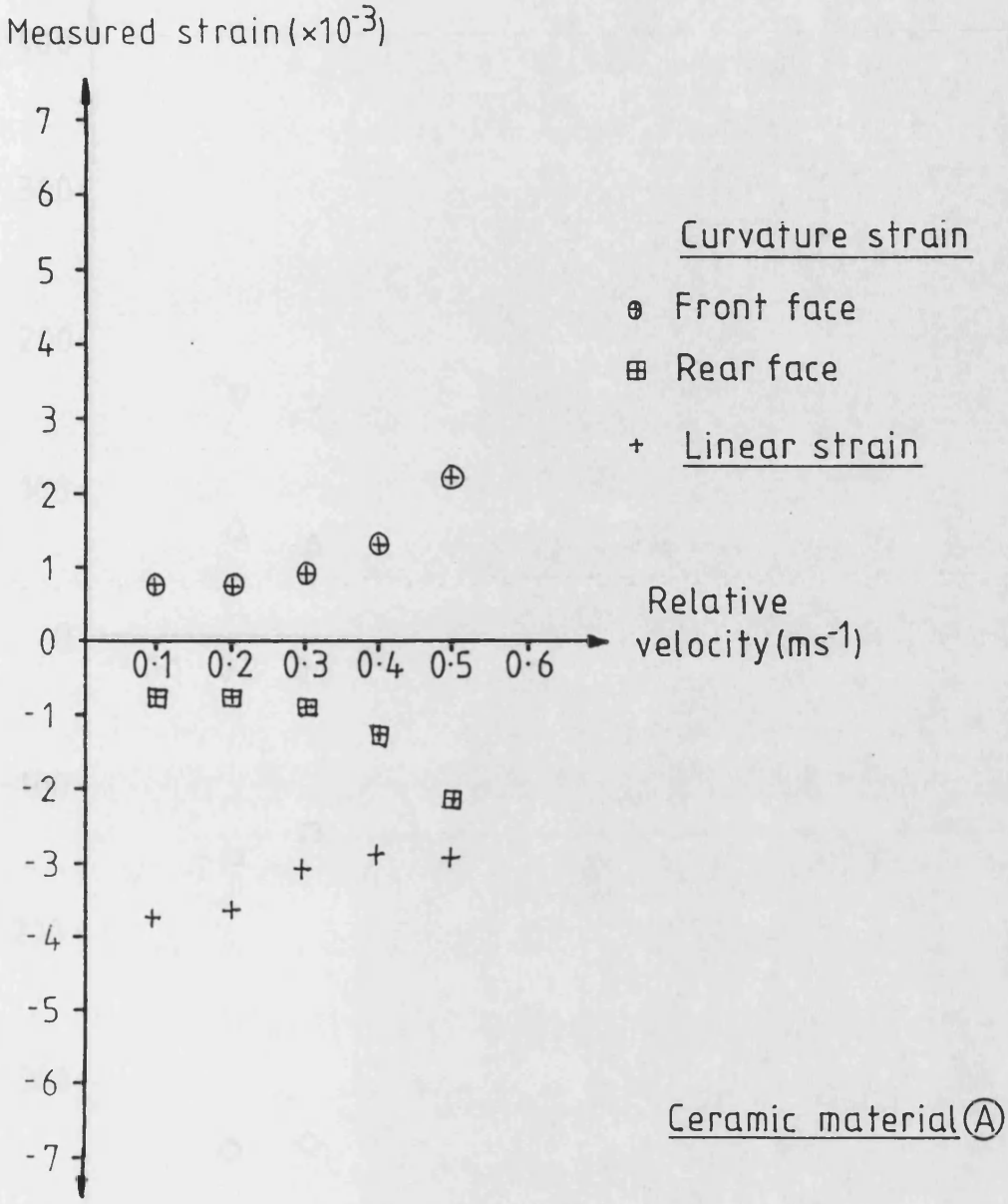

Figure 5·14 Graph illustrating the relationship between measured values of both curvature and linear residual strain and workpiece/sprayhead relative velocity. Spray distance = 110 mm.

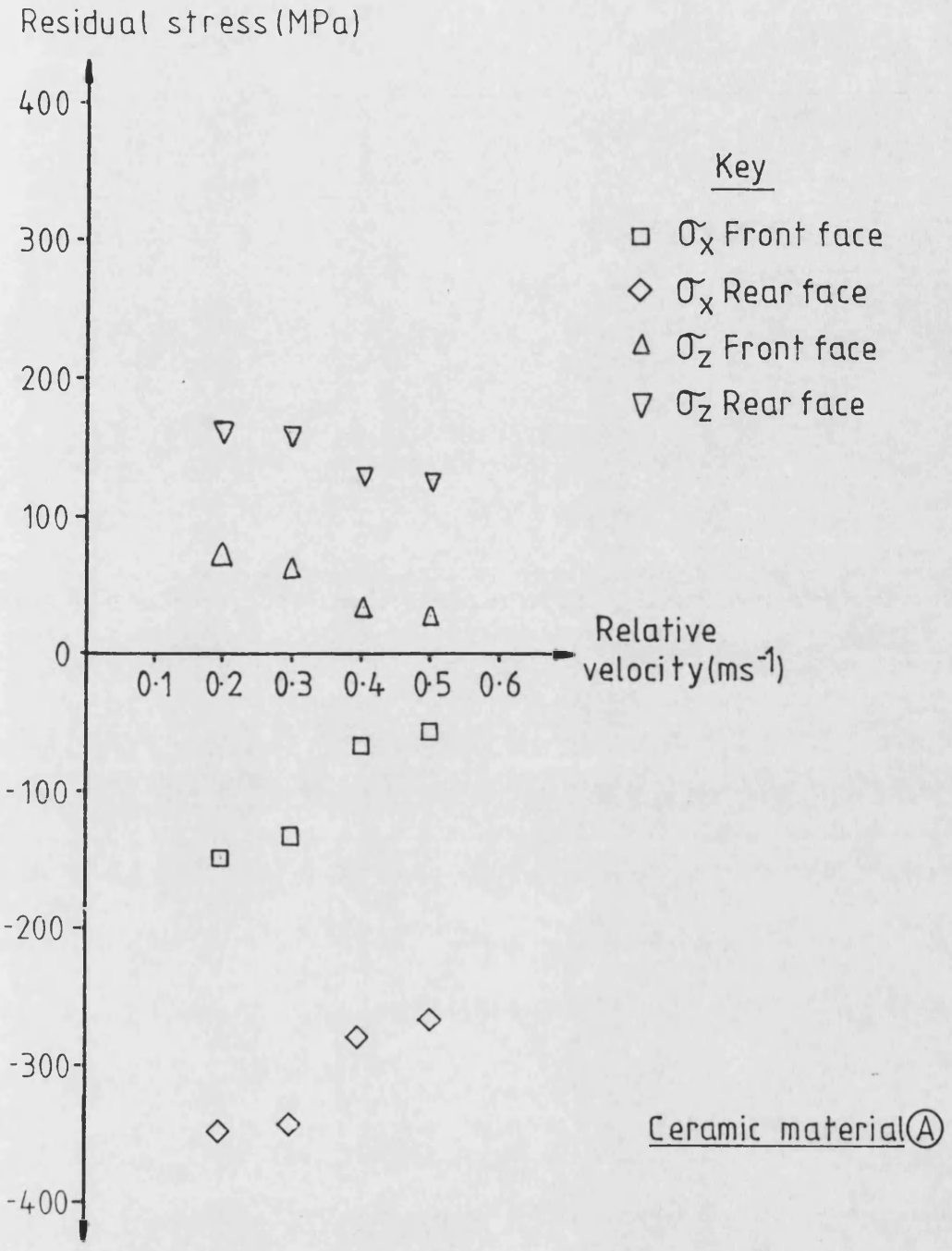

Figure 5·15 Graph illustrating the relationship between coating residual stresses and workpiece/sprayhead relative velocity. Spray distance = 65 mm.

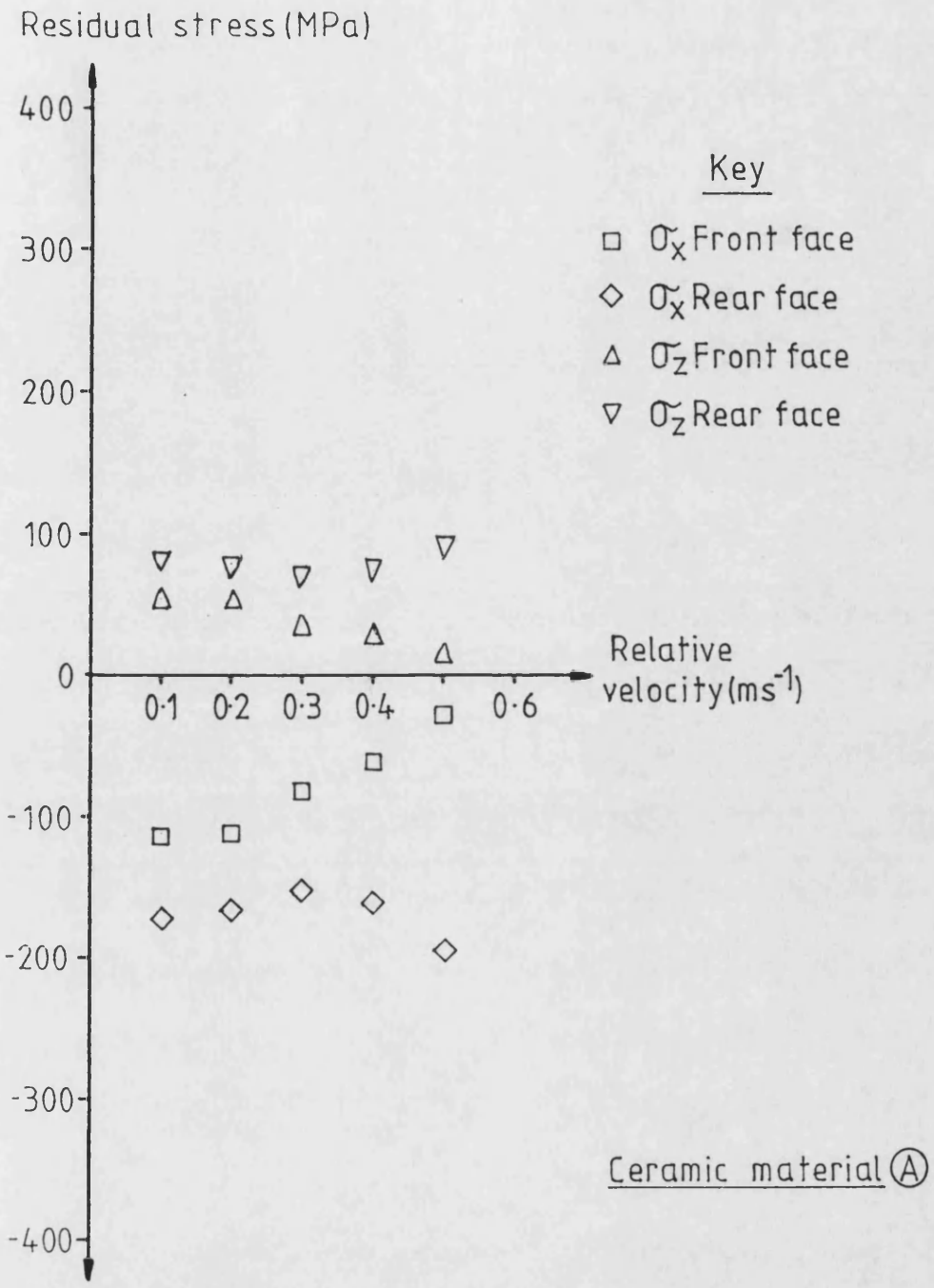

Figure 5·16 Graph illustrating the relationship between coating residual stresses and workpiece/sprayhead relative velocity. Spray distance = 110 mm.

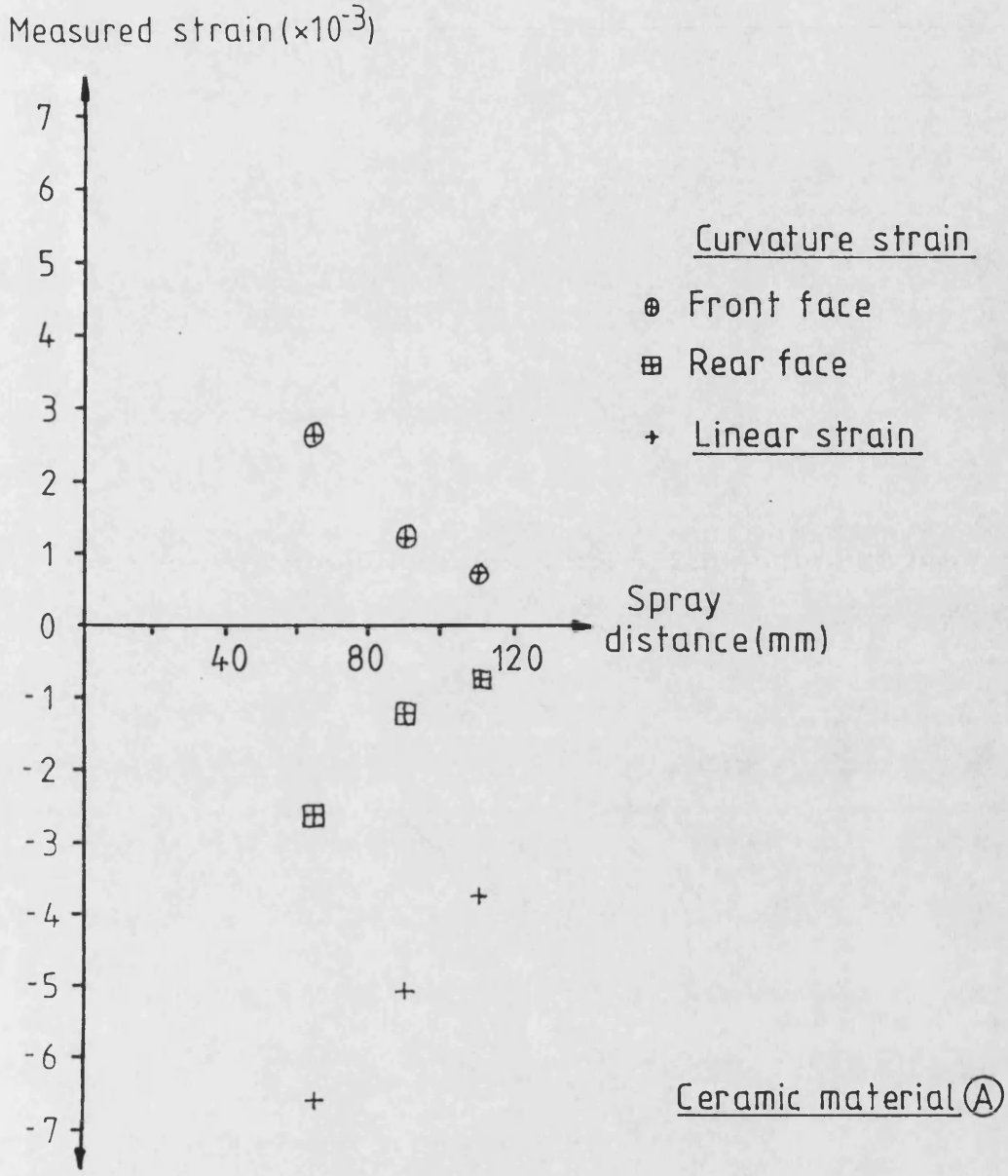

Figure 5·17 Graph illustrating the relationship between measured values of both curvature and linear residual strain and spray distance. Relative velocity=0·2 ms^{-1}

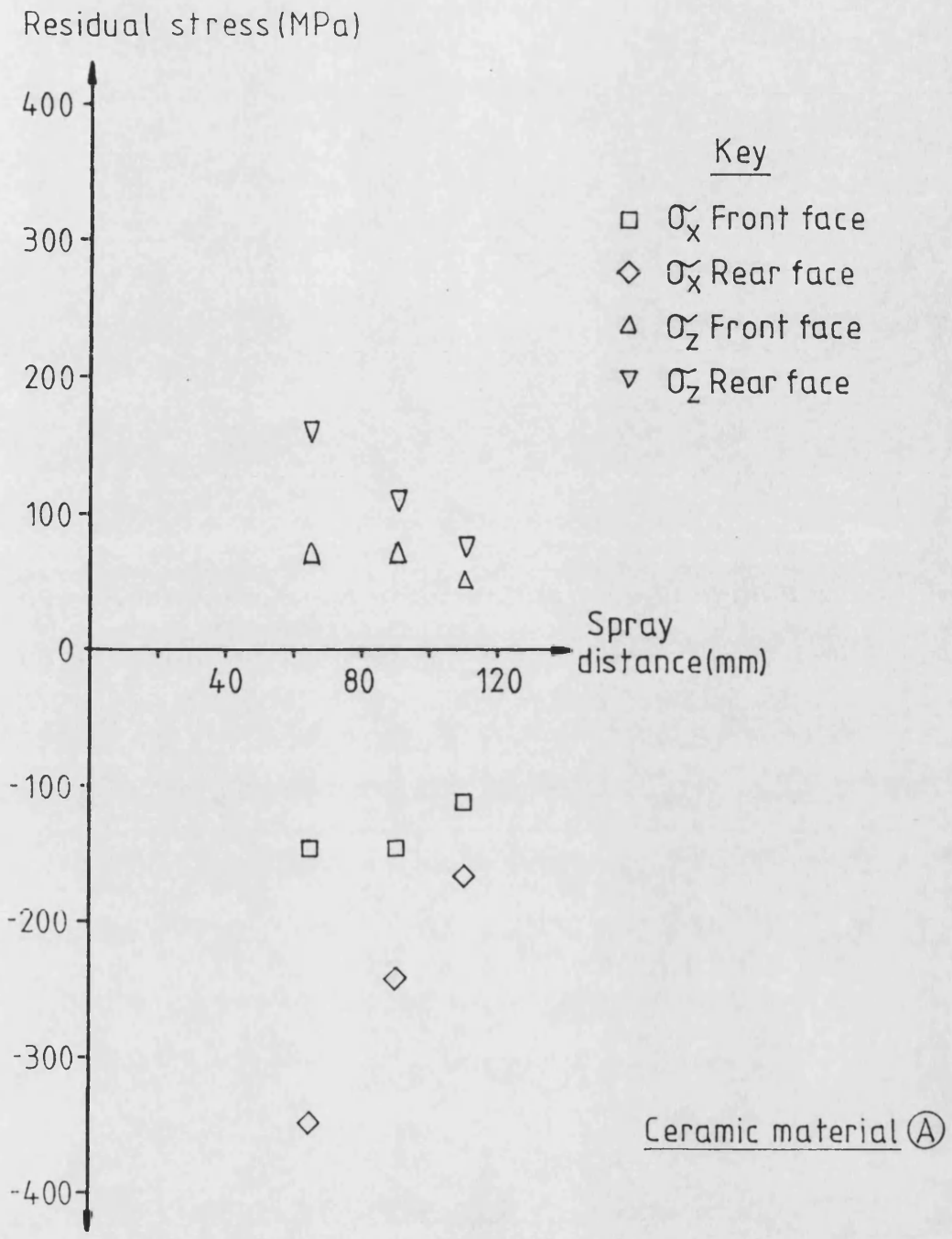

Figure 5·18 Graph illustrating the relationship between coating residual stresses and spray distance. Relative velocity = 0·2 ms^{-1}

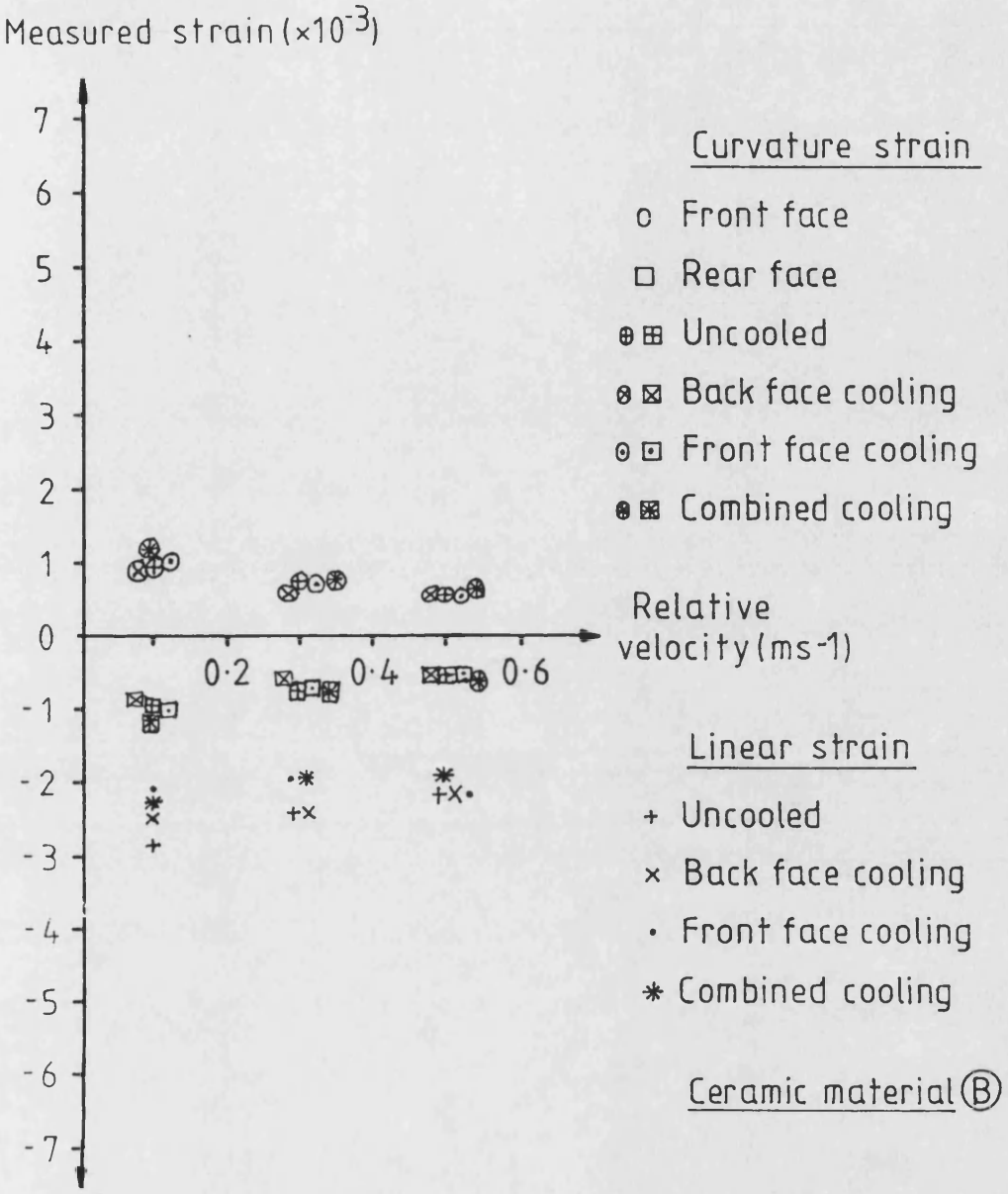

Figure 5·19 Graph illustrating the relationship between measured values of both curvature and linear residual strain and workpiece/sprayhead relative velocity. Coatings were deposited under various cooling conditions.

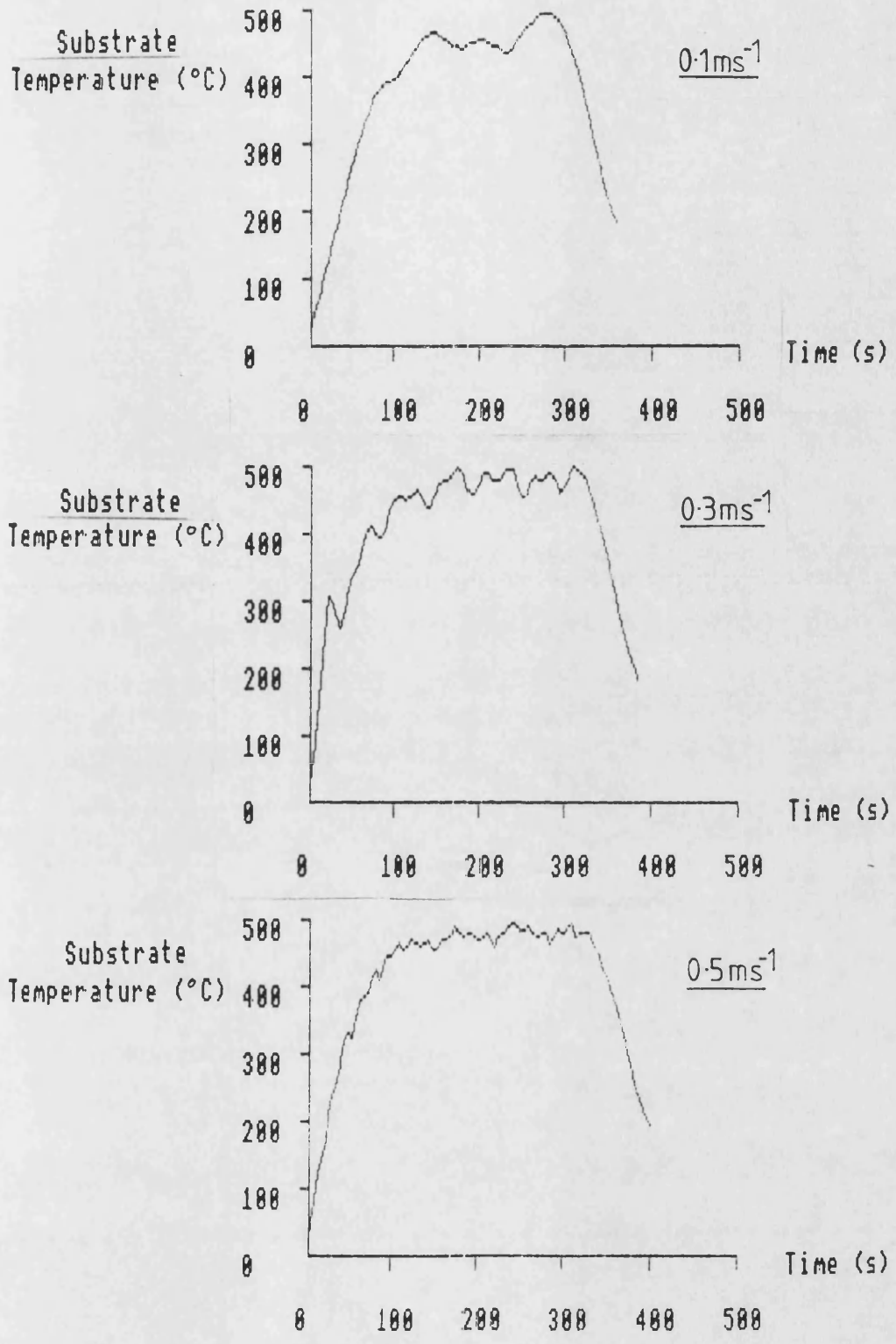

Figure 5·20 Graphs showing substrate temperature during spraying at 0·1, 0·3 and 0·5ms^{-1} without air cooling.

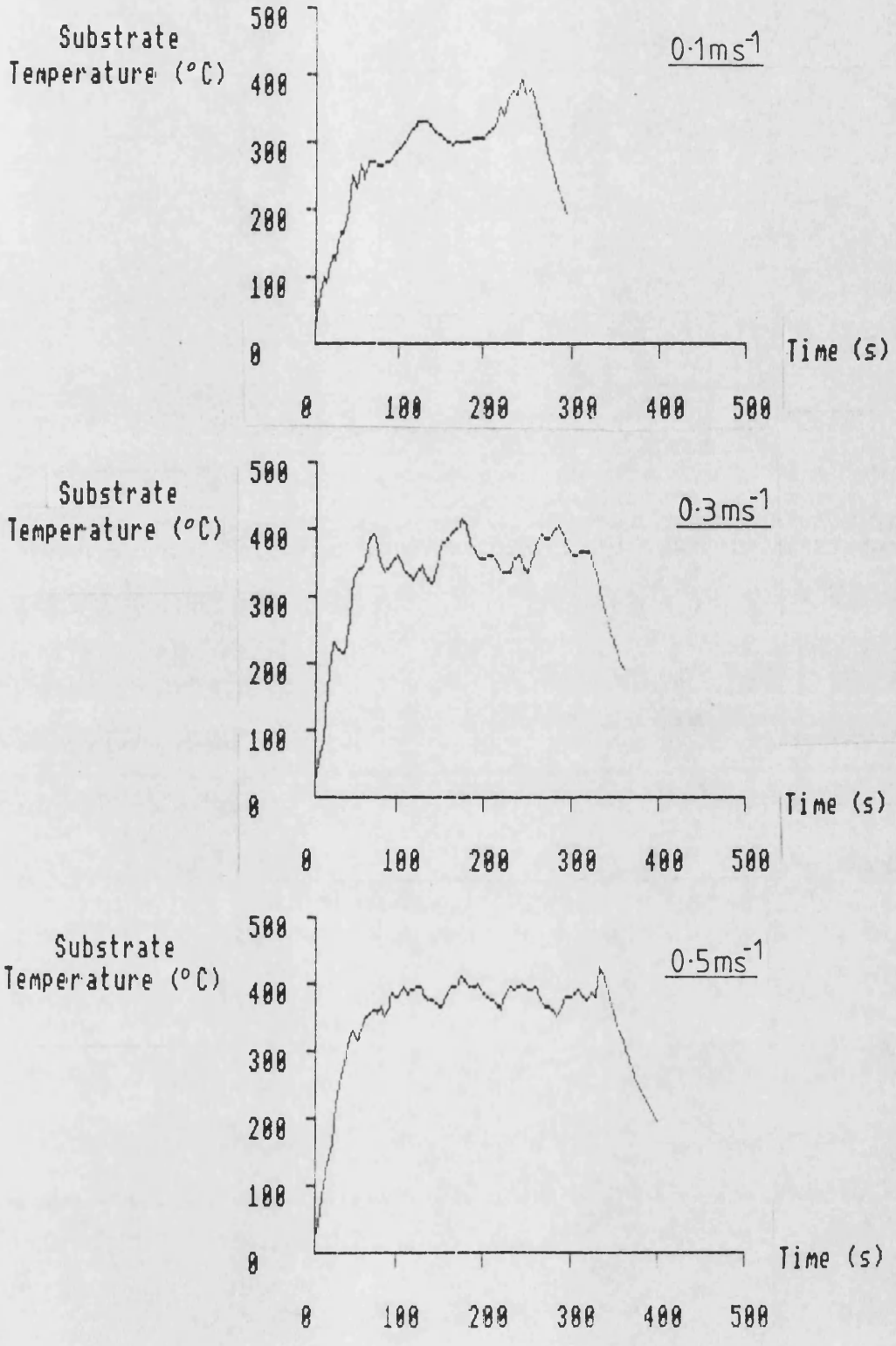

Figure 5·21 Graphs showing substrate temperature during spraying at 0·1, 0·3 and 0·5 ms^{-1} with back face air cooling.

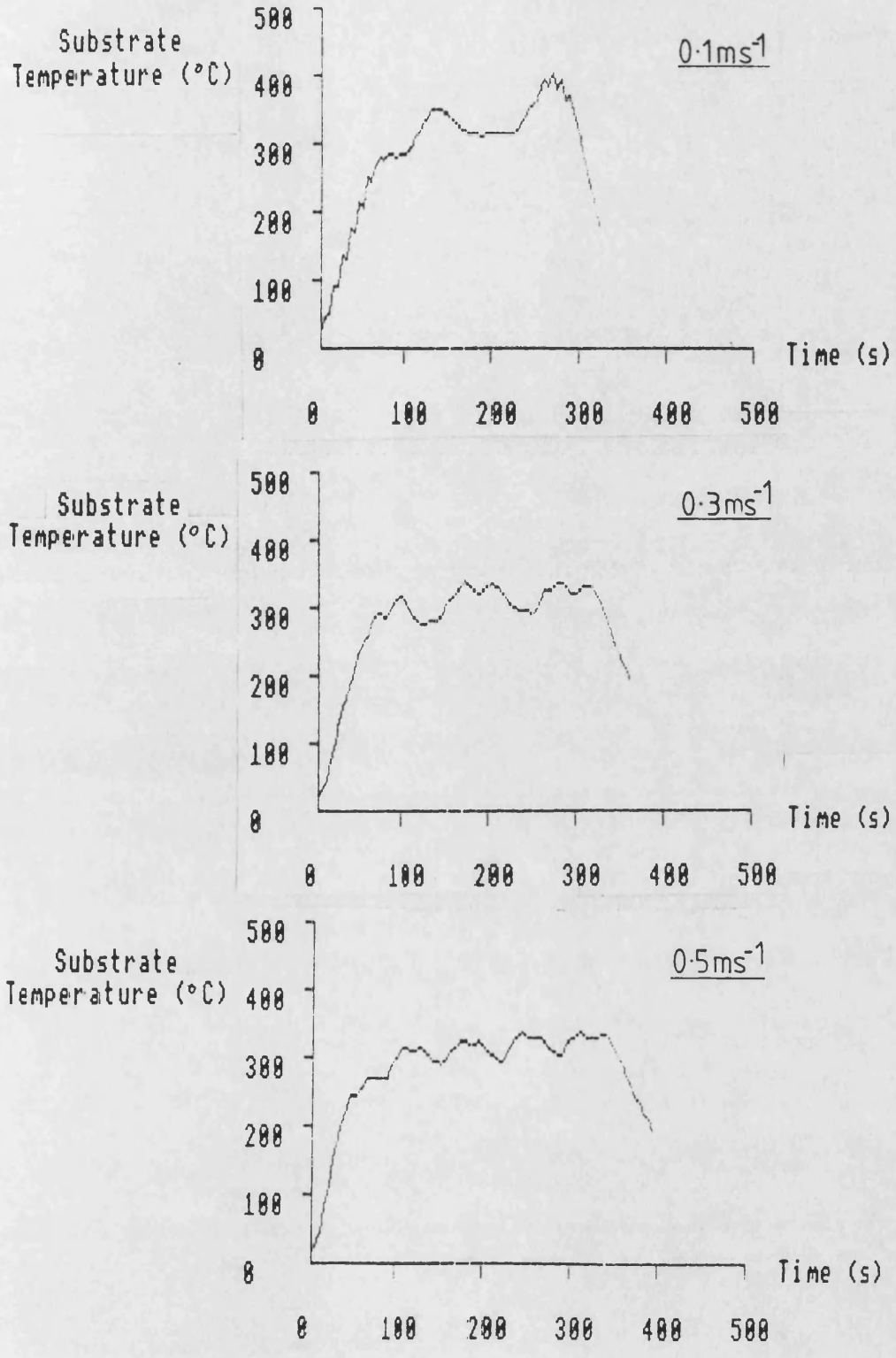

Figure 5·22 Graphs showing substrate temperature during spraying at 0·1, 0·3 and 0·5ms^{-1} with front face air cooling.

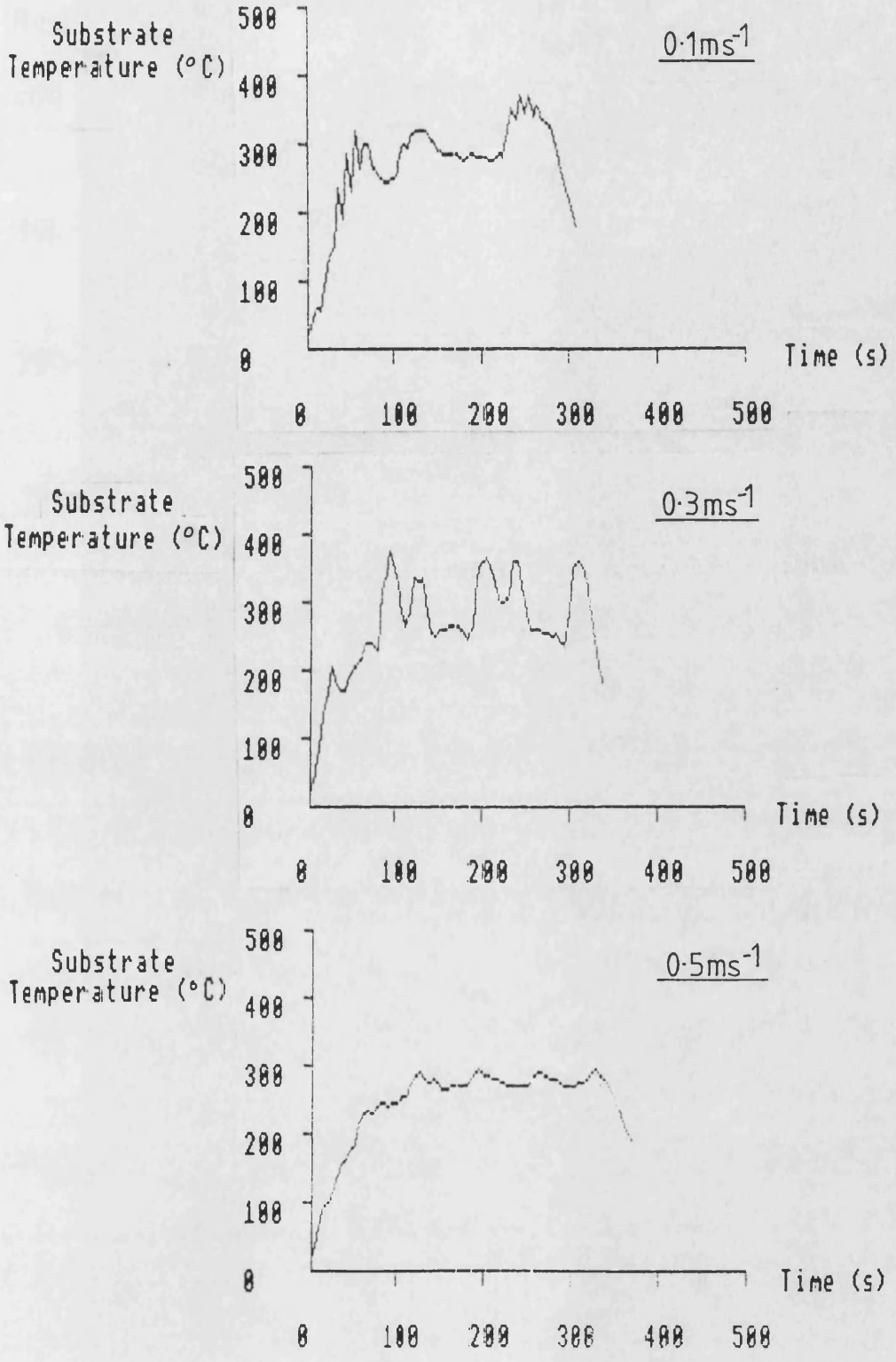

Figure 5·23 Graphs showing substrate temperature during spraying at 0·1, 0·3 and 0·5ms^{-1} with combined front and back face air cooling.

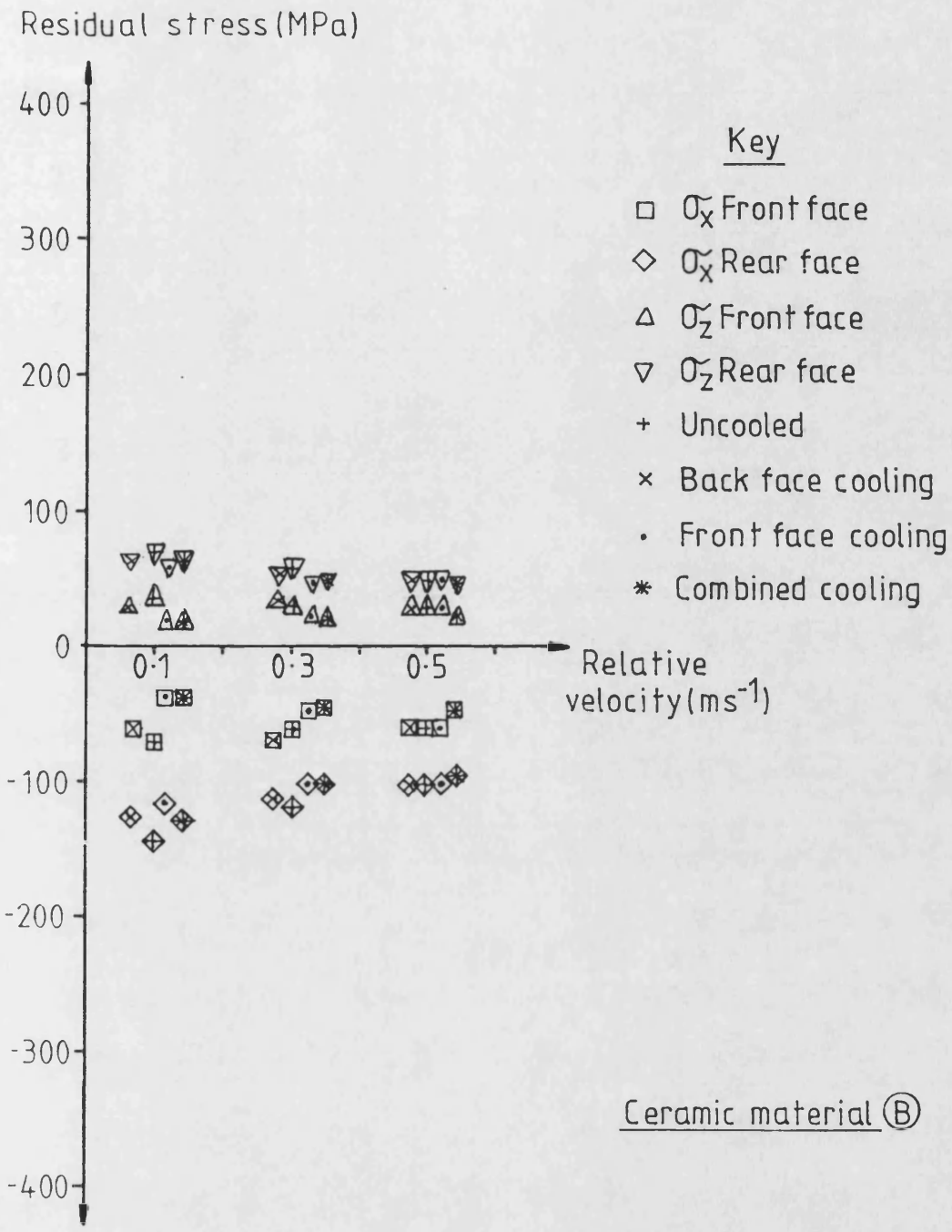

Figure 5·24 Graph illustrating the relationship between coating residual stresses and workpiece/sprayhead relative velocity. Coatings were deposited under various cooling conditions.

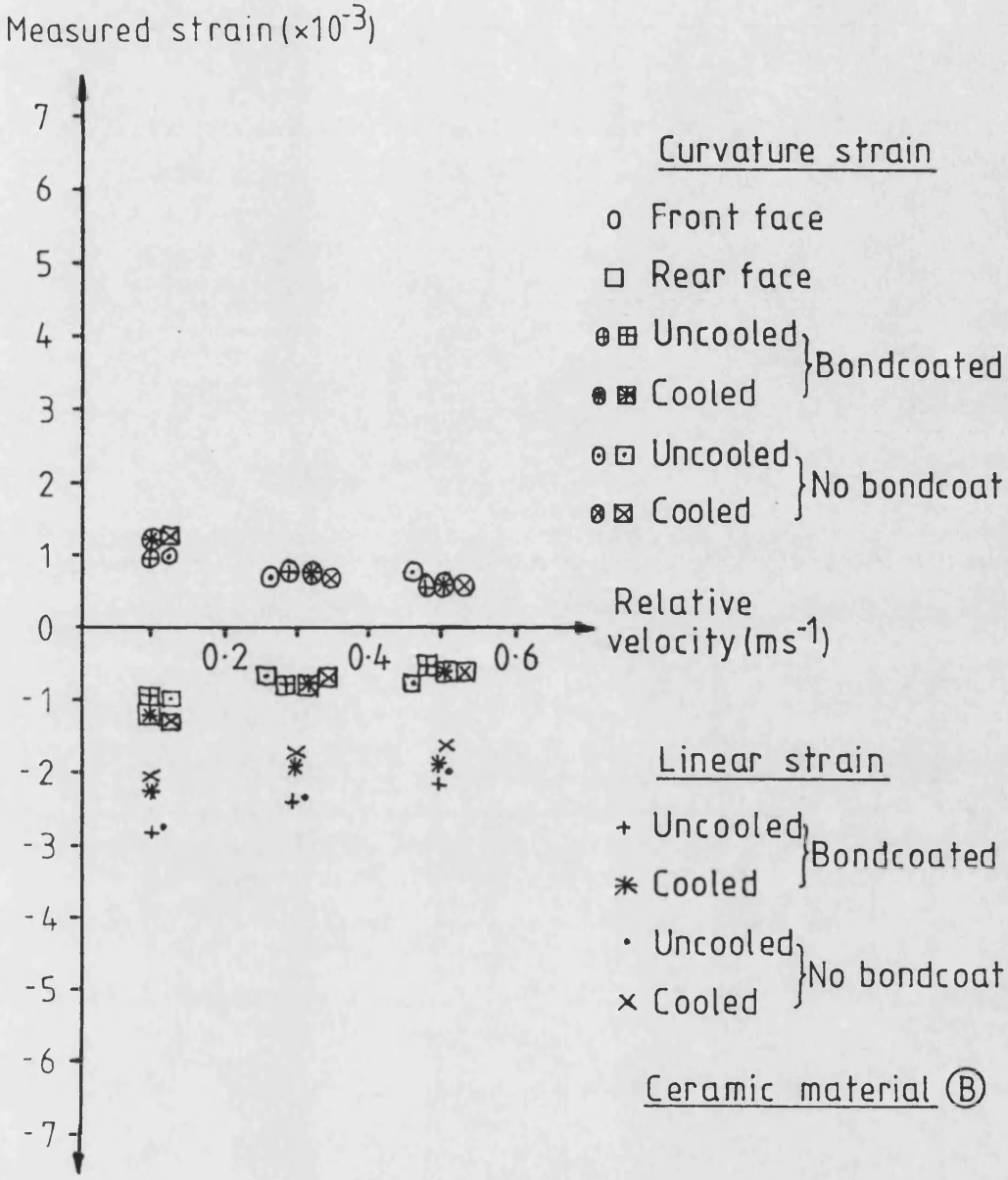

Figure 5·25 Graph illustrating the relationship between measured values of both curvature and linear residual strain and workpiece/sprayhead relative velocity. Coatings were deposited with and without bondcoats and air cooling.

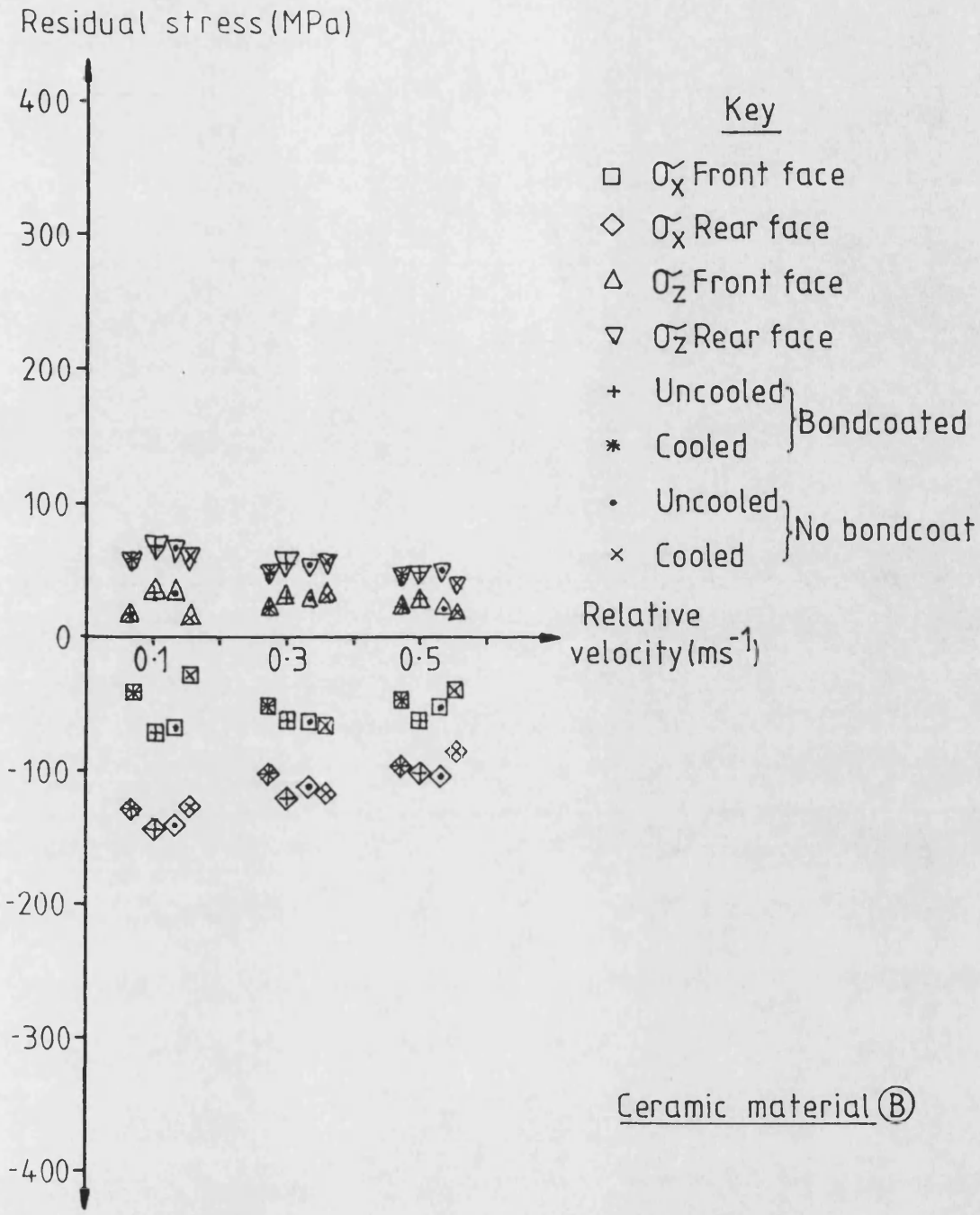

Figure 5·26 Graph illustrating the relationship between coating residual stresses and workpiece/sprayhead relative velocity. Coatings were deposited with and without bondcoats and air cooling.

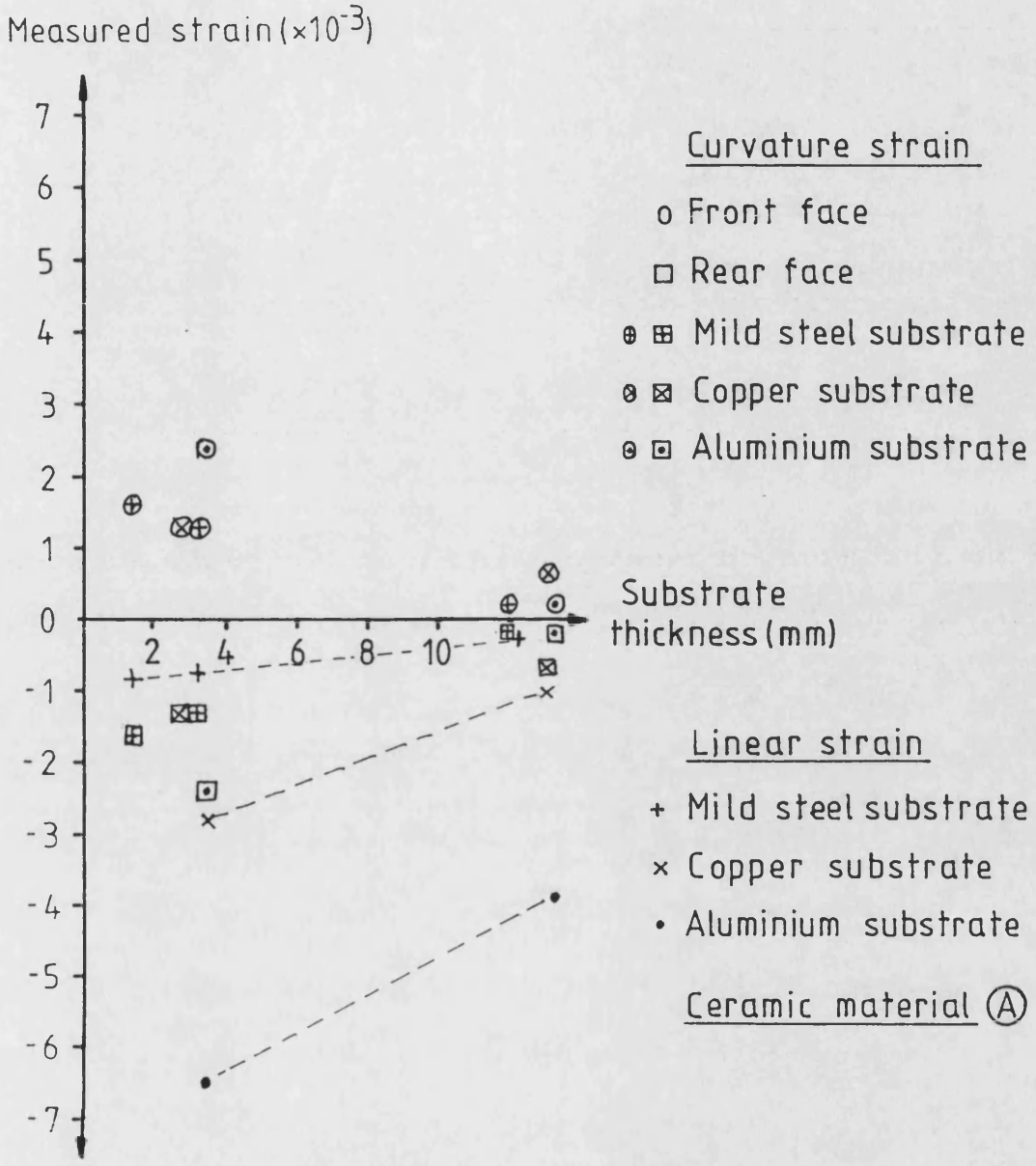

Figure 5·27 Graph illustrating the relationship between measured values of both curvature and linear residual strain and substrate thickness. Coatings were deposited on various substrate materials.

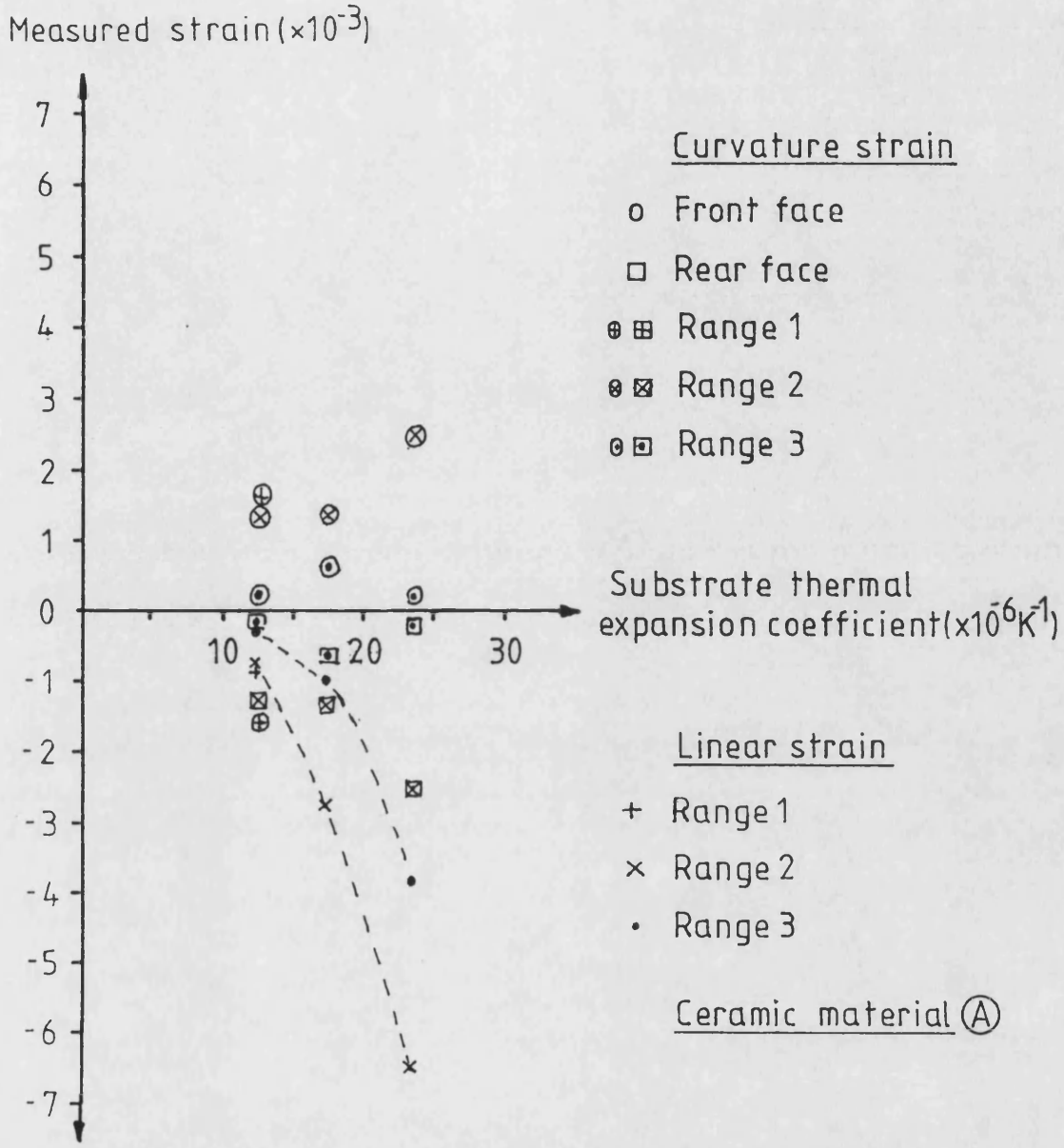

Figure 5·28 Graph illustrating the relationship between measured values of both curvature and linear residual strain and substrate thermal expansion coefficient. Three ranges of substrate thickness were used.

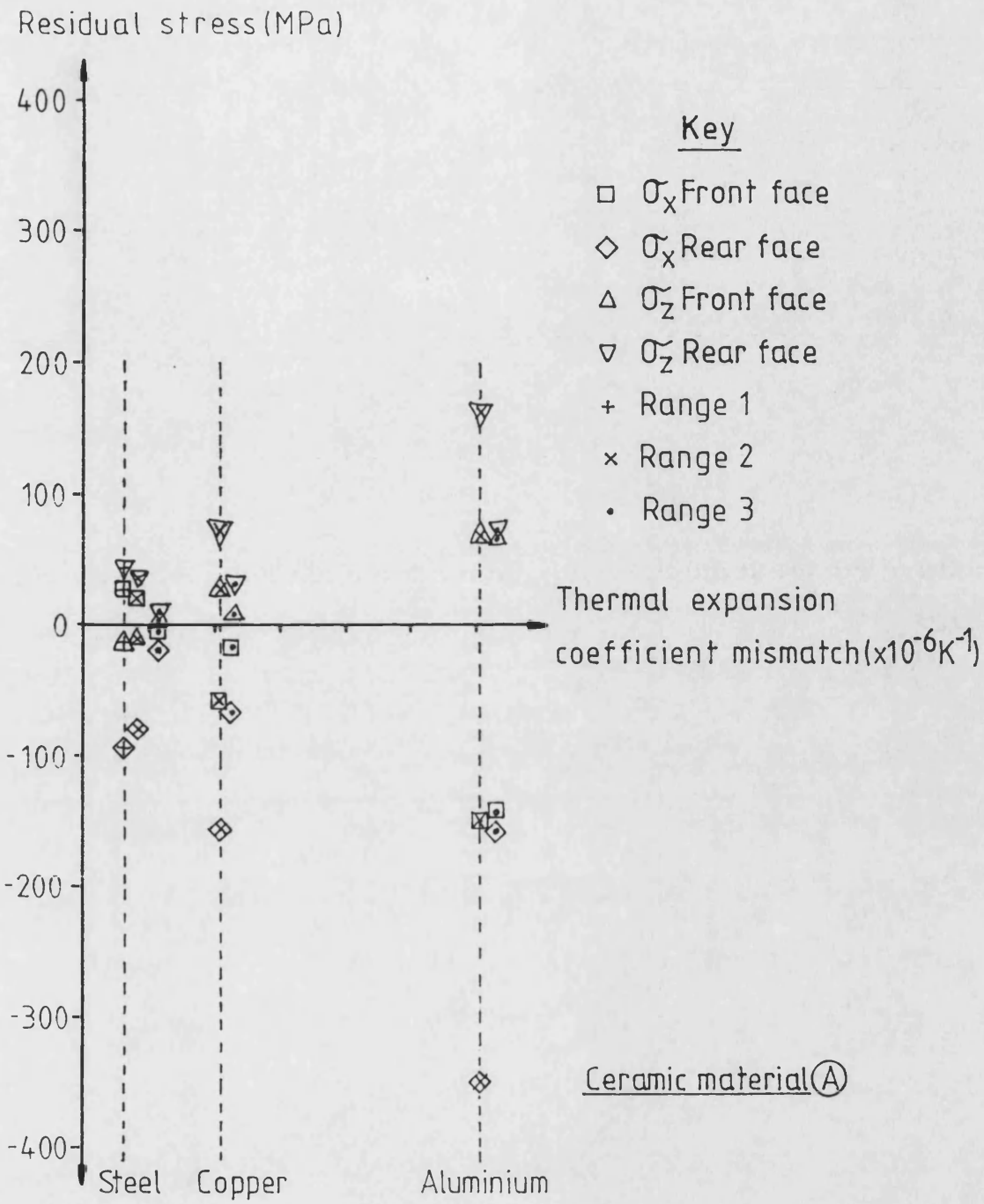

Figure 5·29 Graph illustrating the relationship between coating residual stresses and coating/substrate thermal expansion coefficient mismatch. Three ranges of substrate thickness were used.

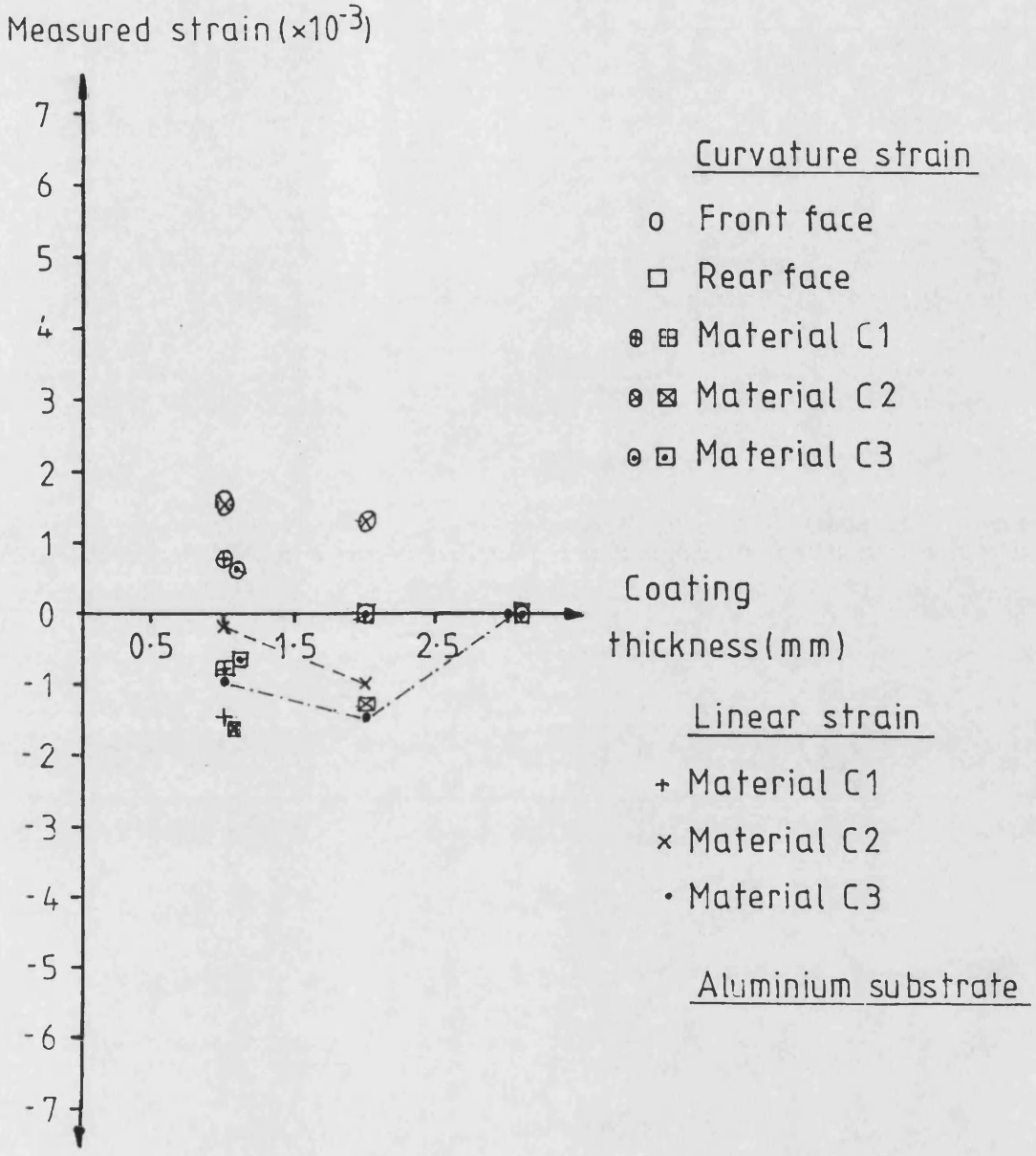

Figure 5·30 Graph illustrating the relationship between measured values of both curvature and linear residual strain and coating thickness. Coatings were manufactured from three grades of powder.

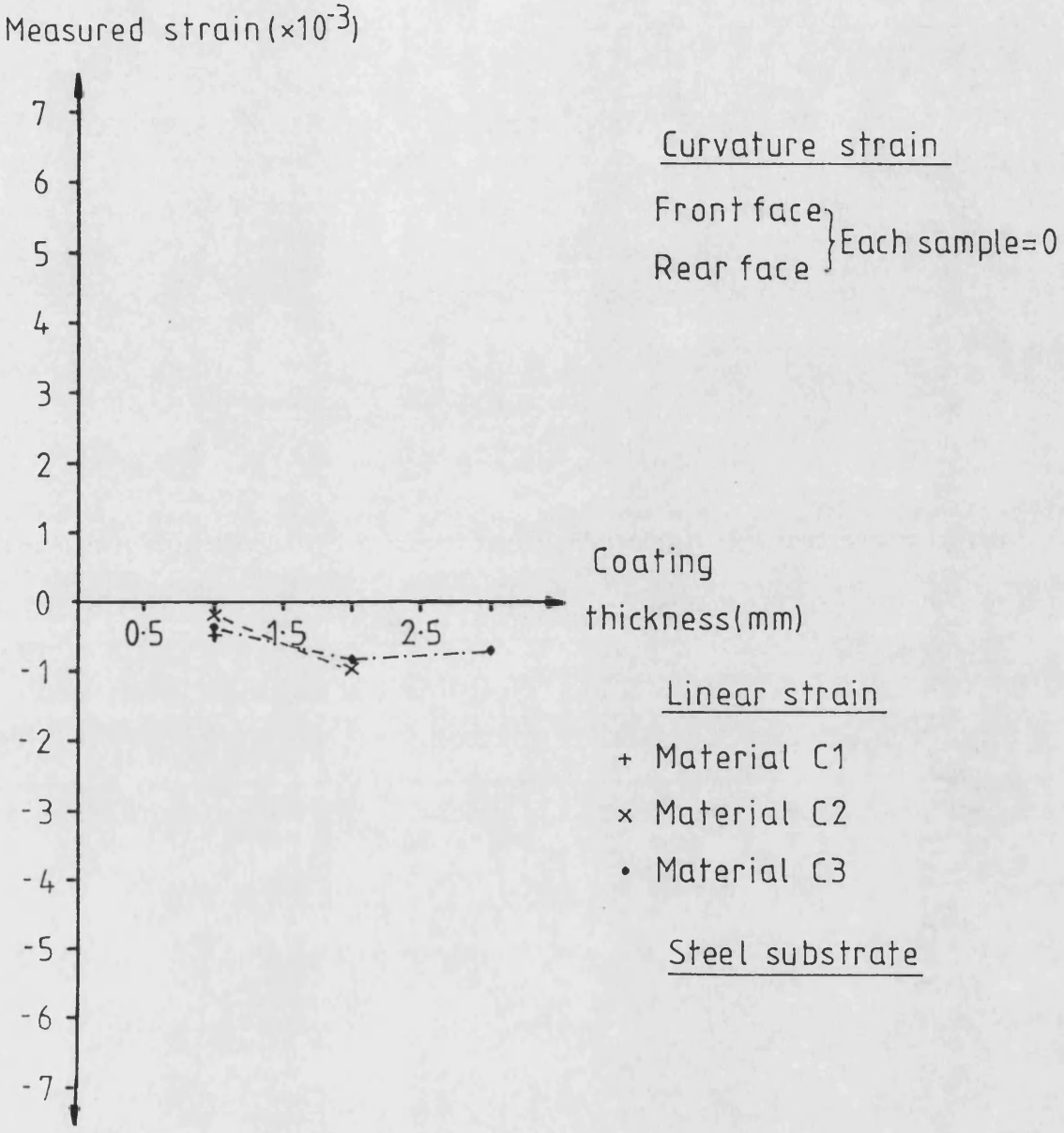

Figure 5·31 Graph illustrating the relationship between measured values of both curvature and linear residual strain and coating thickness. Coatings were manufactured from three grades of powder.

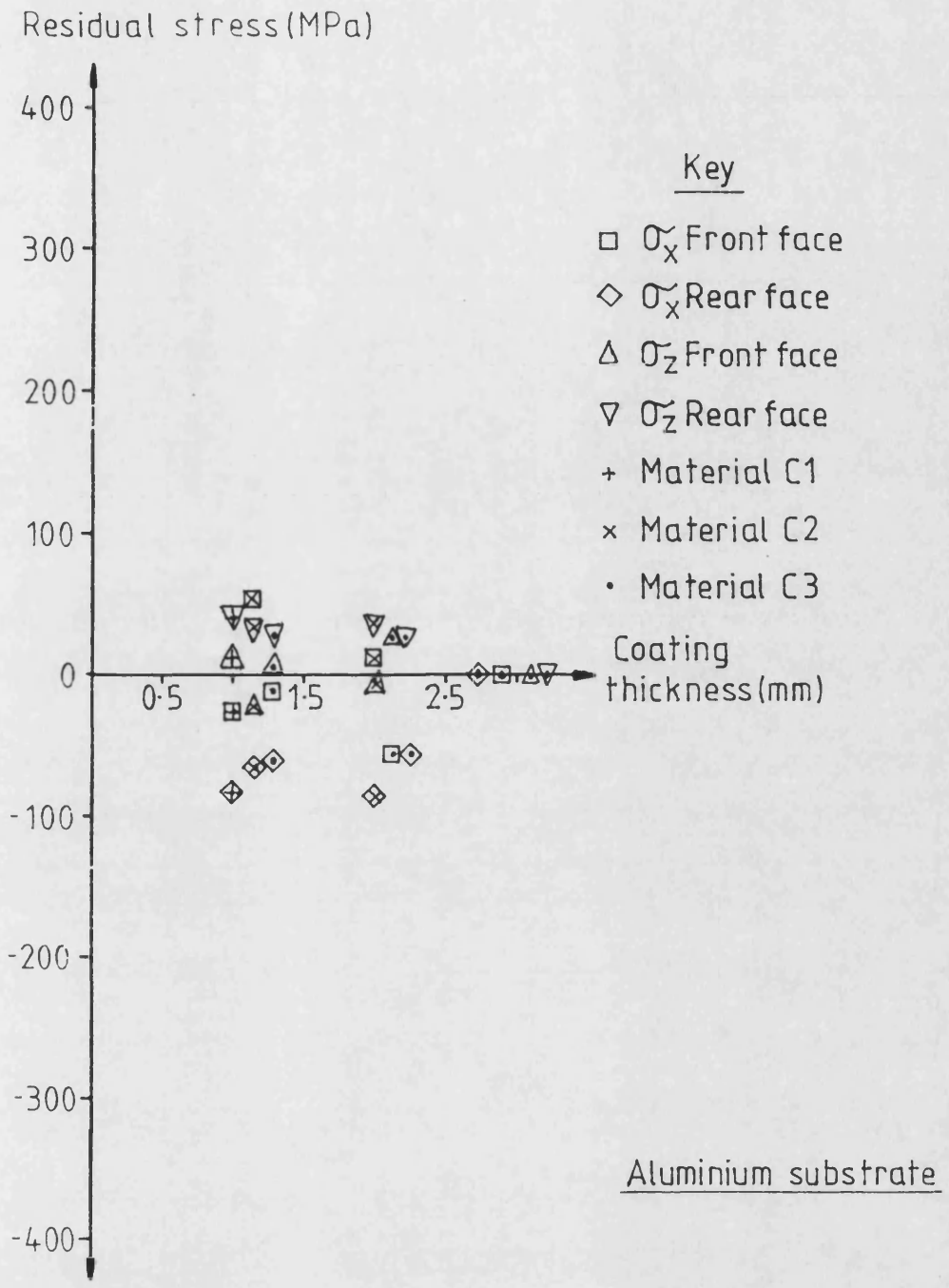

Figure 5·32 Graph illustrating the relationship between coating residual stresses and coating thickness. Coatings were manufactured from three grades of powder.

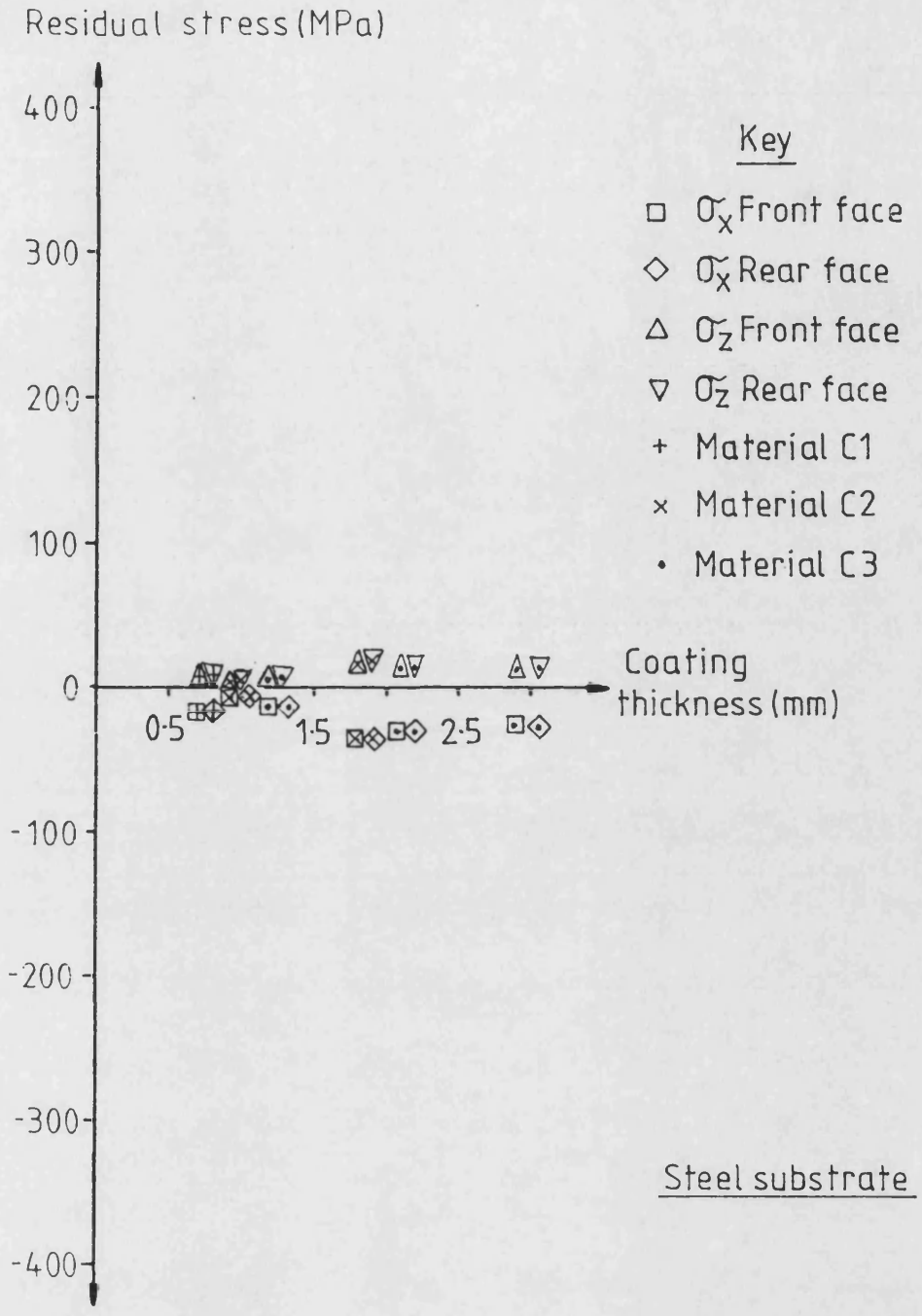

Figure 5·33 Graph illustrating the relationship between coating residual stresses and coating thickness. Coatings were manufactured from three grades of powder.

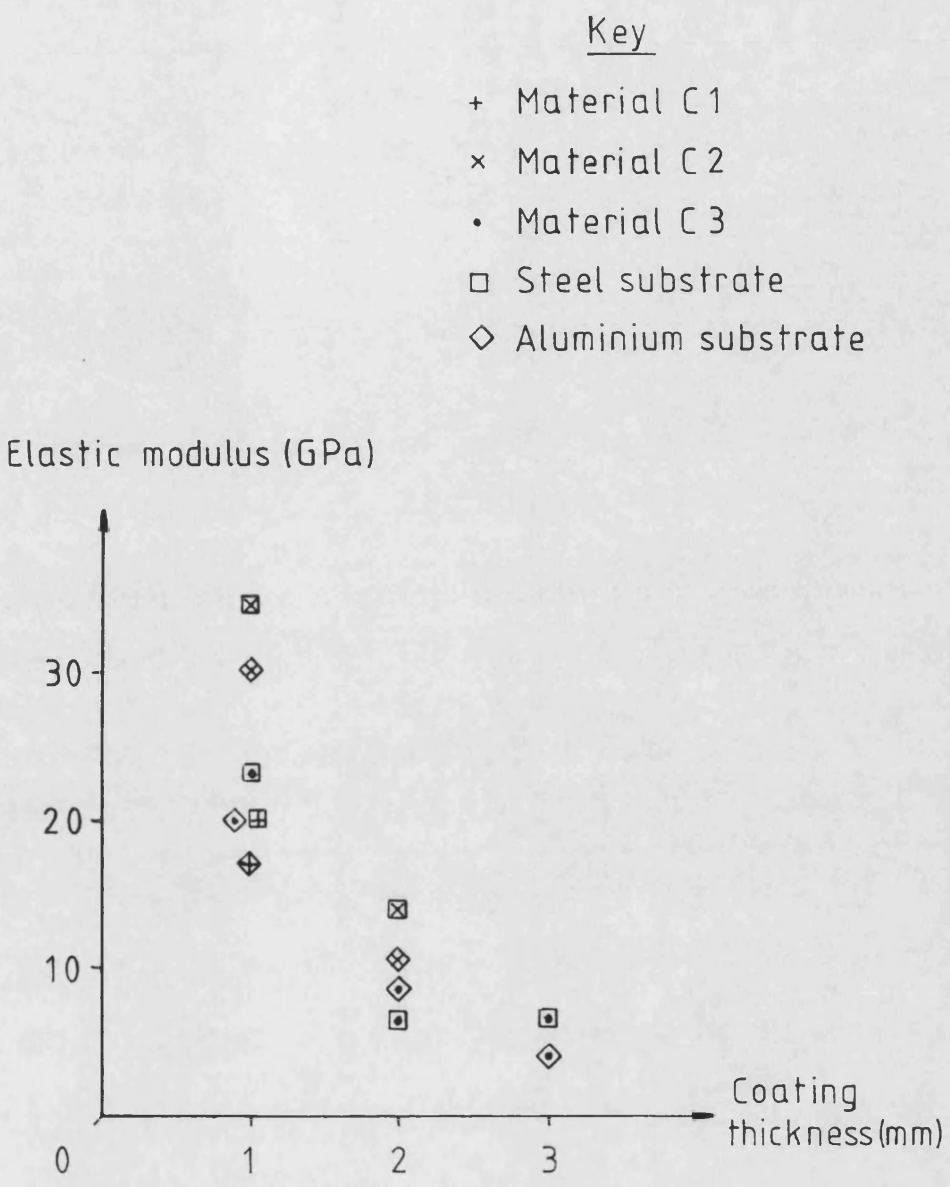

Figure 5·34 Graph showing the variation of dynamic elastic modulus with coating thickness, substrate and coating material type.

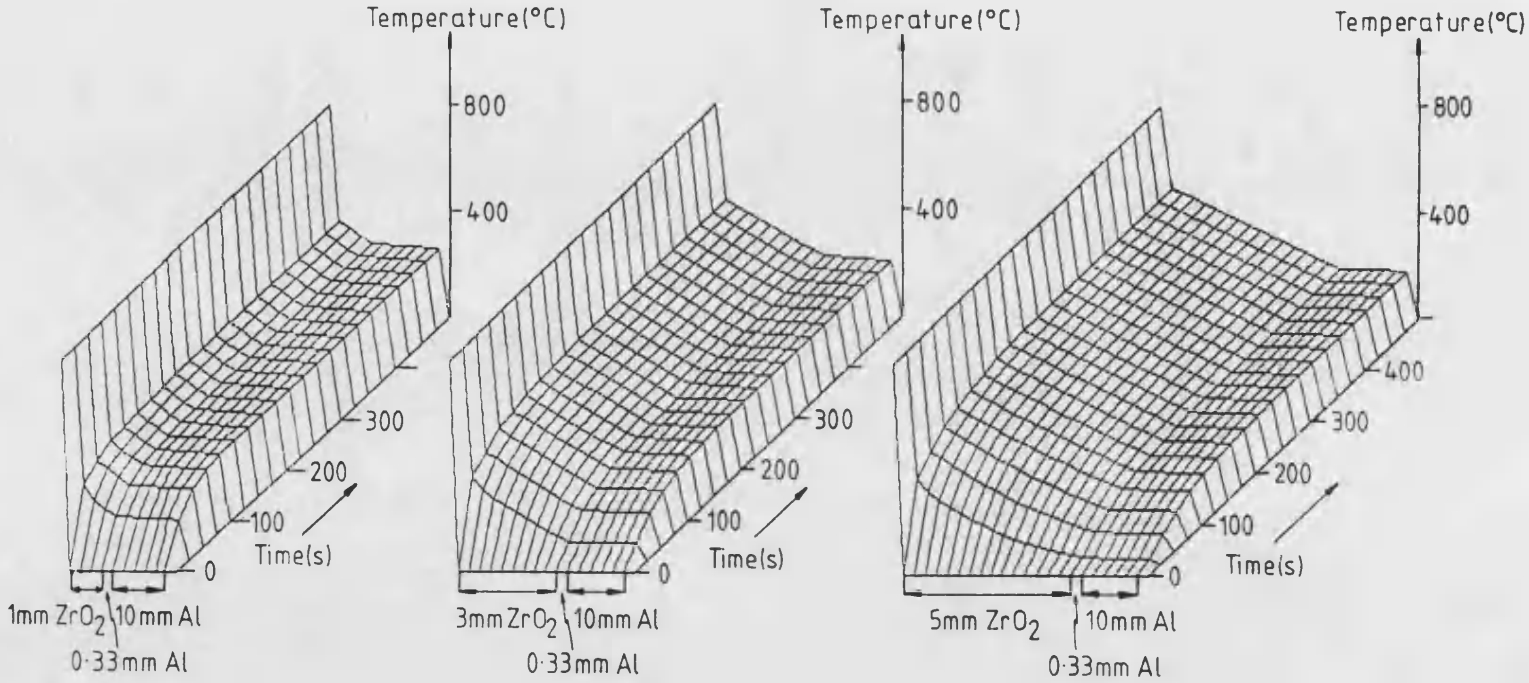

A 1mm. of ZrO_2 B 3mm. of ZrO_2 C 5mm of ZrO_2

Figure 5·35a-c Diagrams illustrating the heating of model thermal barrier coatings, of different thicknesses, subject to a static thermal gradient.

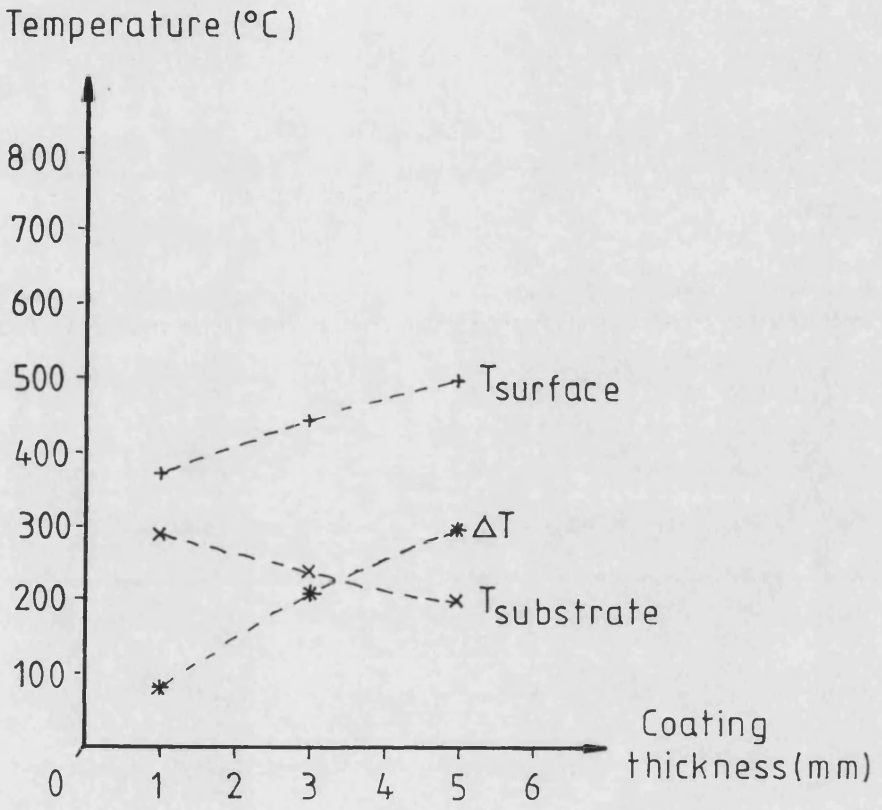

Figure 5·36 Graph showing the variation of maximum substrate and surface temperatures with model coating thickness.

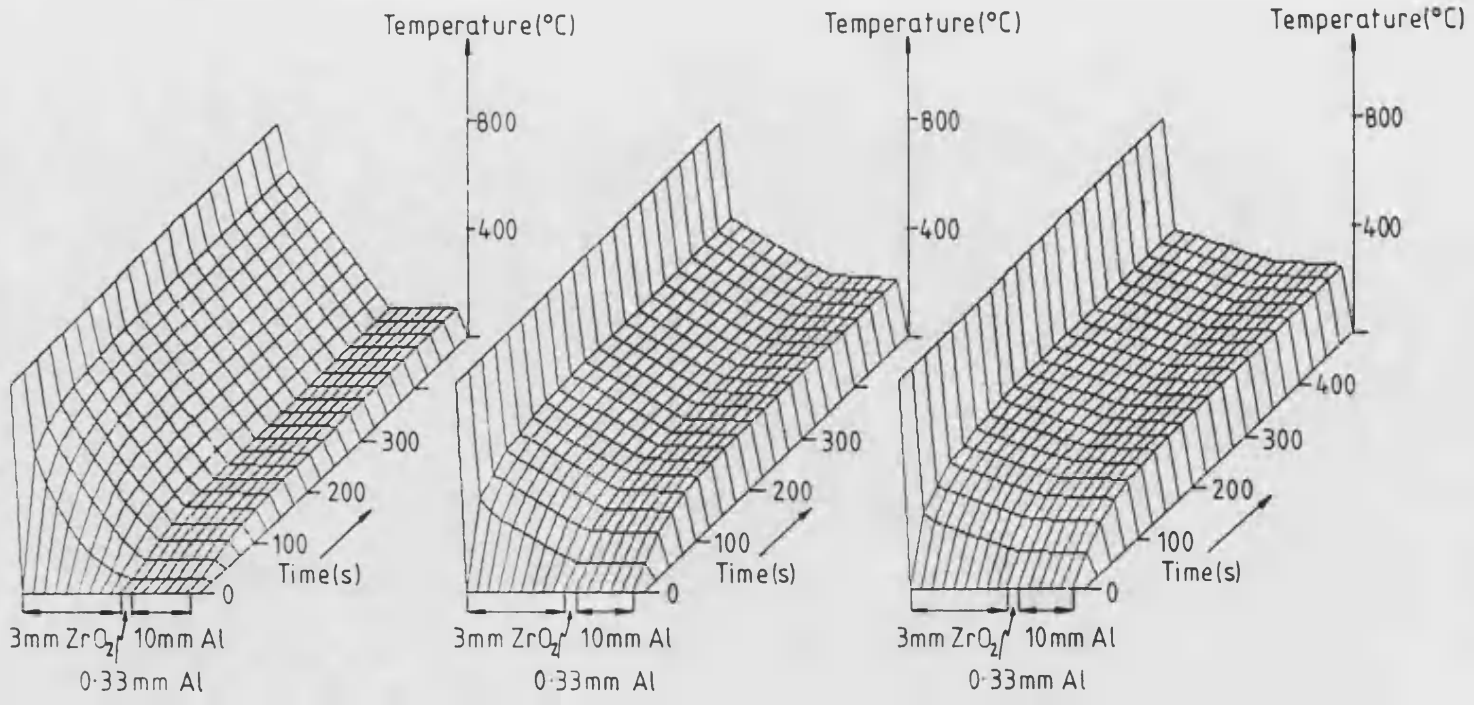

A $k = 0{\cdot}1 Wm^{-1}K^{-1}$ B $k = 0{\cdot}5 Wm^{-1}K^{-1}$ C $k = 1{\cdot}0 Wm^{-1}K^{-1}$

Figure 5·37a-c Diagrams illustrating the heating of model thermal barrier coatings, of different conductivities, subject to a static thermal gradient.

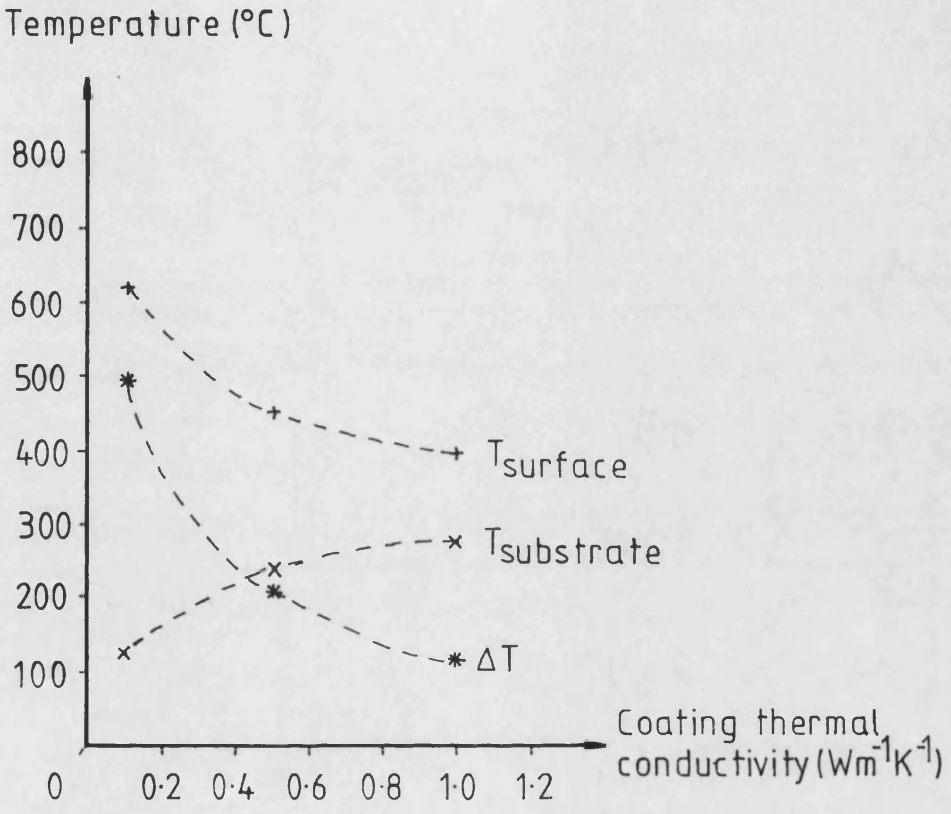

Figure 5·38 Graph showing the variation of maximum substrate and surface temperatures with model coating thermal conductivity.

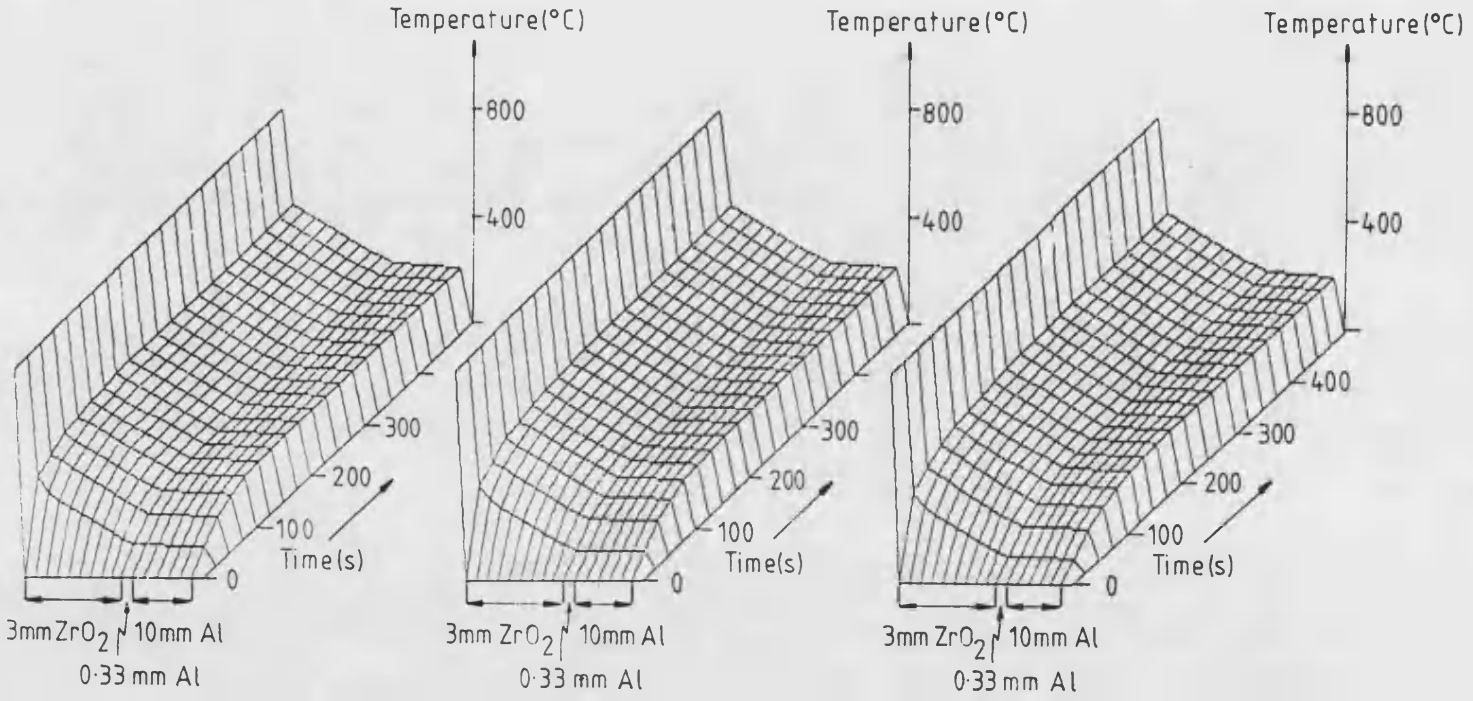

A $C_p = 400\ JKg^{-1}K^{-1}$ B $C_p = 500\ JKg^{-1}K^{-1}$ C $C_p = 600\ JKg^{-1}K^{-1}$

Figure 5·39 a-c Diagrams illustrating the heating of model thermal barrier coatings, of different heat capacities, subject to a static thermal gradient.

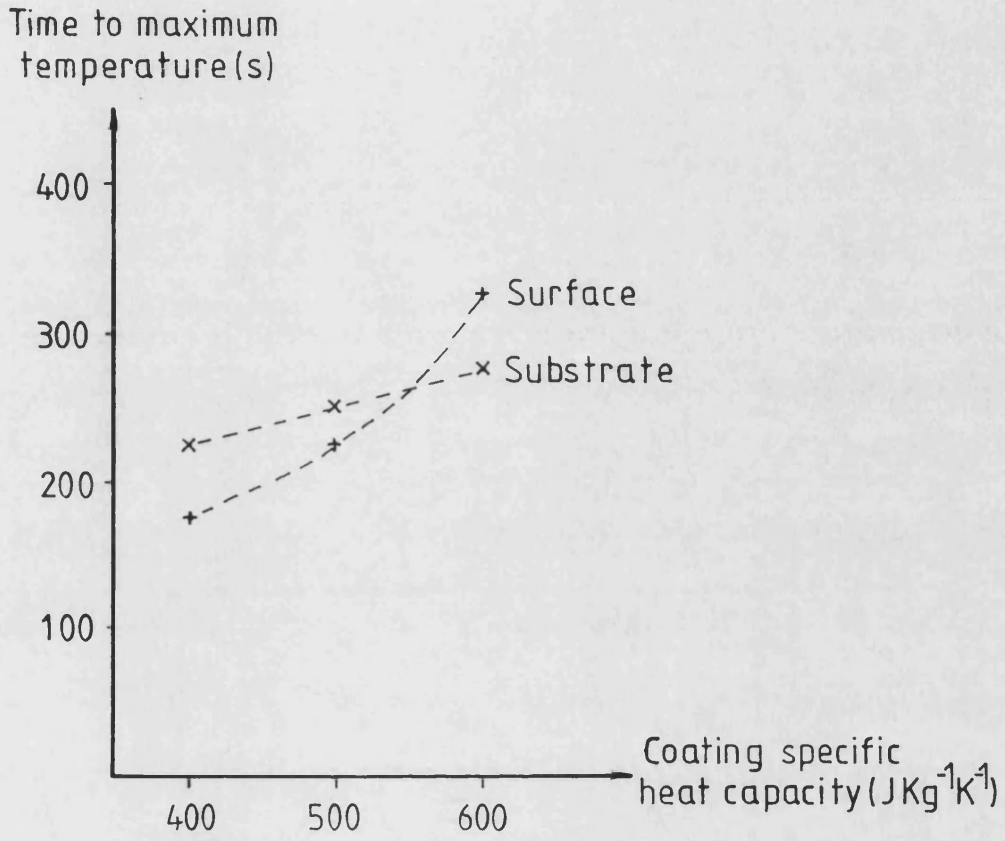

Figure 5·40 Graph showing the variation in time to maximum temperature with model coating specific heat capacity.

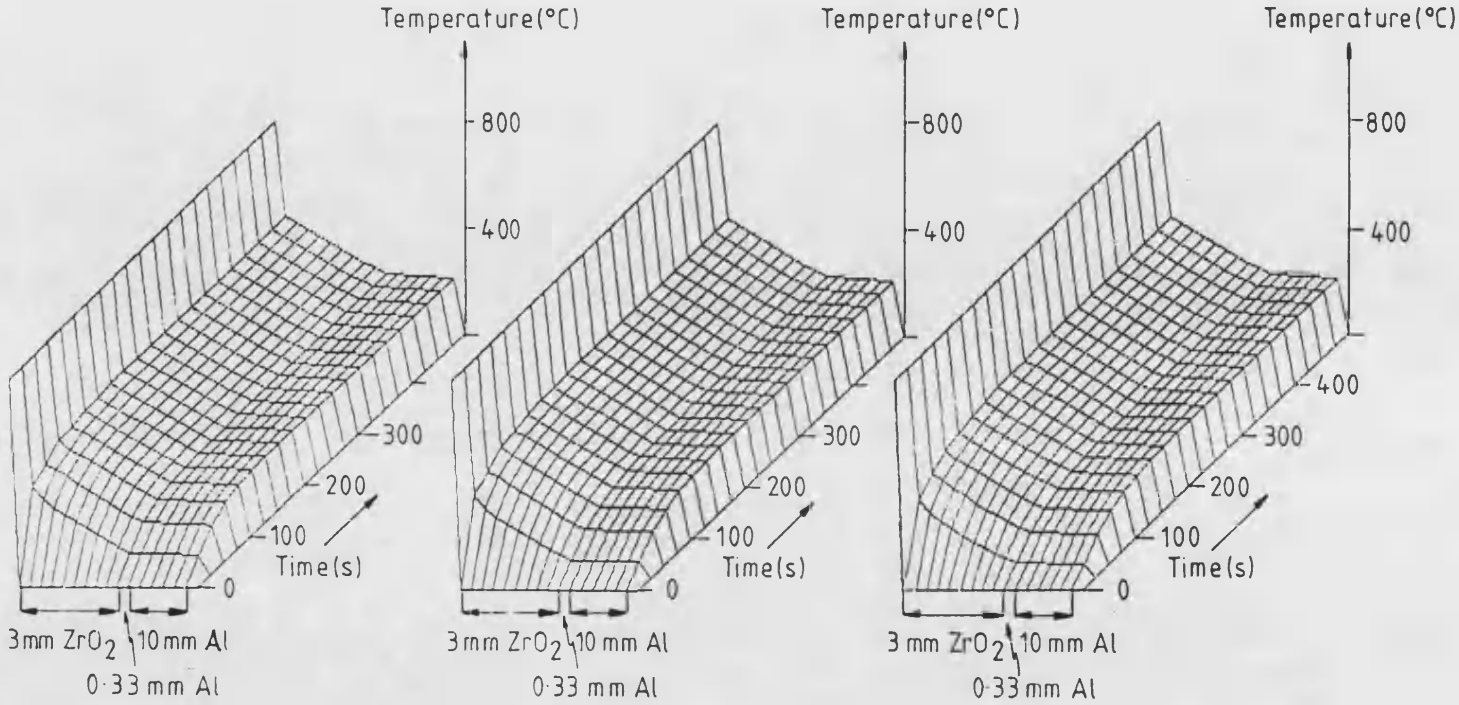

A $\rho = 3000 Kgm^{-3}$ B $\rho = 4000 Kgm^{-3}$ C $\rho = 5000 Kgm^{-3}$

Figure 5·41a-c Diagrams illustrating the heating of model thermal barrier coatings, of different densities, subject to a static thermal gradient.

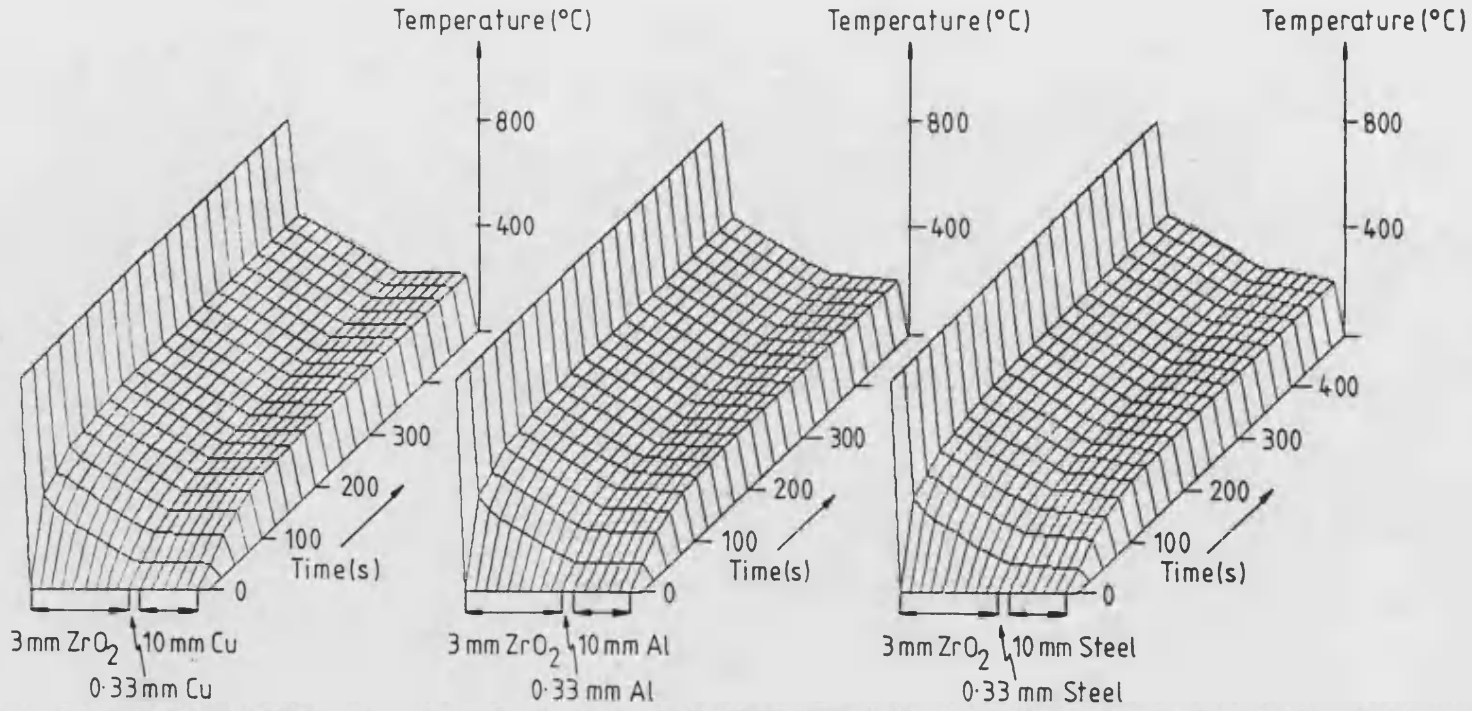

A Copper substrate B Aluminium substrate C Steel substrate

Figure 5·42 a-c Diagrams illustrating the heating of model thermal barrier coatings, deposited on different substrate materials, subject to a static thermal gradient.

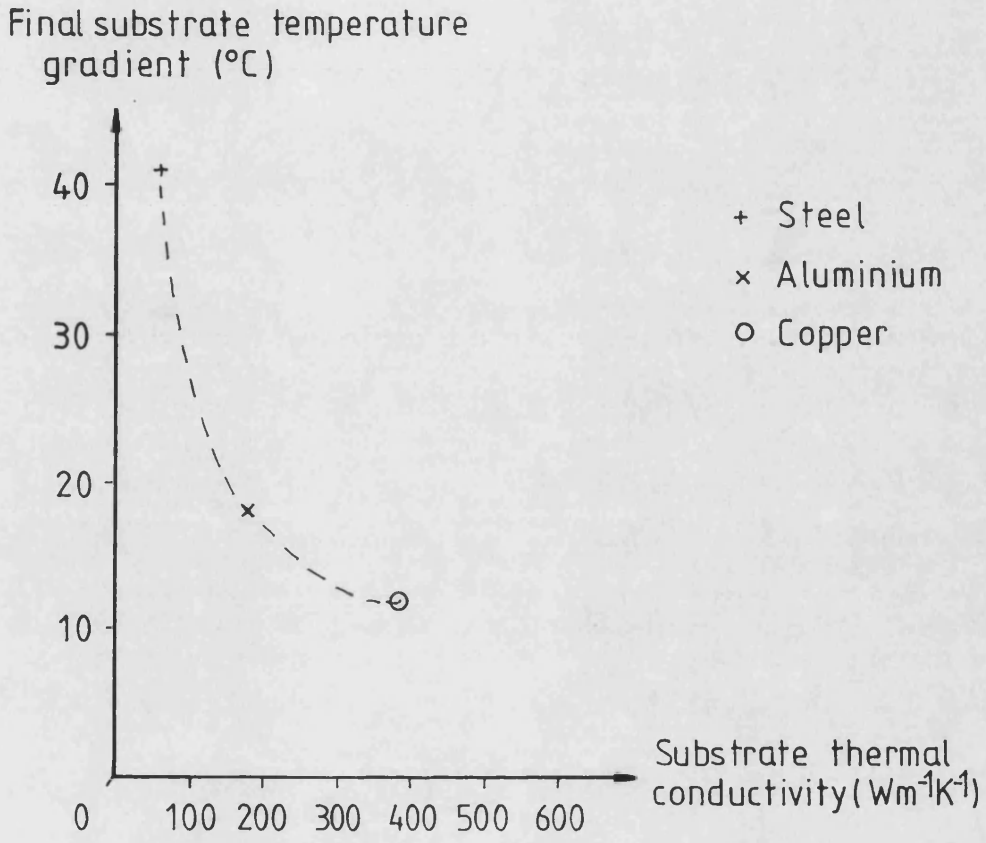

Figure 5·43 Graph showing the variation in final substrate temperature gradient with model substrate thermal conductivity.

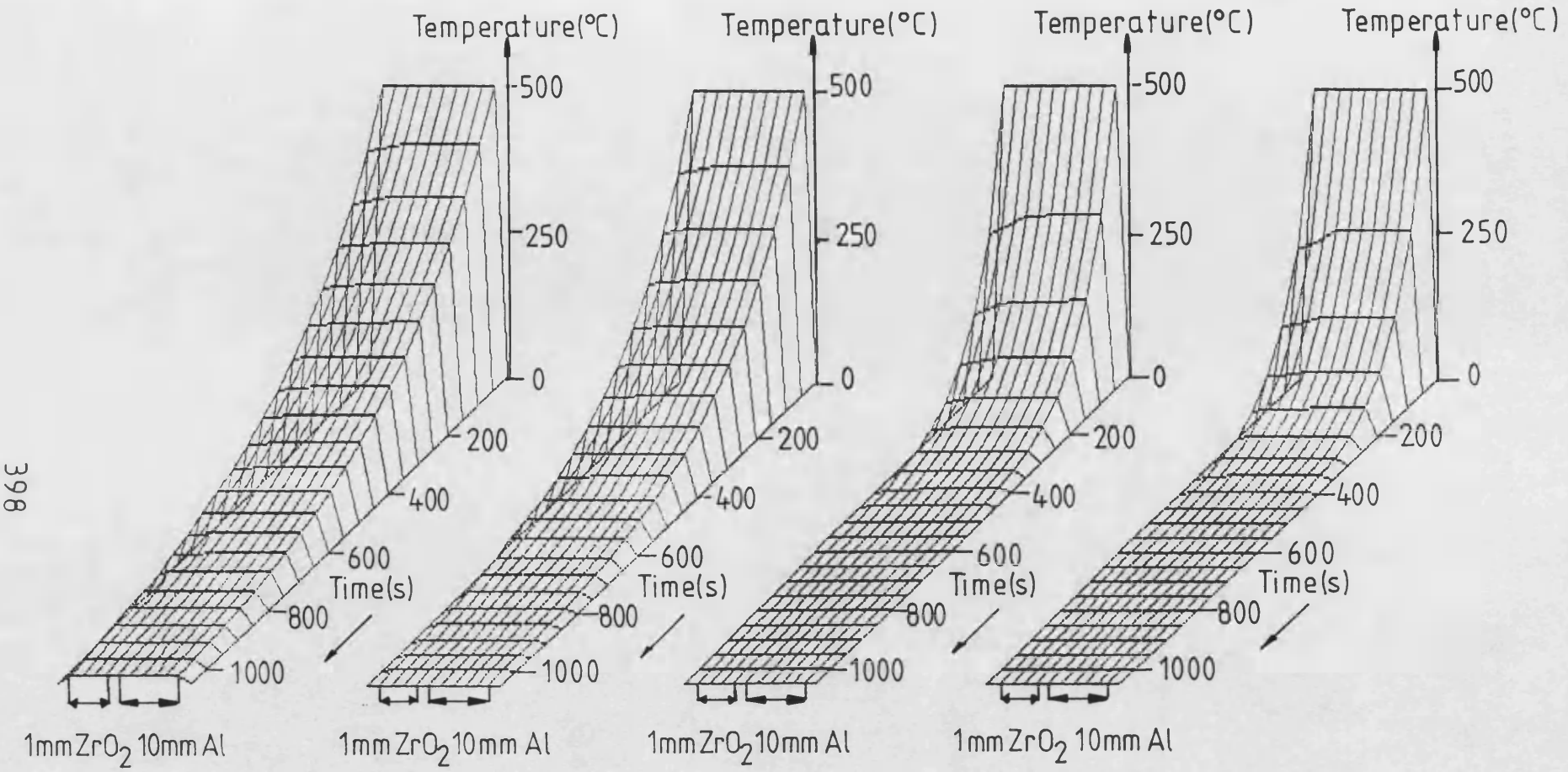

Figure 5·44 a-d Diagrams illustrating the cooling of model thermal barrier coatings after spraying, with and without air cooling jets.

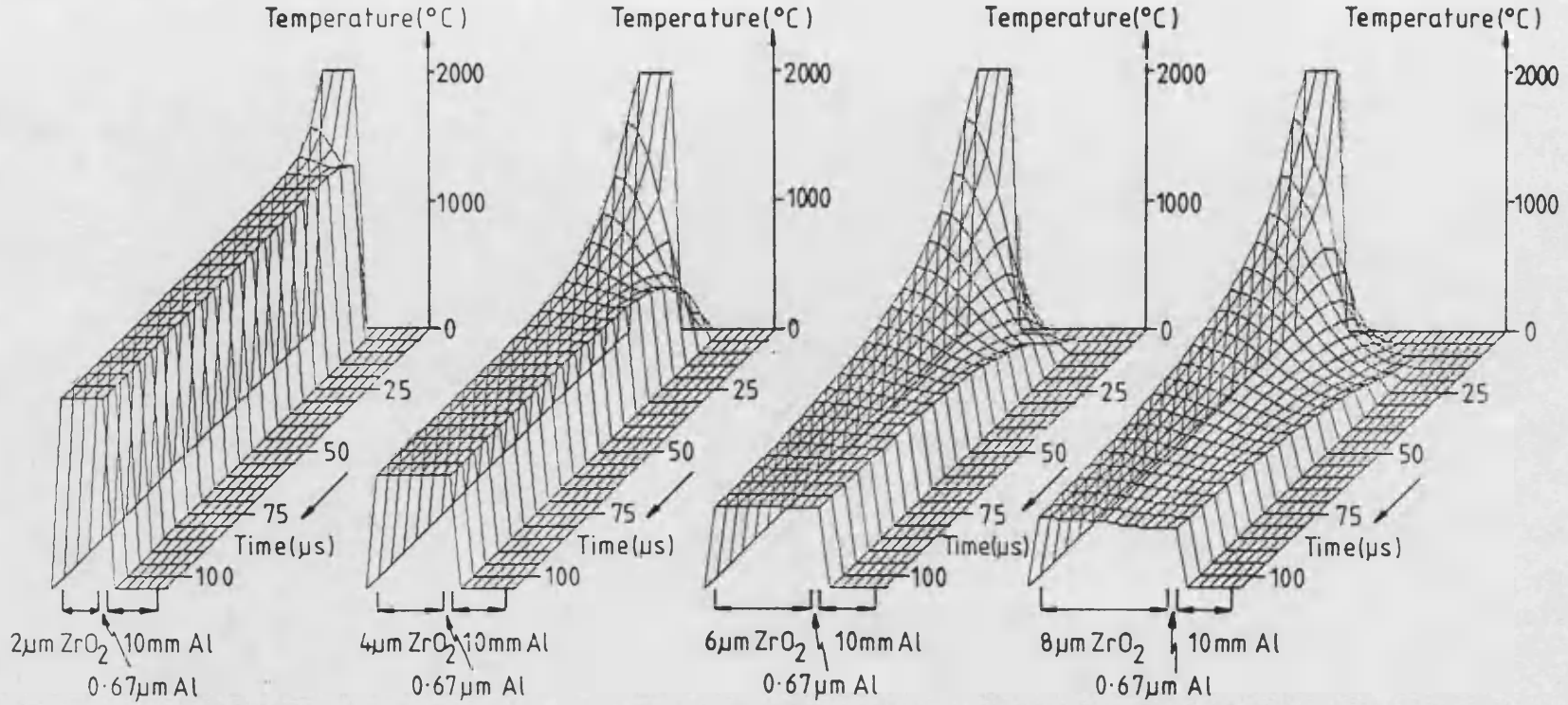

Figure 5·45 a-d Diagrams illustrating the cooling of a single model coating particle, impacted with increasing numbers of existing particles.

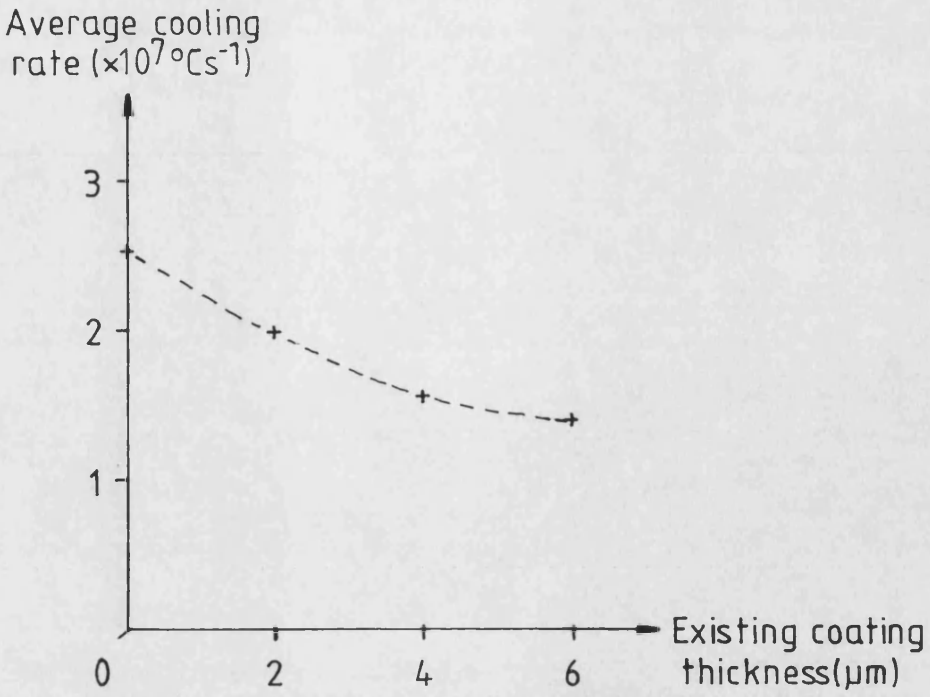

Figure 5·46 Graph showing the variation in predicted, initial, average cooling rates of impacted particles with existing coating thickness.

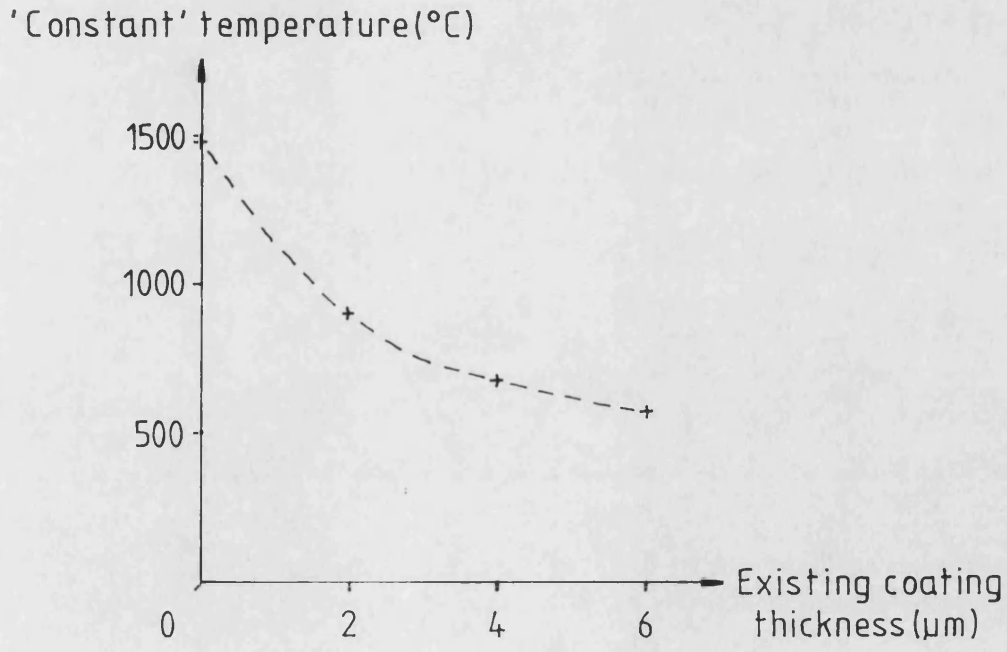

Figure 5·47 Graph showing the variation in predicted 'constant' temperature of newly impacted particles with existing coating thickness.

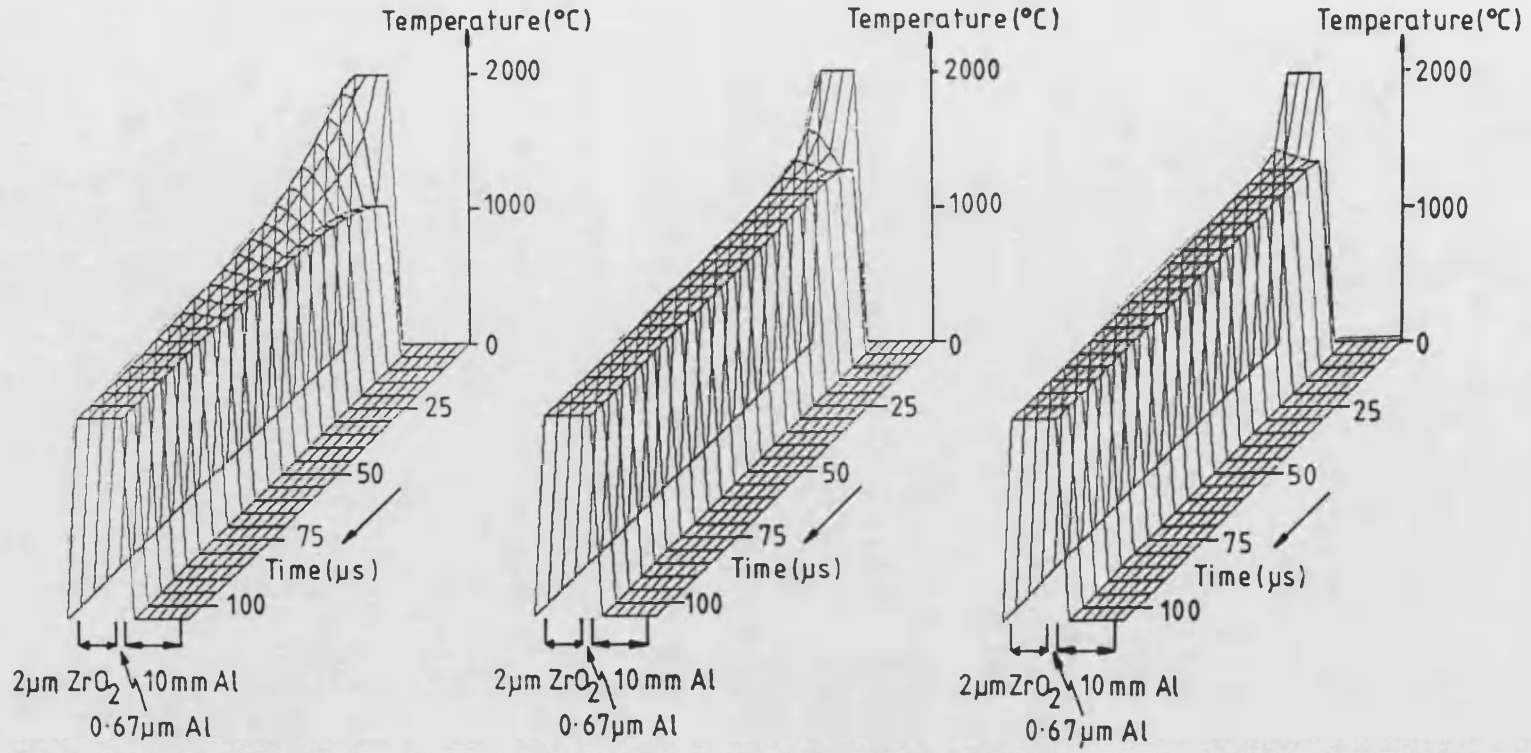

Figure 5·48 a-c Diagrams illustrating the cooling of impacted model coating particles with different thermal conductivities.

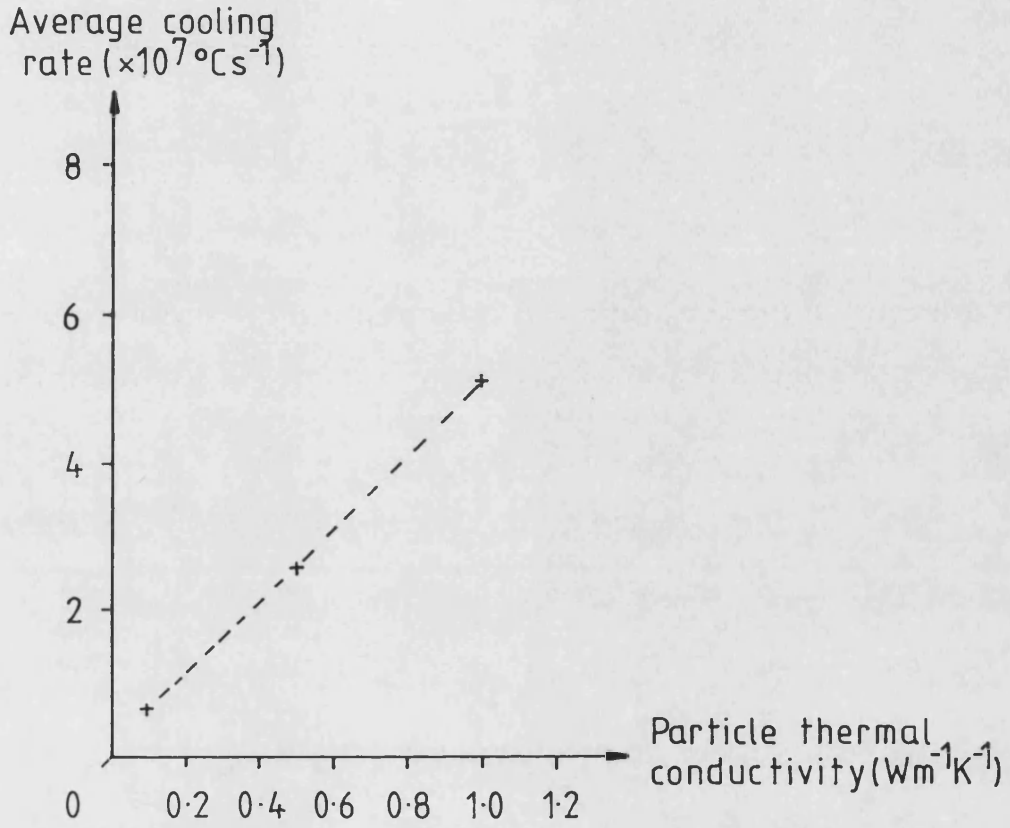

Figure 5·49 Graph showing the variation in predicted, initial, average cooling rates of impacted particles with ceramic thermal conductivity.

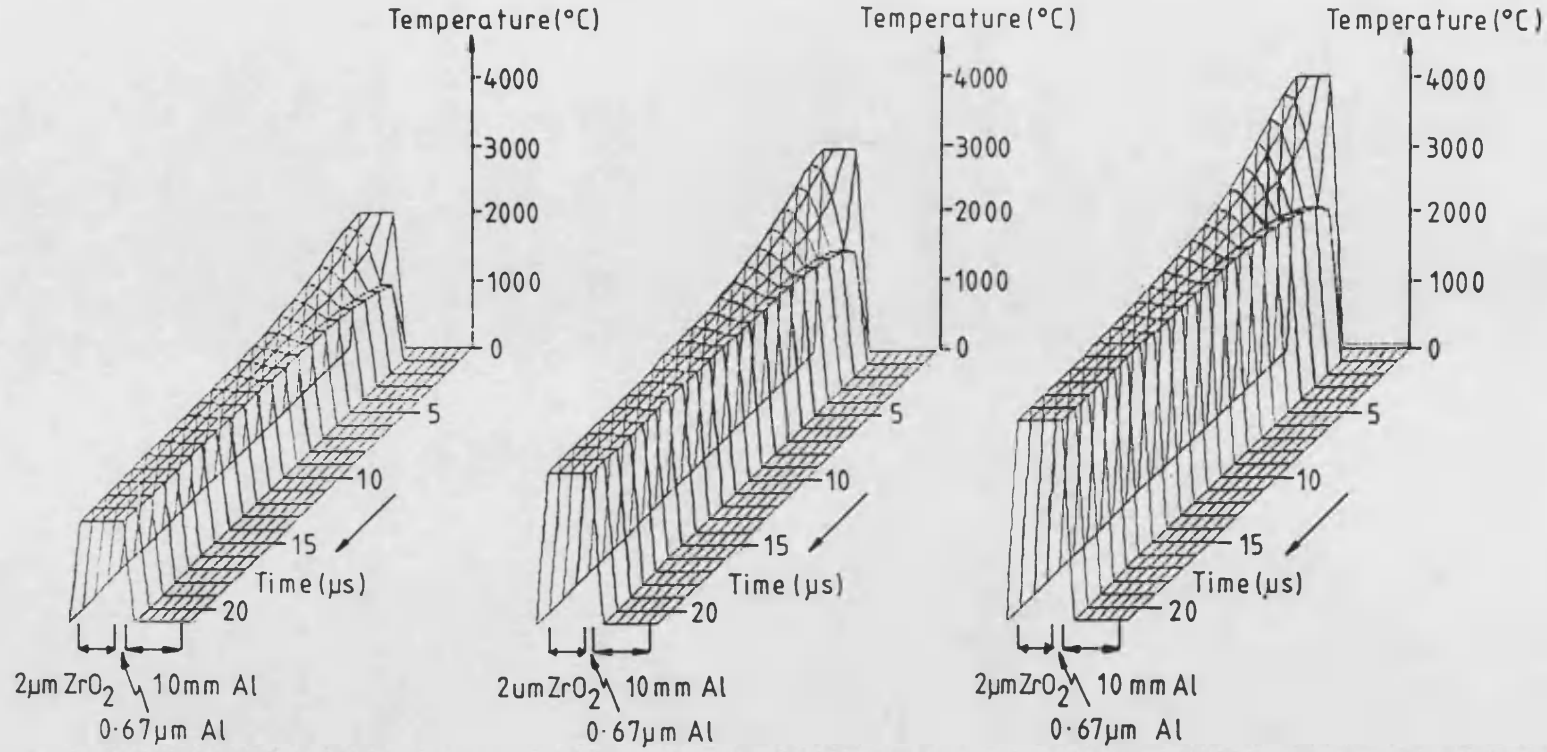

A Tp = 2000°C B Tp = 3000°C C Tp = 4000°C

Figure 5·50 a-c Diagrams illustrating the cooling of impacted model coating particles with different initial temperatures.

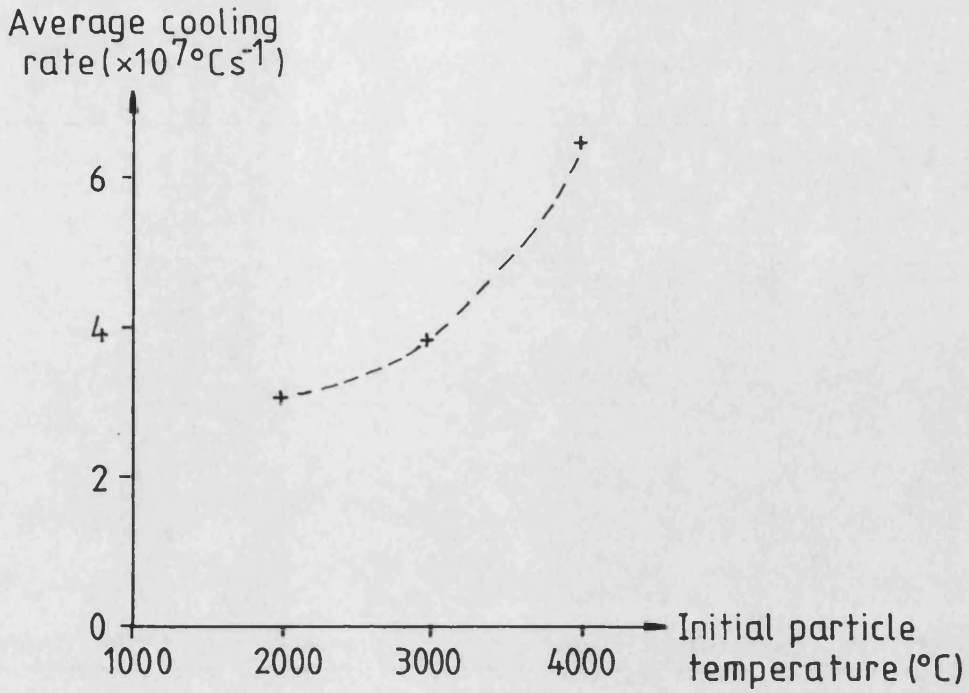

Figure 5·51 Graph showing the variation in predicted, initial, average cooling rate of impacted particles with initial particle temperature.

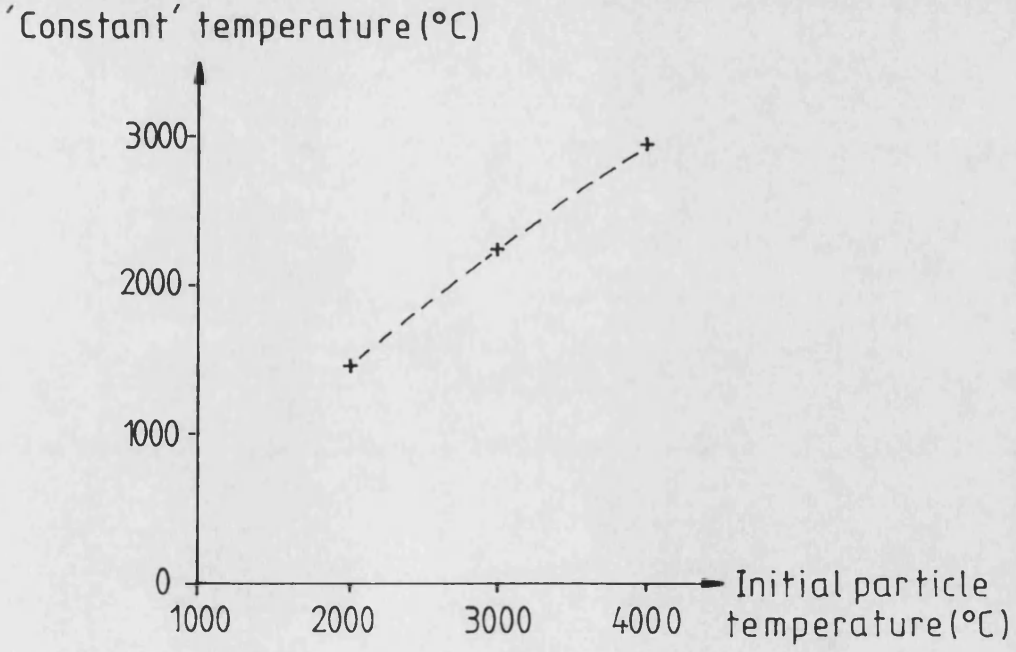

Figure 5·52 Graph showing the variation in predicted 'constant' temperature of newly impacted particles with initial particle temperature.

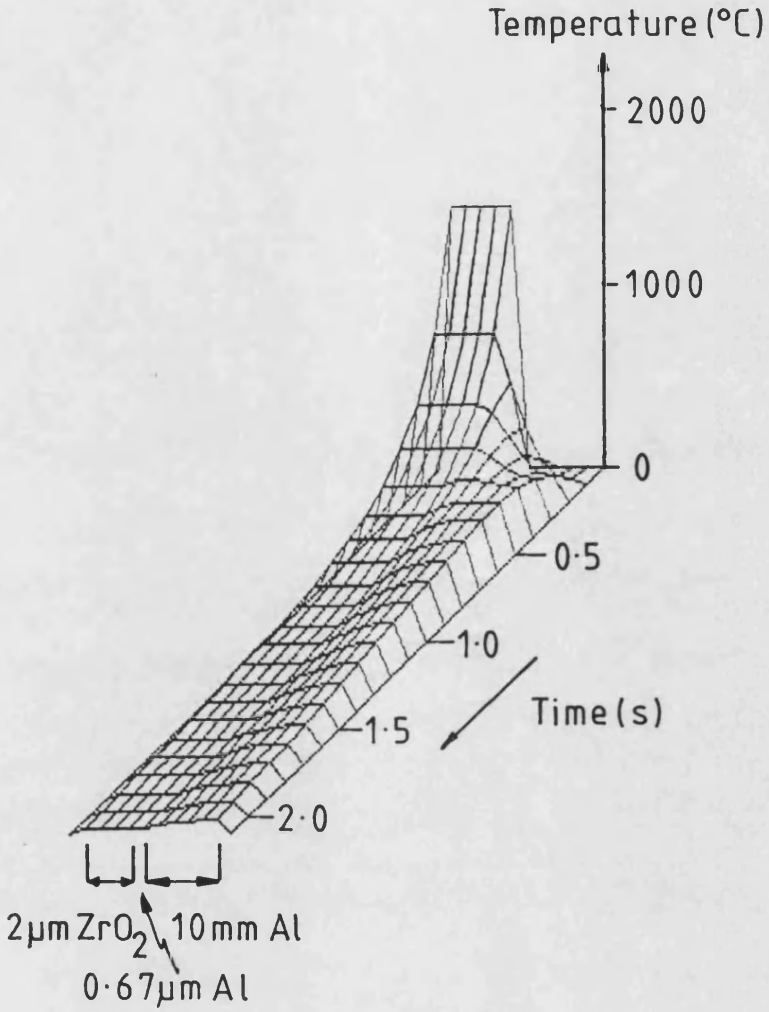

Figure 5·53 Diagram illustrating the long term cooling of an impacted ceramic particle, following initial, rapid cooling to the 'constant' temperature, described by figure 5·45a.

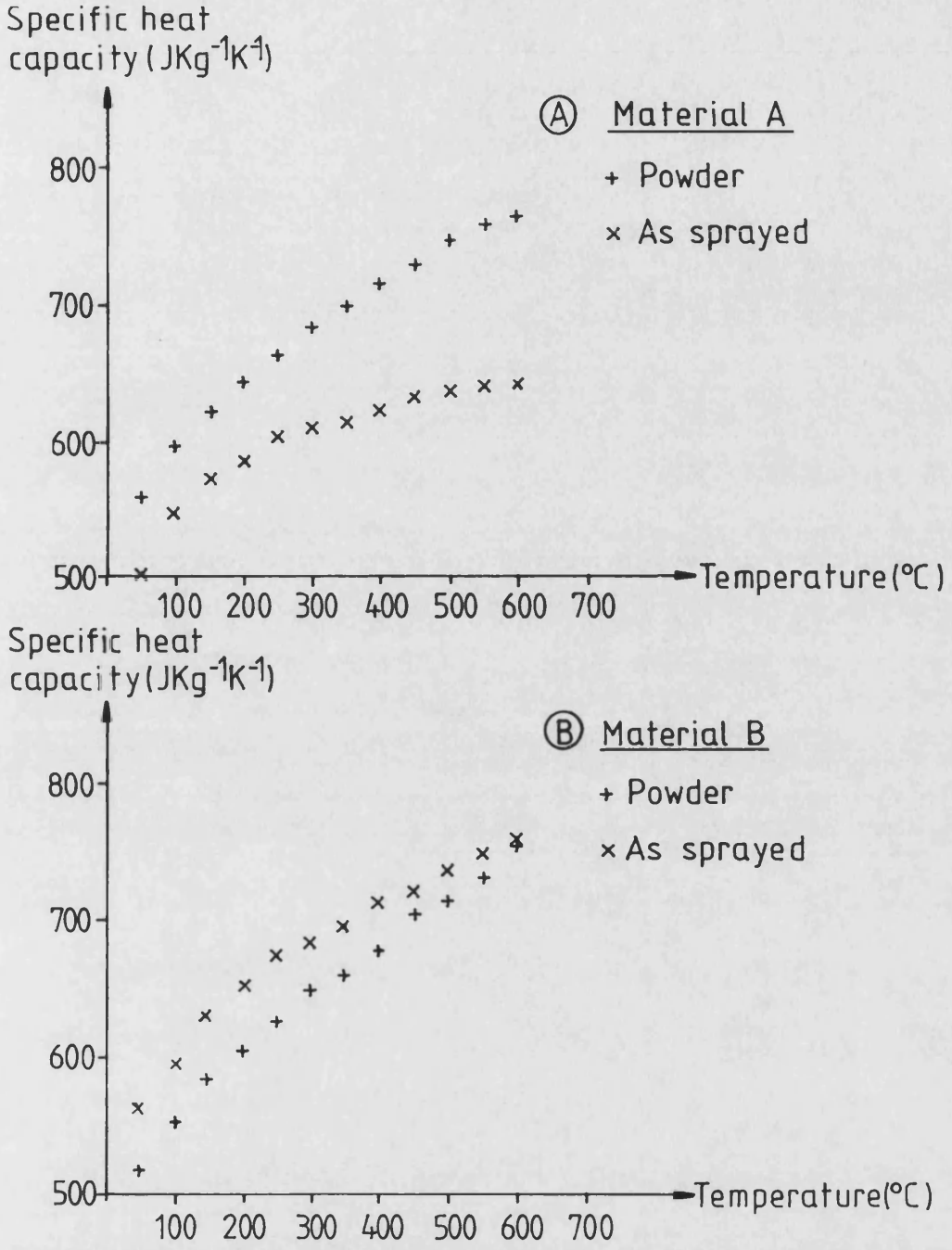

Figure 5·54 a-b Graphs illustrating the variation of specific heat capacity of zirconia coating materials with temperature.

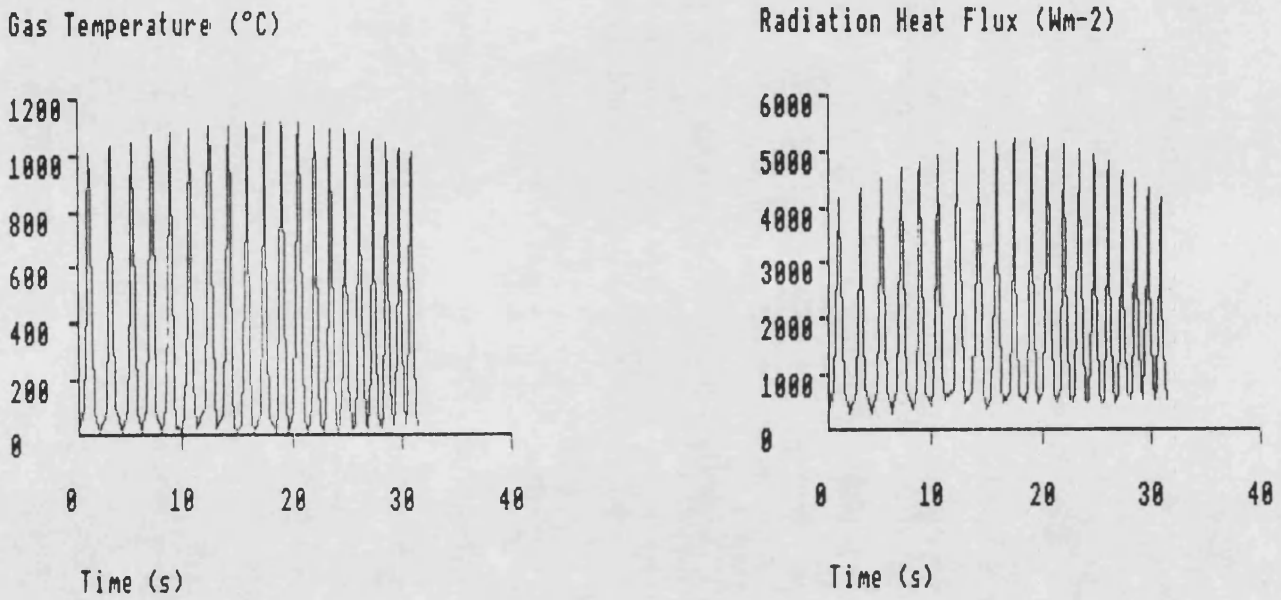

Figure 5·55 a-b Graphs summarising complex model input conditions during one complete traverse, with and without air cooling.

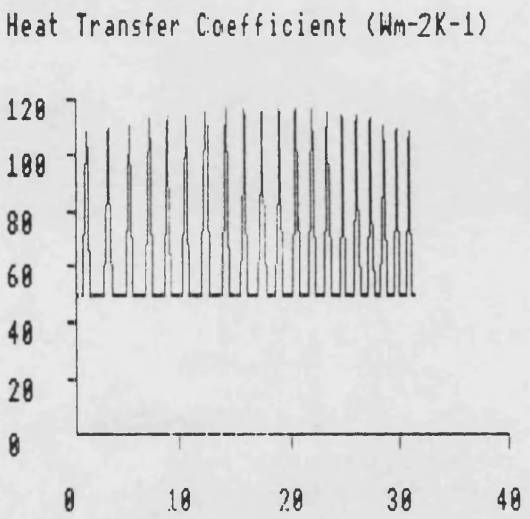

(C)

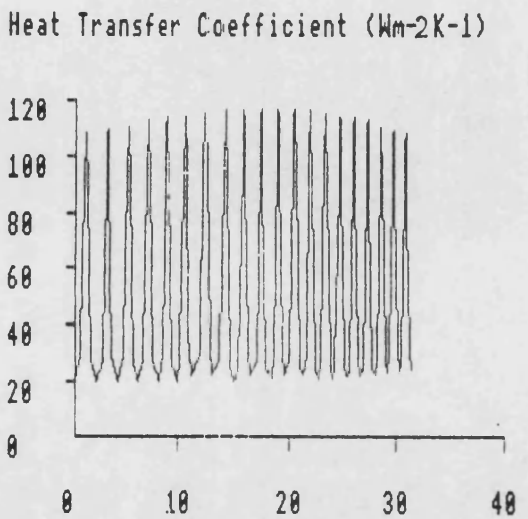

(D)

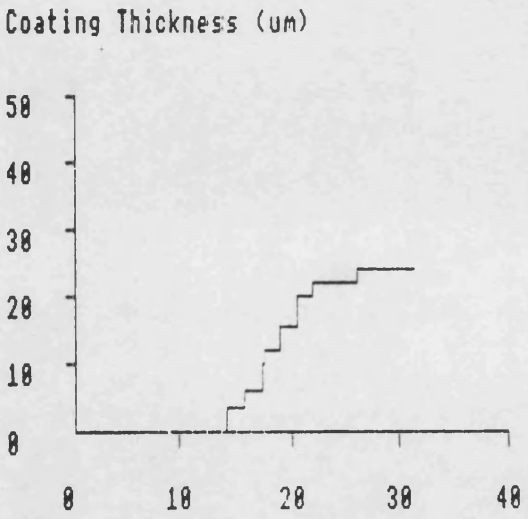

(E)

Figure 5·55 c-e Graphs summarising complex model input conditions during one complete traverse, with (C) and without (D) air cooling.

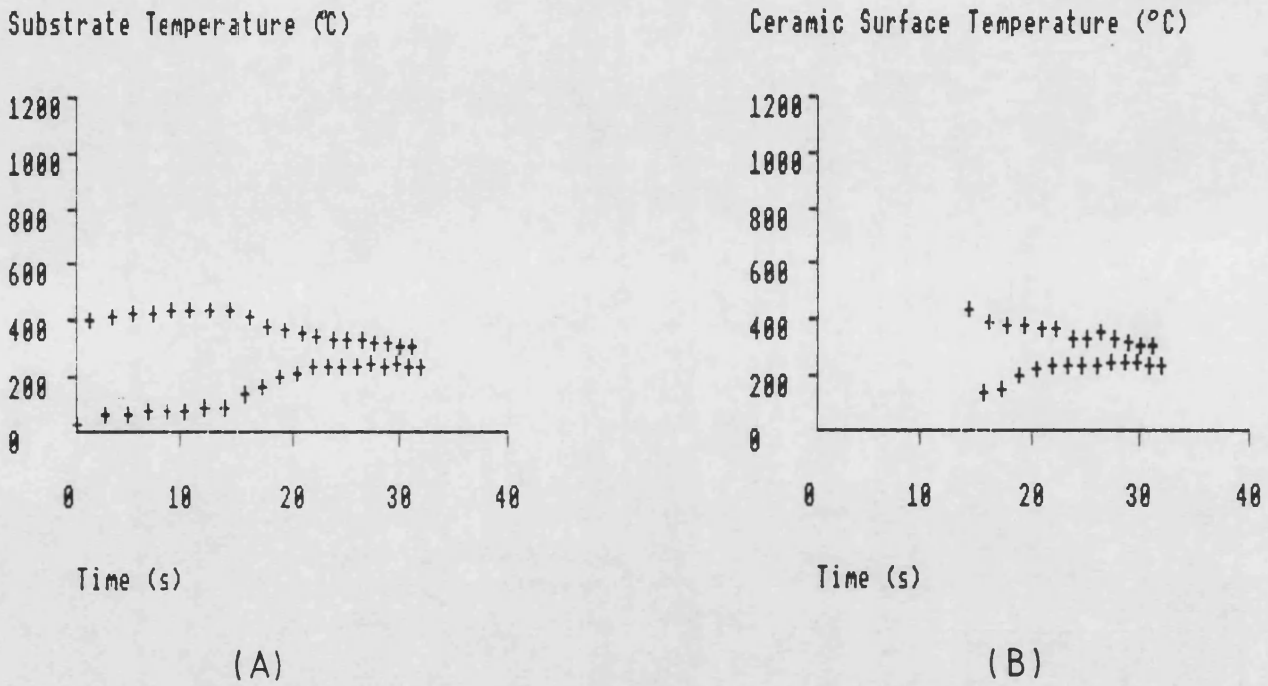

Figure 5·56 a-b Graphs showing predicted maximum/minimum substrate and coating front face temperatures for each pass, during one traverse without air cooling.

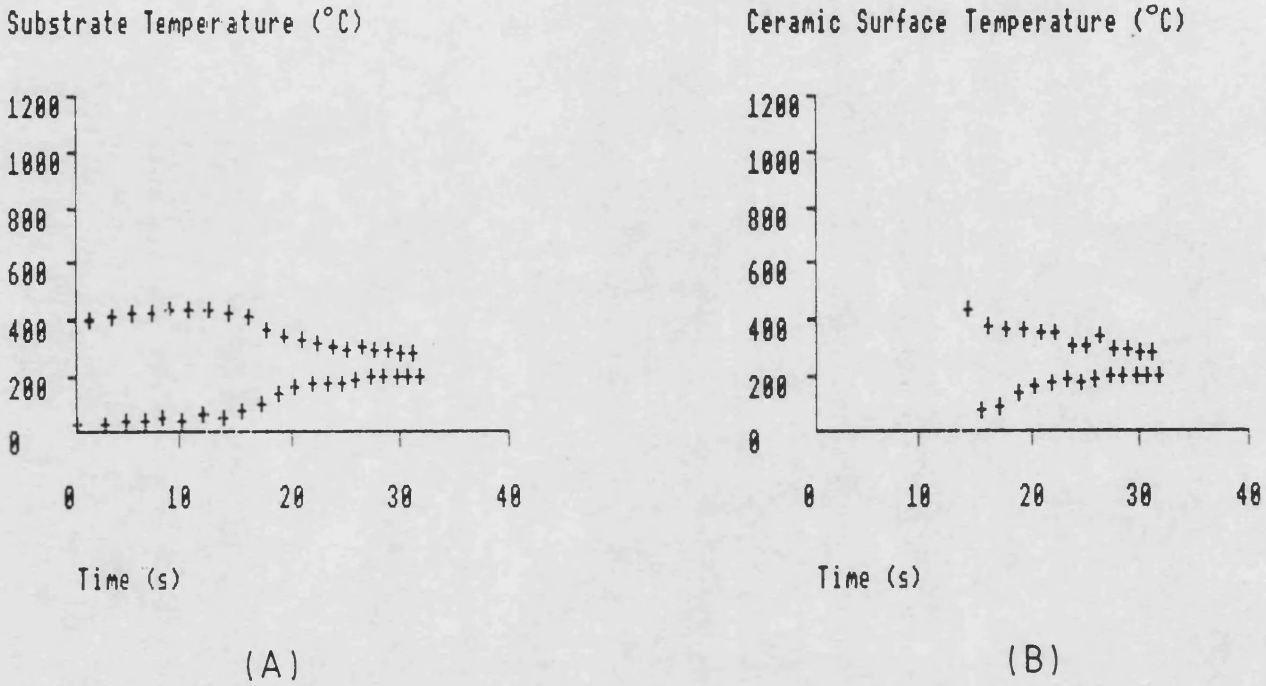

Figure 5·57a-b Graphs showing predicted maximum/minimum substrate and coating front face temperatures for each pass, during one traverse with air cooling.

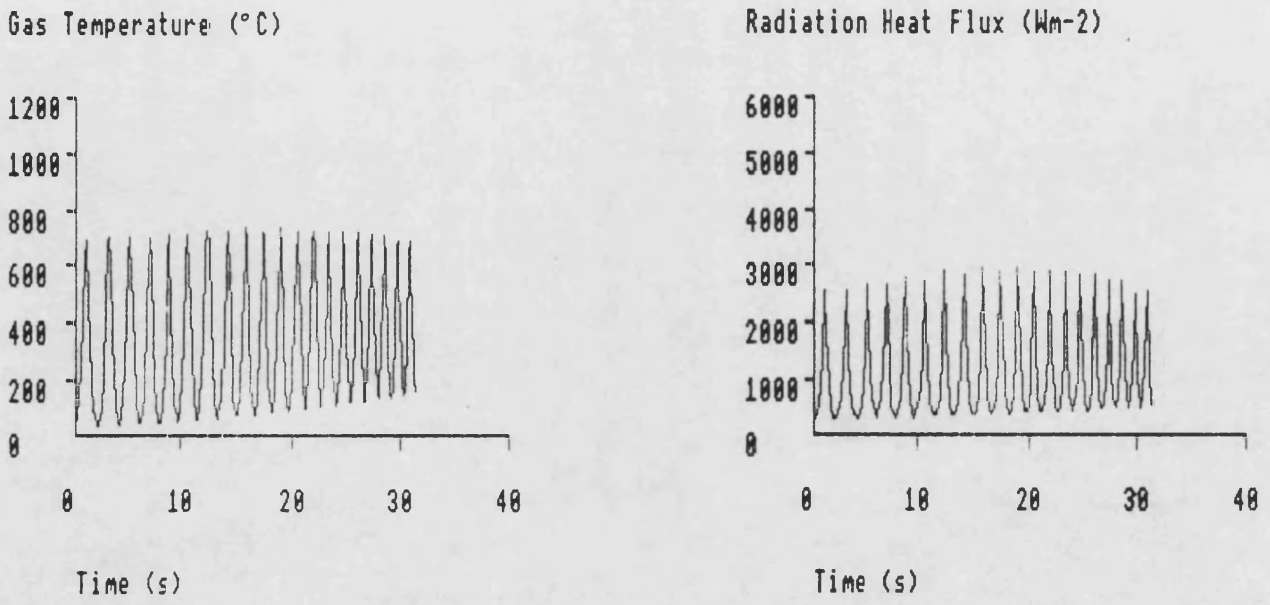

Figure 5·58 a-d Graphs summarising complex model input conditions during one complete traverse at 100 mm. spray distance.

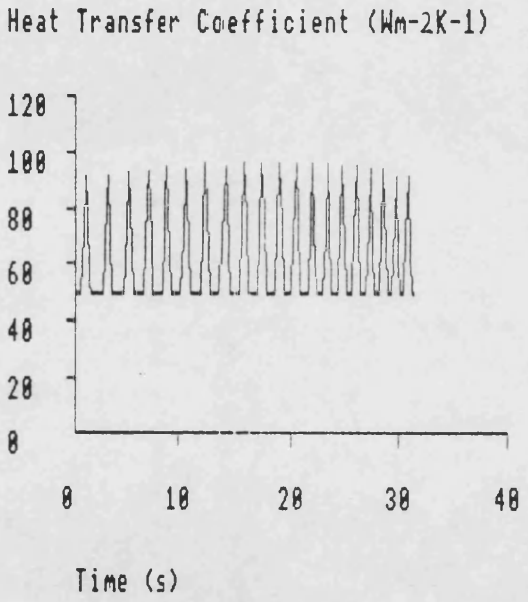

(C)

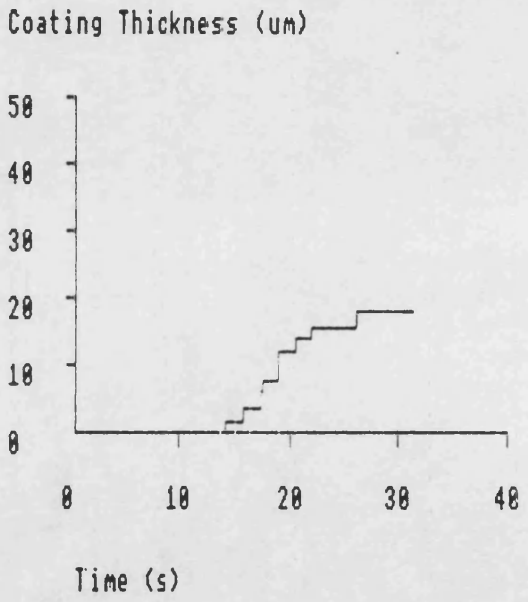

(D)

Figure 5·58 a-d Cont.

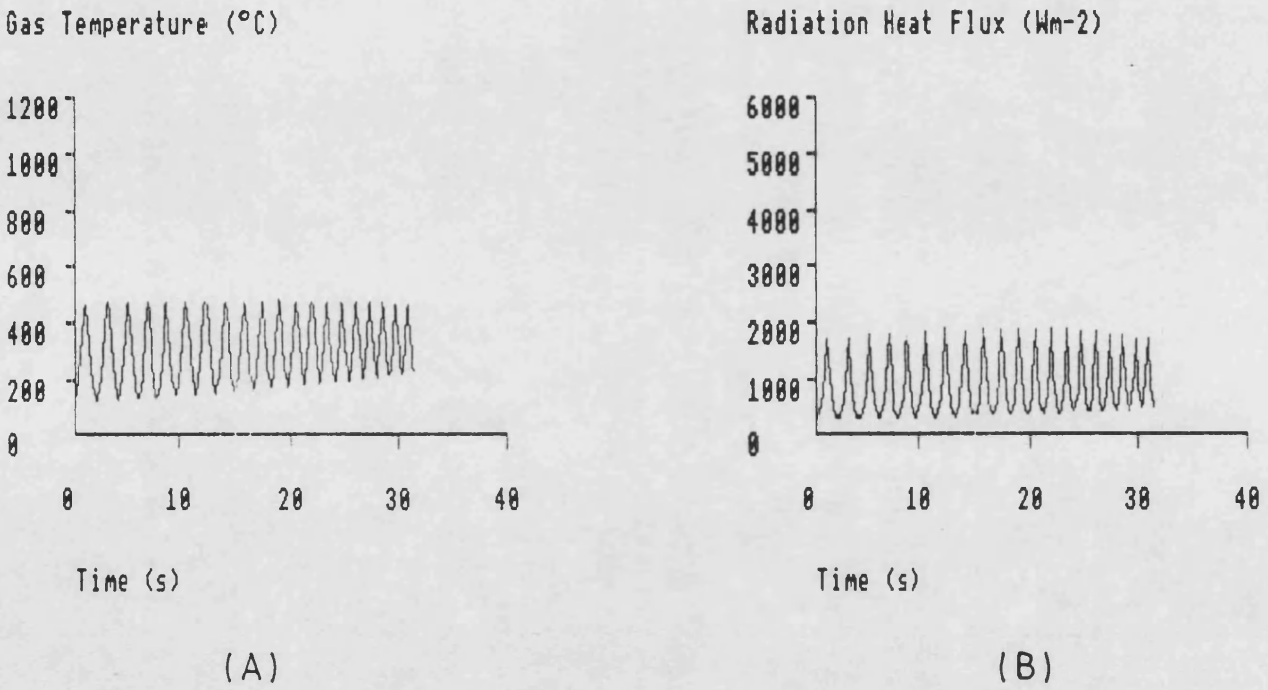

Figure 5·59a-d Graphs summarising complex model input conditions during one complete traverse at 125 mm. spray distance.

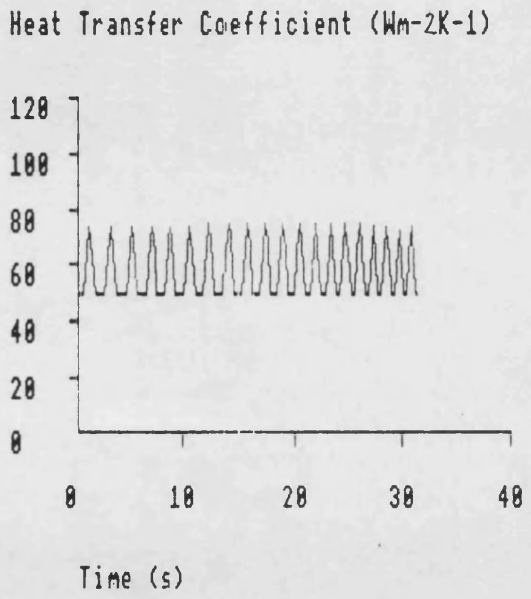

(C)

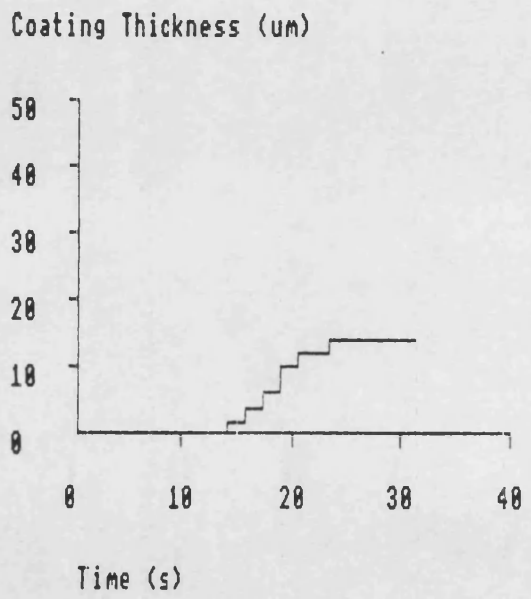

(D)

Figure 5·59 a-d Cont.

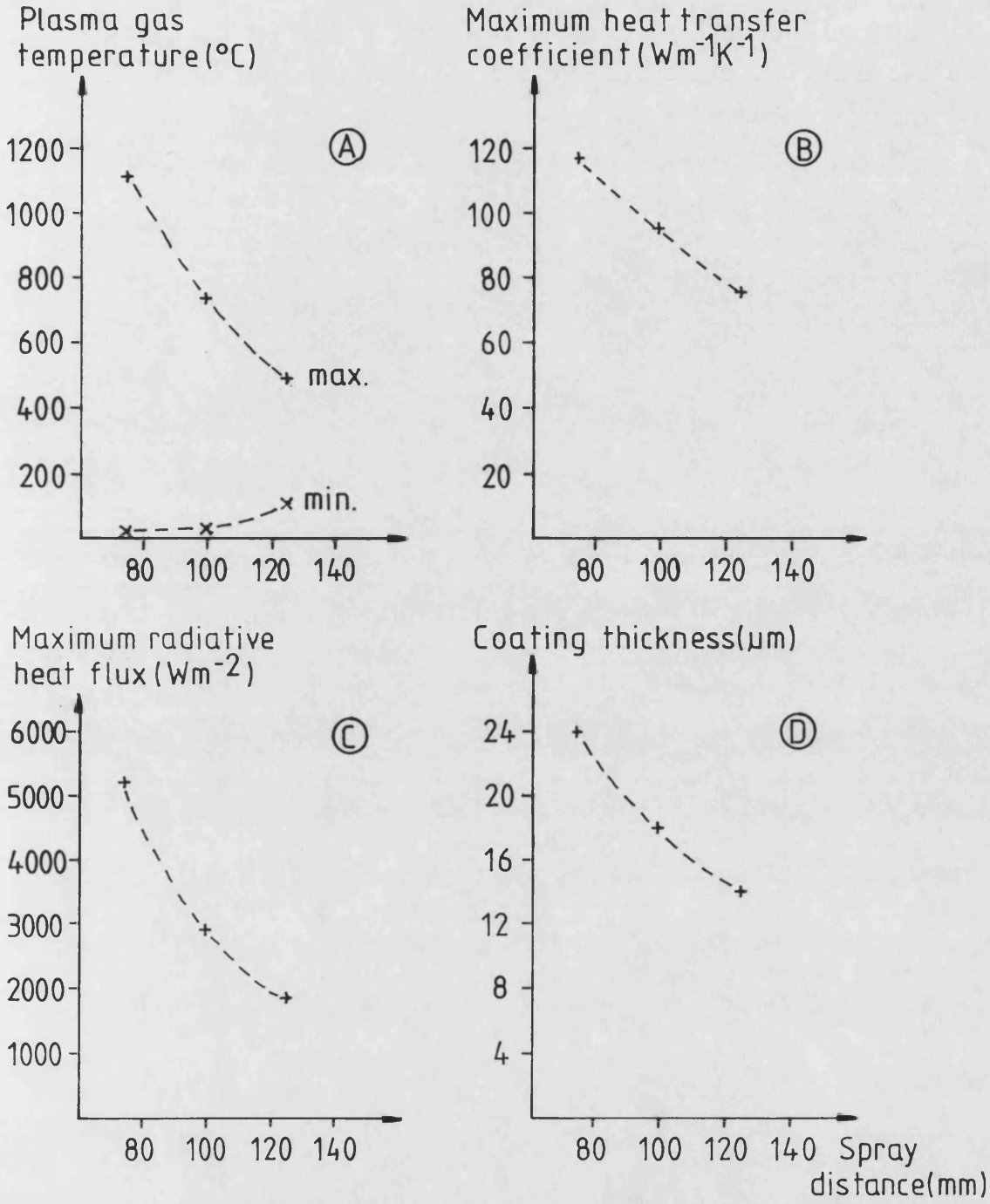

Figure 5·60 a-d Graphs showing the predicted variation of;

Ⓐ maximum/minimum plasma gas temperature,

Ⓑ maximum heat transfer coefficient,

Ⓒ maximum radiative heat flux,

Ⓓ coating thickness,

with spray distance during one traverse.

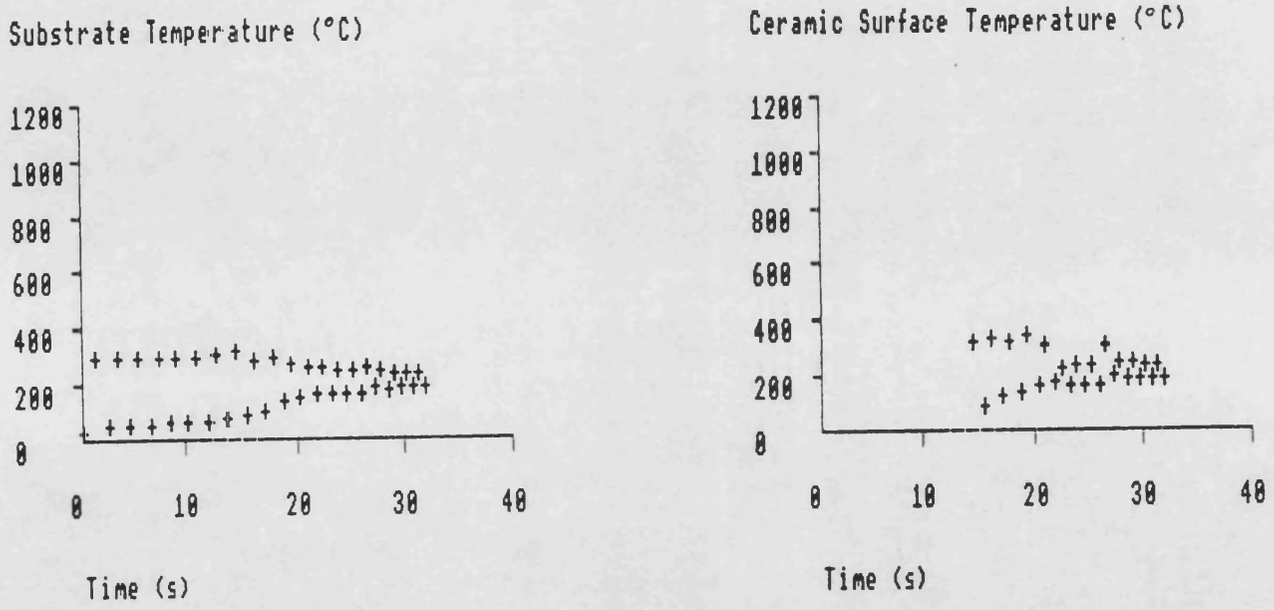

Figure 5·61 a-b Graphs showing predicted maximum/minimum substrate and coating front face temperatures for each pass, during one traverse at 100 mm. spray distance.

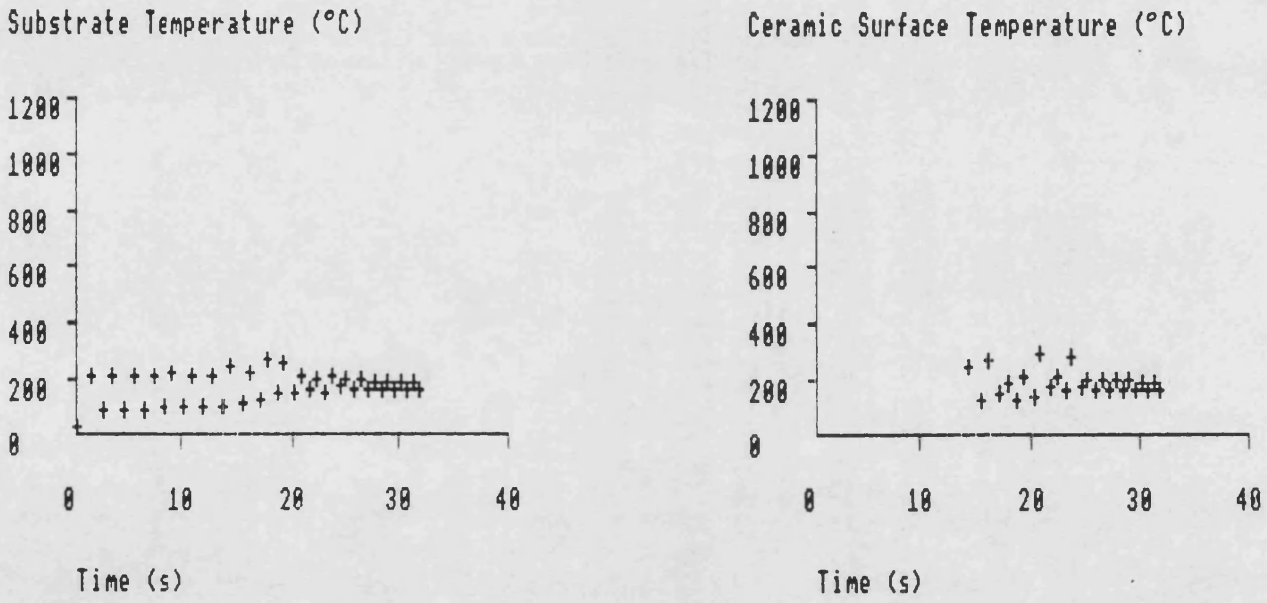

(A) (B)

Figure 5·62 a-b Graphs showing predicted maximum/minimum substrate and coating front face temperatures for each pass, during one traverse at 125 mm. spray distance.

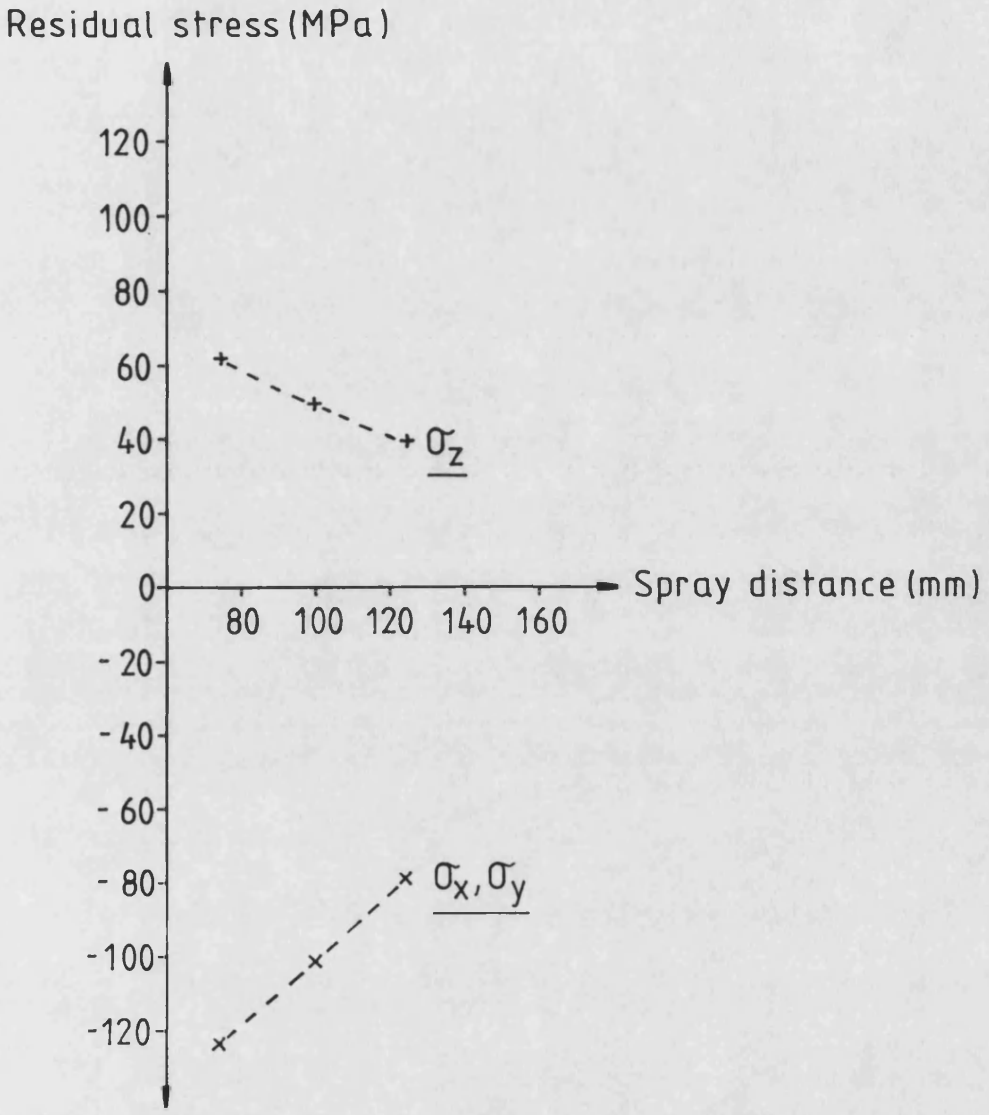

Figure 5·63 Graph illustrating the predicted relationship between coating residual stress and spray distance.

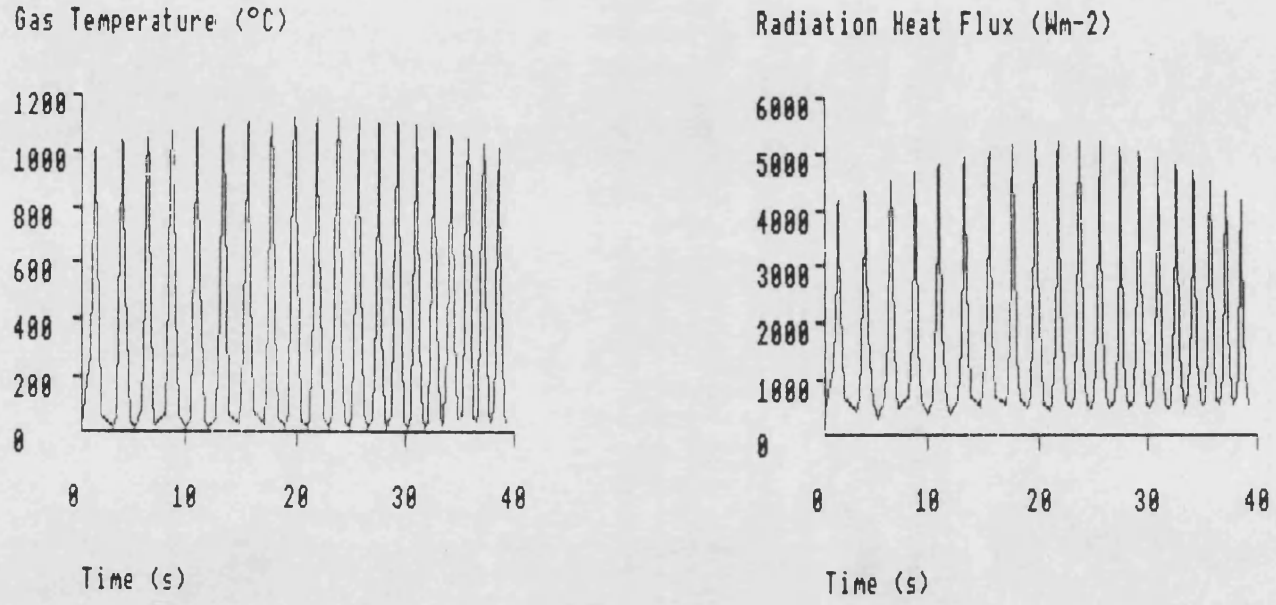

Figure 5·64 a-d Graphs summarising complex model input conditions during one complete traverse at 0·4 ms^{-1} relative velocity.

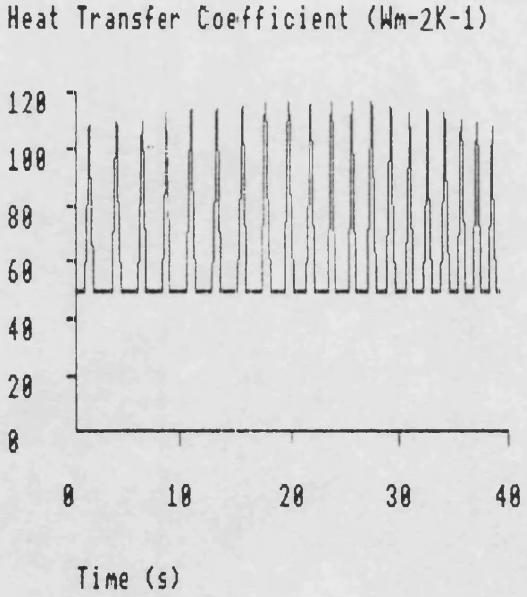

(C)

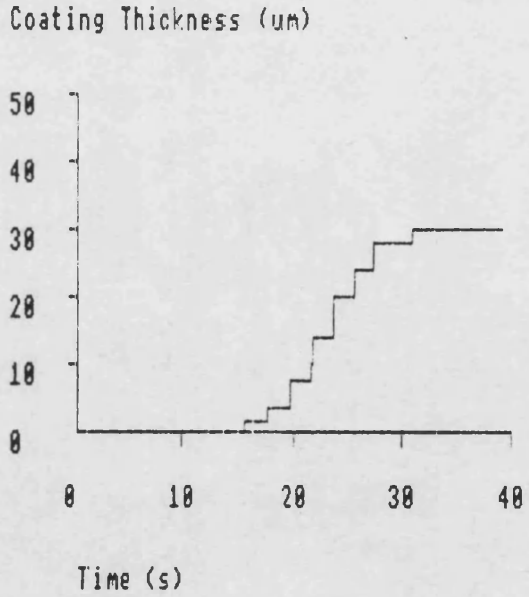

(D)

Figure 5·64 a-d Cont.

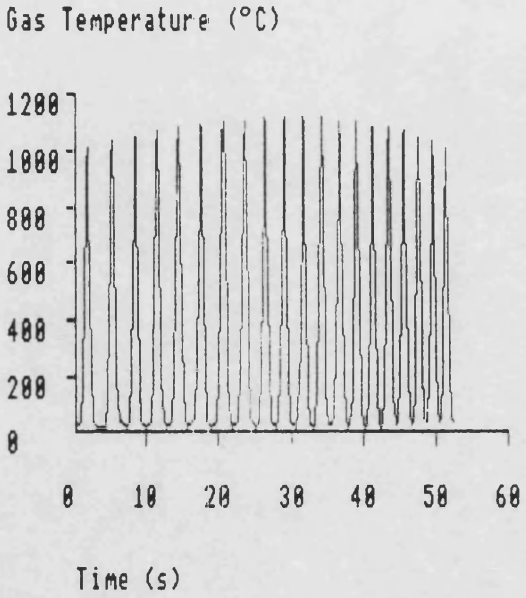

(C)

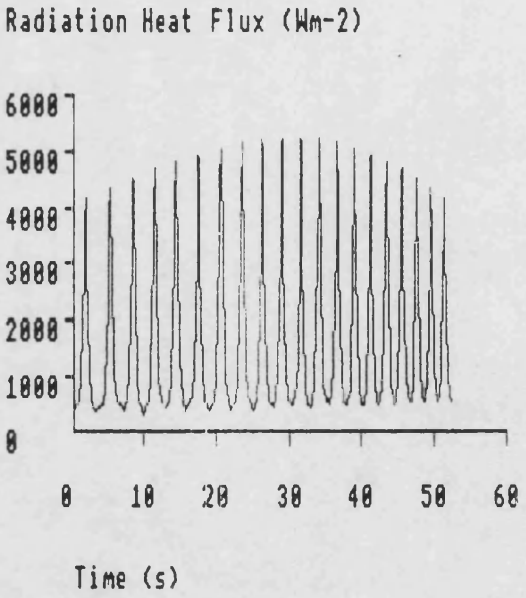

(D)

Figure 5·65 a-d Graphs summarising complex model input conditions during one complete traverse at 0·5ms^{-1} relative velocity.

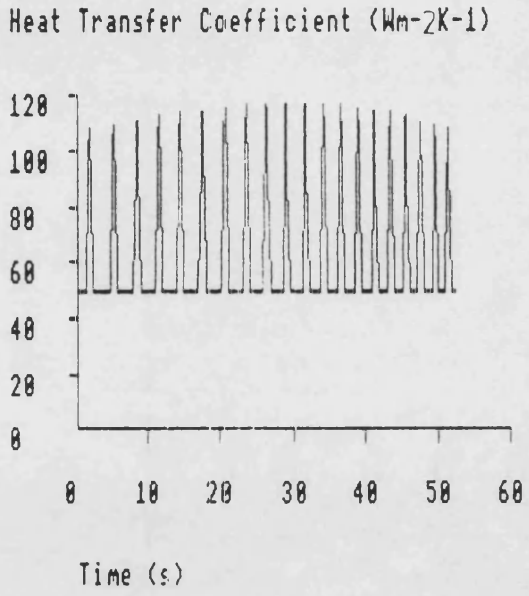

(C)

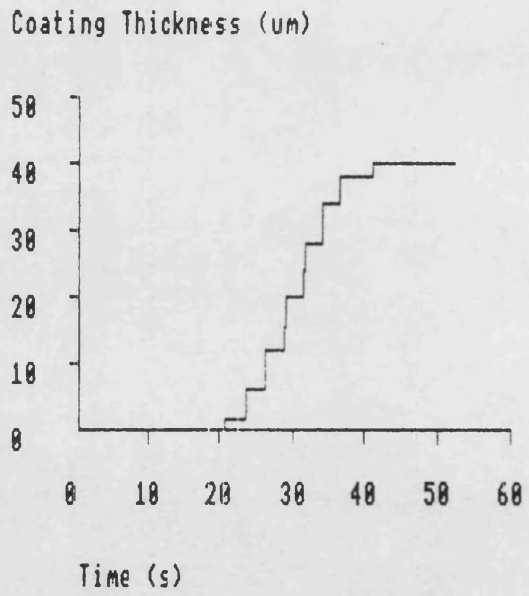

(D)

Figure 5·65 a-d Cont.

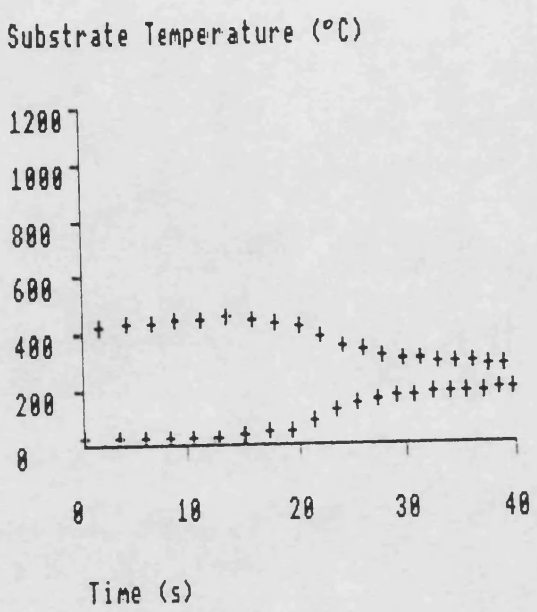

(A)

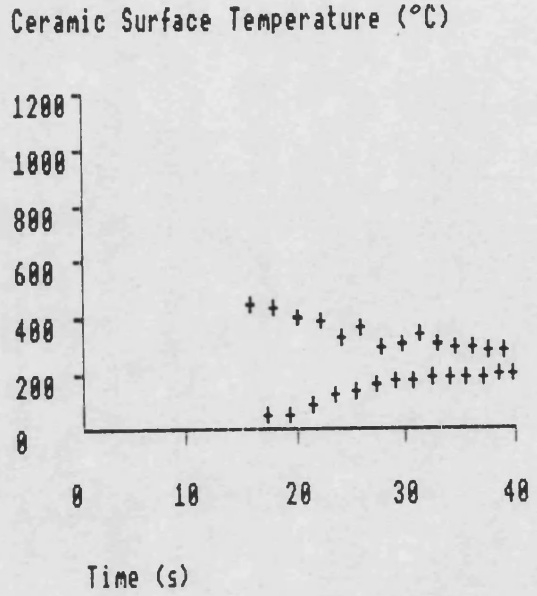

(B)

Figure 5·66 a-b Graphs showing predicted maximum/minimum substrate and coating front face temperatures for each pass, during one traverse at 0·4 ms^{-1} relative velocity.

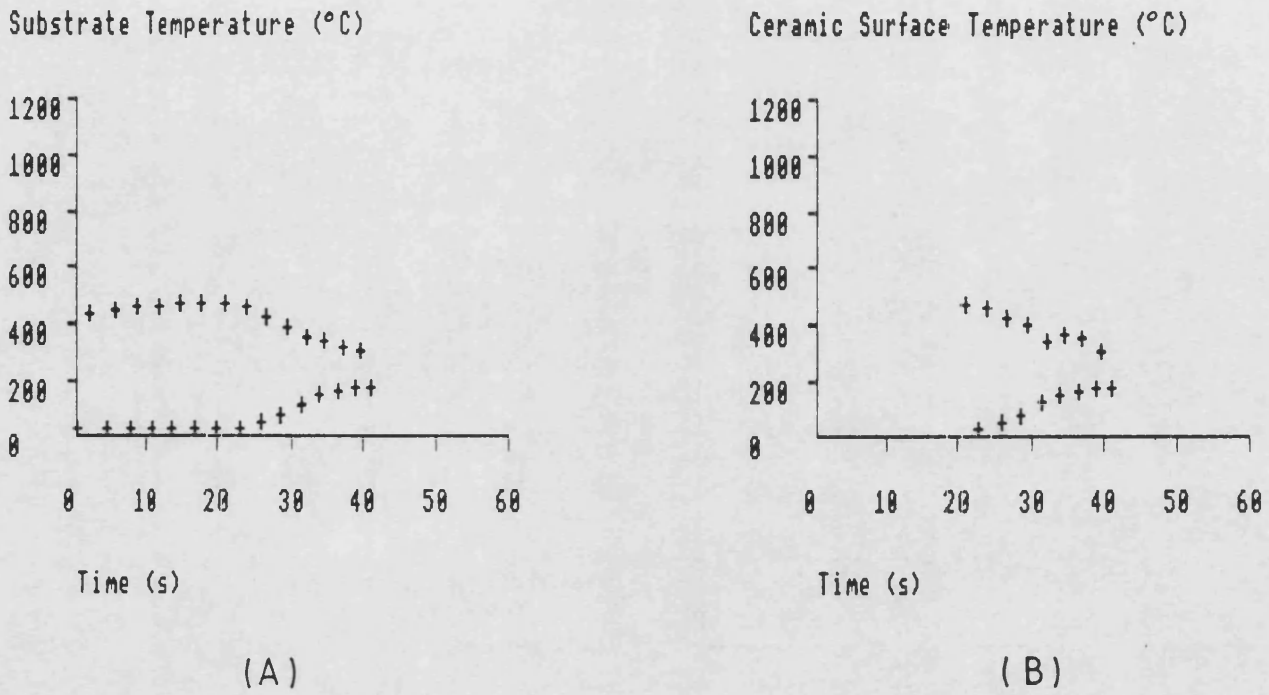

Figure 5·67 a-b Graphs showing predicted maximum/minimum substrate and coating front face temperatures for each pass, during one traverse at 0·3ms^{-1} relative velocity.

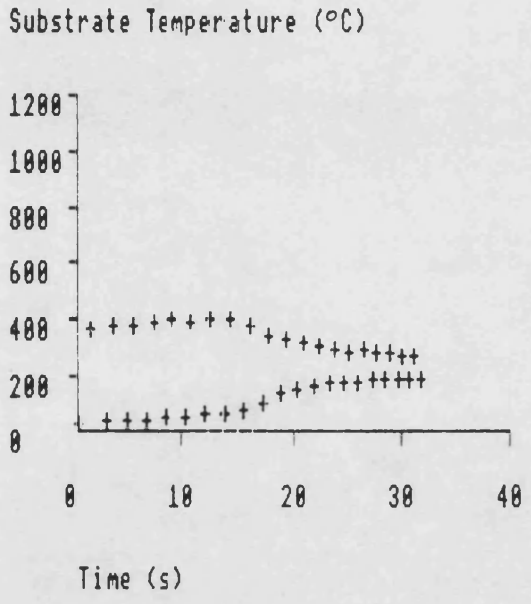

(A)

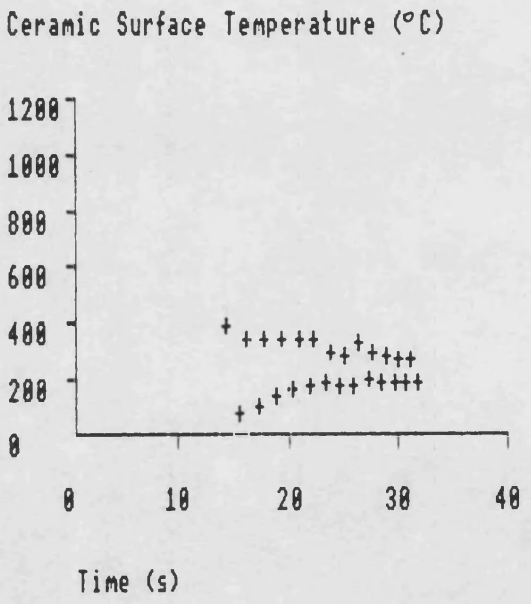

(B)

Figure 5·68 a-b Graphs showing predicted maximum/minimum substrate and coating front face temperatures for each pass, during one traverse over a copper substrate.

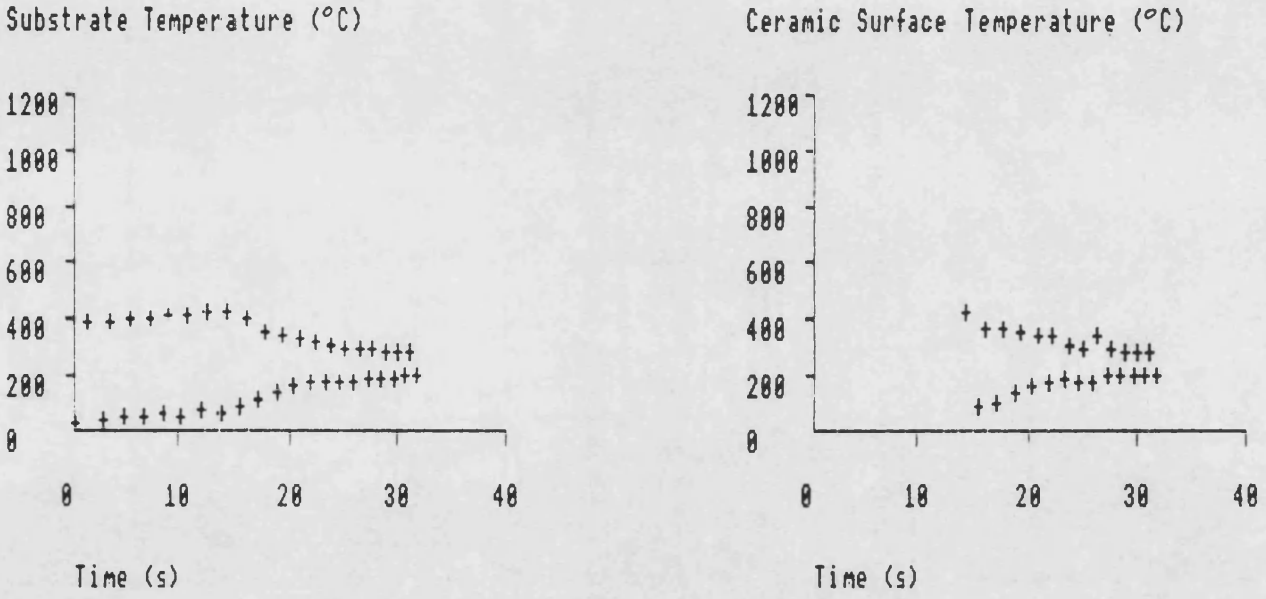

Figure 5·69 a-b Graphs showing predicted maximum/minimum substrate and coating front face temperatures for each pass, during one traverse over a steel substrate.

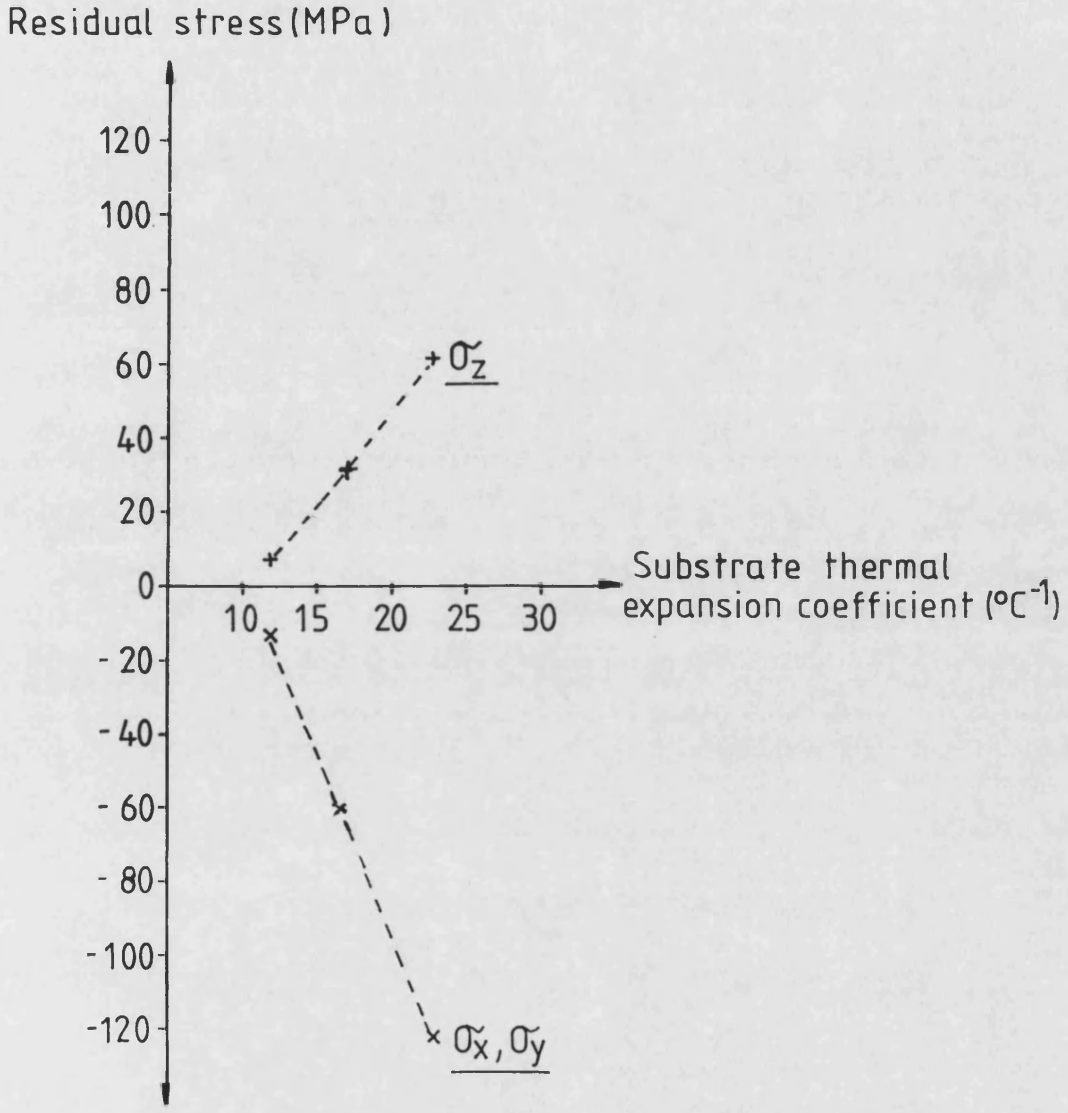

Figure 5·70 Graph illustrating the predicted relationship between coating residual stress and substrate thermal expansion coefficient.

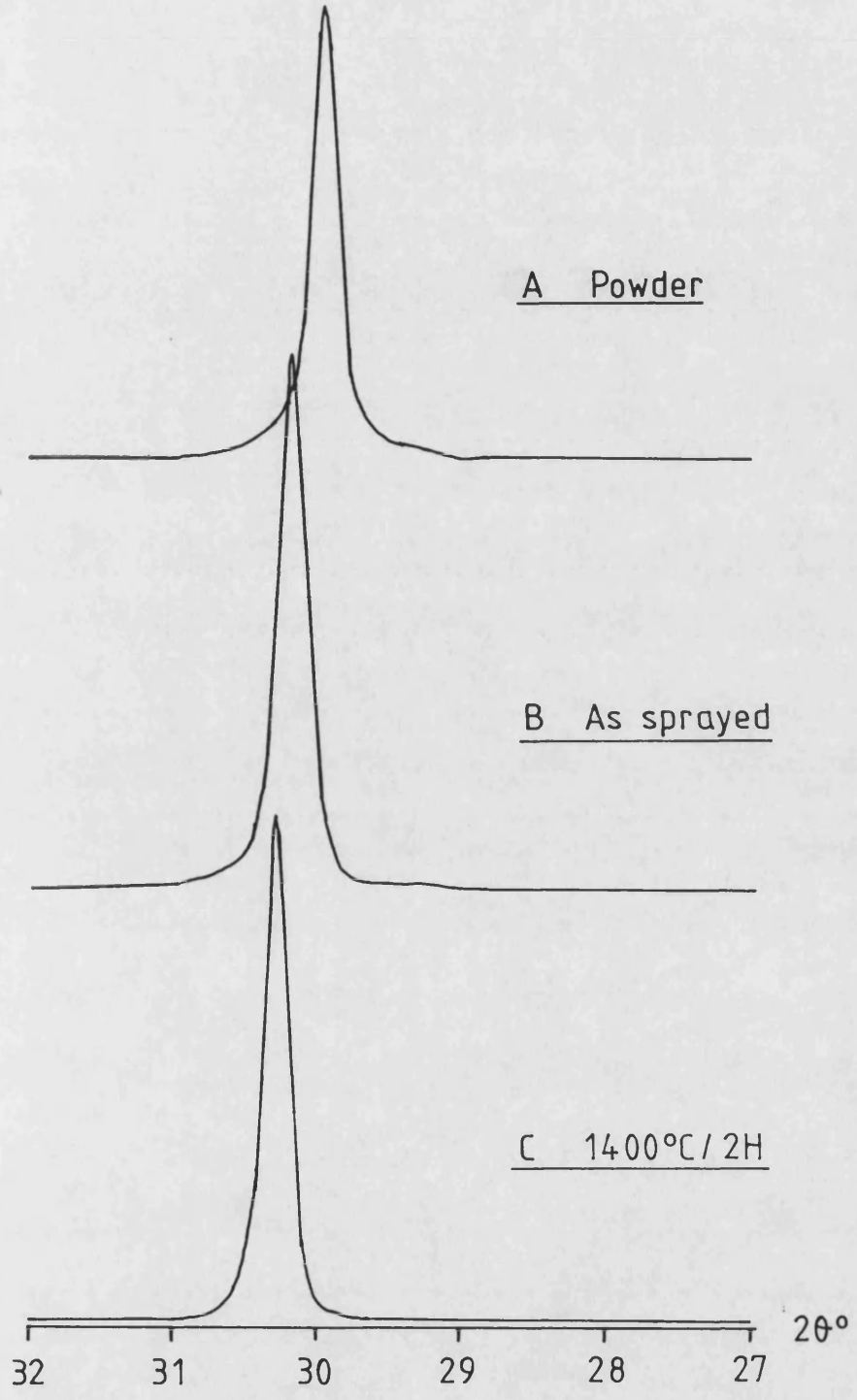

Figure 5·71 a-c Low angle diffractometer traces from powder, as sprayed and sprayed, heat treated samples of material A.

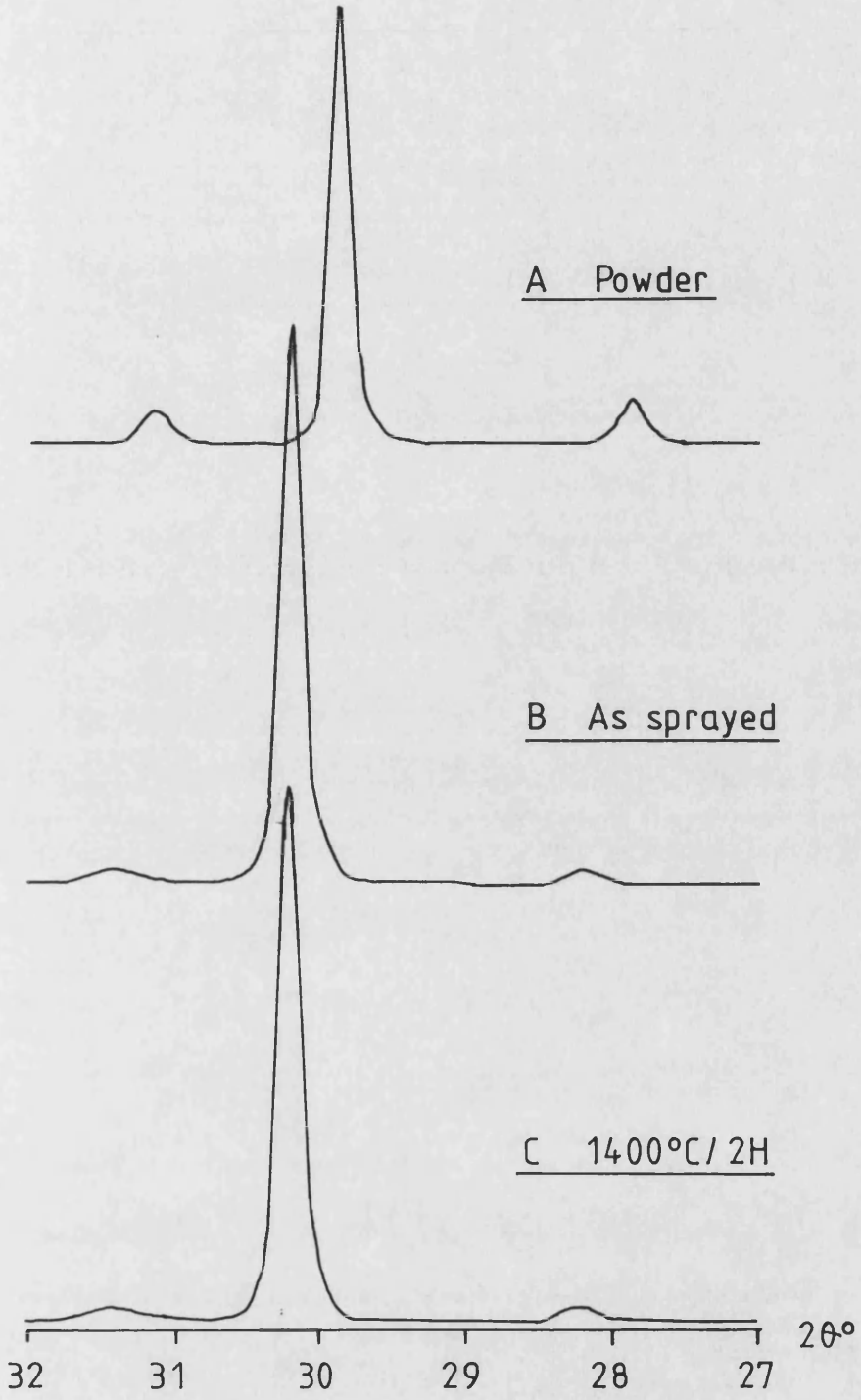

Figure 5·72 a-c Low angle diffractometer traces from powder, as sprayed and sprayed, heat treated samples of material B.

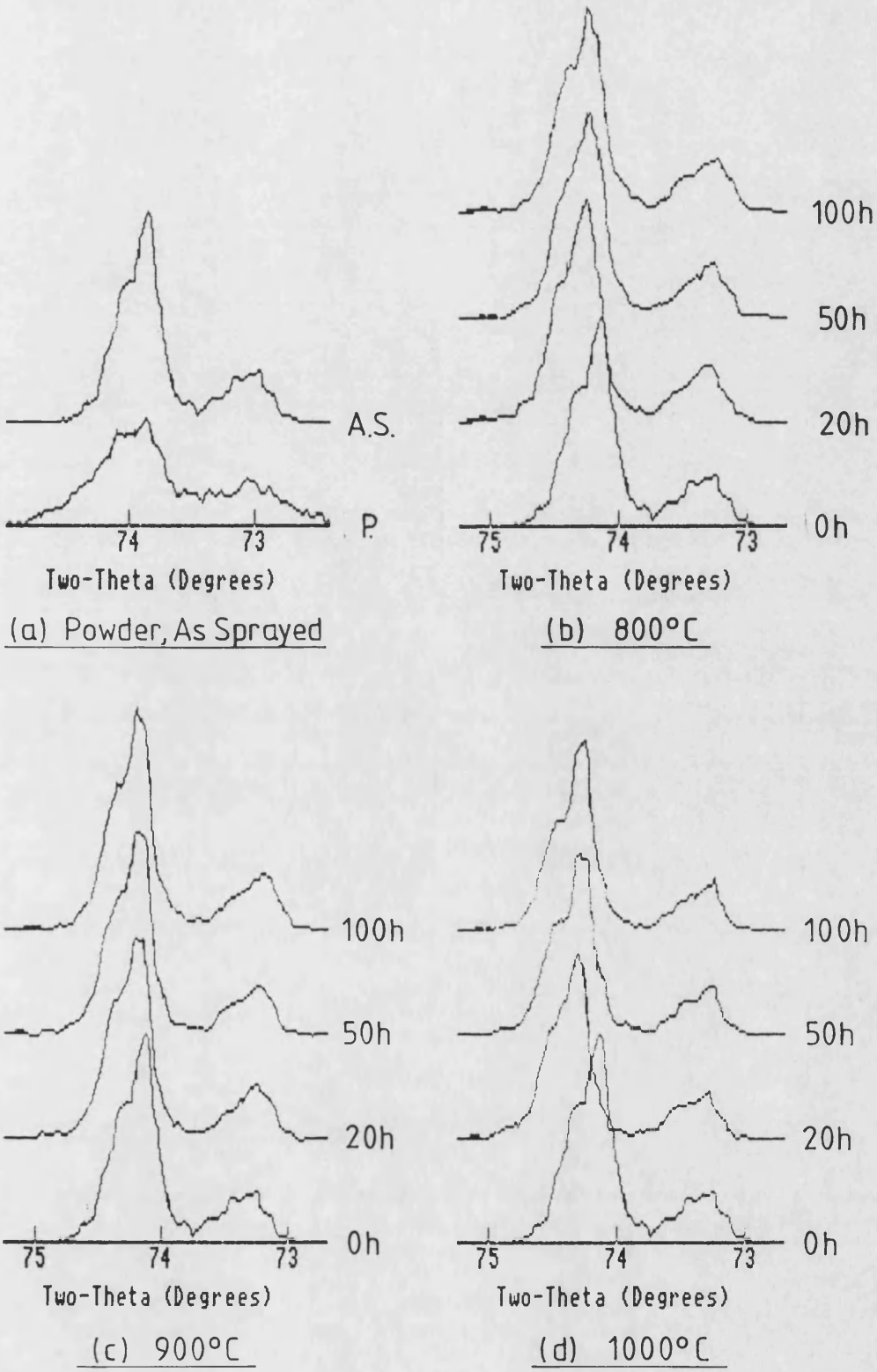

Figure 5·73 a-d High angle diffractometer traces from powder, plasma-sprayed and sprayed, heat treated samples of material A.

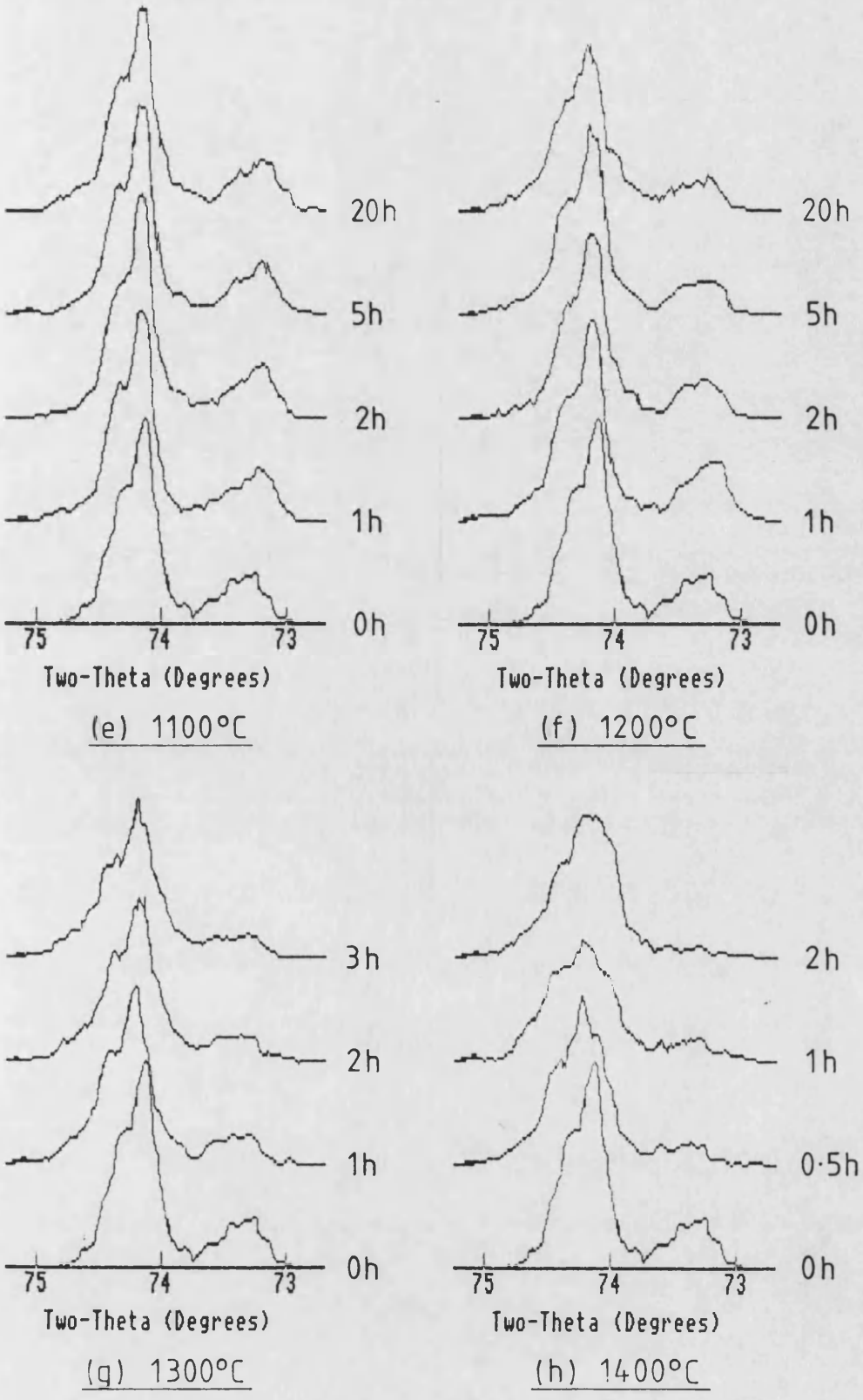

Figure 5·73 e-h High angle diffractometer traces from plasma-sprayed, heat treated samples of material A.

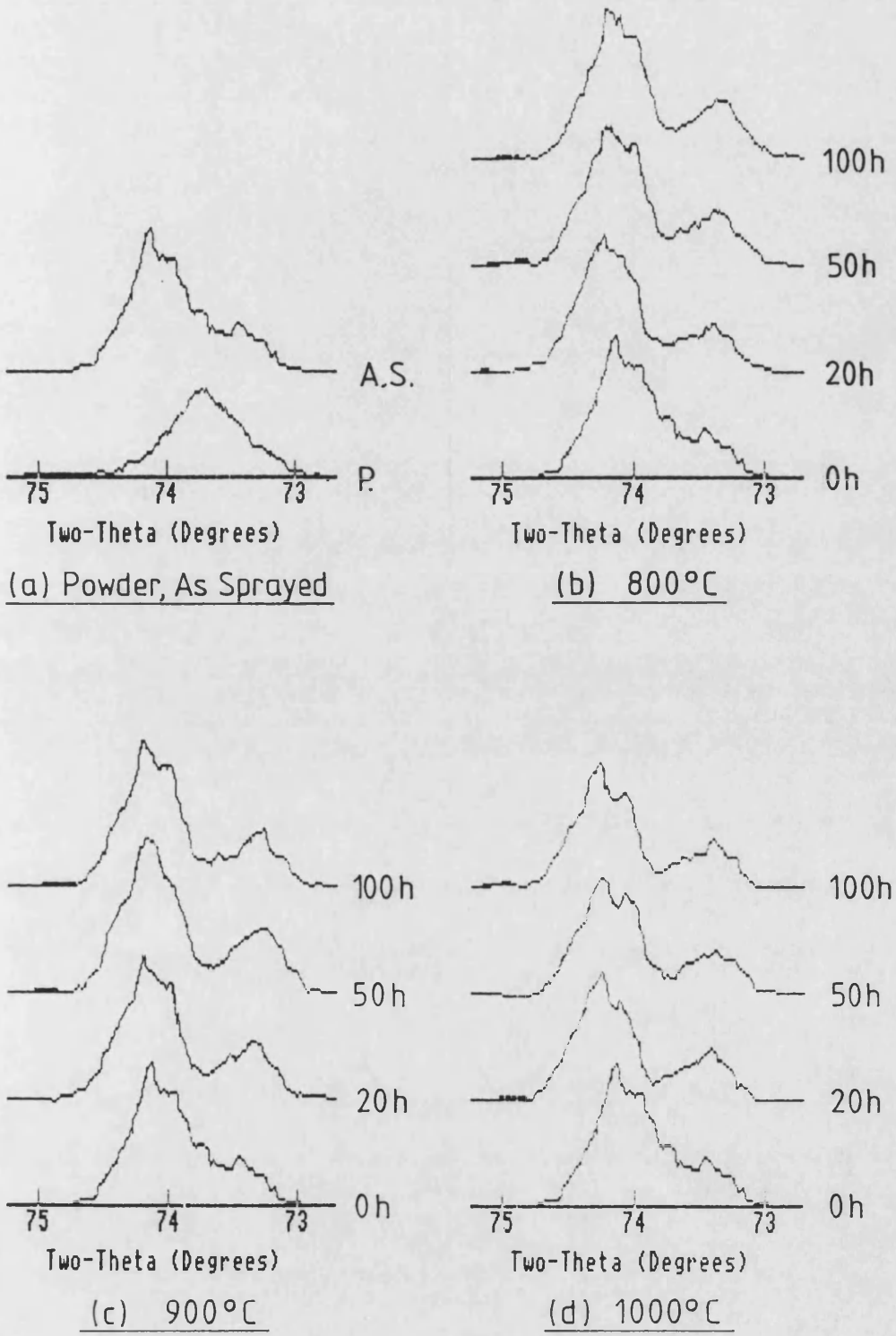

Figure 5·74 a-d High angle diffractometer traces from powder, plasma-sprayed and sprayed, heat treated samples of material B.

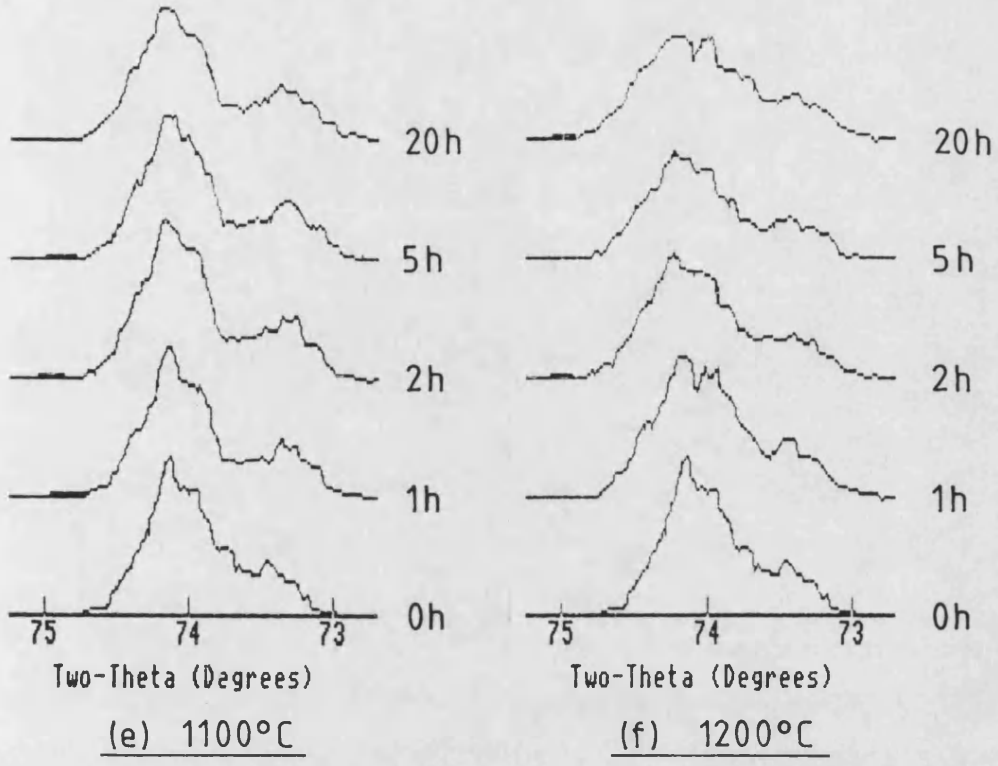

(e) 1100°C (f) 1200°C

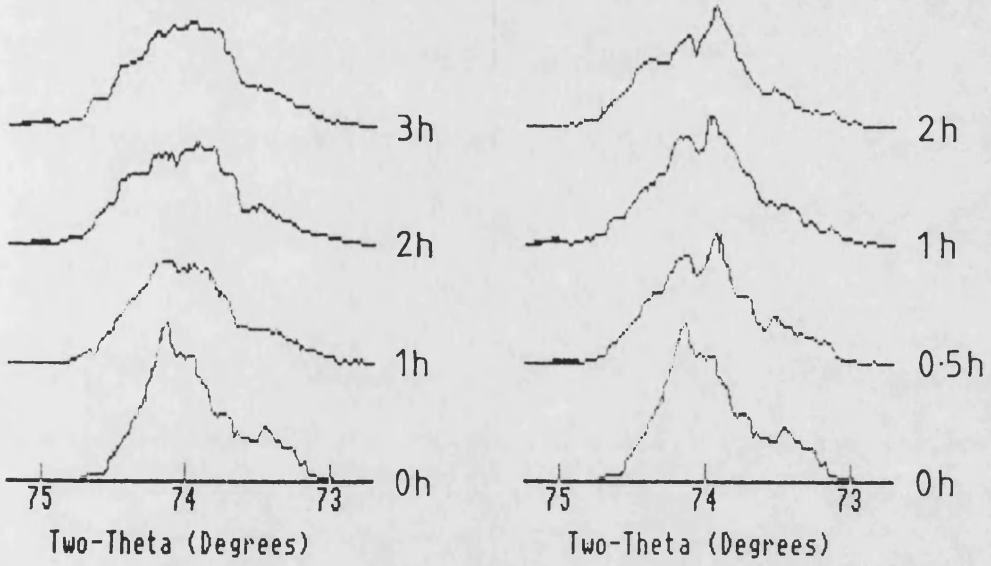

(f) 1300°C (g) 1400°C

Figure 5·74 e-h High angle diffractometer traces from plasma-sprayed, heat treated samples of material B.

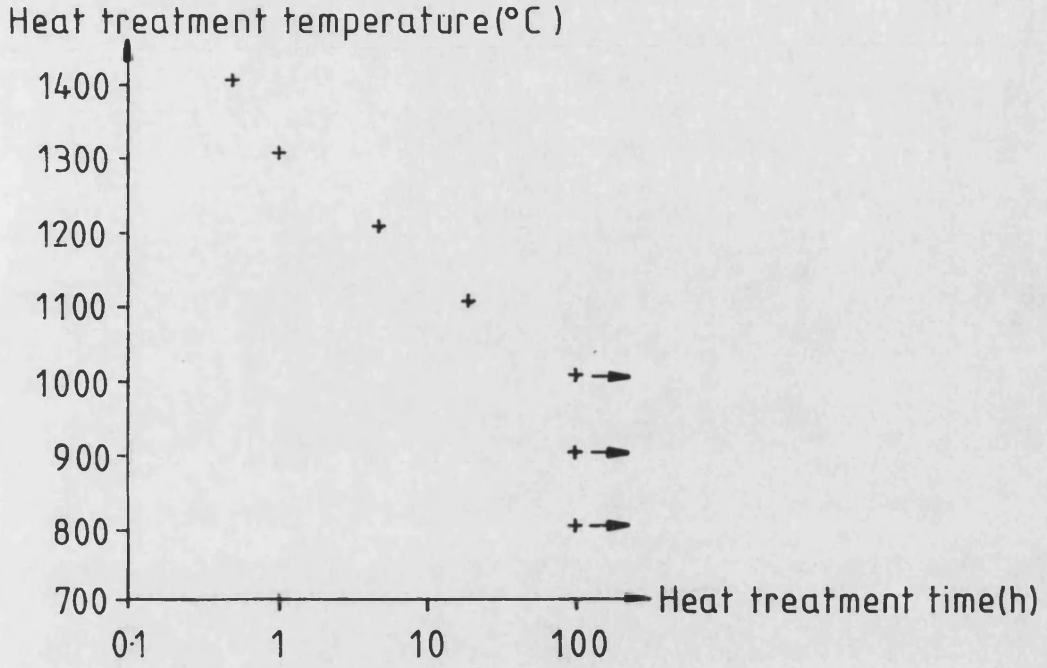

Figure 5·75 Graph showing the onset of structural change in coatings of material A with heat treatment.

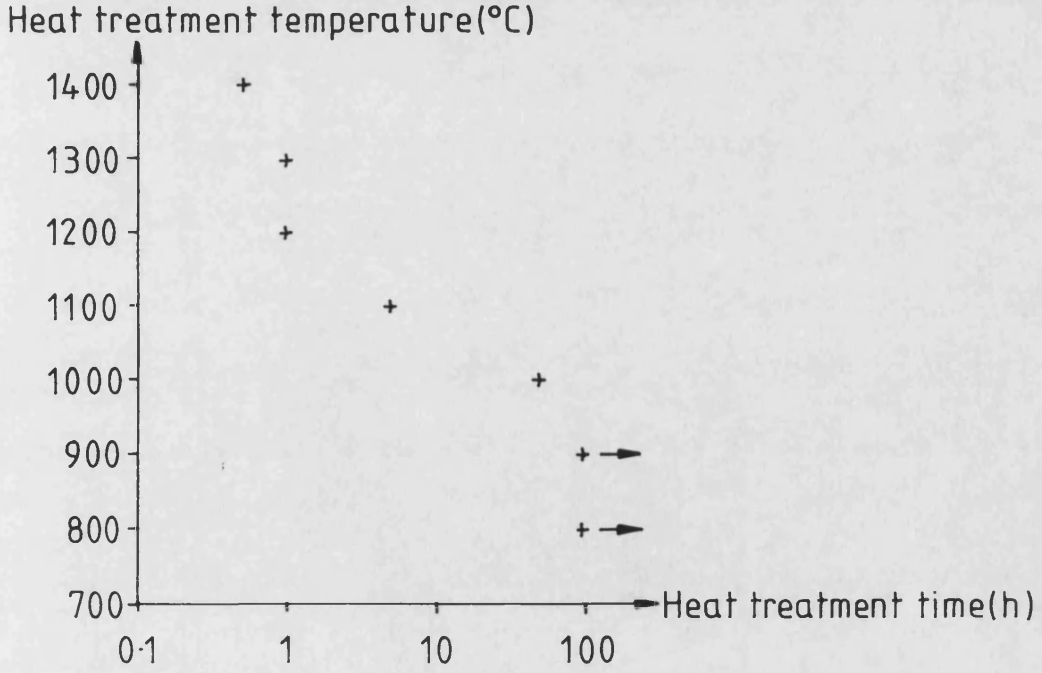

Figure 5·76 Graph showing the onset of structural change in coatings of material B with heat treatment.

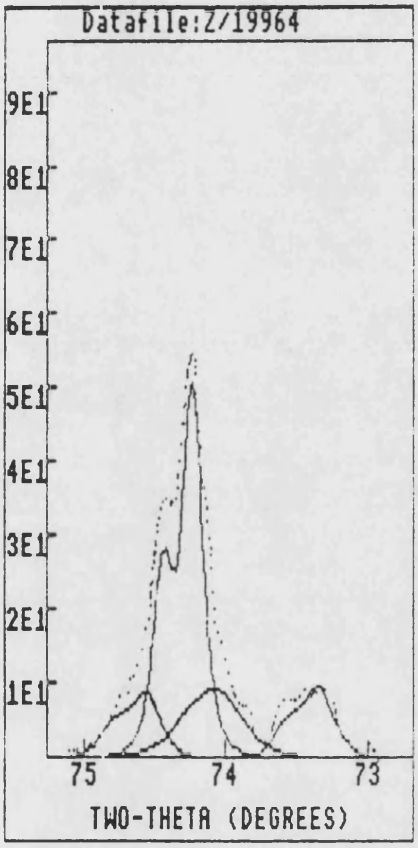

PEAK DATA

Datafile :Z/19964
Date :27/4/87
Comments :1300/1H
Reflections :4

Pk.	Centre	PWHM	Imax	Area
1a1	74.57	0.23	8.205	2.320
1a2	74.79	0.23	3.988	1.127
SUM			8.872	3.448
2a1	74.23	0.17	48.88	10.21
2a2	74.45	0.17	24.33	5.085
SUM			50.75	15.30
3a1	74.04	0.38	7.293	3.407
3a2	74.25	0.38	3.532	1.650
SUM			8.992	5.057
4a1	73.34	0.23	8.888	2.513
4a2	73.55	0.23	4.330	1.224
SUM			9.651	3.738

Figure 5·77 An example of a deconvoluted high angle diffractometer trace showing the individual component reflections. Details of each reflection are given in the table.

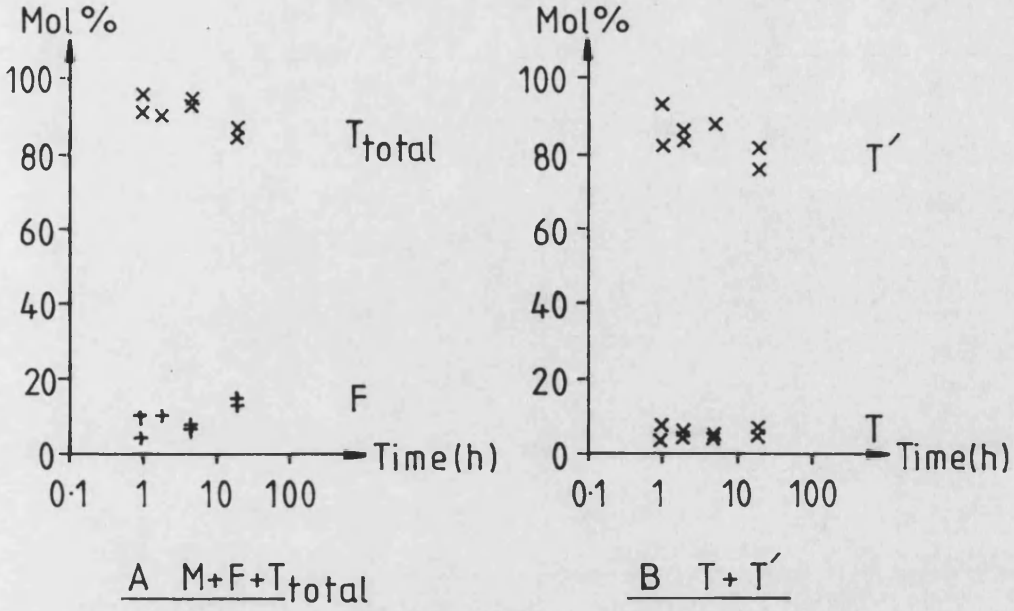

Figure 5·78 a-b Graphs showing the change in phase composition of plasma sprayed coatings of material A with heat treatment time at 1100°C.

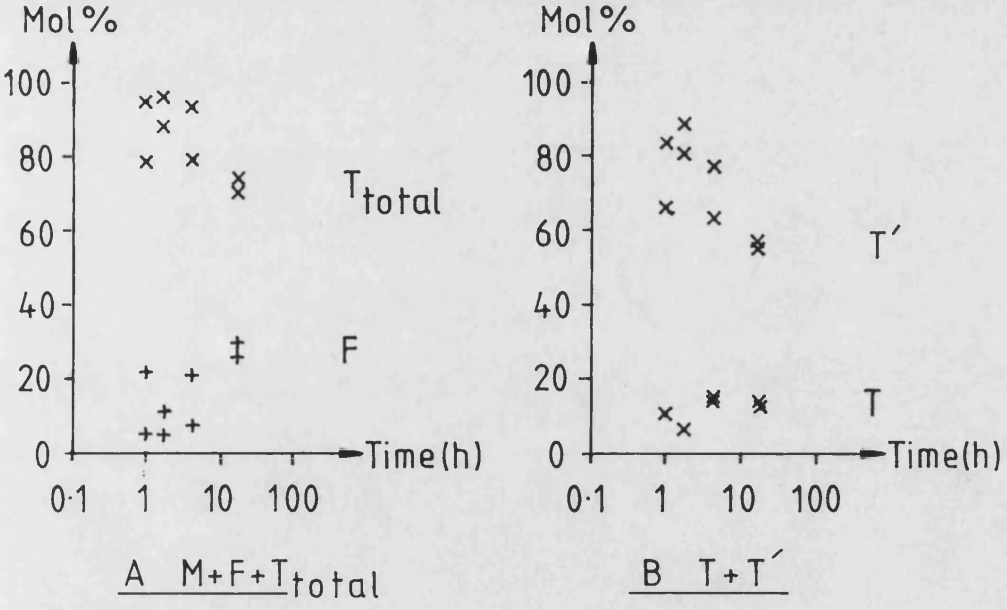

Figure 5·79 a-b Graphs showing the change in phase composition of plasma sprayed coatings of material A with heat treatment time at 1200°C.

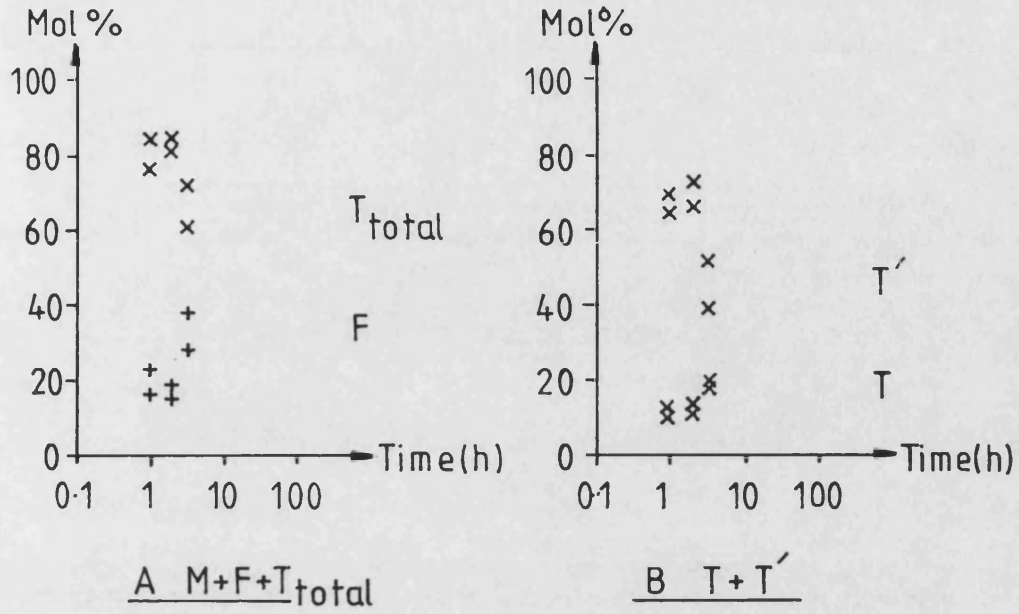

Figure 5·80 a-b Graphs showing the change in phase composition of plasma sprayed coatings of material A with heat treatment time at 1300°C.

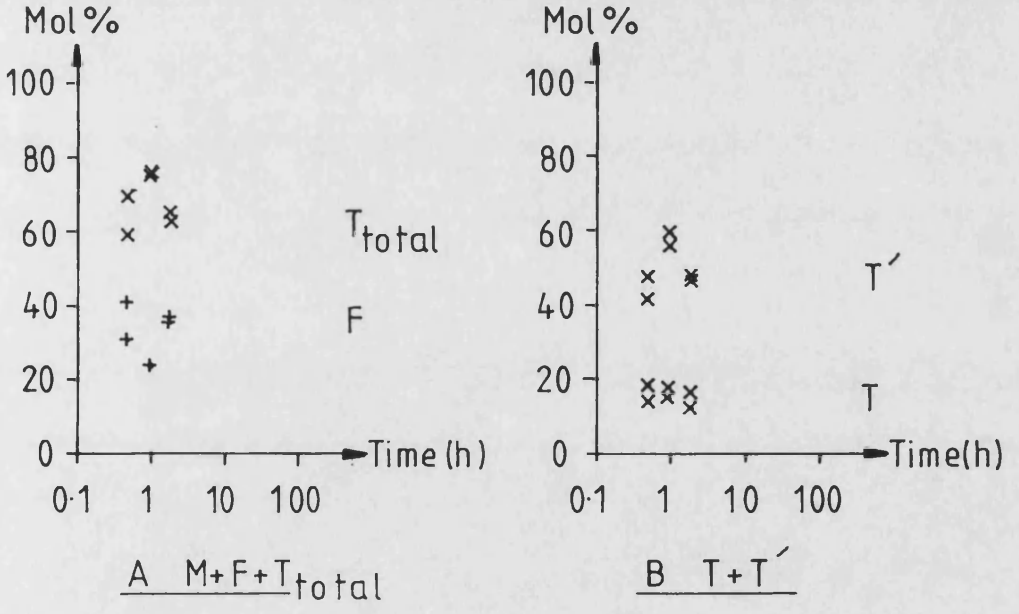

Figure 5·81 a-b Graphs showing the change in phase composition of plasma sprayed coatings of material A with heat treatment time at 1400°C.

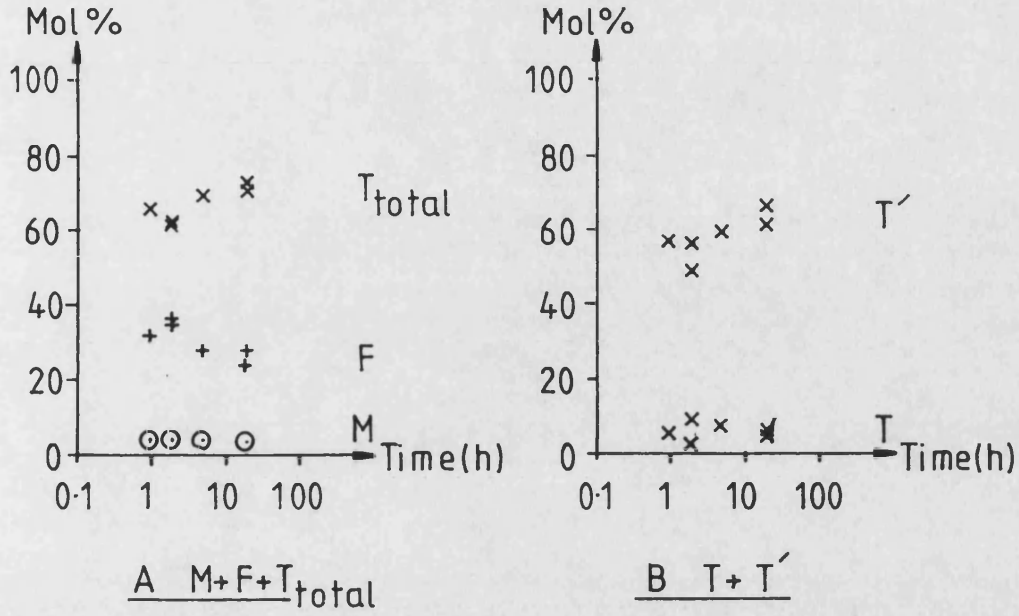

Figure 5·82 a-b Graphs showing the change in phase composition of plasma sprayed coatings of material B with heat treatment time at 1100°C.

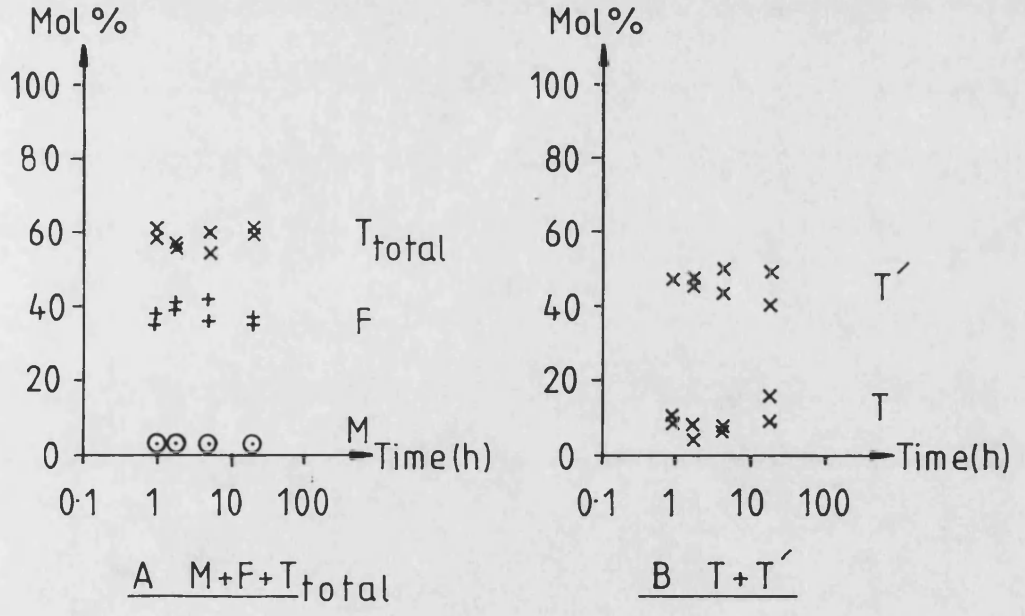

Figure 5·83 a-b Graphs showing the change in phase composition of plasma sprayed coatings of material B with heat treatment time at 1200°C.

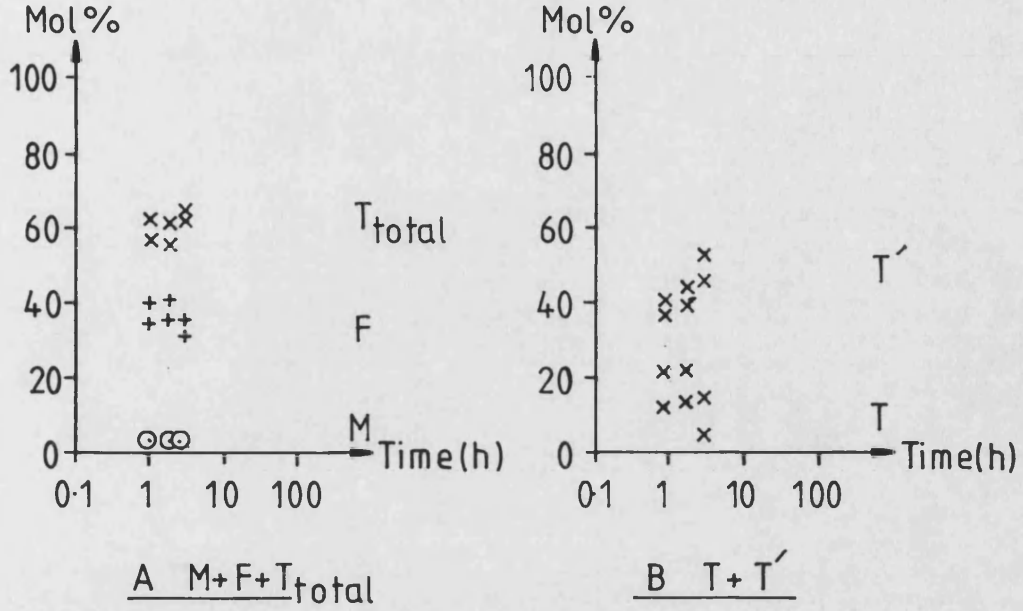

Figure 5·84 a-b Graphs showing the change in phase composition of plasma sprayed coatings of material B with heat treatment time at 1300°C.

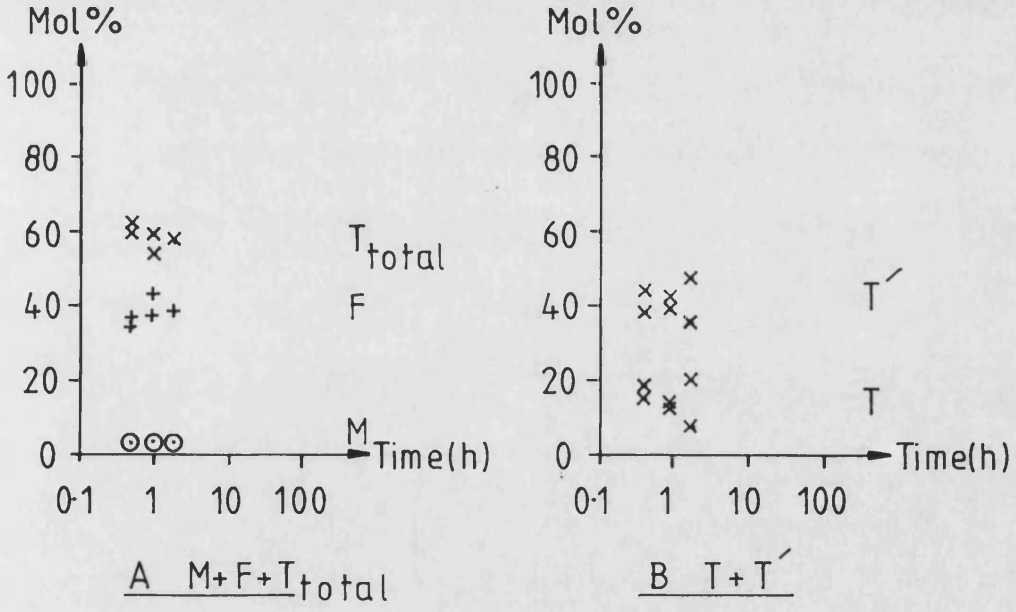

Figure 5·85 a-b Graphs showing the change in phase composition of plasma sprayed coatings of material B with heat treatment time at 1400°C.

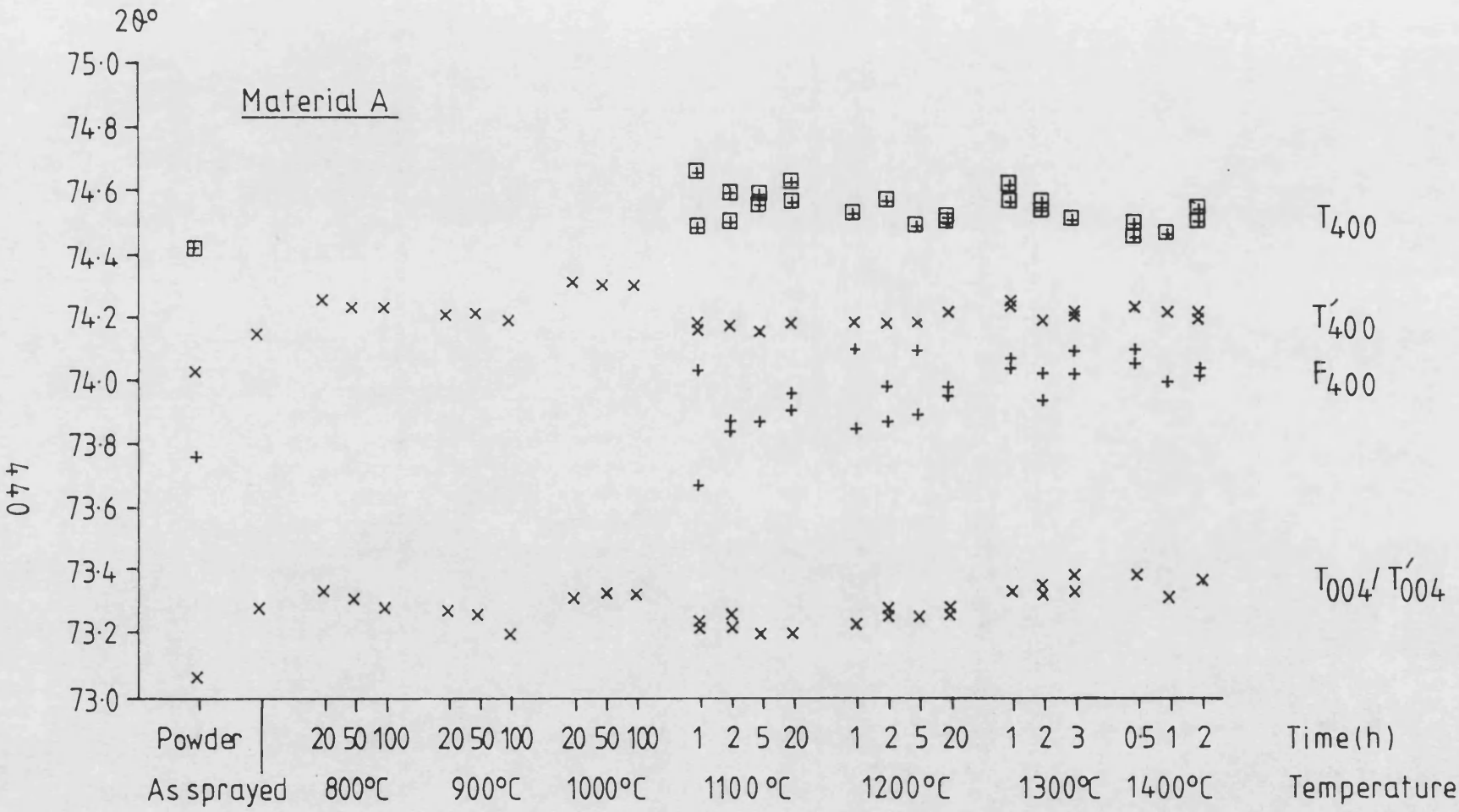

Figure 5·86 Graph showing the angular positions of tetragonal and cubic reflections obtained from deconvoluted high-angle X-ray data.

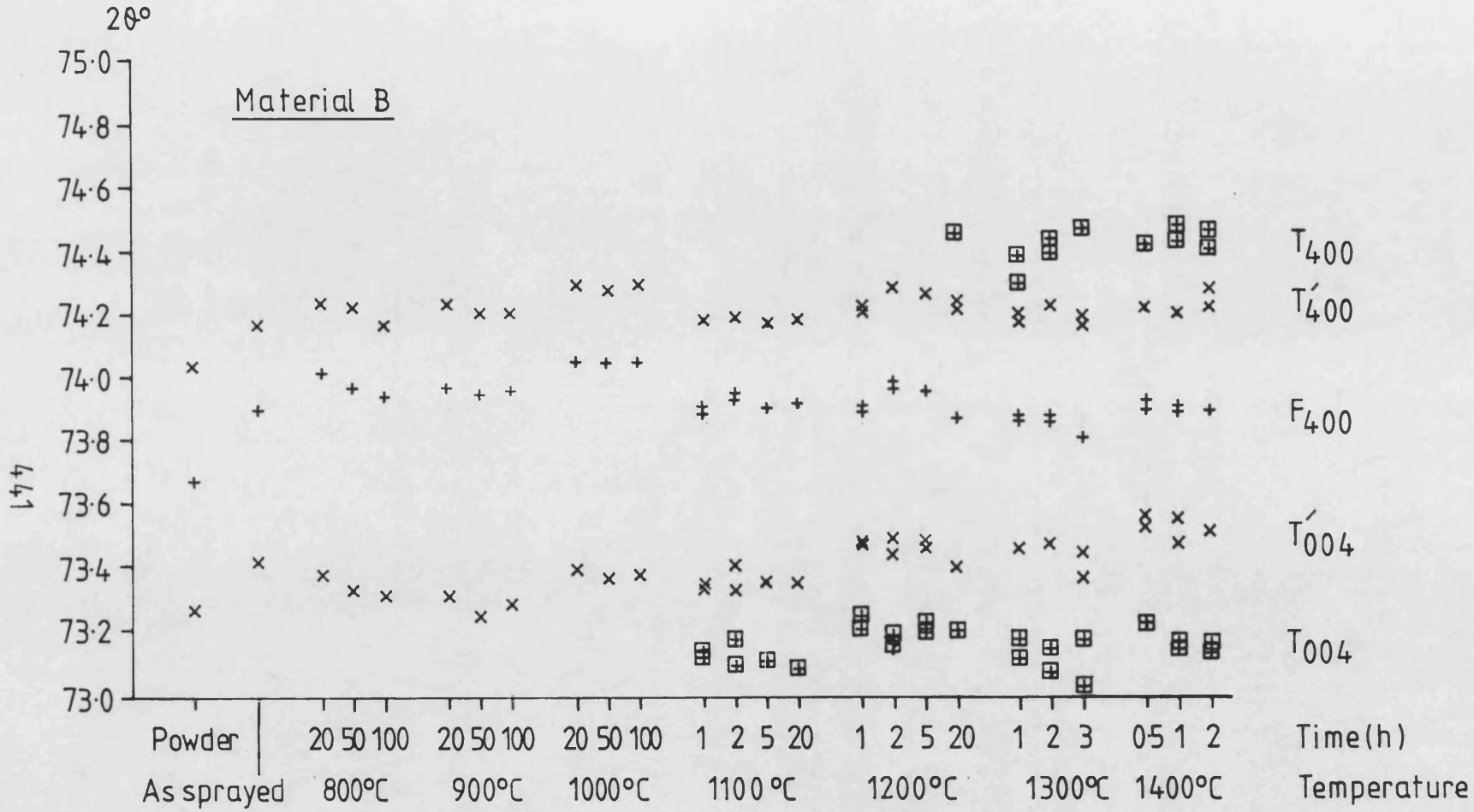

Figure 5·87 Graph showing the angular positions of tetragonal and cubic reflections, obtained from deconvoluted high-angle X-ray data.

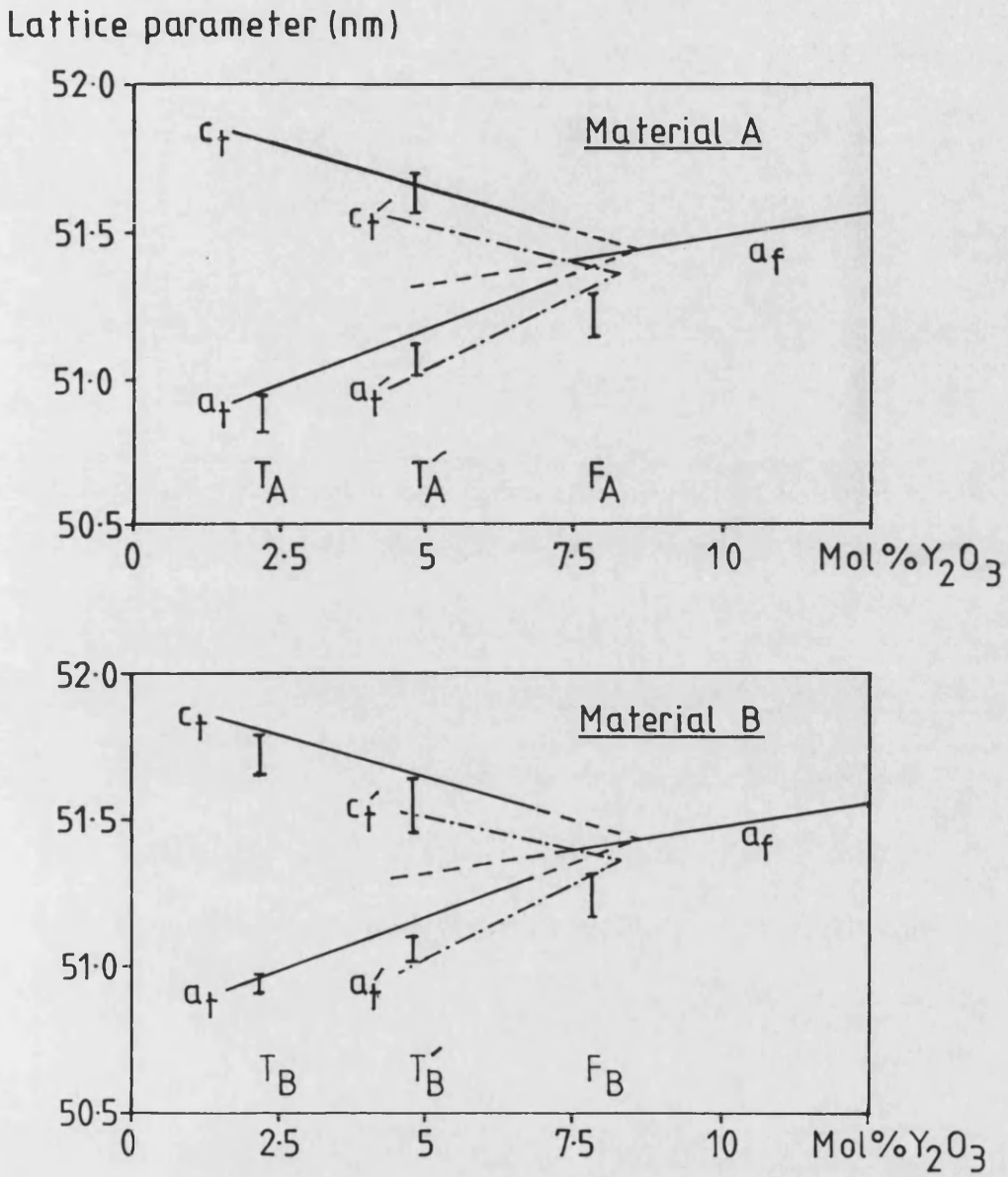

Figure 5·88 a-b Graphs showing a comparison between lattice parameters from:

reference [39] ———— - - -

reference [137] —·—·—·—·—

this investigation. I

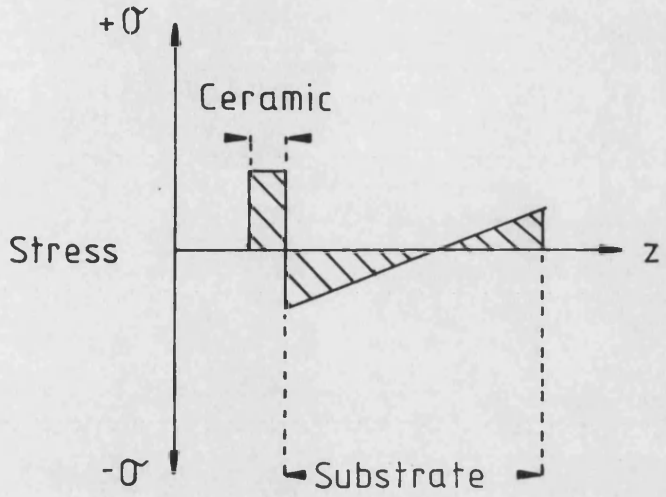

Figure 6·1 Graph illustrating the through thickness stress distribution derived from a simple elastic model of a ceramic coating, attached as a single slab at high temperature onto a cold substrate, and allowed to cool to room temperature.

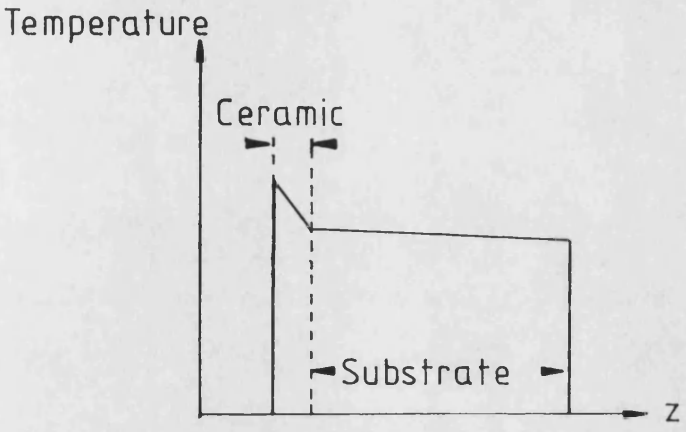

Figure 6·2 Graph illustrating the through thickness temperature profile in a practical coating on completion of spraying.

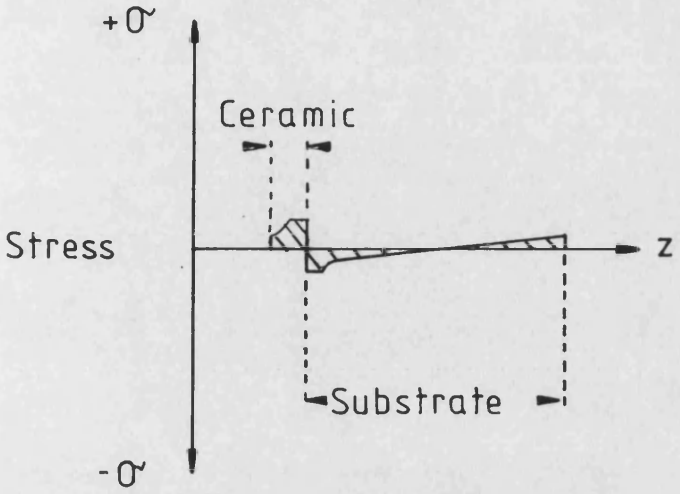

Figure 6·3 Graph illustrating the through thickness stress distribution in a practical coating, subject to shrinkage cracking and yielding, on completion of spraying.

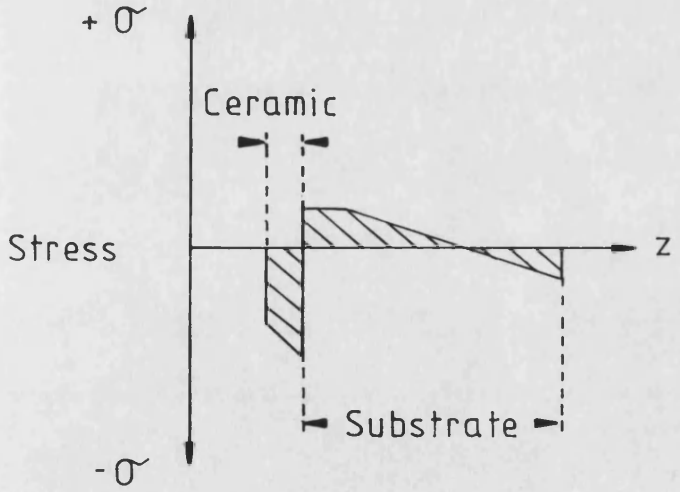

Figure 6·4 Graph illustrating the through thickness stress distribution in a practical coating on cooling to room temperature

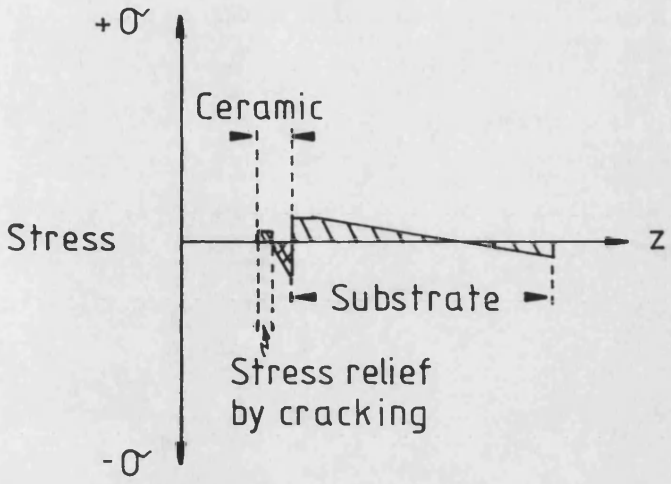

Figure 6·5 Graph illustrating the through thickness stress distribution in a practical coating on cooling. Relief of tensile stress has occurred by microcracking.

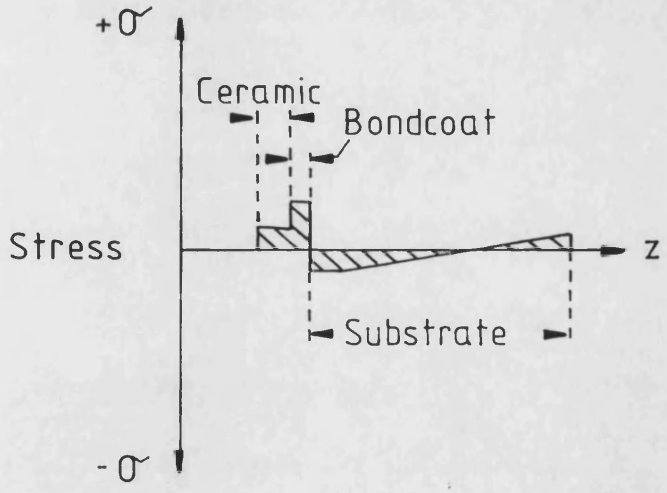

Figure 6·6 Graph illustrating the through thickness stress distribution in a practical coating, containing a bondcoat, on completion of spraying.

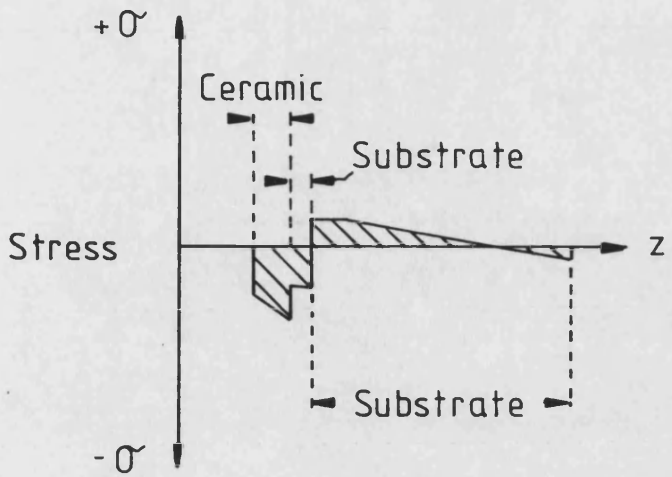

Figure 6·7 Graph illustrating the through thickness stress distribution in a practical coating, containing a bondcoat, on cooling to room temperature after spraying.

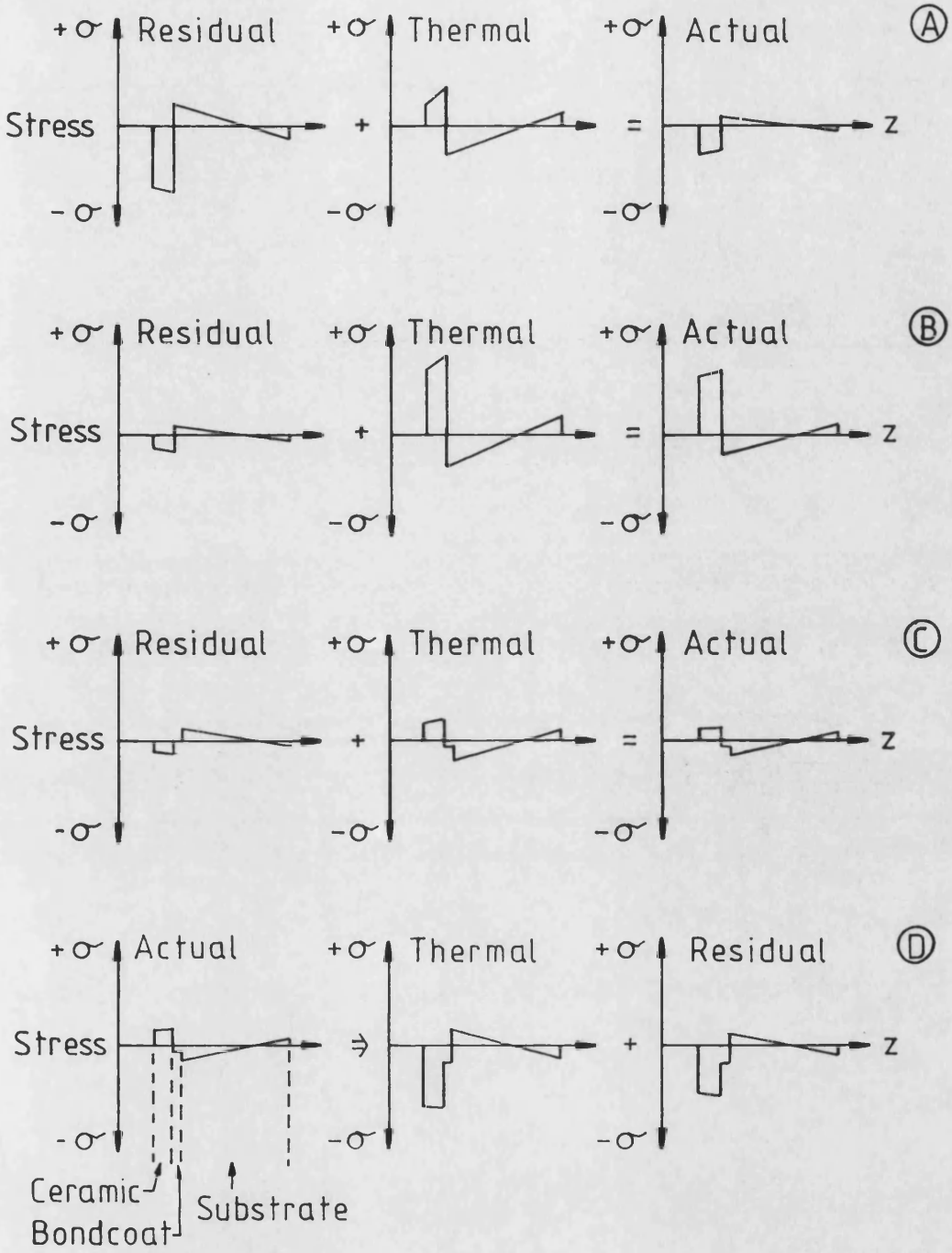

Figure 6·8 a-d Graphs illustrating the through thickness stress distribution components and their sum in simple (Ⓐ, Ⓑ) and two-layer (Ⓒ, Ⓓ) coatings, subject to:

Ⓐ Transient heating. Ⓑ, Ⓒ Static thermal gradient.

Ⓓ Transient cooling with limited bondcoat deformation.

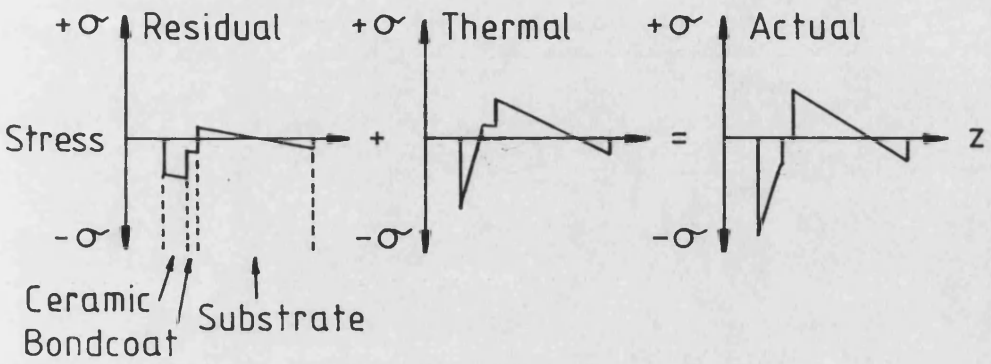

Figure 6·9 Graphs illustrating the through thickness stress distribution components and their sum in a thick, two layer coating subject to a heating transient.

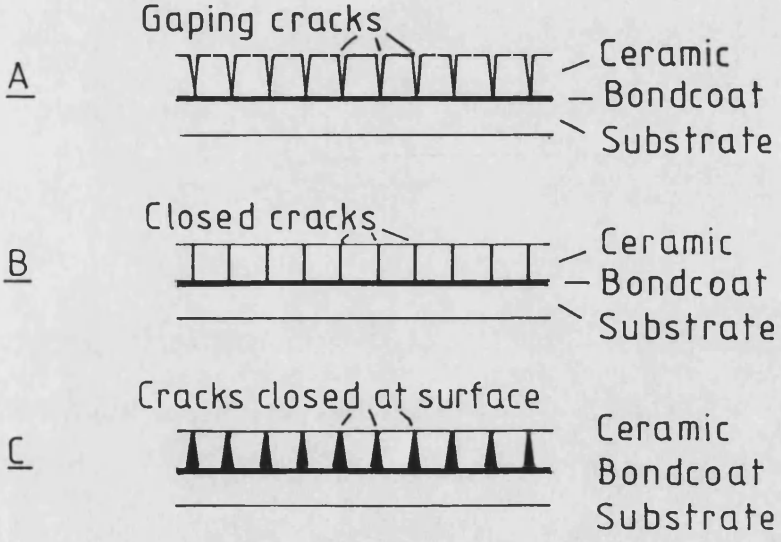

Figure 6·10 a-c Diagrams illustrating the cross-sectional form of thick, segmented two-layer coatings: A, As-sprayed. B, During a heating transient. C, At static operating temperature.

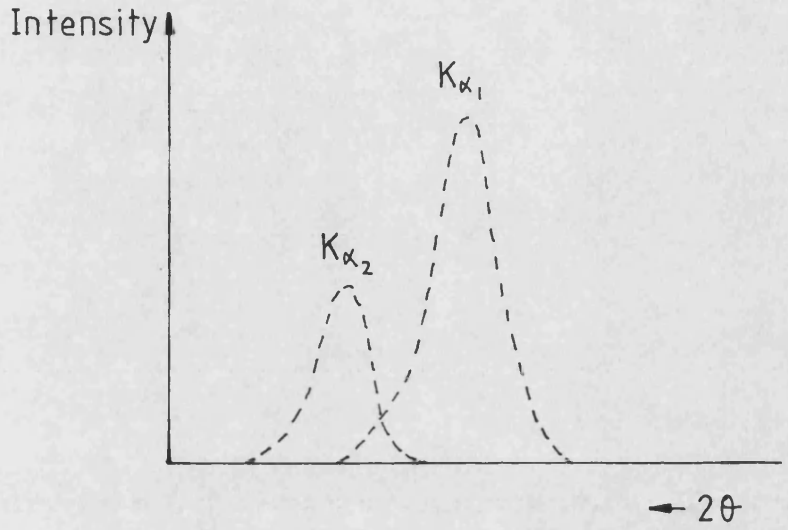

Figure A1 Graph showing the twin intensity profiles obtained for each reflection with Cu K_α radiation.

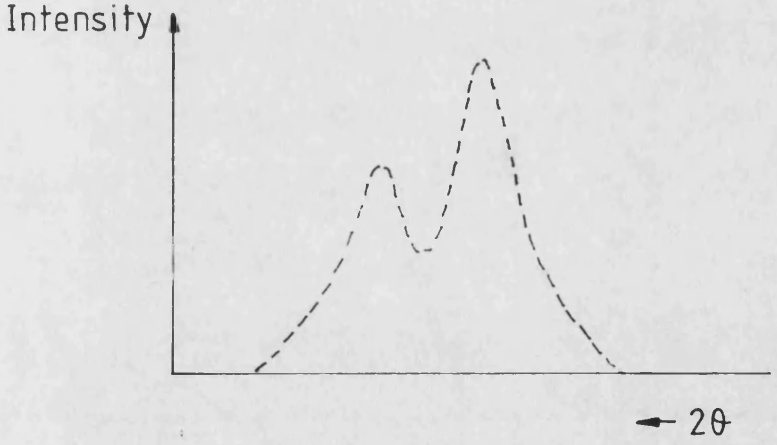

Figure A2 Graph showing the convoluted intensity profile obtained from a single high-angle reflection with Cu K_α radiation.

Plate 2.1a. S.E.M. micrograph showing the morphology of the atomised Ni-20%Cr-6%Al bondcoat alloy powder used in this study.

Plate 2.1b. S.E.M. micrograph showing the morphology of the fused/crushed ZrO_2-8%Y_2O_3 ceramic powder, denoted material A, used in this study.

Plate 2.1c. S.E.M. micrograph showing the morphology of the sintered/spray dried ZrO_2-8%Y_2O_3 ceramic powder, denoted material B, used in this study.

Plate 2.1d. S.E.M. micrograph showing the morphology of a chemically prepared/sintered ZrO_2-8%Y_2O_3 ceramic powder.

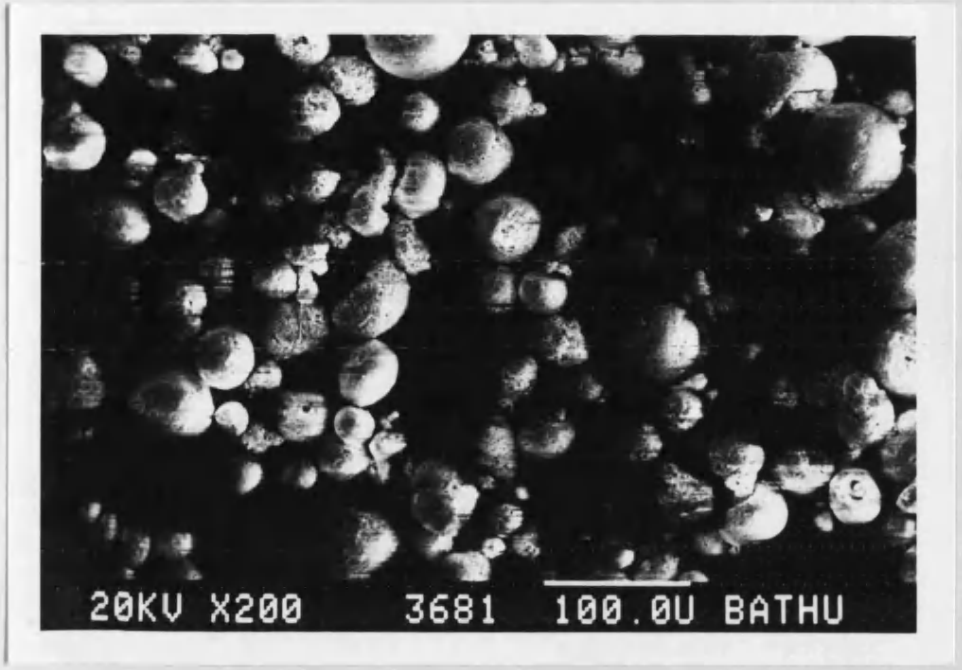

Plate 2.1e. S.E.M. micrograph showing the morphology of an unreacted/spray dried ZrO_2-20%Y_2O_3 ceramic powder.

Plate 2.1f. S.E.M. micrograph showing the morphology of an unreacted/ground ZrO_2-25%MgO ceramic powder.

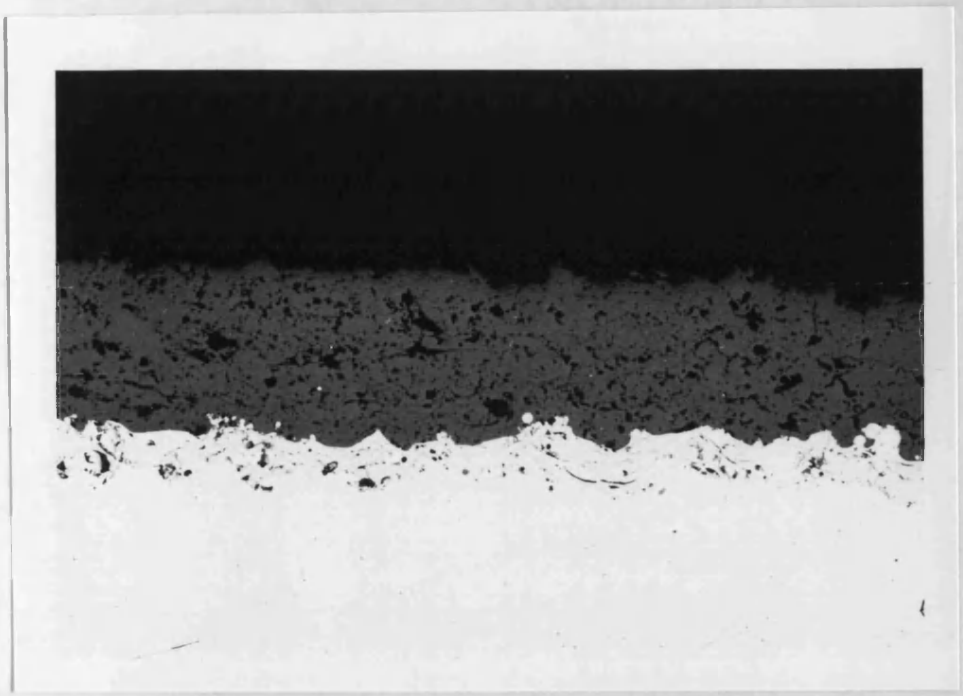

Plate 2.2. Optical micrograph showing a two-layer zirconia-8% yttria thermal barrier coating deposited on an aluminium substrate. Ceramic thickness = 0.25mm. (Magnification x75)

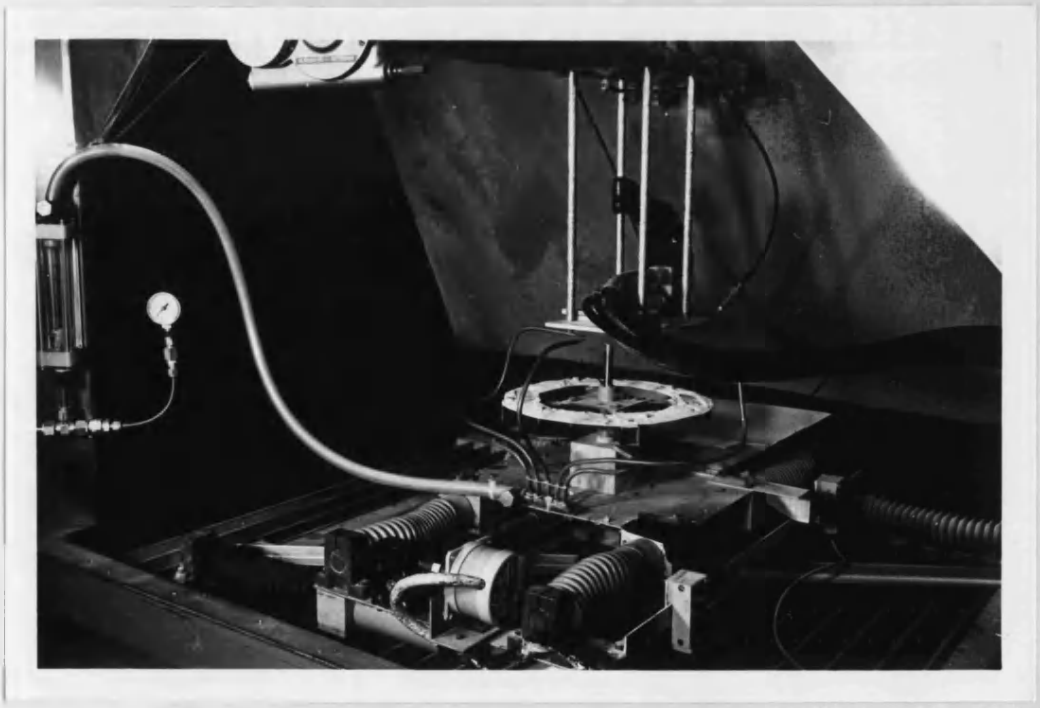

Plate 3.1. General view of plasma spray coating apparatus.

Plate 3.2. General view of twin powder feed unit. The right hand hopper is used for ceramic powder and is fitted with an optional stirring unit to aid material flow.

Plate 3.3. General view showing control computer and motor drive interface unit.

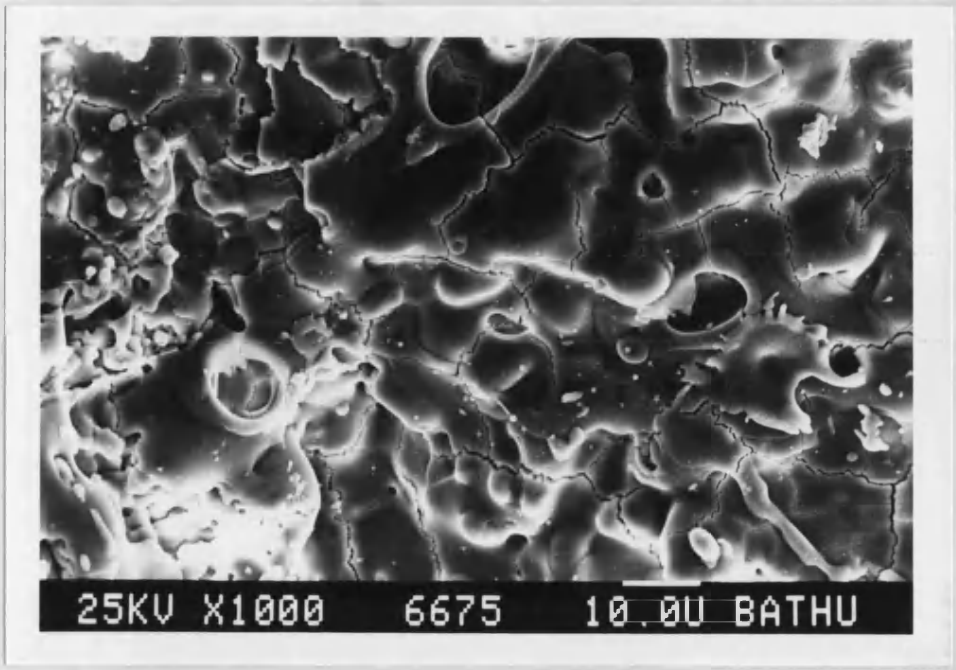

Plate 5.1a. S.E.M. micrograph of the surface of a coating of material A in which particles were optimally melted. Note the extensive shrinkage cracks in the 'splats'.

Plate 5.1b. S.E.M. micrograph of the surface of a coating of material A in which particles were poorly melted. Note the large unmelted particle which has retained its original morphology.

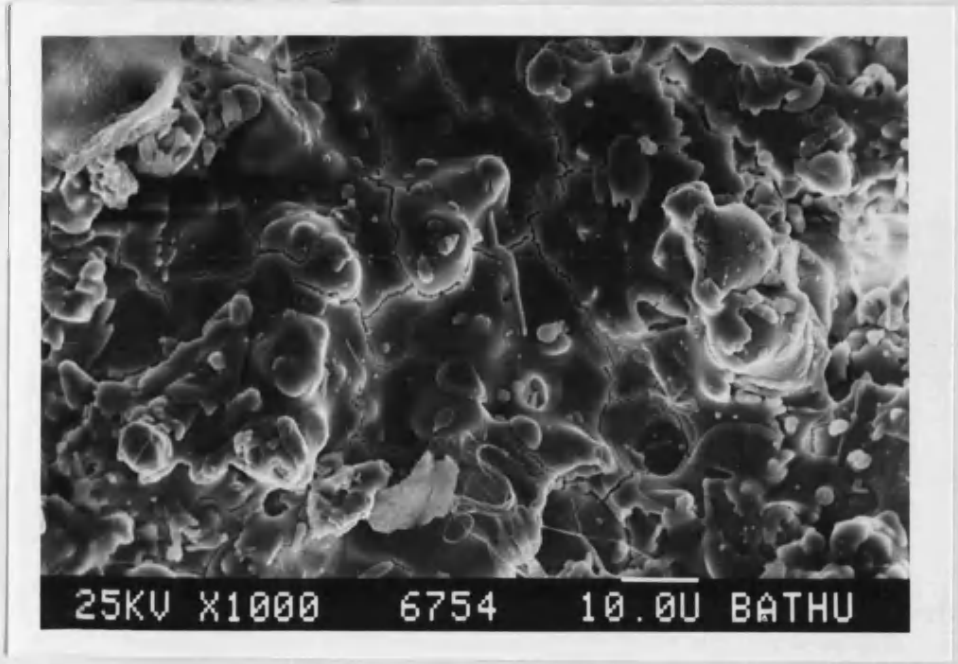

Plate 5.2a. S.E.M. micrograph of the surface of a coating of material B in which particles were optimally melted. Note the extensive shrinkage cracks in the 'splats'.

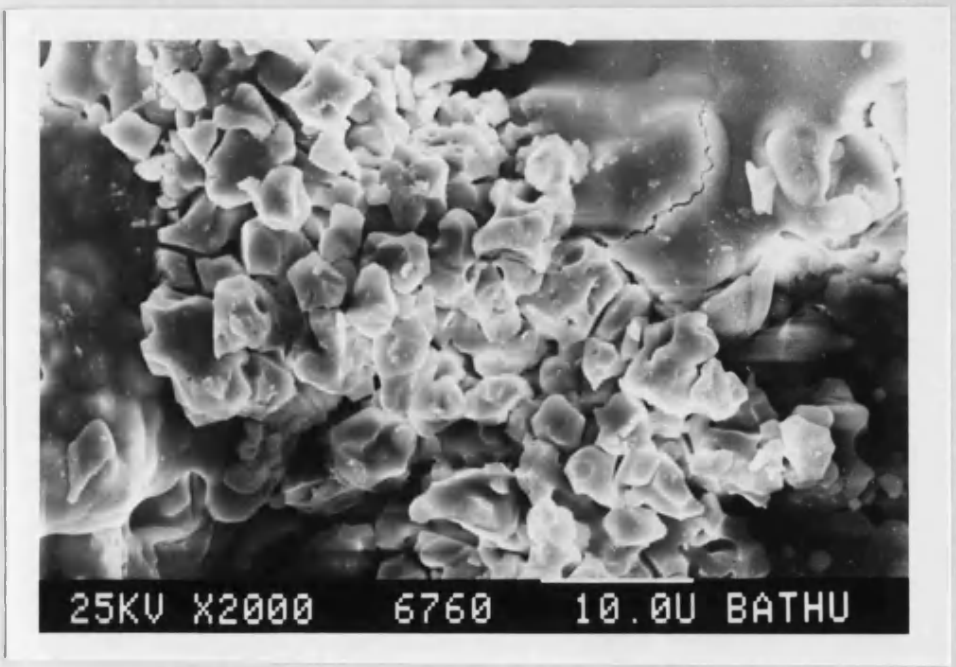

Plate 5.2b. S.E.M. micrograph of the surface of a coating of material B in which particles were poorly melted. Note the large unmelted particle which has fractured on impact, exposing the fine constituent particles.

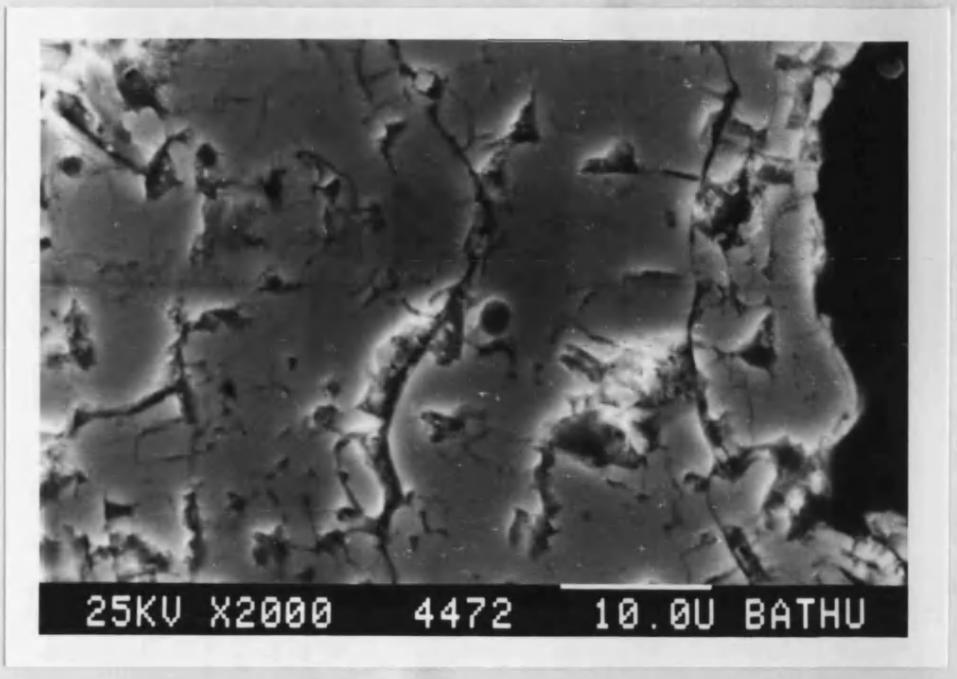

Plate 5.3. S.E.M. micrograph detailing the fine structure of the zirconia layer. The exposed surface is on the right.

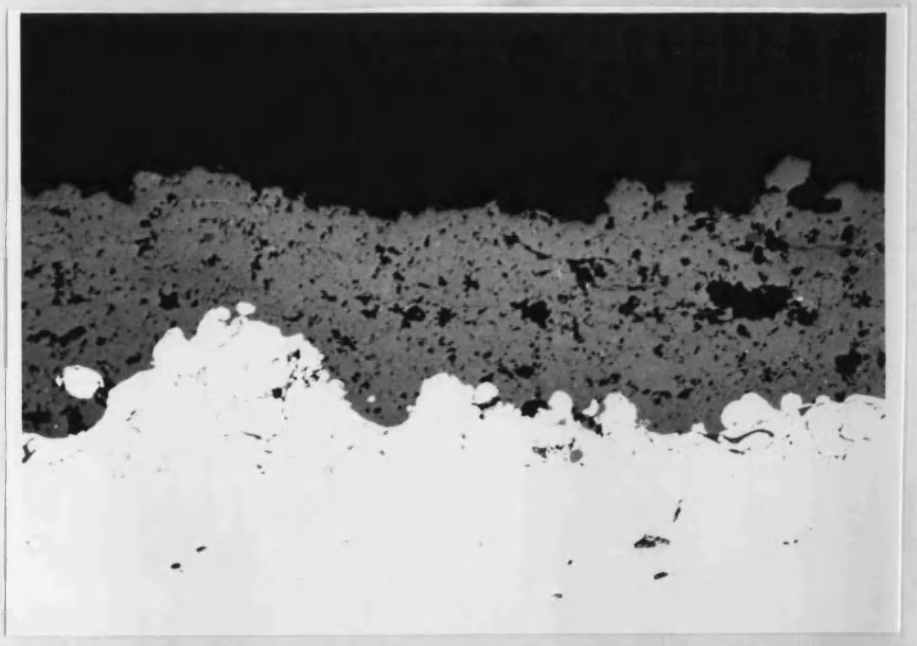

Plate 5.4a. Optical micrograph showing a 0.2mm thick zirconia coating of material A. The coating was deposited at $0.2ms^{-1}$ with intermittent cooling. (Magnification x125).

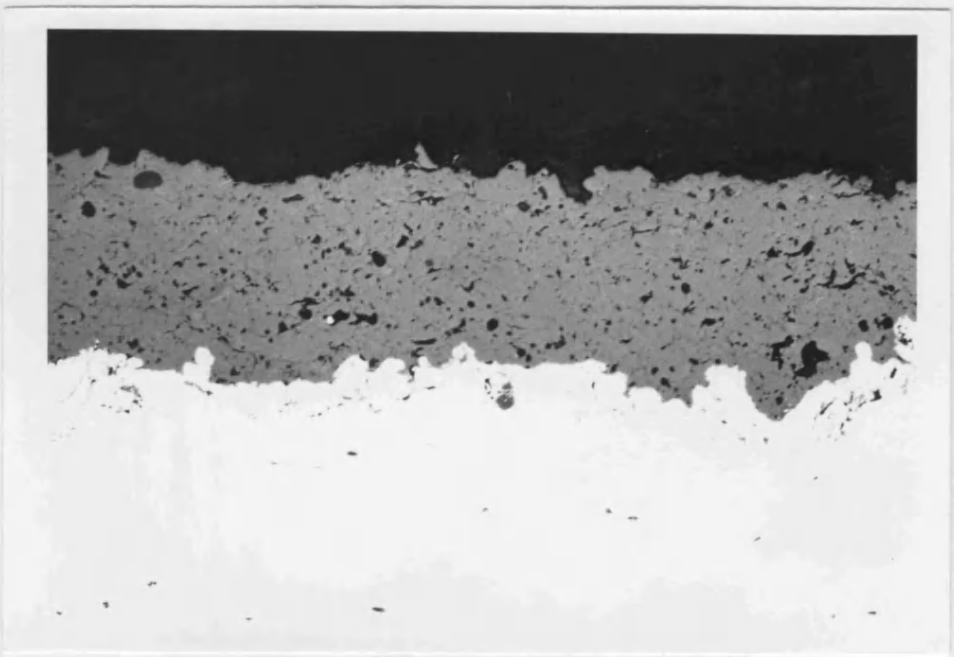

Plate 5.4b. Optical micrograph showing a 0.2mm thick zirconia coating of material A. The coating was deposited at 0.5ms^{-1} without intermittent cooling. (Magnification x125).

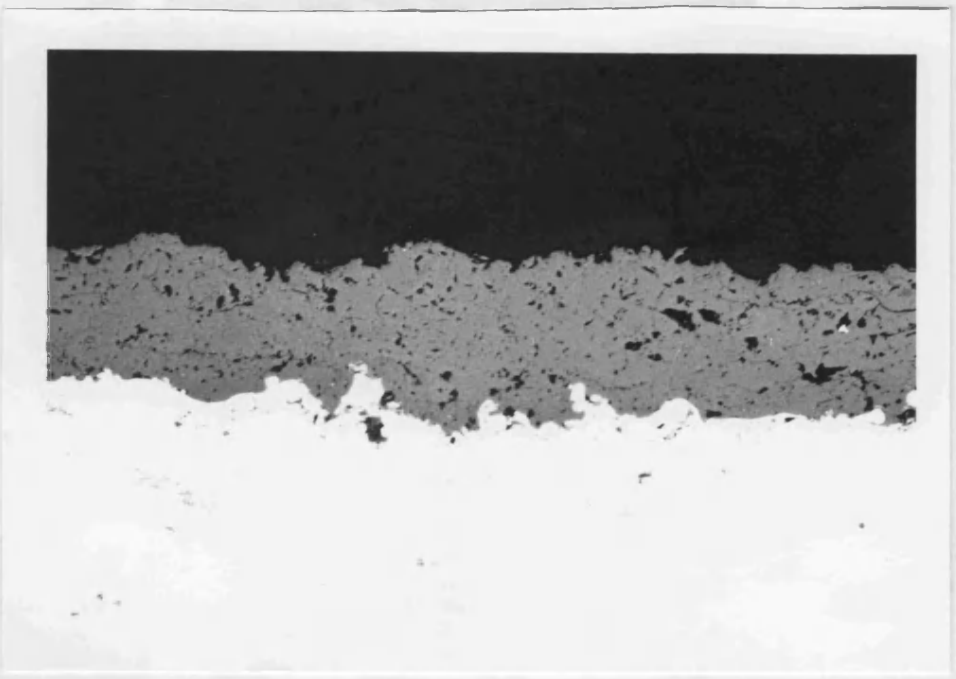

Plate 5.5a. Optical micrograph showing a 0.2mm thick zirconia coating of material A. The coating contains no instances of gross cracking (Magnification x100).

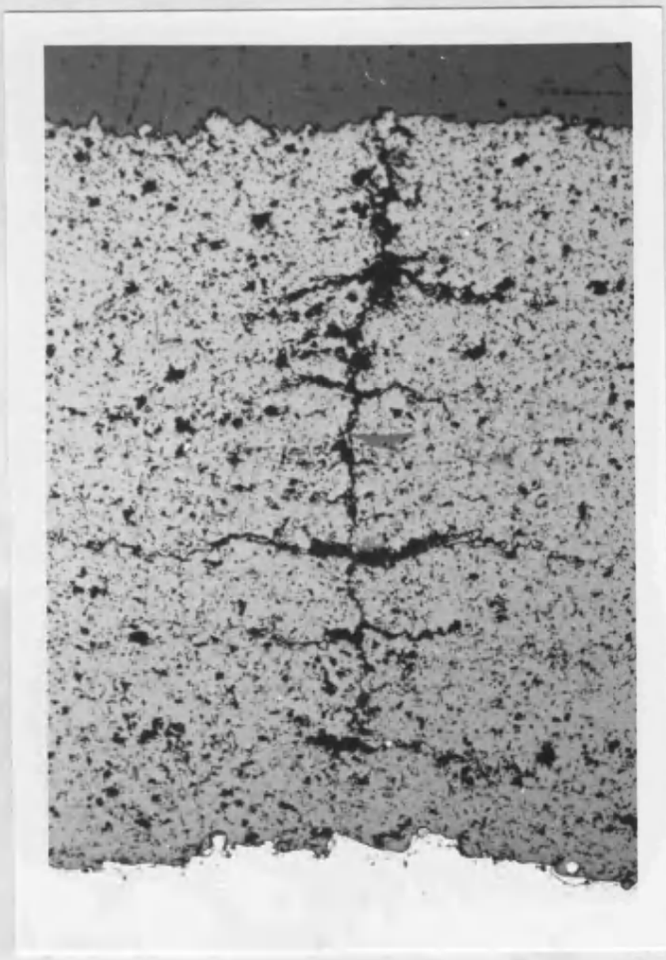

Plate 5.5b. Optical micrograph showing a 1.25mm thick zirconia coating of material A. The coating contains instances of vertical (tensile) and horizontal (shear) cracking (Magnification x80).

Plate 5.6a. Optical micrograph showing a 0.3mm thick zirconia coating of material A, containing a crack. The coating was deposited at a spray distance of 65mm, at $0.2ms^{-1}$. Note the large unmelted particle. (Magnification x100).

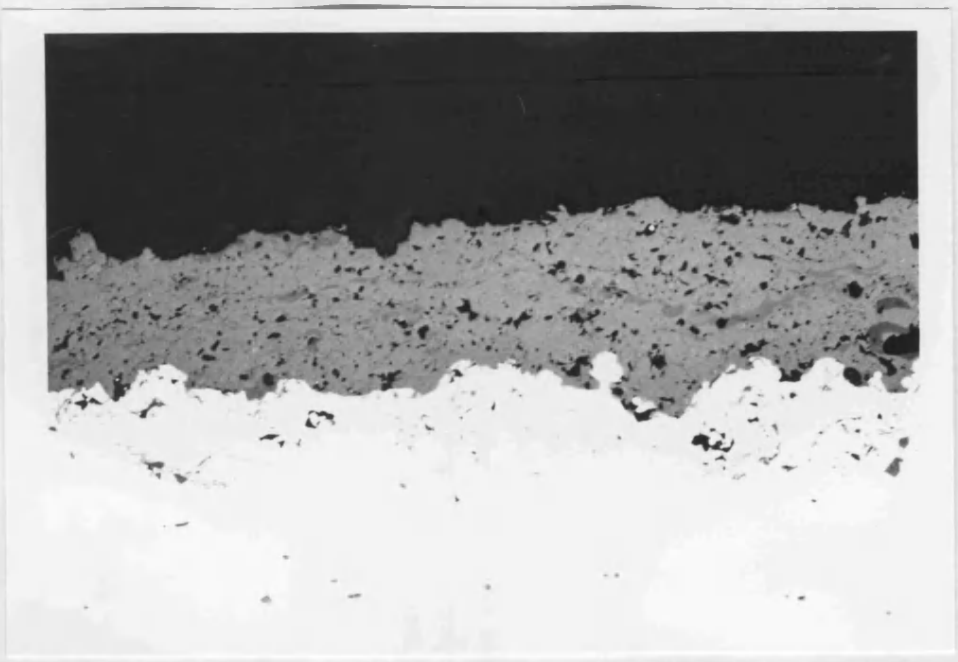

Plate 5.6b. Optical micrograph showing a 0.2mm thick zirconia coating of material A. The coating was deposited at a spray distance of 110mm, at $0.3ms^{-1}$. (Magnification x100).

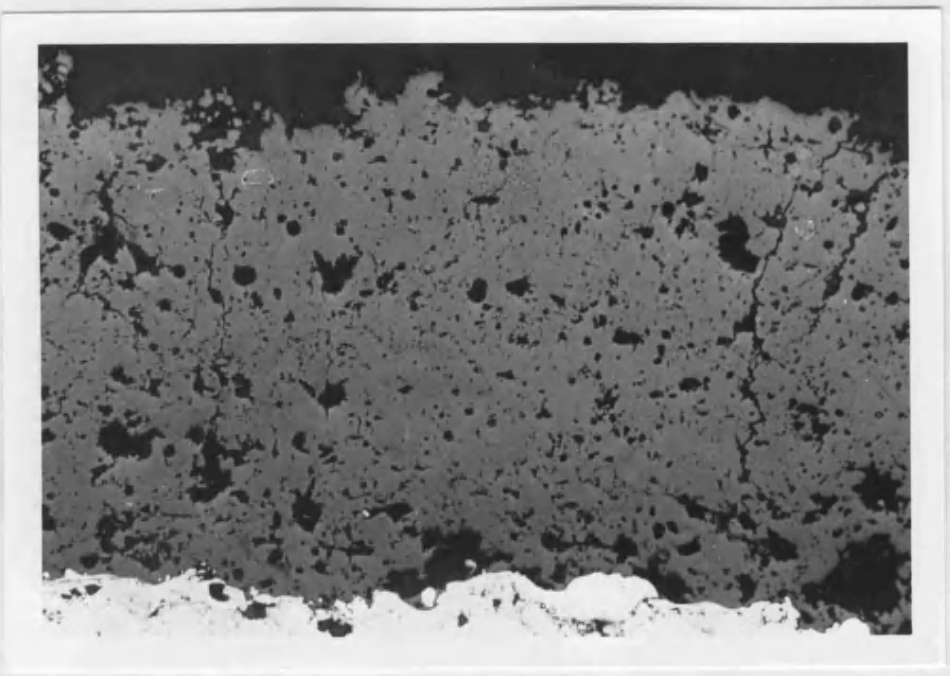

Plate 5.7a. Optical micrograph showing a 0.35mm thick zirconia coating of material B. The coating was deposited at $0.1ms^{-1}$ with combined air cooling. Note the vertical (tensile) crack. (Magnification x160).

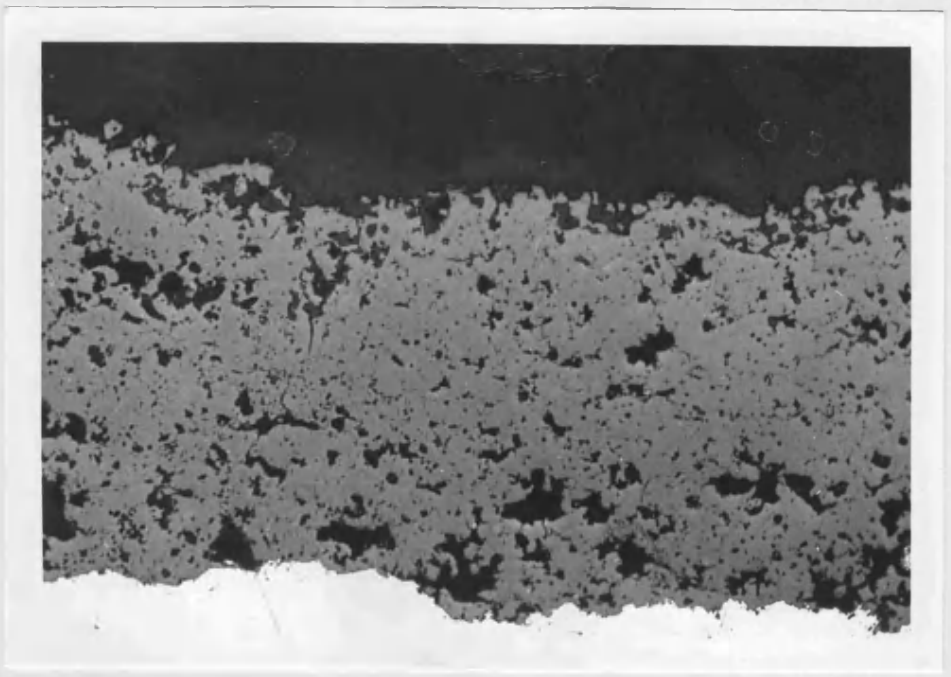

Plate 5.7b. Optical micrograph showing a 0.35mm thick zirconia coating of material B. The coating was deposited at $0.3ms^{-1}$ with combined air cooling. (Magnification x160).

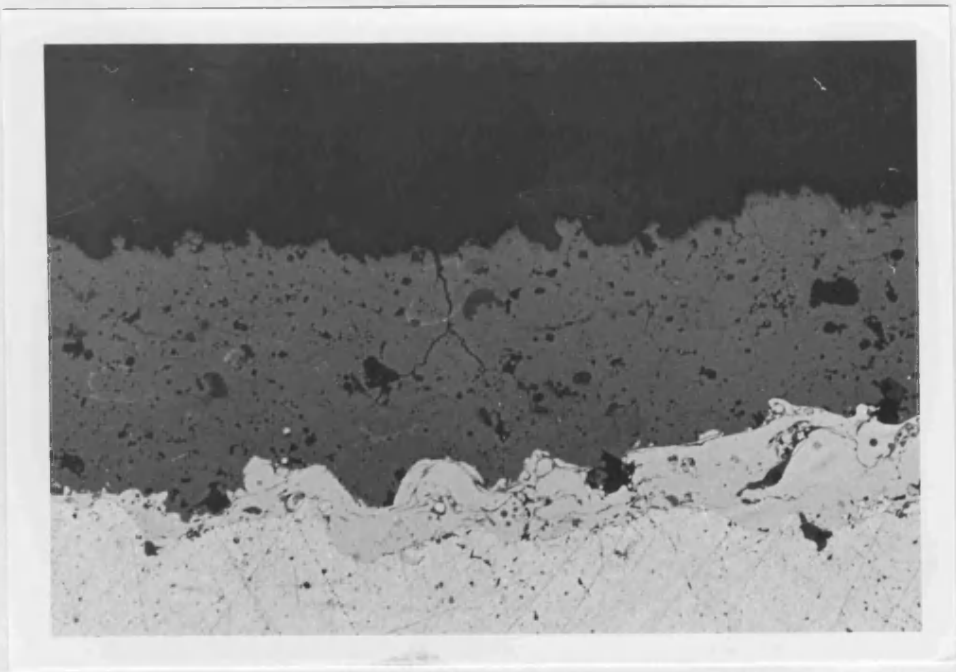

Plate 5.8a. Optical micrograph showing a 0.3mm thick zirconia coating of material A. The coating was deposited on a 1.85mm thick aluminium substrate and contains vertical (tensile) cracks. (Magnification x100).

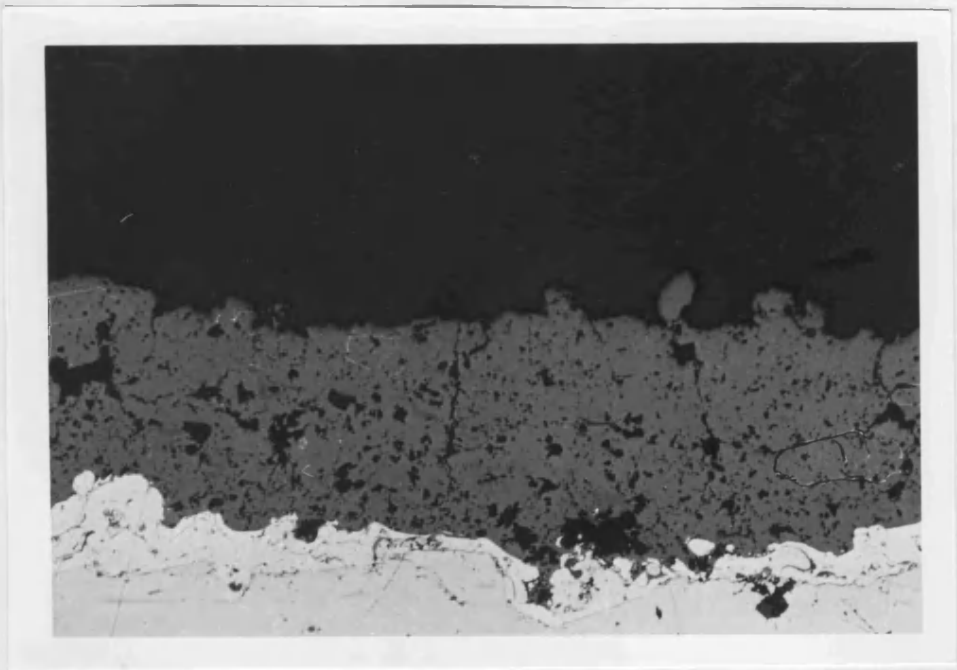

Plate 5.8b. Optical micrograph showing a 0.3mm thick zirconia coating of material A. The coating was deposited on a 1.5mm thick steel substrate and contains vertical (tensile) cracks. (Magnification x100).

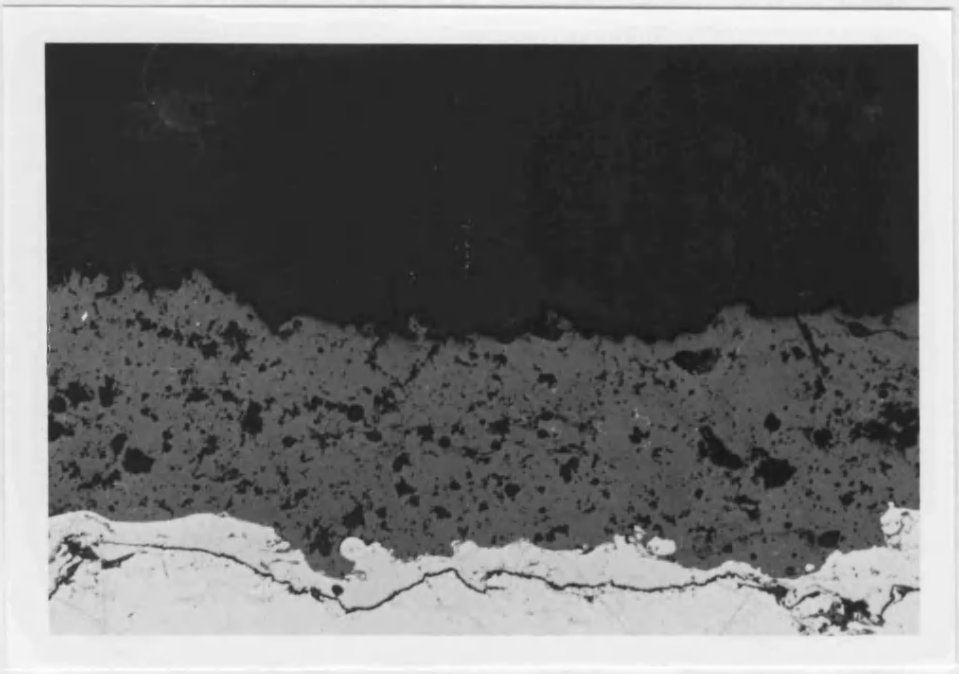

Plate 5.9. Optical micrograph showing a 0.3mm thick zirconia coating of material A. The coating was deposited on a copper substrate and contains a layer of black copper oxide beneath the bondcoat. (Magnification x100).

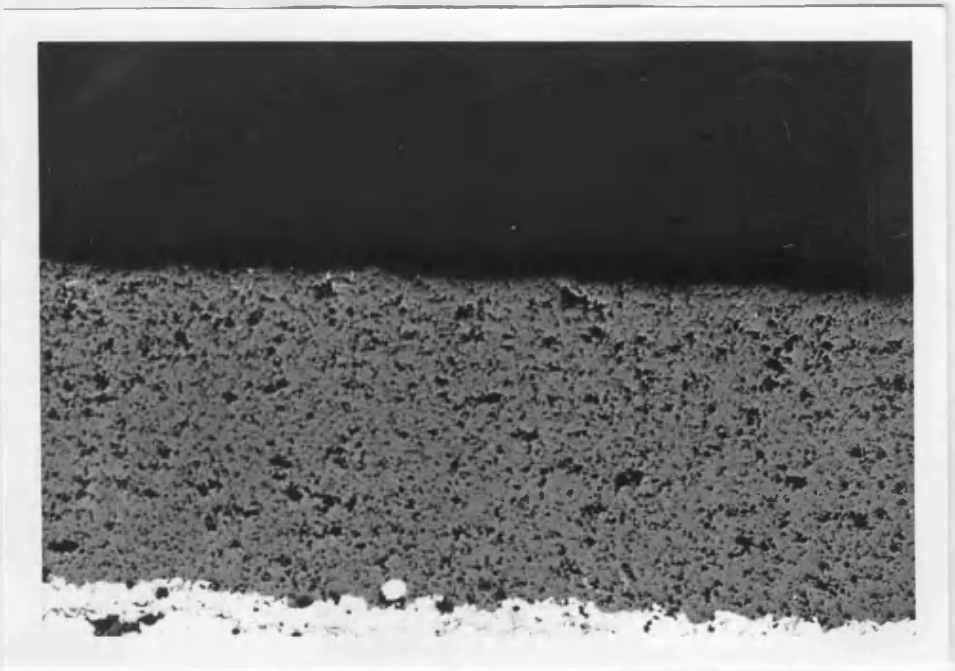

Plate 5.10a. Optical micrograph showing a 1.0mm thick zirconia coating of material C2, deposited on an aluminium substrate. (Magnification x40).

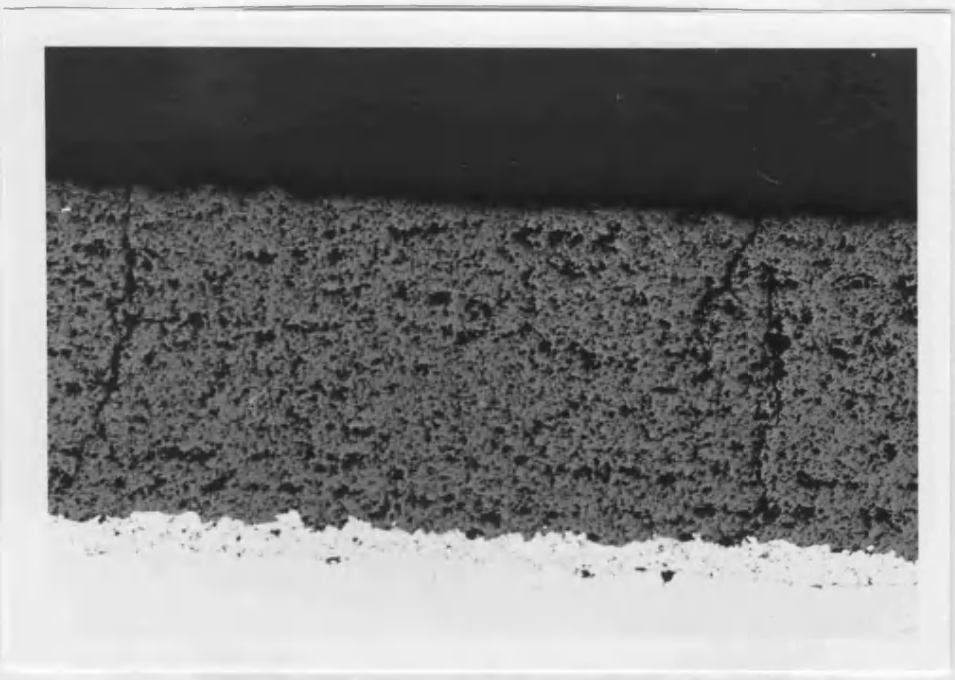

Plate 5.10b. Optical micrograph showing a 1.0mm thick zirconia coating of material C2, deposited on a steel substrate. The sample contains occasional vertical (tensile) cracks. (Magnification x40).

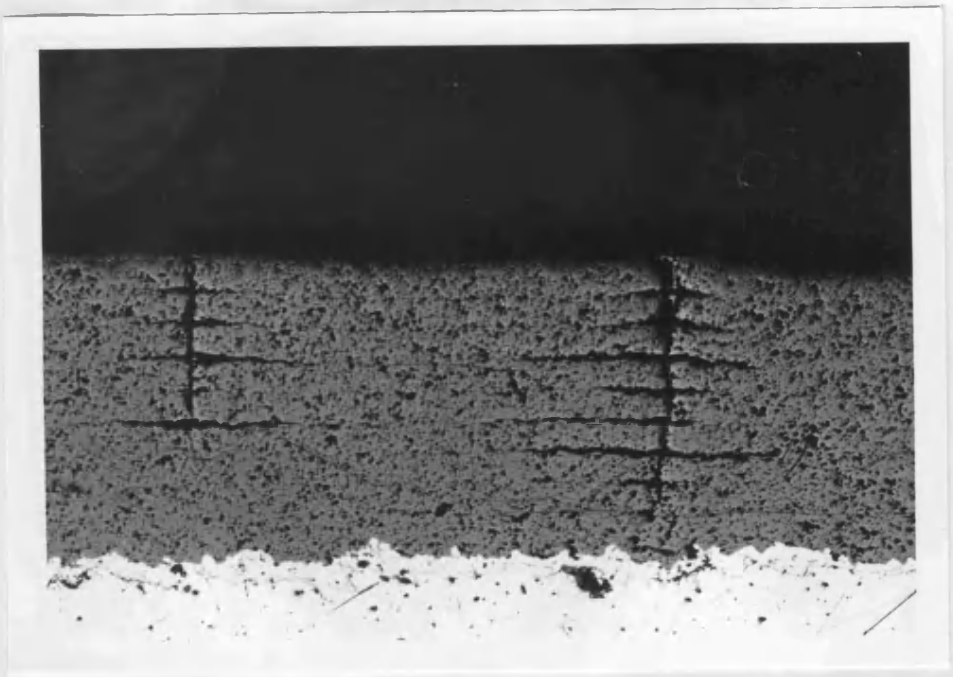

Plate 5.10c. Optical micrograph showing a 1.0mm thick zirconia coating of material C1, deposited on an aluminium substrate. The sample contains extensive vertical and horizontal crack networks. (Magnification x40).

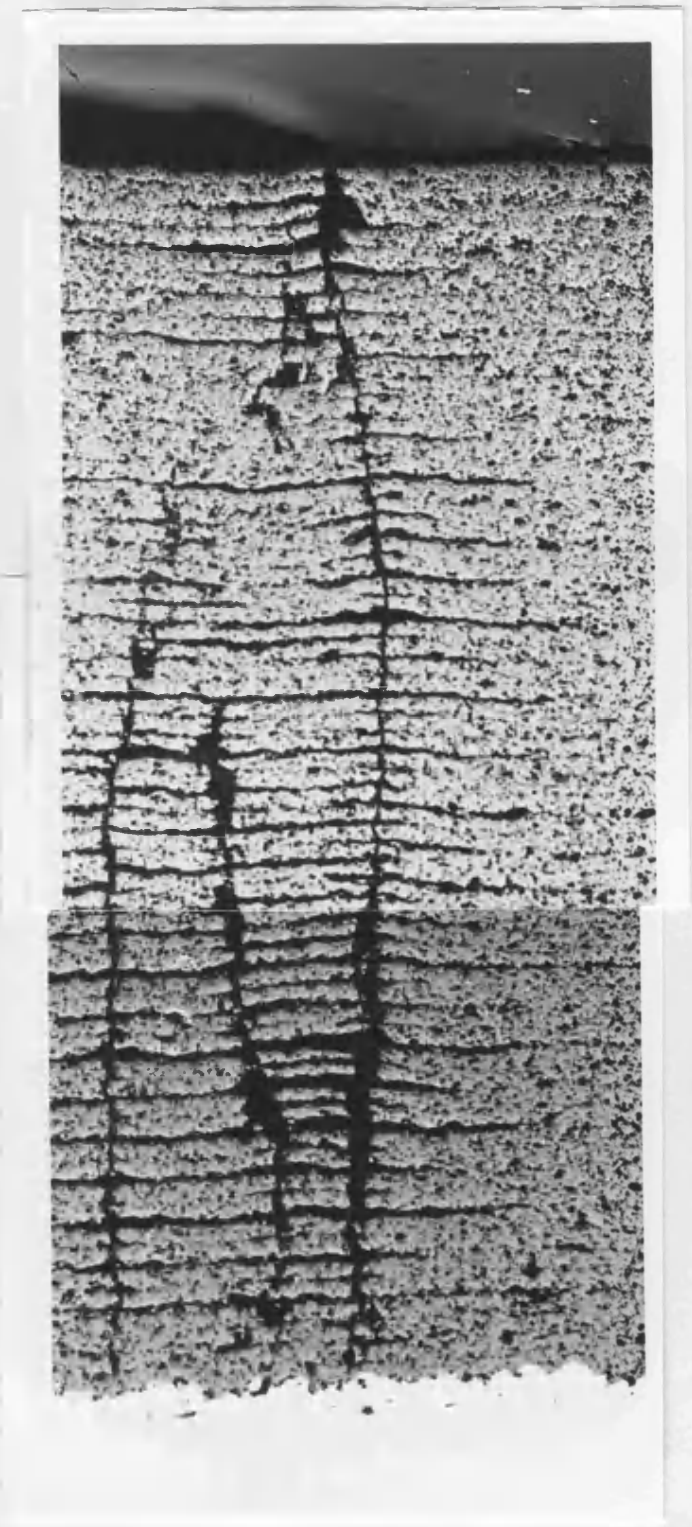

Plate 5.11a. Optical micrograph showing a 3.0mm thick zirconia coating of material C1, deposited on a steel substrate. The sample contains horizontal crack networks between layers deposited in different directions. (Magnification x50).

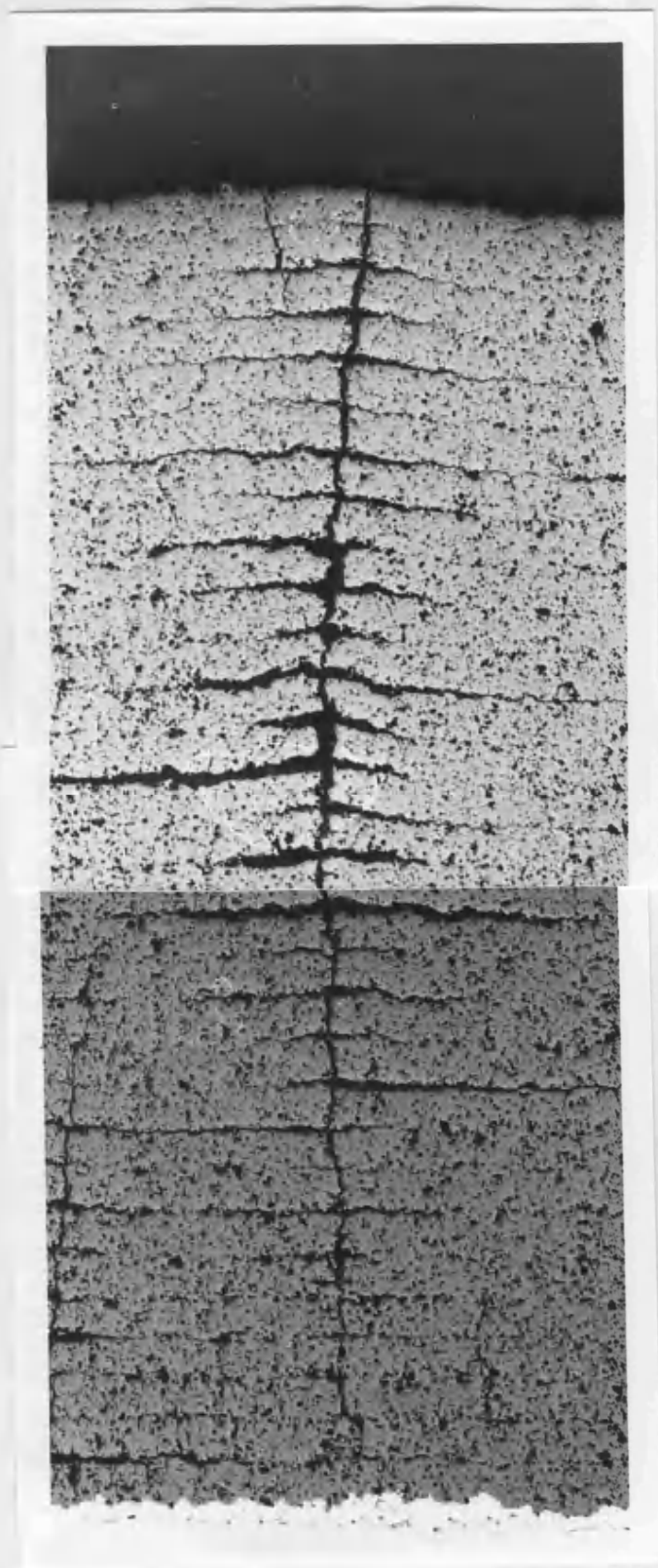

Plate 5.11b. Optical micrograph showing a 3.0mm thick zirconia coating of material C2, deposited on a steel substrate. The sample contains horizontal crack networks between consecutive layers. (Magnification x50).

Plate 5.11c. Optical micrograph showing a 3.0mm thick zirconia coating of material C3, deposited on a steel substrate. The sample contains horizontal crack networks between alternate layers. (Magnification x50).